University of Nevada, Reno

Role of Spin-Dependent Interactions in Chemical Reactions and Molecular Physics

A dissertation submitted in partial fulfillment of the

requirements for the degree of Doctor of Philosophy in

Chemical Physics

by

Vsevolod D. Dergachev

Dr. Sergey A. Varganov/Dissertation Advisor

December, 2021

THE GRADUATE SCHOOL

We recommend that the dissertation
prepared under our supervision by

VSEVOLOD D. DERGACHEV

entitled

Role of Spin-Dependent Interactions in Chemical Reactions and Molecular Physics

be accepted in partial fulfillment of the
requirements for the degree of

DOCTOR OF PHILOSOPHY

Sergey A. Varganov, Ph.D.
Advisor

David M. Leitner, Ph.D.
Committee Member

Samuel O. Odoh, Ph.D.
Committee Member

Timur V. Tscherbul, Ph.D.
Committee Member

David C. Cantu, Ph.D.
Graduate School Representative

David W. Zeh, Ph.D., Dean
Graduate School

December, 2021

ABSTRACT

This work describes development of theoretical models for applications where spin-dependent interactions play a key role. Specifically, we focus on the spin-orbit and hyperfine interactions in atoms and molecules, which are important for applications in photochemistry, photophysics, materials science, quantum sensing, and quantum computing. In the first part of this work, we discuss development and application of the nonadiabatic statistical theory (NAST) to predict kinetics of spin-forbidden chemical reactions, intersystem crossings and spin-crossovers. We describe the newly developed NAST software package and its capabilities. The package predicts the microcanonical and canonical rate constants for the nonadiabatic spin-orbit coupling driven and traditional adiabatic unimolecular reactions. In addition, the NAST package can calculate the probabilities and rate constants for transitions between individual M_S components of the spin multiplets, and process the results of electronic structure calculations to generate the necessary input data for the rate calculations. The second part of this work is motivated by the proposed applications of ultracold atoms in the quantum information science. The ultracold alkali atoms trapped in inert parahydrogen matrix have been shown to possess long coherence times between the hyperfine states $|F, m_F\rangle$. The long coherence times make these atoms promising candidates for spin-based qubits and quantum sensors. This coherence is limited by interaction between the electron spin of the alkali metal atom and the host matrix. To explain the experimental coherence times of ^{39}K, ^{85}Rb, ^{87}Rb, and ^{133}Cs atoms, we develop a model of

inhomogeneous broadening of the transitions between the $|F, m_F\rangle$ states due to the anisotropic hyperfine interaction between the metal and the host matrix. In the third part of this work, we model the effect of extreme variations in the speed of light on the electronic and atomic structures of small molecules. This part of work is motivated by the theories beyond the Standard Model of physics that treat the fundamental constants as dynamic entities.

DEDICATION

This dissertation is dedicated to the memory of my father Dmitry A. Dergachev, who passed away before completion of my doctoral study, and to my mother Marina M. Dergacheva and brothers Ilya D. Dergachev and Mikhail A. Dergachev for their support.

ACKNOWLEDGEMENTS

This work would not be possible without the guidance and support of my advisor Sergey A. Varganov. I also thank Jonathan Weinstein, Timur Tscherbul and Andrei Derevianko for productive collaborations. I am also grateful for help and support from the current and former members of Varganov's group at the University of Nevada, Reno.

TABLE OF CONTENTS

LIST OF TABLES

LIST OF FIGURES

CHAPTER 1. INTRODUCTION

I. Electron Spin as Relativistic Property of Matter

Spin is a property of matter carried by elementary particles – fermions with half-integer spin and bosons with integer spin. At the atomic level, the spin is carried by electrons and atomic nuclei. Therefore, understanding the properties of matter, as well as the interaction of matter with external electromagnetic field, requires consideration of the effects associated with electron and nuclear spins. A few examples, where the electron spin effects drive applications in chemistry, include light harvesting[1,2], electroluminescence of organic materials[3,4], catalytic activity of metalloproteins[5], and design of molecular electron spin-based qubits, sensors and memory devices[6–8].

The role of electron spin in electronic structure of atoms and molecules can be studied using different physical frameworks. There are essentially three choices. First is the Schrödinger one-component (scalar) wave equation postulated by Erwin Schrödinger in 1925. The Schrödinger equation rests on the postulates of quantum mechanics only and does not consider special relativity. Therefore, it does not describe interactions arising from electron and nuclear spins. However, the theory accounts for the electron spin in an *ad hoc* manner by antisymmetrizing the electronic wavefunction to satisfy the Pauli exclusion principle.

Second is the four-component Dirac equation, or equivalently, a system of four coupled first-order differential equations. The Dirac equation, derived by Paul Dirac in 1928, describes a fully relativistic electron in an external potential, but can be

generalized to many-electron problems as well. The Dirac equation is formulated to fulfill the postulates of special relativity, which require the speed of light to be constant and the laws of physics be identical in all inertial frames of reference. A change between inertial frames is described by the Lorentz transformation. Therefore, to fulfill the postulate of constant physical laws, the equations that describe these laws should be invariant under the Lorentz transformation. The Schrödinger equation is not invariant under the Lorentz transformation because it contains the partial derivatives of different orders with respect to time and space coordinates. In contrast, the Dirac equation is equivalent, first-order in both time and space coordinates, and therefore consistent with the postulates of special relativity. Two degrees of freedom of the Dirac equation are interpreted as two different particles – electron and positron – while the remaining two are accounted for by assigning particles' spin. Therefore, spin appears naturally in the Dirac equation. The degrees of freedom of the Dirac equation are usually arranged to form large and small components, where the small component vanishes in the non-relativistic limit, i.e. $c \rightarrow \infty$, where c is the speed of light.

Third, there exist approximation methods[9–14] based on derivation of the spin-free and spin-dependent relativistic correction terms from the power series expansion of the Dirac Hamiltonian in orders of $1/c^2$. These correction terms are either added as a perturbation to the Schrödinger equation or themselves form Schrödinger-like equations. Notably, using different approaches on how to decouple large and small components of the Dirac equation and wheatear or not the spin-free form is desired (two-component vs. one component), the resulting relativistic correction terms can take different forms. Some of these corrections are easier to interpret than the others and some are easier to calculate. The approximation methods include the Pauli

Hamiltonian[9,13], n-Order Regular Approximation (nORA)[10,11,13], eXact 2-Component (X2C)[13], and n-order Douglass-Kroll-Hess (nDKH)[12,13].

There are two fundamental aspects in which relativity impacts the electronic structure of atoms. To better understand these aspects, let us locally adhere to the language of relativistic corrections. An advantage of this is in bringing the correction terms whose form is useful in interpreting various interactions in atoms due to relativity. The first aspect is various magnetic interactions among electrons and nucleus. The motion of an electron in electrostatic field **E** created by a nucleus gives rise to internal magnetic field **B**. The magnetic moment $\mathbf{M_S}$ of electron then interacts with **B**, with the interaction energy $W = -\mathbf{M_S}\cdot\mathbf{B}$. As $\mathbf{M_S}$ and **B** are proportional to electron spin **S** and orbital angular momentum **L**, correspondingly, the interaction reduces to the well-known form of the spin-orbit interaction $\mathbf{S}\cdot\mathbf{L}$. Moreover, if a nucleus carries a non-zero spin, there appear interactions between the magnetic moment $\mathbf{M_I}$ of proton and $\mathbf{M_S}$, and between $\mathbf{M_I}$ and **B**. In turn, these interactions can be reduced to a more familiar form of $\mathbf{I}\cdot\mathbf{S}$ and $\mathbf{I}\cdot\mathbf{L}$, correspondingly. The interactions, which are due to the electron spin **S** only, are the spin-orbit (SO), spin-spin (SS) and orbit-orbit (OO) interactions. The SO interaction terms are described by the Breit-Pauli Spin-Orbit Hamiltonian[15], which was originally derived by Pauli in 1927:

$$\hat{H}_{\mathrm{SO}}^{\mathrm{BP}} = \frac{e^2}{2m_e^2c^2}\left\{\sum_i\left(-\nabla_i\left(\sum_A\frac{Z_A}{\mathbf{r}_{iA}}\right)\times\mathbf{p}_i\right)\cdot\mathbf{s}_i\right.$$

$$+\sum_i\sum_{j\neq i}\left(-\nabla_i\left(\frac{1}{\mathbf{r}_{ij}}\right)\times\mathbf{p}_i\right)\cdot\mathbf{s}_i$$

$$\left.+\sum_i\sum_{j\neq i}\left(-\nabla_j\left(\frac{1}{\mathbf{r}_{ij}}\right)\times\mathbf{p}_j\right)\cdot\mathbf{s}_i\right.$$

$$+\sum_{j}\sum_{i\neq j}\left(-\nabla_i\left(\frac{1}{\mathbf{r}_{ij}}\right)\times\mathbf{p}_i\right)\cdot\mathbf{s}_j\Bigg\}, \tag{1.1}$$

where e and m_e are the charge and mass of an electron, c is the speed of light, i and j are electron indices, A labels nuclei, Z_A is the charge of nucleus A, $\mathbf{r}_{iA}$ is the distance between an electron i and nucleus A, $\mathbf{r}_{ij}$ is the distance between electrons i and j, and $\mathbf{p}_i$ and $\mathbf{s}_i$ are momentum and spin of electron i. The first two terms in Eq. (1.1) are the one- and two-electron parts of the spin-same-orbit interaction. The third and fourth terms describe the spin-other-orbit interaction, where the magnetic moment of electron i interacts with orbital momentum of electron j and vice versa. The SS and OO interactions are described by separate correction terms:

$$\widehat{H}_{\mathrm{SS}}=\frac{e^2}{2m_e^2c^2}\sum_{i}\sum_{j\neq i}\left(\frac{\mathbf{s}_i^T\cdot\mathbf{s}_j}{r_{ij}^3}-3\frac{\left(\mathbf{s}_i^T\cdot\mathbf{r}_{ij}\right)\left(\mathbf{r}_{ij}^T\cdot\mathbf{s}_j\right)}{r_{ij}^5}-\frac{8\pi}{3}(\mathbf{s}_i^T\cdot\mathbf{s}_j)\delta(\mathbf{r}_{ij})\right), \tag{1.2}$$

$$\widehat{H}_{\mathrm{OO}}=-\frac{e^2}{2m_e^2c^2}\sum_{i}\sum_{j\neq i}\left(\frac{\mathbf{p}_i^T\cdot\mathbf{p}_j}{r_{ij}}+\frac{\left(\mathbf{p}_i^T\cdot\mathbf{r}_{ij}\right)\left(\mathbf{r}_{ij}^T\cdot\mathbf{p}_j\right)}{r_{ij}^3}\right), \tag{1.3}$$

For the states of non-zero total orbital angular momentum L and total spin angular momentum S, the spin-orbit coupling splits these electronic states into components. For example, the first excited doublet state of sodium, ^{2}P, where S = 1/2 and L = 1, is split into two components, $^2P_{1/2}$ and $^2P_{3/2}$, where subscripts 1/2 and 3/2 stand for two values of the total angular momentum J. The SS and OO interactions contribute to the zero-field splitting (ZFS), which lifts the degeneracy of magnetic levels in the absence of external magnetic field, in molecules with more than one unpaired electron. These electron-spin interactions constitute the fine structure of an

atom. The interactions between magnetic moments of electrons and nucleus, described above, are responsible for the hyperfine structure of an atom.

The second aspect is the scalar relativistic effects. The correction terms that describe these effects act in the position space only. Therefore, an equation that incorporates the scalar relativistic effects will resemble in structure the nonrelativistic Schrödinger equation. For this reason, calculation of the scalar relativistic effects is often added to capabilities of nonrelativistic electronic structure codes. There are two kinds of scalar relativistic effects. The first kind arises when velocity of the core electrons of an atom increases to the values comparable with the speed of light *c*. Relativistic corrections, describing different orders of this kind, can be derived from the power series expansion of the relativistic kinetic energy expression. Neglecting fourth- and higher-order terms of the expansion, the resulting terms are the rest-mass energy of electron, the non-relativistic kinetic energy, and the first kinetic energy correction called the mass-velocity term. The relativistic kinetic energy effect leads to energy stabilization and radial contraction of the core *s* orbitals. The joint effect of the relativistic kinetic energy correction and the spin-orbit coupling (SOC) results in overall stabilization of $s_{1/2}$ and $p_{1/2}$ orbitals (direct effect). As a consequence, orbitals in the same shell but with higher value of the total angular momentum J, i.e. $p_{3/2}$ and $d_{5/2}$, experience increased nuclear screening and, therefore, destabilize in energy, which is an indirect effect. The second kind of scalar relativistic effect is described by the Darwin term named after the English physicist Charles Galton Darwin. The Darwin term can be interpreted as the correction to the effective potential at the nucleus felt by an electron due to Zitterbewegung – rapid quantum oscillations of the electron. Since

the Darwin term corrects the potential at the nucleus, it affects only *s* electrons because the electron wavefunctions with a higher angular momentum are zero at the nucleus.

It is well-known that the special relativity is strongly manifested in heavy elements for which the non-relativistic description often leads to the predictions that are not even in qualitative agreement with experiments[16–18]. For example, the nonrelativistic coupled cluster single and double excitations CCSD method predicts the values of the electron affinity and ionization potential of Au atom to be almost 50 and 24 percent off the respective experimental values, while the relativistic CCSD predicts deviations within fraction of percent[19]. There are many famous examples of the effects of relativity, including the yellow color of gold, the low melting point of mercury, and the high voltage of a lead-acid battery[19]. Among heavy elements, of rising importance are studies of lanthanide (atomic numbers 57-71) complexes as candidates for electron spin-based single-molecule magnets[20,21]. Of great importance are studies of impact of relativistic effects on trends in properties of heavy elements[19,22–24]. These studies had probably started with the work of Descalux[22], where the author, solving the relativistic Dirac-Fock equation, systematically studied changes in the total electron energies of atoms, orbitals energies and positions of maximum orbital densities in comparison with nonrelativistic Hartree-Fock results. Modern studies[19,24] predict orbital destabilization and expansion for elements with the $(n+1)s \rightarrow nd$ electron shift (e.g., element 41, Nb: [Kr]$4d^4 5s^1$) and stabilization and contraction for elements with the $(n-1)f \rightarrow nd$ electron shift (e.g., element 91, Pa: [Rn] $5f^2 6d^1 7s^2$). These studies suggest that these trends are non-monotonic due to complex interplay of relativistic kinematic effects, SOC, relativistically modified nuclear screening, shell structure and electron correlation.

It is important to note that relativistic effects are not negligible even for the 1st–5th row elements. In chemistry of these elements, relativity is often manifested through the intersystem crossing (ISC)[25–27], i.e. non-radiative transitions between a pair of coupled electronic states with different spin multiplicities, mediated by the spin-dependent interactions. Among these, SOC is generally the largest in magnitude. The effects of SOC on the properties and structure of molecules containing 4th row transition metals like Cr, Fe, Ni and Cu are well known[2,5,28,29]. For example, in the metal-sulfur[5] and heme[2] proteins, the functioning mechanism often involves change in the spin state of the metal center of the protein active site via SOC-mediated ISC, which affects the light-harvesting and catalytic properties of these proteins. In addition, the SOC-mediated ISC transitions between two electronic states are involved in many other chemical reactions[30–35]. These reactions are named spin-forbidden due to their formal 'forbiddenness' in the dipole approximation because the transition electric dipole moment is independent of the electron spin, and therefore forbiddenness results from orthogonality of the spin parts of the wavefunctions of two electronic states. The reaction rates associated with the spin-forbidden reaction pathways are often assumed to be low. However, ISC can open competitive low-energy pathways in many reactions. For example, ISC is often encountered in the gas-[3,32,36] and solutionphase[34,37] reactions of organic molecules and polymers. Many of these reactions find application in artificial photosynthesis and organic light-emitting diodes (OLEDs)[3,34].

II. Dirac Equation

The Schrödinger equation is not invariant under the Lorentz transformation and, therefore, does not fulfill the requirements of special relativity. The search for the relativistic wave equation for an electron starts with the classical expression for the relativistic energy of a free moving particle:

$$E = \sqrt{\mathbf{p}^2c^2 + m^2c^4}, \tag{1.4}$$

where E is the energy of a free moving particle, $\mathbf{p}$ is the linear momentum, m is the mass of a particle, and c is the speed of light. Solving Eq. (1.4) is complicated because of the square root over the differentiation operator ∇^2 in $\mathbf{p}^2$. A possible solution of the power series expansion of the square root is not satisfactory, because it will lead to high-order derivatives with respect to spatial coordinates while leaving the time derivative order unchanged. Therefore, one would arrive at the Lorentz noninvariant wave equation, which violates the requirements of special relativity. Instead, the square-root problem can be overcome by squaring Eq. (1.4). After squaring and replacing the energy and momentum with the corresponding quantum mechanical operators ($E \rightarrow i\hbar\partial/\partial t$ and $\mathbf{p^2} \rightarrow -\hbar^2\nabla^2$), we arrive at the Klein-Gordon (KG) equation:

$$\left[-\frac{1}{c^2}\frac{\partial^2}{\partial t^2} + \nabla^2\right]\psi = \frac{m^2c^2}{\hbar^2}\psi. \tag{1.5}$$

This equation was derived by W. Gordon in 1926 and by O. Klein in 1927. The time and space coordinates enter the KG equation in the equivalent, second order. Therefore, the KG equation is Lorentz invariant. The KG equation predicts existence of both

positive and negative energy solutions, $E = \pm\sqrt{mc^2 + p^2}$. Later we will see that the solutions of negative energy predict the existence of antiparticles.

The KG equation cannot be accepted as the relativistic wave equation of an electron for two reasons. First, the KG equation describes spinless particles. As a consequence, it fails to describe the electron spin. Second, the following quantity – $\rho = (i\hbar/2mc^2)[\psi^*\partial\psi/\partial t - \psi\partial\psi^*/\partial t]$ – aimed to represent the probability density associated with the KG equation, is not positive definite. The KG equation is the second-order differential equation. Therefore, its solution requires two arbitrary initial conditions, i.e. it allows to choose independently initial values of ψ and $\partial\psi/\partial t$ such that the probability density can take both positive and negative values. In contrast, Paul Dirac's intention was to linearize the relativistic energy equation as:

$$\sqrt{\mathbf{p}^2c^2 + m^2c^4}\psi = c(\alpha_1 \mathrm{p}_1 + \alpha_2 \mathrm{p}_2 + \alpha_3 \mathrm{p}_3 + \beta mc)\psi, \tag{1.6}$$

where $\alpha_1, \alpha_2, \alpha_3$ and β are yet unknown coefficients. If α_1, α_2 and α_3 are scalars, Eq. (1.6) is invariant to spatial rotations. Dirac postulated that $\boldsymbol{\alpha}_1, \boldsymbol{\alpha}_2, \boldsymbol{\alpha}_3$ and $\boldsymbol{\beta}$ are quadratic matrices of yet unknown dimension. Then, ψ cannot be a scalar, but rather is a column vector. The desired relativistic equation for an electron must i) fulfill Eq. (1.4), ii) be invariant under the Lorentz transformation, and iii) have a positive define probability density. To fulfill these requirements, i) the smallest matrix dimension of $\boldsymbol{\alpha}_i$ must be four, ii) $\boldsymbol{\alpha}_i$ and $\boldsymbol{\beta}$ must possess as many negative as positive eigenvalues and 3) $\boldsymbol{\alpha}_i$ and $\boldsymbol{\beta}$ must obey the following anticommutation relations:

$$\begin{aligned} \boldsymbol{\alpha}_i\boldsymbol{\alpha}_j + \boldsymbol{\alpha}_j\boldsymbol{\alpha}_i &= 2\delta_{ij}\mathbf{I}, \\ \boldsymbol{\alpha}_i\boldsymbol{\beta} + \boldsymbol{\beta}\boldsymbol{\alpha}_i &= 0, \end{aligned} \tag{1.7}$$

$$\boldsymbol{\alpha}_i^2 = \boldsymbol{\beta}^2 = \mathbf{I}.$$

Based on these considerations, Dirac proposed the following quantum mechanical wave equation of a free electron:

$$\hat{h}^D\psi = [c\boldsymbol{\alpha}\cdot\mathbf{p} + \boldsymbol{\beta}'m_e c^2]\psi, \tag{1.8}$$

where $\hat{h}$ denotes a one-particle Hamiltonian. In the Dirac-Pauli representation:

$$\alpha_i = \begin{pmatrix} 0_2 & \boldsymbol{\sigma}_i \\ \boldsymbol{\sigma}_i & 0_2 \end{pmatrix},\ \boldsymbol{\beta} = \begin{pmatrix} \mathbf{I} & 0_2 \\ 0_2 & -\mathbf{I} \end{pmatrix},\ \boldsymbol{\beta}' = \begin{pmatrix} 0_2 & 0_2 \\ 0_2 & -2\mathbf{I} \end{pmatrix}$$

$$0_2 = \begin{pmatrix} 0 & 0 \\ 0 & 0 \end{pmatrix},\ \boldsymbol{\sigma}_x = \begin{pmatrix} 0 & 1 \\ 1 & 0 \end{pmatrix},\ \boldsymbol{\sigma}_y = \begin{pmatrix} 0 & -i \\ i & 0 \end{pmatrix},\ \boldsymbol{\sigma}_z = \begin{pmatrix} 1 & 0 \\ 0 & -1 \end{pmatrix} \tag{1.9}$$

In Eq. (1.5), $\boldsymbol{\beta}$ is replaced by $\boldsymbol{\beta}'$ to align the relativistic and nonrelativistic energy scales.

The Dirac theory fulfills the requirements of special relativity by introducing a system of four coupled first-order differential equations. Therefore, ψ appearing in Eq. (1.8) is a four-component wavefunction:

$$\psi = \begin{pmatrix} \psi_{\mathrm{L}}^{\alpha} \\ \psi_{\mathrm{L}}^{\beta} \\ \psi_{\mathrm{S}}^{\alpha} \\ \psi_{\mathrm{S}}^{\beta} \end{pmatrix} = \begin{pmatrix} \psi_{\mathrm{L}} \\ \psi_{\mathrm{S}} \end{pmatrix}, \tag{1.10}$$

where L and S correspond to the large and small components of the wavefunction, and not to be confused with orbital and spin angular momenta, and α and β describe spin degrees of freedom . Like in case of the KG equation, the solutions of the Dirac equation form continua of positive and negative energy states, where the negative energy continuum is often called the 'Dirac sea'. In the Dirac theory, the energetically lowest stable state, also called the vacuum state, is defined so all positive energy states are

empty, and all states of negative energy are occupied. Since a positron represents a hole in the lower continuum, such definition of the vacuum state implies that neither free electrons nor free positrons are present in the lowest energy state. The two continua, without and with alignment of the relativistic and nonrelativistic energy scales, are shown in panels A and B of Figure 1.1. In the presence of an external potential, for example, the electrostatic potential of a proton, the electrons are bound to the potential well and a manifold of electronic states E_0, E_1, … are lowered into the energy gap between two continua (Figure 1.1 C).

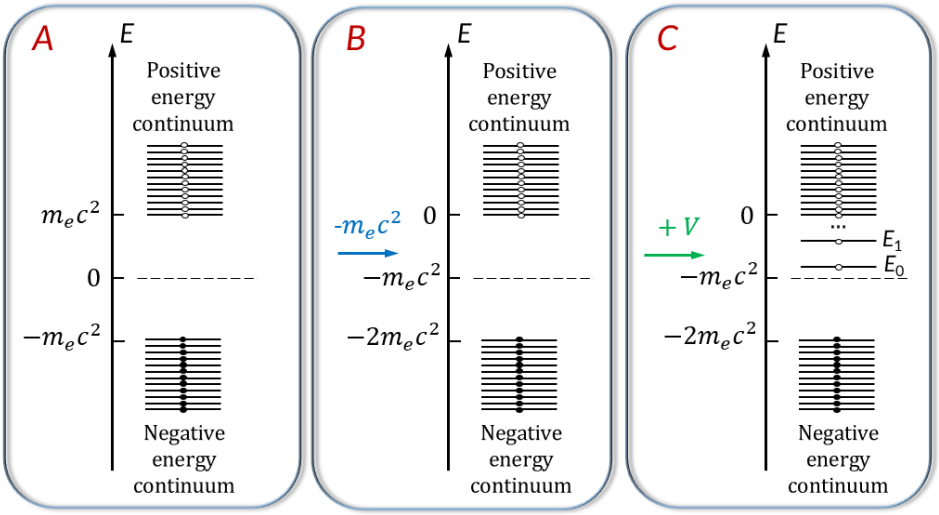

Figure 1.1. The vacuum state of the Dirac theory defined so all positive energy states are empty (○) and all states of negative energy are occupied (●). The panel A shows the vacuum state in the relativistic energy scale. In the panel B, the relativistic and nonrelativistic energy scales are aligned. In the panel C, the vacuum state is shown in the presence of bounding electrostatic potential V, which lowers a manifold of electronic states into the gap between two continua.

To describe relativistic electrons in atoms and molecules, the one-particle Dirac equation need to be generalized to a many-body equation. Such generalization requires an expression for the electron-electron interaction to be invariant to the Lorentz

transformation. Such expression can be derived from quantum electrodynamics by using the time-dependent perturbation theory. In practice, calculation of the associated two-electron matrix elements (integrals) is impractical due to n^8 scaling, where n is the number of one-electron basis functions. Instead, relativistically modified potential terms are added to the one-electron Dirac Hamiltonian. In atomic units ($\hbar = 1$ and $e = 1$), the total Hamiltonian containing the modified potential terms and nuclei electromagnetic field, but excluding external fields reads

$$\hat{H}^D = \sum_i \hat{h}_i^D + \hat{V}_{ee}^{CB} + \hat{V}_{nn} + e\boldsymbol{A}, \tag{1.11}$$

$$\hat{h}^D = \left[c\boldsymbol{\alpha}\cdot\mathbf{p} + \boldsymbol{\beta}' m_e c^2 + \hat{V}_{ne}\right], \qquad \hat{V}_{ne} = -\sum_A \frac{Z_A}{R_{iA}}, \tag{1.12}$$

$$\hat{V}_{ee}^{CB} = \sum_i \sum_{j>i} \frac{1}{r_{12}}\left(1 - \frac{1}{2c^2}\left[c\boldsymbol{\alpha}_1 \cdot c\boldsymbol{\alpha}_2 + \frac{(c\boldsymbol{\alpha}_1\cdot\boldsymbol{r}_{12})(c\boldsymbol{\alpha}_2\cdot\boldsymbol{r}_{12})}{2r_{12}^2}\right]\right), \tag{1.13}$$

$$\hat{V}_{nn} = \sum_A \sum_{B>A} \frac{Z_A Z_B}{R_{AB}}, \qquad \boldsymbol{A} = \sum_i \sum_A \gamma_A \frac{\mathbf{I}_A \times \boldsymbol{R}_{iA}}{R_{iA}^3}, \tag{1.14}$$

where $\hat{h}^D$ is the one-electron Dirac Hamiltonian for an electron in the electrostatic field of nuclei, $\hat{V}_{ee}^{CB}$ is the Coulomb-Breit modified electron-electron interaction, $\hat{V}_{nn}$ is the nuclear-nuclear repulsion term, $\boldsymbol{A}$ is the sum of vector potentials of all nuclei, and γ_A is the nuclear gyromagnetic factor of nucleus A. Relativistic corrections for $\hat{V}_{ne}$ are of order $1/c^3$ and even smaller for $\hat{V}_{nn}$, and therefore can be neglected.

In non-relativistic picture, the electron-electron interaction is instantaneous and described by the Coulomb potential. In relativistic picture, the Coulomb potential is only a zeroth-order term in the $1/c^2$ power series expansion of the full Lorentz-invariant electron-electron interaction and alone violates the principles of general relativity since

an instantaneous interaction is forbidden. The terms in the square brackets of Eq. (1.13) include the first-order corrections to the Coulomb potential. The first term in the brackets is the magnetic Gaunt interaction, and the second term is the gauge interaction that describes the retardation effect of the electron-electron interaction. Together, the Gaunt and gauge terms are called the Breit interaction. Adding the Coulomb interaction leads to the Coulomb-Breit potential of Eq. (1.13). Decoupling of the large and small components in the Dirac equation, followed by the expansion of the large component Hamiltonian to the order $1/c^2$, gives a set of well-known spin-free (scalar relativistic) and spin-dependent one- and two-electron correction terms, including the mass-velocity, Darwin, spin-orbit, spin-spin, spin-other-orbit, and orbit-orbit. If the nuclear spin degrees of freedom and an external magnetic field are included in Eq. (1.11), the correction terms, which correspond to coupling between the electron and nuclear magnetic moments and to coupling of either moment to the external magnetic field, can as well be derived. A well-known form of these correction terms are the Fermi-contact, nuclear dipole-dipole and Zeeman interaction terms . In this work, the focus is on the SOC and nuclear hyperfine (HFI) interactions. SOC is often the strongest coupling that mediates the ISC transitions between the electronic states with different spin multiplicities. The HFI interaction plays an important role in paramagnetic species, including spin decoherence in atoms and single-molecule magnets, which can be used as spin qubits in quantum sensing and computing.

III. Nonadiabatic Statistical Theory

Unimolecular reactions, which include isomerization, decomposition and dissociation processes, are an important class of chemical transformations. The transition state theory (TST)[38–41] is a powerful tool used to describe kinetics of such processes. TST is formulated based on statistical mechanics, and describes chemical transformations using the statistical quantities, such as a partition function and density of states. The nonadiabatic statistical theory (NAST)[35,42,43] extends TST to a nonadiabatic realm, where chemical processes involve more than one electronic state. The spin-dependent processes, including spin-forbidden reactions in chemistry, intersystem crossings (ISCs) in photochemistry and spin-crossovers in material science, form a special class of such nonadiabatic processes. In these processes, the reactant to product transformation induces change of the total electron spin of a system. The spin-dependent processes are important in many areas of molecular science, including photochemical reactions[44,45], chemical reactions on surfaces,[46,47] design of high efficiency organic light-emitting diodes,[3,4] and development of atomic and molecular spin systems for applications in the quantum information science.[20,21]

The formulation of the transition state theory starts with defining the phase space of the reaction, where the total energy of a system, described by the classical Hamiltonian $H(\mathbf{q},\mathbf{p})$ is a function of the coordinates $\mathbf{q}$ and momenta $\mathbf{p}$ of all the constituent atoms.[30,40,48] Associated with the phase space are four fundamental assumptions, to which any traditional TST or NAST obeys. The first assumption is the existence of a hypersurface in the phase space that divides the reaction space into the reactant and product regions. The second assumption is that the trajectories that come

from the reactant region and cross the dividing surface do not re-cross back. A third assumption states that the distribution of energy among the internal degrees of freedom (DOF) of a molecule is much faster than the reaction rate. A fourth assumption is that there exists a coordinate system that allows separation of the internal DOF into a one-dimensional reaction coordinate and remaining spectator DOF. Together, these assumptions form a basis for statistical formulation of the unimolecular reaction rate theories by describing the chemical transformation as a function of the internal states of a molecule. Both microcanonical and canonical ensembles can be used to describe such internal states. To calculate the reaction rate, it is necessary to compute either the density of states (microcanonical ensemble) or the partition function (canonical ensemble) of molecular system. The density of states can be defined as:[48]

$$\rho(E) = \frac{dW(E)}{dE}, \tag{1.15}$$

$$W(E) = \frac{1}{h^n} \int_{H(\mathbf{q},\mathbf{p})=0}^{H(\mathbf{q},\mathbf{p})=E} dq_1 .. dq_n dp_1 .. dp_n, \tag{1.16}$$

where $\rho(E)$ is the density of states of a system with the internal energy E, $W(E)$ is the number of states counted as an integral over the phase space in the energy range from zero to E. The corresponding partition function can be obtained via the Laplace transform:

$$Q(\beta) = \mathcal{L}\{\rho\}(E) = \int_0^\infty dE\, \rho(E) e^{-\beta E}, \tag{1.17}$$

where $\mathcal{L}\{\rho\}$ is the Laplace transform of the density of states, $\beta = 1/(k_\mathrm{B}T)$, k_B is the Boltzmann constant, and T is the temperature. A rigorous statistical formulation of the

unimolecular reactions was developed by Rice, Ramsperger and independently by Kassel, and later generalized by Marcus (RRKM theory).[49–51] An underlying idea of the RRKM theory is dependence of the reaction rate on internal energy states of a molecule. Having enough internal energy for a molecule to react is not a sufficient condition. The energy is distributed among all internal DOF, and the reaction will not occur until enough energy is accumulated in the reaction coordinate. Applied to unimolecular reactions in the high-pressure limit, RRKM theory becomes the microcanonical TST (μ-TST).[40,52,53] In μ-TST, a reaction rate is represented as a reaction flux, i.e. the number of molecules near the critical (transition) region of the phase space ($\mathbf{q}^* + d\mathbf{q}^*, \mathbf{p}^* + d\mathbf{p}^*$) per unit of time:

$$\text{Flux (reaction rate)} = \frac{dN(\mathbf{q}^*, \mathbf{p}^*)}{dt}, \tag{1.18}$$

$$\frac{dN(\mathbf{q}^*, \mathbf{p}^*)}{dt} = \frac{Nd\varepsilon^* \int_{H(\mathbf{q},\mathbf{p})=0}^{H(\mathbf{q},\mathbf{p})=E-\varepsilon-E_0} dq^*_1 .. dq^*_{n-1} dp^*_1 .. dp^*_{n-1}}{\int_{H(\mathbf{q},\mathbf{p})=0}^{H(\mathbf{q},\mathbf{p})=E} dq_1 .. dq_n dp_1 .. dp_n} = Nk(E, \varepsilon), \tag{1.19}$$

where N is the total number of molecules, ε is the energy stored in the reaction coordinate, $d\varepsilon^*$ is the infinitesimal change in the energy accumulated in the reaction coordinate near the critical region, E_0 is the energy of the transition state, and $k(E, \varepsilon)$ is the microcanonical rate constant. Note that the reaction coordinate is factored out in the numerator due to assumption of separability of the DOF. A considerable simplification of μ-TST can be achieved by averaging the phase-space integrals (Eq. 1.19) over microcanonical ensemble. It can be shown that after ensemble averaging,[30,48] the expression for the μ-TST rate constant takes the well-known form:

$$k(E) = \int_0^{E-E_0} d\varepsilon\, k(E,\varepsilon) = \frac{N^*(E-E_0)}{h\rho(E)}, \tag{1.20}$$

where $N^*(E-E_0)$ is the number of internal states of a molecule at the transition state, h is the Planck constant, $\rho(E)$ is the density of states at reactant's configuration. Note that $k(E,\varepsilon)$ is integrated over energy ε stored in the reaction coordinate to account for all possible distributions of the internal energy $E-E_0$ between the reaction coordinate and the transition state spectator DOF.

NAST is the extension of μ-TST to spin-dependent processes involving two electronic states with different spin multiplicities. For such processes, the hypersurface that divides the reactant and product regions of the phase space is the 3*N*-7 crossing seam between the potential energy surfaces of the two spin states, where 3*N*-7 is the number of the vibrational modes associated with the spectator DOF. The one-dimensional reaction coordinate corresponds to a single vibrational mode orthogonal to the spectator DOF of the crossing seam. The main NAST assumption, additional to those inherited from μ-TST, is that the spin-flip transitions take place at a minimum energy crossing point (MECP), which is a minimum on the crossing seam. NAST is discussed in detail in Chapter 3 of this dissertation.

This dissertation describes several examples of atomic and molecular systems where interactions due to electron spin play central role. The computational methods used in this work are described in Chapter 2. Chapter 3 is dedicated to the development and implementation of the Non-Adiabatic Statistical Theory (NAST) code to predict the rates of the spin-forbidden chemical reactions driven by SOC. Chapters 4 and 5 describe the spin coherence of alkali-metal atoms in solid parahydrogen, which are

promising candidates for quantum sensors and qubits. It is shown that the coherence time is defined by the strength of the hyperfine (HFI) interaction, which depends on interaction between the metal atom and the matrix. Chapter 6 discusses the effect of variation of the fundamental constants of physics, with focus on the speed of light, on the electronic and atomic structures of atoms and small molecules. Finally, Conclusion summarizes the key results of this work. These results cover capabilities of the recently implemented NAST code, development of theory of inhomogeneous broadening of hyperfine transitions of alkali-metal atoms, and changes in electronic structure properties of atoms and molecules when the speed of light is promoted to dynamical entity.

References

(1) Cianetti, S.; Négrerie, M.; Vos, M. H.; Martin, J. L.; Kruglik, S. G. Photodissociation of Heme Distal Methionine in Ferrous Cytochrome c Revealed by Subpicosecond Time-Resolved Resonance Raman Spectroscopy. *J. Am. Chem. Soc.* **2004**, *126* (43), 13932–13933. https://doi.org/10.1021/ja046442i.

(2) Falahati, K.; Tamura, H.; Burghardt, I.; Huix-Rotllant, M. Ultrafast Carbon Monoxide Photolysis and Heme Spin-Crossover in Myoglobin via Nonadiabatic Quantum Dynamics. *Nat. Commun.* **2018**, *9* (1), 1-8. https://doi.org/10.1038/s41467-018-06615-1.

(3) Goushi, K.; Yoshida, K.; Sato, K.; Adachi, C. Organic Light-Emitting Diodes Employing Efficient Reverse Intersystem Crossing for Triplet-to-Singlet State

Conversion. *Nat. Photonics* **2012**, *6* (4), 253–258. https://doi.org/10.1038/nphoton.2012.31.

(4) Mitschke, U.; Bäuerle, P. The Electroluminescence of Organic Materials. *J. Mater. Chem.* **2000**, *10* (7), 1471–1507. https://doi.org/10.1039/a908713c.

(5) Lykhin, A. O.; Kaliakin, D. S.; DePolo, G. E.; Kuzubov, A. A.; Varganov, S. A. Nonadiabatic Transition State Theory: Application to Intersystem Crossings in the Active Sites of Metal-Sulfur Proteins. *Int. J. Quantum Chem.* **2016**, *116* (10), 750–761. https://doi.org/10.1002/qua.25124.

(6) Bayliss, S. L.; Laorenza, D. W.; Mintun, P. J.; Kovos, B. D.; Freedman, D. E.; Awschalom, D. D. Optically Addressable Molecular Spins for Quantum Information Processing. *Science* **2020**, *370* (6522), 1309–1312. https://doi.org/10.1126/science.abb9352.

(7) Gaita-Ariño, A.; Luis, F.; Hill, S.; Coronado, E. Molecular Spins for Quantum Computation. *Nat. Chem.* **2019**, *11* (4), 301–309. https://doi.org/10.1038/s41557-019-0232-y.

(8) Goldman, M. L.; Doherty, M. W.; Sipahigil, A.; Yao, N. Y.; Bennett, S. D.; Manson, N. B.; Kubanek, A.; Lukin, M. D. State-Selective Intersystem Crossing in Nitrogen-Vacancy Centers. *Phys. Rev. B - Condens. Matter Mater. Phys.* **2015**, *91* (16), 1–11. https://doi.org/10.1103/PhysRevB.91.165201.

(9) Chang, C.; Pelissier, M.; Durand, P. Regular Two-Component Pauli-like Effective Hamiltonians in Dirac Theory. *Phys. Scr.* **1986**, *34* (5), 394–404. https://doi.org/10.1088/0031-8949/34/5/007.

(10) Dyall, K. G.; Van Lenthe, E. Relativistic Regular Approximations Revisited: An Infinite-Order Relativistic Approximation. *J. Chem. Phys.* **1999**, *111* (4), 1366–1372. https://doi.org/10.1063/1.479395.

(11) Filatov, M.; Cremer, D. On the Physical Meaning of the ZORA Hamiltonian. *Mol. Phys.* **2003**, *101* (14), 2295–2302. https://doi.org/10.1080/0026897031000137670.

(12) Reiher, M. Douglas-Kroll-Hess Theory: A Relativistic Electrons-Only Theory for Chemistry. *Theor. Chem. Acc.* **2006**, *116* (1), 241–252. https://doi.org/10.1007/s00214-005-0003-2.

(13) Dyall, K. G.; Faegri, K. J. *Introduction to Relativistic Quantum Chemistry*; Oxford University Press, 2007.

(14) Reiher, M.; Wolf, A. *Relativistic Quantum Chemistry.*, 2nd ed.; Wiley, 2015.

(15) Marian, C. M. Spin-Orbit Coupling in Molecules. In *Reviews in Computational Chemistry*; Lipkowitz, K. B., Boyd, D. B., Eds.; Wiley, 2001; Vol. 17, pp 99–204. https://doi.org/10.1002/0471224413.ch3.

(16) Pyykkö, P. Relativistic Effects in Structural Chemistry. *Chem. Rev.* **1988**, *88* (3), 563–594. https://doi.org/10.1021/cr00085a006.

(17) Pitzer, K. S. Relativistic Effects on Chemical Properties. *Acc. Chem. Res.* **1979**, *12* (8), 271–276. https://doi.org/10.1021/ar50140a001.

(18) Kutzelnigg, W. Solved and Unsolved Problems in Relativistic Quantum Chemistry. *Chem. Phys.* **2012**, *395* (1), 16–34.

https://doi.org/10.1016/j.chemphys.2011.06.001.

(19) Pyykkö, P. The Physics behind Chemistry and the Periodic Table. *Chem. Rev.* **2012**, *112* (1), 371–384. https://doi.org/10.1021/cr200042e.

(20) Bogani, L.; Wernsdorfer, W. Molecular Spintronics Using Single-Molecule Magnets. *Nat. Mater.* **2008**, *7* (1), 179–186. https://doi.org/10.1201/b11086-37.

(21) Ullah, A.; Cerdá, J.; Baldoví, J. J.; Varganov, S. A.; Aragó, J.; Gaita-Ariño, A. In Silico Molecular Engineering of Dysprosocenium-Based Complexes to Decouple Spin Energy Levels from Molecular Vibrations. *J. Phys. Chem. Lett.* **2019**, *10* (24), 7678–7683. https://doi.org/10.1021/acs.jpclett.9b02982.

(22) Desclaux, J. P. Relativistic Dirac-Fock Expectation Values for Atoms with Z = 1 to Z = 120. *At. Data Nucl. Data Tables* **1973**, *12* (4), 311–406. https://doi.org/10.1016/0092-640X(73)90020-X.

(23) Schwerdtfeger, P.; Heath, G. A.; Bennett, M. A.; Dolg, M. Low Valencies and Periodic Trends in Heavy Element Chemistry. A Theoretical Study of Relativistic Effects and Electron Correlation Effects in Group 13 and Period 6 Hydrides and Halides. *J. Am. Chem. Soc.* **1992**, *114* (19), 7518–7527. https://doi.org/10.1021/ja00045a027.

(24) Autschbach, J.; Siekierski, S.; Seth, M.; Schwerdtfeger, P.; Schwarz, W. H. E. Dependence of Relativistic Effects on Electronic Configuration in the Neutral Atoms of D- and f-Block Elements. *J. Comput. Chem.* **2002**, *23* (8), 804–813. https://doi.org/10.1002/jcc.10060.

(25) Marian, C. M. Understanding and Controlling Intersystem Crossing in Molecules. *Annu. Rev. Phys. Chem.* **2021**, *72*, 617–640. https://doi.org/10.1146/annurev-physchem-061020-053433.

(26) Mukherjee, S.; Fedorov, D. A.; Varganov, S. A. Modeling Spin-Crossover Dynamics. *Annu. Rev. Phys. Chem.* **2021**, *72*, 515–540. https://doi.org/10.1146/annurev-physchem-101419-012625.

(27) Fedorov, D. G.; Koseki, S.; Schmidt, M. W.; Gordon, M. S. Spin-Orbit Coupling in Molecules: Chemistry beyond the Adiabatic Approximation. *Int. Rev. Phys. Chem.* **2003**, *22* (3), 551–592. https://doi.org/10.1080/0144235032000101743.

(28) Yu-Tzu Li, E.; Jiang, T. Y.; Chi, Y.; Chou, P. T. Semi-Quantitative Assessment of the Intersystem Crossing Rate: An Extension of the El-Sayed Rule to the Emissive Transition Metal Complexes. *Phys. Chem. Chem. Phys.* **2014**, *16* (47), 26184–26192. https://doi.org/10.1039/c4cp03540b.

(29) Forster, L. S. Intersystem Crossing in Transition Metal Complexes. *Coord. Chem. Rev.* **2006**, *250* (15–16), 2023–2033. https://doi.org/10.1016/j.ccr.2006.01.023.

(30) Lorquet, J. C.; Leyh-Nihant, B. Nonadiabatic Unimolecular Reactions. 1. A Statistical Formulation for the Rate Constants. *J. Phys. Chem.* **1988**, *92* (16), 4778–4783. https://doi.org/10.1021/j100327a043.

(31) Poli, R.; Harvey, J. N. Spin Forbidden Chemical Reactions of Transition Metal Compounds. New Ideas and New Computational Challenges. *Chem. Soc. Rev.* **2003**, *32* (1), 1–8. https://doi.org/10.1039/b200675h.

(32) Lykhin, A. O.; Varganov, S. A. Intersystem Crossing in Tunneling Regime: T1 → S0 Relaxation in Thiophosgene. *Phys. Chem. Chem. Phys.* **2020**, *22* (10), 5500–5508. https://doi.org/10.1039/c9cp06956a.

(33) Pohlman, A. J.; Kaliakin, D. S.; Varganov, S. A.; Casey, S. M. Spin Controlled Surface Chemistry: Alkyl Desorption from Si(100)-2×1 by Nonadiabatic Hydrogen Elimination. *Phys. Chem. Chem. Phys.* **2020**, 22, 16641–16647. https://doi.org/10.1039/D0CP01913E.

(34) Kraabel, B.; Moses, D.; Heeger, A. J. Direct Observation of the Intersystem Crossing in Poly(3-Octylthiophene). *J. Chem. Phys.* **1995**, *103* (12), 5102–5108. https://doi.org/10.1063/1.470597.

(35) Harvey, J. N. Understanding the Kinetics of Spin-Forbidden Chemical Reactions. *Phys. Chem. Chem. Phys.* **2007**, *9* (3), 331–343. https://doi.org/10.1039/b614390c.

(36) Janaway, G. A.; Brauman, J. I. Direct Observation of Spin Forbidden Proton-Transfer Reactions: 3NO- + HA → 1HNO + A-. *J. Phys. Chem. A* **2000**, *104* (9), 0–3. https://doi.org/10.1021/jp992511h.

(37) Shafirovich, V.; Lymar, S. V. Spin-Forbidden Deprotonation of Aqueous Nitroxyl (HNO). *J. Am. Chem. Soc.* **2003**, *125* (21), 6547–6552. https://doi.org/10.1021/ja034378j.

(38) Truhlar, D. G.; Garrett, B. C.; Klippenstein, S. J. Current Status of Transition-State Theory. *J. Phys. Chem.* **1996**, *100*, 12771–12800. https://doi.org/doi.org/10.1021/jp953748q.

(39) Laidler, K. J.; King, M. C. The Development of Transition-State Theory. *J. Phys. Chem.* **1983**, *87* (15), 2657–2664. https://doi.org/10.1021/j100238a002.

(40) Garrett, B. C.; Truhlar, D. G. Variational Transition State Theory. *Theory Appl. Comput. Chem.* **2005**, 67–87. https://doi.org/10.1016/B978-044451719-7/50048-2.

(41) Garett, B. C.; Truhlar, D. G. Generalized Transition State Theory. Classical Mechanical Theory and Applications to Collinear Reactions of Hydrogen Molecules. *J. Phys. Chem.* **1978**, *83* (8), 1052–1079.

(42) Hammes-Schiffer, S.; Tully, J. C. Nonadiabatic Transition State Theory and Multiple Potential Energy Surface Molecular Dynamics of Infrequent Events. *J. Chem. Phys.* **1995**, *103* (19), 8513–8527. https://doi.org/10.1063/1.470162.

(43) Cui, Q.; Morokuma, K.; Bowman, J. M.; Klippenstein, S. J. The Spin-Forbidden Reaction $CH(^2\Pi)+N_2 \rightarrow HCN + N(^4S)$ Revisited. II. Nonadiabatic Transition State Theory and Application. *J. Chem. Phys.* **1999**, 110 (19), 9469-9482. https://doi.org/10.1063/1.478949.

(44) Hahn, S.; Stock, G. Femtosecond Secondary Emission Arising from the Nonadiabatic Photoisomerization in Rhodopsin. *Chem. Phys.* **2000**, *259* (2–3), 297–312. https://doi.org/10.1016/S0301-0104(00)00201-9.

(45) Yonemitsu, H.; Kawazoe, T.; Kobayashi, K.; Ohtsu, M. Nonadiabatic Photochemical Reaction and Application to Photolithography. *J. Lumin.* **2007**, *122–123* (1–2), 230–233. https://doi.org/10.1016/j.jlumin.2006.01.115.

(46) Frischorn, C.; Wolf, M. Femtochemistry at Metal Surfaces: Nonadiabatic

Reaction Dynamics. *Chem. Rev.* **2006**, *106* (10), 4207–4233. https://doi.org/10.1021/cr050161r.

(47) Pohlman, A. J.; Kaliakin, D. S.; Varganov, S. A.; Casey, S. M. Spin Controlled Surface Chemistry: Alkyl Desorption from Si(100)-2×1 by Nonadiabatic Hydrogen Elimination. *Phys. Chem. Chem. Phys.* **2020**, *22* (29), 16641–16647. https://doi.org/10.1039/d0cp01913e.

(48) Baer, T.; Hase, W. L. *Unimolecular Reaction Dynamics. Theory and Experiments.*; Oxford University Press: New York, 1996.

(49) Rice, O. K.; Ramsperger, H. C. Theories of Unimolecular Gas Reactions at Low Pressures. *J. Am. Chem. Soc.* **1927**, *49* (7), 1617–1629. https://doi.org/10.1097/00006324-199207000-00016.

(50) Kassel, L. S. Studies in Homogeneous Gas Reactions I. *J. Phys. Chem.* **1927**, *32* (2), 225–242.

(51) Marcus, R. A. Unimolecular Dissosiations and Free Radical Recombination Reactions. *J. Chem. Phys.* **1952**, *20* (3), 359–364.

(52) Tucker, S. C.; Pollak, E. Microcanonical Variational Transition-State Theory for Reaction Rates in Dissipative Systems. *J. Stat. Phys.* **1992**, *66* (3–4), 975–990. https://doi.org/10.1007/BF01055711.

(53) Klippenstein, S. J. Implementation of RRKM Theory for Highly Flexible Transition States with a Bond Length as the Reaction Coordinate. *Chem. Phys. Lett.* **1990**, *170* (1), 71–77. https://doi.org/10.1016/0009-2614(90)87092-6.

CHAPTER 2. METHODS

I. Hartree-Fock Theory

The Schrödinger equation describes interaction among non-relativistic electrons and nuclei in molecules. In the atomic units, it reads

$$\hat{H}\Phi_j(\mathbf{r},\mathbf{R}) = E_j\Phi_j(\mathbf{r},\mathbf{R}), \tag{2.1}$$

$$\hat{H} = -\sum_{A=1}^{M}\frac{1}{2M_A}\nabla_A^2 - \sum_{i=1}^{N}\frac{1}{2}\nabla_i^2 - \sum_{i=1}^{N}\sum_{A=1}^{M}\frac{Z_A}{r_{iA}} + \sum_{i=1}^{N}\sum_{j>i}^{N}\frac{1}{r_{ij}} + \sum_{A=1}^{M}\sum_{B>A}^{M}\frac{Z_AZ_B}{R_{AB}}, \tag{2.2}$$

where $\hat{H}$ is the total Hamiltonian, Φ_j is the total wavefunction of state *j*; **r** and **R** are the vectors of electronic and nuclear coordinates, correspondingly. The first term in Eq. (2.2) is the kinetic energy operator of *M* nuclei, $\hat{T}_n$; the second term is the kinetic energy operator of *N* electrons, $\hat{T}_e$; the third term describes the electron-nuclear attraction energy, $\hat{V}_{ne}$; the fourth term is the electron-electron repulsion energy, $\hat{V}_{ee}$; and the last term is the nuclear repulsion energy, $\hat{V}_{nn}$.

The Schrödinger equation (Eq. 2.1) cannot be solved analytically for systems with more than two particles (electrons and nuclei) due to particle-particle interactions. There exist approximations, however, that make numerical solution of Eq. (2.1) more tractable. Among these, the Born-Oppenheimer (BO) approximation is fundamental. The BO picture assumes separation of electronic and nuclear degrees of freedom in the total wavefunction $\Phi(\mathbf{r},\mathbf{R})$ due to their different variation timescales.[1] As a

consequence, the BO approximation allows to transform Eq. (2.1) into separate electronic and nuclear parts as:

$$\Phi_j(\mathbf{r},\mathbf{R}) = \Phi_j(\mathbf{r};\mathbf{R})\Phi_{nj}(\mathbf{R}), \tag{2.3}$$

$$\hat{H}_e\Phi_j(\mathbf{r};\mathbf{R}) = \left(\hat{T}_e + \hat{V}_{ne} + \hat{V}_{ee} + \hat{V}_{nn}\right)\Phi_j(\mathbf{r};\mathbf{R}) = E_j(\mathbf{R})\Phi_j(\mathbf{r};\mathbf{R}), \tag{2.4}$$

$$\hat{H}_n\Phi_{nj}(\mathbf{R}) = (\hat{T}_n + E_j(\mathbf{R}))\Phi_{nj}(\mathbf{R}) = E_T\Phi_{nj}(\mathbf{R}), \tag{2.5}$$

where Φ_j is the electronic wavefunction of state *j*; Φ_{nj} is the nuclear wavefunction of state *j*; $\hat{H}_e$ and $\hat{H}_n$ are the electronic and nuclear Hamiltonians, respectively. Eq. (2.4) is the electronic Schrödinger equation, whose eigenvectors $\Phi(\mathbf{r};\mathbf{R})$ and eigenvalues $E(\mathbf{R})$ depend parametrically on the nuclear positions **R**. Equation (2.5) describes the nuclear time-independent Schrödinger equation, where nuclei move in the electron potential $E_j(\mathbf{R})$. In this dissertation, we consider numerical solutions of the electronic Schrödinger equation only. A many-body Eq. (2.4) can be solved numerically by means of approximation of the wavefunction $\Phi_j(\mathbf{r};\mathbf{R})$ by $\Phi'_j(\mathbf{r};\mathbf{R})$ and applying variational principle to optimize trial function $\Phi'_j(\mathbf{r};\mathbf{R})$:

$$E'_j = \frac{\langle\Phi'_j|\hat{H}_e|\Phi'_j\rangle}{\langle\Phi'_j|\Phi'_j\rangle}, \tag{2.6}$$

where the electron and nuclear degrees of freedom are dropped for simplicity, and the bra-ket notation is used for the expectation values and overlap integrals. Generally, the variational principle is applied to find approximate solution of Eq. (2.4) for the ground state, $j = 0$. We now drop index *j* assuming the ground state energy and wavefunction and replace Φ' by Φ.

The simplest approach to solving Eq. (2.6) is a self-consistent field (SCF) method,[1-2] also known as the mean-field approximation or the Hartree-Fock (HF) method. The central approximation behind the HF method is replacement of the electron-electron interaction term by an effective one-electron potential, experienced by each electron from averaged motion of all other electrons. This is achieved by using a single Slater determinant as a trial wavefunction Φ:

$$\Phi = \frac{1}{\sqrt{N!}}\begin{vmatrix} \chi_1(1) & \chi_2(1) & \dots & \chi_N(1) \\ \chi_1(2) & \chi_2(2) & \dots & \chi_N(2) \\ \dots & \dots & \ddots & \vdots \\ \chi_1(N) & \chi_2(N) & \dots & \chi_N(N) \end{vmatrix}, \tag{2.7}$$

where the determinant form ensures the antisymmetry of Ψ with respect to electron exchange, and $1/\sqrt{N!}$ is the normalization constant. The wavefunction Φ is written in a basis of one-electron functions, molecular spin-orbitals, that describe both the spatial and spin degrees of freedom of each electron. The spatial part of Molecular Orbitals is represented as a Linear Combination of Atomic Orbitals (MO-LCAO):

$$\psi_i(\mathbf{r}) = \sum_{\mu=1}^{K} C_{\mu i}\phi_\mu(\mathbf{r}), \qquad i = \overline{1,N} \tag{2.8}$$

where *i* is the electron index, ϕ_μ are the atomic orbitals used to describe the molecular orbital ψ_i, and $C_{\mu i}$ are the linear variational parameters optimized to minimize the ground state energy (Eq. 2.6). Variational optimization of the $C_{\mu i}$ coefficients leads to the Hartree-Fock-Roothaan (HFR) equation:

$$\mathbf{FC} = \boldsymbol{\varepsilon}\mathbf{SC}, \tag{2.9}$$

where **F** is the $K \times K$ Fock matrix containing one- and two-electron integrals of the $\hat{T}_e$, $\hat{V}_{ne}$ and $\hat{V}_{ee}$ operators of the electronic Schrödinger equation in the basis of atomic orbitals, **C** is $K \times K$ matrix of $C_{\mu i}$ coefficients. The $K \times K$ matrix **S** represents the overlap integral $\langle \Phi | \Phi \rangle$ in the basis of atomic orbitals, and $\boldsymbol{\varepsilon}$ is the diagonal matrix of molecular orbital energies. The matrix elements of the two-electron part of the Fock matrix **F** are the Coulomb (J) and exchange (K) integrals[2] of the form:

$$J_{ij} = \int |\psi_i(\mathbf{r}_1)|^2 \frac{1}{r_{12}} \left|\psi_j(\mathbf{r}_2)\right|^2 d\mathbf{r}_1 d\mathbf{r}_2, \tag{2.10}$$

$$K_{ij} = \int \psi_i(\mathbf{r}_1)\psi_j(\mathbf{r}_1) \frac{1}{r_{12}} \psi_i(\mathbf{r}_2)\psi_j(\mathbf{r}_2) d\mathbf{r}_1 d\mathbf{r}_2. \tag{2.11}$$

The HFR equation is solved iteratively: an initial guess of molecular orbitals in Eq. (2.8) is given by choosing initial values of the expansion coefficients **C**. Then, Eq. (2.9) is solved in a self-consistent manner by using $\mathbf{C}^n$ and $\boldsymbol{\varepsilon}^n$ solutions at iteration n as a starting guess for the $n + 1$ iteration, until convergence is reached. Upon convergence, the total electronic energy E of the closed-shell ground state is

$$E = 2\sum_{i=1}^{N/2} h_{ii} + \sum_{i=1}^{N/2}\sum_{j=1}^{N/2} (2J_{ij} - K_{ij}), \tag{2.12}$$

where h_{ii} are matrix elements of the one-electron part of the Fock matrix, and J_{ij} and K_{ij} are two-electron matrix elements associated with the Coulomb (Eq. 2.10) and exchange (Eq. 2.11) interactions.

In the mean-field HF method, the correlation between the electrons of different spin is missing. However, the HF method includes the exchange correlation between electrons of parallel spin: the probability of two electrons with parallel spins to occupy

the same point in space equals zero. The missing electron correlation can be recovered by improving the HF wavefunction, Φ. The dynamic part of missing correlation comes from the correlated motion of electrons due to the Coulomb repulsion. The remaining static correlation is due to possible degeneracy or near degeneracy of some electronic configurations. This static correlation can be accounted for using a multi-determinant form of the wavefunction Ψ. Because of the lack of electron correlation, the HF method usually cannot provide quantitative predictions of atomic and molecular properties, but rather provides a reference wavefunction that is further improved by the post-HF methods described below.

II. Density Functional Theory

A well-known disadvantage of the multi-electron Hartree-Fock wavefunction is its hard interpretability due to electrons being essentially independent to each other in the Hartree-Fock method. It had been shown that instead of a wavefunction, an electronic energy of a system and its Hamiltonian can be linked to a physical observable, an electron density ρ.[1] Integration of the electron density over all space gives the total number of electrons N:

$$N = \int \rho(\mathbf{r}) d\mathbf{r} = \sum_{i=1}^{N} \int |\psi_i(\mathbf{r})|^2 d\mathbf{r}. \tag{2.13}$$

The electron density can be spanned in the basis of one-electron wavefunctions, $\psi_i(\mathbf{r})$. In the density functional theory (DFT), the total electron energy is defined as a functional of electron density:

$$E[\rho(\mathbf{r})] = T[\rho(\mathbf{r})] + V_{\mathrm{ne}}[\rho(\mathbf{r})] + V_{\mathrm{ee}}[\rho(\mathbf{r})], \tag{2.14}$$

$$V_{\mathrm{ne}}[\rho(\mathbf{r})] = \sum_{A=1}^{M} \int \frac{Z_A}{r_A} \rho(\mathbf{r}) d\mathbf{r}, \tag{2.15}$$

$$V_{\mathrm{ee}}[\rho(\mathbf{r})] = \frac{1}{2} \int \int \frac{\rho(\mathbf{r}_1)\rho(\mathbf{r}_2)}{r_{12}} d\mathbf{r}_1 \, d\mathbf{r}_2, \tag{2.16}$$

where E is the total electronic energy. The first term in Eq. (2.14) is the kinetic energy written as a functional of electron density. In 1927, Thomas and Fermi derived an expression for $T[\rho(\mathbf{r})]$ using the uniform electron gas model. However, this expression was found inaccurate and is no longer used in computational chemistry. Instead, T is expressed as a functional of molecular orbitals ψ_i, as will be shown below. The V_{ne} term in Eq. (2.14) is an attractive nuclear potential, and V_{ee} is the electron-electron repulsion energy.

DFT was implemented into a practical and quantitative quantum mechanical methodology by Hohenberg, Kohn and Sham. In 1964, Hohenberg and Kohn proved two theorems. The existence theorem[3] postulates that the electron density of the ground state is sufficient to determine the system Hamiltonian, and, therefore, to determine the system energy. The variational theorem[4] postulates that the electron density obeys the variational principle. Therefore, a procedure similar to the self-consistent field used in the Hartree-Fock theory can be applied to minimize the $E[\rho(\mathbf{r})]$ functional. A practical computational protocol of DFT was subsequently formulated by Kohn and Sham.[4] The exact energy functional takes the form

$$E[\rho(\mathbf{r})] = T[\rho(\mathbf{r})] + V_{\mathrm{ne}}[\rho(\mathbf{r})] + V_{\mathrm{ee}}[\rho(\mathbf{r})] + \Delta T[\rho(\mathbf{r})] + \Delta V_{\mathrm{ee}}[\rho(\mathbf{r})], \tag{2.17}$$

where ΔT is the correction term to the kinetic energy due to interacting electrons, and ΔV_{ee} is correlation correction for the electron-electron repulsion. Usually, the ΔT and ΔV_{ee} correction terms are combined into the exchange-correlation functional E_{XC}. A breakthrough of Kohn and Sham was to show that tremendous simplification can be made if one i) starts with a system of non-interacting electrons and ii) given that the density of the ground state of such non-interacting system is the same as the density of a real system with interacting electrons, use this density of the non-interacting electrons as an initial guess. Written in the orbital basis ψ_i, the energy functional reads

$$E[\rho(\mathbf{r})] = \sum_{i=1}^{N} \left(\left\langle \psi_i \middle| -\frac{1}{2}\nabla_i^2 \middle| \psi_i \right\rangle - \left\langle \psi_i \middle| \sum_{A=1}^{M} \frac{Z_A}{r_{iA}} \middle| \psi_i \right\rangle \right) + \sum_{i=1}^{N} \left\langle \psi_i \middle| \frac{1}{2} \int \frac{\rho(\mathbf{r}')}{r_{i'}} d\mathbf{r}' \middle| \psi_i \right\rangle + E_{\mathrm{XC}}[\rho(\mathbf{r})], \tag{2.18}$$

The one-electron orbitals ψ_i and the orbital energies ε_i can be found solving the following Kohn-Sham equations using variational procedure :

$$\hat{h}_i^{\mathrm{KS}} \psi_i = \varepsilon_i \psi_i, \tag{2.19}$$

$$\hat{h}_i^{\mathrm{KS}} = -\frac{1}{2}\nabla_i^2 - \sum_{A=1}^{M} \frac{Z_A}{r_{iA}} + \int \frac{\rho(\mathbf{r}')}{r_{i'}} d\mathbf{r}' + V_{\mathrm{XC}}, \tag{2.20}$$

where $\hat{h}_i^{\mathrm{KS}}$ is the one-electron Kohn-Sham operator and V_{XC} is a derivative of E_{XC} with respect to density. Unfortunately, the theorems of Hohenberg and Kohn do not say anything about the form of corrections to the kinetic and electron-electron repulsion energies. Therefore, a general form of the exchange-correlation functional is unknown. In practice, it is a choice of E_{XC} that defines a specific DFT method. There are several

approaches that guide a practical choice of this functional. One is the local spin density approximation (LSDA),[5] where E_{XC} depends only on the local electron density ρ at position **r**. However, there exist limitations to LSDA due to non-uniform nature of the electron density. The non-local correction takes the form of the density gradient and leads to a generalized gradient approximation (GGA)[6] for the exchange-correlation functional:

$$E_{\mathrm{XC}}^{\mathrm{GGA}}[\rho(\mathbf{r})] = E_{\mathrm{XC}}^{\mathrm{LSDA}}[\rho(\mathbf{r})] + \Delta E_{\mathrm{XC}}\left[\frac{|\nabla\rho(\mathbf{r})|}{\rho^{4/3}(\mathbf{r})}\right]. \tag{2.21}$$

One of the most popular GGA exchange functionals (B88) was developed by Becke[7] and is parametrized with two empirical parameters δ and γ:

$$E_{\mathrm{X}}^{\mathrm{B88}} = E_{\mathrm{X}}^{\mathrm{LSDA}} - \delta \sum_{i=\alpha,\beta} \int \rho_i^{4/3} \frac{\left(|\nabla\rho_i|/\rho_i^{4/3}\right)^2}{1+\gamma\left(|\nabla\rho_i|/\rho_i^{4/3}\right)^2} d\mathbf{r}, \tag{2.22}$$

where index i runs over spin-up and spin-down electrons. Parameter-free GGA exchange functionals include B86, PBE, *m*PBE and others. One of the famous GGA functionals to describe correlation energy was developed by Lee, Yang, and Parr (LYP).[8]

A significant improvement of the DFT accuracy was achieved by Becke who introduced the Hartree-Fock exchange ($E_{\mathrm{X}}^{\mathrm{HF}}$) into the exchange-correlation functionals[9]:

$$E_{\mathrm{XC}} = cE_{\mathrm{X}}^{\mathrm{HF}} + (1-c)\mathrm{E}_{\mathrm{X}}^{\mathrm{GGA}} + \mathrm{E}_{\mathrm{C}}^{\mathrm{GGA}}, \tag{2.23}$$

where c is a weighting coefficient. The B2LYP exchange-correlation functional includes Becke's B88 exchange formula, HF exchange and LYP correlation, and two

empirical parameters. B3LYP is a more modern version of this functional with three fitted parameters:

$$E_{\mathrm{X}}^{\mathrm{B3LYP}} = (1-a)E_{\mathrm{X}}^{\mathrm{LSDA}} + aE_{\mathrm{X}}^{\mathrm{HF}} + bE_{\mathrm{X}}^{\mathrm{B88}} + (1-c)E_{\mathrm{C}}^{\mathrm{VWN3}} + cE_{\mathrm{C}}^{\mathrm{LYP}}, \quad (2.24)$$

where $a = 0.20$, $b = 0.72$, $c = 0.81$, and VWN3 is a correlation functional.[10]

III. Post Hartree-Fock Methods

Utility of the computational quantum chemistry depends on the accuracies of predictions it can make. Understanding complex phenomena, including dynamics of ultrafast processes, high-resolution molecular spectroscopy, as well as designing spin-based qubits, quantum sensors and molecular nanomagnets, requires highly accurate solutions for the atomic and molecular quantum wave equations. An accurate solution of the Schrödinger equation beyond the Hartree-Fock approximation requires inclusion of electron correlation. Electron correlation is usually divided into the static and dynamic contributions. The static correlation arises due to partial occupation of degenerate or nearly degenerate molecular orbitals. As a result, the wave function of such electronic state cannot be described by a single Slater determinant but must include multiple determinants. Such situation is often the case when describing excited states of a molecule, as well as dissociation and formation of chemical bonds. Accounting for the dynamic correlation is important for accurate prediction of molecular properties.

A. Coupled Cluster Theory

One way to include the electron correlation, proved to be highly accurate, is to apply the following exponential ansatz[18-20] to a reference wave function:

$$\Psi_0 = e^{\hat{T}}\Phi_0, \tag{2.25}$$

where Ψ_0 is the exact wave function of a ground state, $e^{\hat{T}}$ is the exponential electron excitation operator, Φ_0 is the reference Hartree-Fock wave function, and $e^{\hat{T}}\Phi_0$ generates a linear combination of the Slater determinants with all possible electron excitations from the occupied to virtual spin-orbitals of Φ_0. The exponential formalism of the coupled cluster theory is based on the diagrammatic representation of the perturbation theory and therefore ensures the size extensivity of this theory, i.e. correct scaling with the number of electrons. The working equations of the coupled cluster theory were first derived by Čížek.[21] Here, we describe only the main steps of this theory. The cluster form of the $e^{\hat{T}}$ excitation operator is written as the Taylor series:

$$e^{\hat{T}} \equiv 1 + \hat{T} + \frac{\hat{T}^2}{2!} + \frac{\hat{T}^3}{3!} + \cdots = \sum_{m=0}^{\infty} \frac{\hat{T}^m}{m!}, \tag{2.26}$$

$$\hat{T} = \hat{T}_1 + \hat{T}_2 + \hat{T}_3 + \cdots = \sum_{n=0}^{N} \hat{T}_n, \tag{2.27}$$

where $\hat{T}^m$ operator represents the expansion of the exponential operator $e^{\hat{T}}$ up to order m, and $\hat{T}_n$ denotes the electron excitations of an order n, which is all possible excitations of n electrons from the occupied to virtual spin-orbitals of the reference Slater determinant Φ_0. For example, the $\hat{T}_1$ and $\hat{T}_2$ single- and double-excitations can be written as

$$\hat{T}_1\Phi_0 = \sum_{a=N+1}^{K}\sum_{i=1}^{N} t_i^a \Phi_i^a, \qquad \hat{T}_2\Phi_0 = \sum_{a,b>a}\sum_{i,j>i} t_{ij}^{ab}\Phi_{ij}^{ab}, \tag{2.28}$$

where indices i and j run over all occupied spin-orbitals in the reference determinant Φ_0, and indices a and b – over all virtual spin-orbitals. The singly excited Slater determinant Φ_i^a is obtained by promoting an electron from the occupied spin-orbital χ_i to the virtual spin-orbital χ_a, and t_i^a is a weight (*amplitude*) of this determinant. The act of $\hat{T}_2$ on Φ_0 is to generate the doubly excited determinants Φ_{ij}^{ab}, whose amplitudes are t_{ij}^{ab}.

A particular coupled cluster method is defined by truncation of $\hat{T}$ in Eq. (2.27). For example, if $\hat{T} = \hat{T}_2$, the resulting method is called the coupled cluster with doubles (CCD), if $\hat{T} = \hat{T}_1 + \hat{T}_2$ – coupled cluster with singles and doubles (CCSD). To determine the total energy and coupled cluster amplitudes, we first insert the wave function defined in Eq. (2.25) into the Schrödinger equation:

$$\hat{H}e^{\hat{T}}\Phi_0 = E_{\mathrm{CC}}e^{\hat{T}}\Phi_0. \tag{2.29}$$

To determine the ground state energy E_{CC}, Eq. (2.29) is multiplied by Φ_0^* from the left and integrated:

$$\langle\Phi_0|\hat{H}|e^{\hat{T}}\Phi_0\rangle = E_{\mathrm{CC}}\langle\Phi_0|e^{\hat{T}}\Phi_0\rangle. \tag{2.30}$$

In the r.h.s. of Eq. (2.30), the matrix elements contain products like $\Phi_0\hat{T}\Phi_0$, $\Phi_0\frac{1}{2}\hat{T}^2\Phi_0$, and so on. Because of the orthogonality of the spin-orbitals in Φ_0 and excited determinants, integrals over such products vanish and Eq. (2.30) simplifies to

$$\langle\Phi_0|\hat{H}|e^{\hat{T}}\Phi_0\rangle = E_{\mathrm{CC}}, \tag{2.31}$$

$$\langle\Phi_0|e^{\hat{T}}\Phi_0\rangle = \langle\Phi_0|\Phi_0\rangle = 1. \tag{2.32}$$

To determine the amplitudes, Eq. (2.29) is projected on the space of singly, doubly, *etc*. excited determinants. In the case of the CCSD method, the projection becomes

$$\langle \Phi_i^a | \hat{H} | e^{\hat{T}} \Phi_0 \rangle = E_{\mathrm{CC}} \langle \Phi_i^a | e^{\hat{T}} \Phi_0 \rangle, \tag{2.33}$$

$$\langle \Phi_{ij}^{ab} | \hat{H} | e^{\hat{T}} \Phi_0 \rangle = E_{\mathrm{CC}} \langle \Phi_{ij}^{ab} | e^{\hat{T}} \Phi_0 \rangle. \tag{2.34}$$

Resulting from Eqs. (2.33-2.34) are two sets of coupled nonlinear equations with single (Eq. 2.33) and double (Eq. 2.34) amplitudes as unknowns.[18] Once the equations are solved and the amplitudes are computed, the coupled cluster energy can be calculated using Eq. (2.30). While the described procedure produces the exact solution of the Schrodinger equation in a given one-electron basis, in practice it is only feasible to use truncated forms of the operator $\hat{T}$. For the CCD and CCSD methods, the computational cost scales as N^6, where N is the number of one-electron basis functions. The coupled cluster method with single, double, and triple excitations, CCSD(T), is very accurate in recovering the correlation energy. However, the CCSDT method scales as N^8 and is therefore applicable only to small systems. The CCSD(T) method, which scales as N^7 thanks to the triple excitations accounted with the perturbation theory, is considered to be a golden standard of quantum chemistry.[22] Moreover, the equation-of-motion coupled cluster (EOM-CC) theory is one of the most widespread approach to study electronic excited states in atoms and molecules.[23]

B. Multireference Methods

Another approach to include electron correlation is a generalization of the Hartree-Fock wave function to multiple Slater determinants, i.e. *multireference* approach.[1-2] Following the multireference approach, an exact solution of the Schrödinger equation can be obtained using the *full configuration interaction* (full CI) wave function by generating all possible excitations of electrons from the reference Hartree-Fock occupied to virtual spin-orbitals:

$$\Psi = c_0\Phi + \sum_{a=N+1}^{K}\sum_{i=1}^{N} c_i^a \Phi_i^a + \sum_{a,b>a}\sum_{i,j>i} c_{ij}^{ab}\Phi_{ij}^{ab} + \sum_{d>b>a}\sum_{k>j>i} c_{ijk}^{abd}\Phi_{ijk}^{abd} \ldots, (2.35)$$

where Ψ is the full CI wave function and $c_0, c_i^a, c_{ij}^{ab}, c_{ijk}^{abd}$ are CI coefficients in front of the reference, singly, doubly, triply, and higher-order excited determinants. If not stated otherwise, Ψ and Φ denote the exact and reference Hartree-Fock wave functions of a ground state ($\Psi \equiv \Psi_0$ and $\Phi \equiv \Phi_0$), correspondingly. Solving the full CI problem recovers all the static and dynamic electron correlation and is equivalent to the exact solution of the Schrödinger equation. However, it can be done only for systems with very few electrons, since the number of excited determinants grows factorially with the numbers of electrons and orbitals.

A practical way to overcome the dimensionality problem of full CI is to reduce the number of excited determinants that form Ψ. Such methods are used to recover the static electron correlation and as well account for dynamic correlation to some extent. In a multiconfigurational self-consistent field (MCSCF) method[11], both the number of electrons and orbitals involved in the generation of the excited determinants are truncated. A particularly important form of MCSCF is the complete active space SCF

(CASSCF) method,[12] which performs a full CI inside a preselected space of n electrons and m orbitals, CASSCF(n, m), as shown in Figure 2.1.

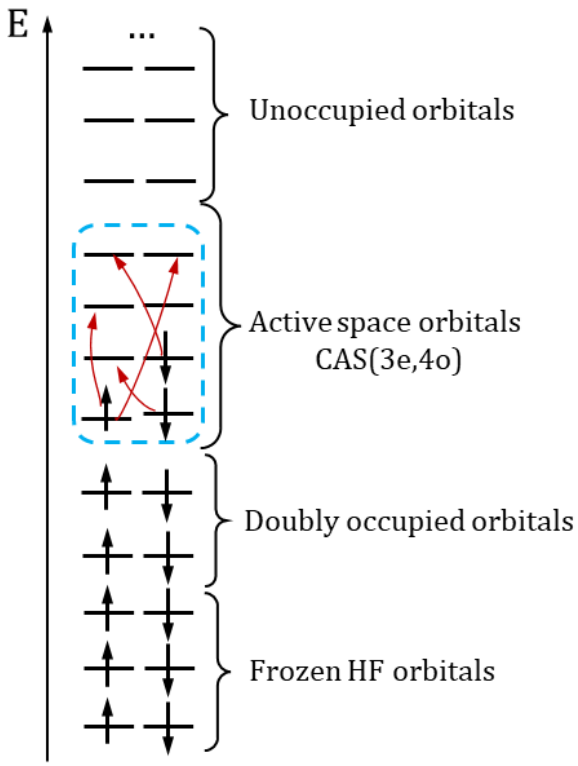

Figure 2.1. Partition of the molecular spin-orbital space in the complete active space (CAS) formalism. The frozen HF spin-orbitals are excluded from the CASSCF orbital optimization, the rest of the spin-orbitals are optimized variationally. In this example, the active space consists of three electrons in four orbitals.

A particular problem of the multireference methods is the choice of the active space to construct excited determinants. The choice of the active space requires a careful analysis of the molecular orbital space. For example, when CASSCF or other multireference method is used to study mechanisms of chemical reactions, the active space must include all the orbitals that are localized on the atoms and bonds involved in the chemical transformations. A more general prescription to determine the active space is based on occupation numbers of the natural orbitals.[13]

There exist different approaches to account for the dynamic correlation in the multireference methods. One is to perform a subsequent configuration interaction to augment the reference wave function with determinants obtained by all possible *n*-tuple excitations from the MCSCF or CASSCF reference determinants to the virtual spin-orbitals. This method is called a multireference configuration interaction (MRCI).[14] In its most widespread version, MRCI includes all single and double excitations from the reference wave function (MRCISD). Whereas the MCSCF (or CASSCF) wave function is optimized with respect to both orbital and expansion coefficients, in the MRCI methods, the orbitals are frozen, and the wave function is variationally optimized by changing the CI expansion coefficients in front of determinants.

Another approach to account for the dynamic correlation in multireference methods is to use perturbative corrections. The resulting class of methods is generally called the multireference perturbation theory (MRPT).[15-17] In these methods, the MCSCF (CASSCF) wave function is chosen as a zero-order wave function. The MRPT methods are differ by the choice of the perturbation and the zero-order Hamiltonian. For example, in the popular complete active space second-order perturbation theory (CASPT2) method,[15] the perturbation is defined as the electron-electron interaction between CAS electrons in the outer space, i.e. in the space of virtual orbitals. Specifically, the perturbation becomes all the double excitations of all CAS electrons to all virtual orbitals, also known as the internally contracted formalism. The single excitations are also included as a subspace. The higher-order excitations do not contribute to the first-order perturbation of the wavefunction. The CASPT2 method

uses the Møller–Plesset zero-order Hamiltonian as a sum of one-electron Fock operators, $\hat{F}$.

Given below is a short summary of the main steps behind multireference calculations. Note that unlike MCSCF, the CI method minimizes energy of a system only with respect to the CI expansion coefficients in front of determinants and leaves orbitals unrelaxed. Therefore, for simplification, we describe main steps of a CI calculation. Energy minimization in the CI method is formulated as a constrained optimization problem with requirement that the total electron wavefunction Ψ (Eq. 2.35) is normalized, leading to minimization of the following Lagrangian:

$$L = \langle \Psi | \hat{H} | \Psi \rangle - \lambda(\langle \Psi | \Psi \rangle - 1), \tag{2.36}$$

where λ is the Lagrange multiplier. A minimum of energy associated with the Lagrangian L has to obey the following condition:

$$\frac{\partial L}{\partial \mathbf{c}} = \mathbf{0}, \qquad (\mathbf{H}_{\mathrm{CI}} - E\mathbf{I})\mathbf{c} = \mathbf{0}, \tag{2.37}$$

where the first expression is the stationary condition, which results in the system of linear equations written in the second expression. This system of equations has a nontrivial solution only when the determinant of the matrix $\mathbf{H}_{\mathrm{CI}}$ is equal to zero:

$$\begin{vmatrix} H_{00} - E & H_{12} & \cdots & H_{1N} \\ H_{21} & H_{11} - E & \cdots & H_{2N} \\ \vdots & \vdots & \ddots & \vdots \\ H_{N1} & H_{N2} & \cdots & H_{NN} - E \end{vmatrix} = 0, \tag{2.38}$$

where $H_{ij} = \langle \Phi_i | \hat{H} | \Phi_j \rangle$ is the Hamiltonian matrix element between two determinants. The main computational efforts associated with the CI method is the construction and diagonalization of the $\mathbf{H}_{\mathrm{CI}}$ matrix. The computational cost is reduced due to the following features:

1) The Hamiltonian $\hat{H}$ bears no reference to the electron spin. Therefore, the H_{ij} matrix elements are zero if Φ_i and Φ_j belong to different spin multiplicities;

2) According to the Slater-Condon rules, all the matrix elements with Φ_i and Φ_j differ by three or more occupied orbitals are equal to zero;

3) According to the Brillouin's theorem, all matrix elements between the HF reference detriment Φ_0 and all singly excited determinants are zero;

4) If a system can be described by a molecular point group symmetry, the number of the matrix H_{ij} that needed to be calculated is reduced;

The size of the very sparse CI matrix $\mathbf{H}_{\mathrm{CI}}$ (see features 1-4) grows factorially with the number of allowed excitations. Therefore, it is impractical to use standard diagonalization methods. In addition, it is usually unnecessary, as only a few lowest eigenvalues that represent the ground and excited state energies are sought for. In practice an iterative direct CI algorithm is usually used, which avoids construction of the full $\mathbf{H}_{\mathrm{CI}}$ matrix and calculates only few lowest eigenvalues.

IV. Dirac-Hartree-Fock Method

In this Section, we briefly describe main ideas behind relativistic electronic structure calculations. The computational protocol of such calculations closely resembles the one used to solve the Schrödinger equation. However, in the case of the

Dirac equation, its compliance with special relativity makes it possible to exploit additional symmetry and algebra to speed up the calculations and, more importantly, better understand the underlying physics.[24-25] There are several general and specific to this work approximations used in the relativistic calculations. For example, it turns out that the Born-Oppenheimer (BO) approximation violates the theory of the special relativity because BO treats atomic nuclei as stationary points and, therefore, creates a preferred reference frame. However, since the BO approximation greatly simplifies the solution of the wave equation by allowing to focus on the electronic degrees of freedom only, it is used in practical relativistic calculations. In addition, the hyperfine interactions between the nuclear and electron spins are usually excluded from relativistic molecular calculations because they break the symmetry of the Dirac equation discussed below. Finally, the relativistic calculations performed in this work employed only the non-relativistic Coulomb term to describe the electron-electron interaction. Therefore, the relativistic corrections for the two-electron part of the Dirac Hamiltonian were neglected.

Assuming the approximations described in the previous paragraph, the Dirac-Coulomb Hamiltonian describes the many-body system of relativistic electrons:

$$\hat{H}^D = \sum_i \hat{h}_i^D + \hat{V}_{ee}^C + \hat{V}_{nn}, \tag{2.39}$$

which is equivalent in form to Eq. (1.8) but with the $\hat{V}_{ee}^{CB}$ Coulomb-Breit operator replaced by the Coulomb interaction and the vector potential $\boldsymbol{A}$ is excluded. The first term in Eq. (1.8) is the sum of the one-electron Dirac operators (Eqs. 1.9-1.11).

In the absence of external electromagnetic fields, the Hamiltonian $\widehat{H}^D$ is Lorentz invariant. Therefore, the properties of $\widehat{H}^D$ can be studied using the symmetry operations of space and time. The spatial symmetry operations are described by unitary operators. In the non-relativistic limit, all possible spatial symmetry operations of a given molecule are described by a symmetry point group. However, in the relativistic case, the spatial symmetry alone is lost due to the coupling of the spatial and spin degrees of freedom.[24] Therefore, to exploit molecular symmetry, symmetry point groups must be extended to include operations in a spinor space. The spatial symmetry properties of a spinor can be studied by considering infinitesimal rotations around a quantization axis:

$$\hat{R}(\phi, \boldsymbol{n}) = e^{-i\phi(\hat{\boldsymbol{J}}\cdot\boldsymbol{n})}, \tag{2.40}$$

where operator $\hat{R}$ represents the rotations generated by the total angular momentum $\hat{\boldsymbol{J}}$ (not to be confused with the Coulomb operator in Eq. (2.11)). Eq. (2.40) shows that for half-integer (fermion) momentum J, rotations by ϕ and $\phi + 2\pi$ are not identical but differ in sign. Therefore, the rotation by 2π cannot be used as identity operator $\hat{E}$ for half-integer spin. Explicitly, it can be shown that the spin rotations are represented as

$$\hat{C}_2^q = -i\rho\alpha_q, \qquad \rho\alpha_q = \begin{pmatrix} \sigma_q & 0_2 \\ 0_2 & \sigma_q \end{pmatrix}, \qquad \rho = \begin{pmatrix} I_2 & 0_2 \\ 0_2 & I_2 \end{pmatrix}, \tag{2.41}$$

where $\hat{C}_2^q$ is the rotation operator around axis $q = x, y, z$, I_2 is the 2 × 2 identity matrix, and α_q are the Dirac matrices. Then, two subsequent rotations around q give $\hat{C}_2^q \hat{C}_2^q = -\hat{I}_4$, where $\hat{I}_4$ is an identity operator. This demonstrates that rather rotations by ϕ and $\phi + 4\pi$ are identical, and therefore the spin identity operator is $\bar{E} = 4\pi \neq \hat{E}$, where $\hat{E} = 2\pi$ is the identity operator of the nonrelativistic spatial symmetry point group.

Other spin symmetry operations can be derived in a similar manner remembering that the operator ($\boldsymbol{\alpha} \cdot \mathbf{p}$) is invariant under all symmetry operations. For molecular systems with the half-integer total angular momentum, the symmetry operations form the so-called double groups, where the number of symmetry operations is doubled.[24-25] However, the number of irreducible representations is generally not doubled. These extra irreducible representations of a double group are spanned by fermionic functions and are often called fermion representations. The regular irreducible representations of single groups are then called boson representations. Therefore, restoring (and extending) the spatial symmetry in relativistic equations allows to exploit the symmetry properties of spinors and operators in a full analogue with non-relativistic calculations.

In addition, the time-reversal symmetry can be used to explore additional properties of the Dirac equation. Specifically, we will see how the algebra of the Pauli spin matrices $\boldsymbol{\sigma}$ forming the Dirac matrices $\boldsymbol{\alpha}$ connects the time-reversal symmetry of the Dirac Hamiltonian and the quaternion algebra. In turn, reformulation of the Dirac equation using the quaternion algebra is a very efficient computational approach as it allows to i) block diagonalize the Fock matrix and ii) due to the time-reversal symmetry, consider only the upper block of the block-diagonalized Fock matrix.

Transformation of the Dirac equation under the time-reversal symmetry can be described with an antiunitary operator $\widehat{\mathrm{A}}$.[24,26,27] Since $\widehat{\mathrm{A}}$ is antiunitary, it can be represented as a product of the unitary operator $\widehat{U}$ and the antiunitary operator $\hat{A}_0$. The explicit form of the time-reversal operator $\widehat{\mathrm{A}}$ is

$$\widehat{\mathrm{A}} = -i\left(I_2 \otimes \sigma_y\right)\hat{A}_0. \tag{2.42}$$

It can be shown that the $\boldsymbol{\alpha}$ matrices transform as coordinates under the time-reversal symmetry. Therefore, the unitary operator $\hat{U}$ can be identified as rotation about the *y*-axis, $\hat{U} = -i(I_2 \otimes \sigma_y)$. Studies of the time-reversal symmetry of the Dirac equation showed the following.

1) The operator $\hat{\mathrm{A}}$ commutes with the Dirac Hamiltonian $\hat{H}^D$. Therefore, eigenstates of $\hat{H}^D$ are simultaneously the eigenstates of $\hat{\mathrm{A}}$. For a system of total half-integer spin, eigenstates of $\hat{\mathrm{A}}$ has a following property

$$\hat{\mathrm{A}}a\psi = a^*\hat{\mathrm{A}}\psi, \qquad \hat{\mathrm{A}}^2\psi = -\psi, \qquad \hat{\mathrm{A}}\psi = \bar{\psi}, \tag{2.43}$$

where a is an arbitrary complex multiplier, and $(\psi, \bar{\psi})$ form Kramer pairs. Therefore, an eigenstate ψ of a system with the total half-integer spin is at least two-fold degenerate. A union of two sets, $\{\psi\}$ and $\{\bar{\psi}\}$, forms a restricted Kramer basis.

2) Algebra of the Pauli spin matrices $\boldsymbol{\sigma} = \{\sigma_x, \sigma_y, \sigma_z\}$ multiplied by the imaginary number i, is identical to the quaternion algebra. Quaternions can be though of as extensions of complex numbers to three dimensions. A quaternion number has the following form:

$$q = a + b\check{\imath} + c\check{\jmath} + d\check{k}, \tag{2.44}$$

where a, b, c, and $d \in \mathbb{R}$, and $\{\check{\imath}, \check{\jmath}, \check{k}\}$ are basic quaternions. Due to the connection of quaternions with the Pauli matrices, the following basis can be defined:

$$e_1 = \check{\imath} \leftrightarrow i\sigma_z, \qquad e_2 = \check{\jmath} \leftrightarrow i\sigma_y, \qquad e_3 = \check{k} \leftrightarrow i\sigma_x. \tag{2.45}$$

In this basis, a quaternion number can be represented as $q = s + i(\boldsymbol{\sigma} \cdot \mathbf{v})$, where s and $\mathbf{v}$ are the scalar and vector parts of the quaternion. The quaternion algebra is not

commutative, and therefore $q_1 q_2 \neq q_2 q_1$. The multiplication algebra of quaternions is identical to those of spin matrices:

$$e_i e_j = -\delta_{ij} - \epsilon_{ijk} e_k, \tag{2.46}$$

where δ is the Kronecker delta and ϵ_{ijk} is the Levi-Cevita symbol.

3) There is an explicit connection between the time-reversal symmetry and the quaternion algebra. In the restricted Kramer basis, a matrix representation of a Hermitian operator $\hat{O}$, which is symmetric under time-reversal symmetry (e.g. Fock operator), takes a special form:

$$\boldsymbol{O} = \begin{pmatrix} \boldsymbol{A} & \boldsymbol{B} \\ -\boldsymbol{B}^* & \boldsymbol{A}^* \end{pmatrix}, \qquad \boldsymbol{A}^\dagger = \boldsymbol{A}, \qquad \boldsymbol{B}^T = -\boldsymbol{B}, \tag{2.47}$$

where matrix $\boldsymbol{A}$ contains the matrix elements of $\hat{O}$ between $\{\psi\}$ eigenstates of $\hat{H}^D$ only, while the elements of $\boldsymbol{B}$ are calculated between $\{\psi\}$ and $\{\bar{\psi}\}$. The matrix $\boldsymbol{O}$ can be expanded in the quaternion basis:

$$\boldsymbol{O} = I_2 \otimes \mathrm{Re}(\boldsymbol{A}) + [i\sigma_z] \otimes \mathrm{Im}(\boldsymbol{A}) + \left[i\sigma_y\right] \otimes \mathrm{Re}(\boldsymbol{B}) + [i\sigma_x] \otimes \mathrm{Im}(\boldsymbol{B}). \tag{2.48}$$

Because the operator $\hat{O}$ is symmetric under the time-reversal transformation, its matrix form $\boldsymbol{O}$ is doubly degenerate. Therefore, $\boldsymbol{O}$ can be block-diagonalized by a unitary transformation $\hat{U}$, which matrix form is:

$$\boldsymbol{U} = \frac{1}{\sqrt{2}} \begin{pmatrix} \boldsymbol{I} & \check{\jmath}\boldsymbol{I} \\ \check{\jmath}\boldsymbol{I} & \boldsymbol{I} \end{pmatrix}, \tag{2.49}$$

$$\boldsymbol{O}^{\mathrm{Q}} = \boldsymbol{U}^\dagger \boldsymbol{O} \boldsymbol{U} = \begin{pmatrix} \boldsymbol{A} + \boldsymbol{B}\check{\jmath} & 0 \\ 0 & -\check{k}(\boldsymbol{A} + \boldsymbol{B}\check{\jmath})\check{k} \end{pmatrix}. \tag{2.50}$$

Therefore, with the aid of the time-reversal symmetry, the Dirac-Hartree-Fock method[26,27] can be formulated in the quaternion form:

$$\boldsymbol{F}^{\mathrm{Q}}\mathbf{c}^{\mathrm{Q}} = \varepsilon \boldsymbol{S}^{\mathrm{Q}}\mathbf{c}^{\mathrm{Q}}, \tag{2.51}$$

where $\boldsymbol{F}^{\mathrm{Q}}$ is the quaternion-form matrix of the Fock operator $\hat{F}$ with the block-diagonal structure of Eq. (2.47), $\mathbf{c}$ is the vector of complex expansion coefficients and the quaternion-form overlap matrix $\boldsymbol{S}^{\mathrm{Q}}$ has a block-diagonal form:

$$\boldsymbol{S}^{\mathrm{Q}} = \begin{pmatrix} \boldsymbol{S}^{LL} & 0 \\ 0 & \boldsymbol{S}^{SS} \end{pmatrix}, \qquad S_{ij}^{XY} = \langle \chi_i^X | \chi_j^Y \rangle \delta_{XY}, \qquad X, Y = \{\mathrm{L}\alpha, \mathrm{L}\beta, \mathrm{S}\alpha, \mathrm{S}\beta\}, \tag{2.52}$$

where α and β refer to two spin degrees of freedom, and L and S denote large and small components of a k-th spinor ψ_k spanned by the real basis $\{\chi\}$:

$$\psi_k = \begin{pmatrix} \psi_k^{\mathrm{L}\alpha} \\ \psi_k^{\mathrm{S}\alpha} \\ \psi_k^{\mathrm{L}\beta} \\ \psi_k^{\mathrm{S}\beta} \end{pmatrix}, \psi_k = \begin{pmatrix} \boldsymbol{\chi}^{\mathrm{L}} & 0 \\ 0 & \boldsymbol{\chi}^{\mathrm{S}} \end{pmatrix} \begin{pmatrix} \mathbf{c}_k^{\alpha} \\ \mathbf{c}_k^{\beta} \end{pmatrix}. \tag{2.53}$$

In conclusion, the time-reversal symmetry naturally leads to reformulation of the Dirac-Hartree-Fock method using the quaternion algebra. Such reformulation allows not only to fully explore the structure and properties of the Dirac equation, but also leads to significant computational benefits. In particular, the matrix of the Fock operator becomes block-diagonal, which reduces the number of operations associated with the construction of the Fock matrix by a factor of two. Additional reductions in the computational cost can be achieved by using the symmetry of spatial molecular point group. It can be shown that for some point groups, the use of spatial symmetry can reduce the quaternion algebra to the complex or real algebras.

References

(1) Cramer, C. J. *Essentials of Computational Chemistry. Theories and Models*, 2nd ed.; Wiley, 2004.

(2) Szabo, A.; Ostlund, N. S. *Modern Quantum Chemistry*. *Introduction to Advanced Electronic Structure Theory*, Dover, 1996.

(3) Hohenberg, P.; Kohn, W. Inhomogeneous Electron Gas. *Phys. Rev.* **1964**, *136* (3), 864-871. https://doi.org/10.1103/PhysRev.136.B864.

(4) Kohn, W.; Sham, L. J. Self-Consistent Equations Including Exchange and Correlation Effects. *Phys. Rev.* **1965**, *140* (a), 1133-1138. https://doi.org/10.1103/PhysRev.140.A1133.

(5) Vosko, S. H.; Wilk, L.; Nusair, M. Accurate Spin-Dependent Electron Liquid Correlation Energies for Local Spin Density Calculations: A Critical Analysis. *Can. J. Phys.* **1980**, *58* (8), 1200-1211. https://doi.org/10.1139/p80-159.

(6) Perdew, J. P.; Burke, K.; Ernzerhof, M. Generalized Gradient Approximation Made Simple. *Phys. Rev. Lett.* **1996**, *77* (18), 3865-3868. https://doi.org/10.1103/PhysRevLett.77.3865.

(7) Becke, A. D. Density-Functional Exchange-Energy Approximation with Correct Asymptotic Behavior. *Phys. Rev. A* **1988**, *38* (6), 3098–3100. https://doi.org/10.1103/PhysRevA.38.3098.

(8) Gill, P. M. W.; Johnson, B. G.; Pople, J. A.; Frisch, M. J. *Chem. Phys. Lett.* **1992**, *197* (4), 499-505. https://doi.org/10.1016/0009-2614(92)85807-M.

(9) Becke, A. D. Density-Functional Thermochemistry. III. the Role of Exact Exchange. *J. Chem. Phys.* **1993**, *98* (7), 5648–5652.

(10) Mardirossian, N.; Head-Gordon, M. Thirty Years of Density Functional Theory in Computational Chemistry: An Overview and Extensive Assessment of 200 Density Functionals. *Mol. Phys.* **2017**, *115* (19), 2315–2372. https://doi.org/10.1080/00268976.2017.1333644.

(11) Werner, H. J.; Meyer, W. A Quadratically Convergent MCSCF Method for the Simultaneous Optimization of Several States Simultaneous Optimization of Several States. **1981**, *74* (10), 5794-5801. https://doi.org/10.1063/1.440892.

(12) Roos, B.; Taylor, P. R. A Complete Active Space SCF Method (CASSCF) Using a Density Matrix Formulated Super CI-Approach. *Chem. Phys.* **1980**, *48* (2), 157–173. https://doi.org/10.1016/0301-0104(80)80045-0.

(13) Sayfutyarova, E. R.; Sun, Q.; Chan, G. K. L.; Knizia, G. Automated Construction of Molecular Active Spaces from Atomic Valence Orbitals. *J. Chem. Theory Comput.* **2017**, *13* (9), 4063–4078. https://doi.org/10.1021/acs.jctc.7b00128.

(14) Thomas, M.; Lischka, H.; Shepard, R. Multiconfiguration Self-Consistent Field and Multireference Configuration Interaction Methods and Applications. *Chem. Rev.* **2012**, *112* (1), 108–181. https://doi.org/10.1021/cr200137a.

(15) Andersson, K.; Malmqvist, P.; Roos, B. O.; Sadlej, A. J.; Wolinski, K. Second-Order Perturbation Theory with a CASSCF Reference Function. *J. Phys. Chem.* **1990**, *94* (14), 5483–5488.

(16) Angeli, C.; Cimiraglia, R.; Evangelisti, S.; Leininger, T.; Malrieu, J.-P. Introduction of *n*-electron valence states for multireference perturbation theory.

J. Chem. Phys. **2001**, *114* (23), 10252-10264. https://doi.org/10.1063/1.1361246.

(17) Celani, P.; Werner, H. J. Multireference Perturbation Theory for Large Restricted and Selected Active Space Reference Wave Functions Space Reference Wave Functions. **2000**, *112* (13), 5546-5557. https://doi.org/10.1063/1.481132.

(18) Levine, I. N. *Quantum Chemistry*. Pearson Education, Inc., 2014.

(19) Bartlett, R. J. Coupled-Cluster Approach to Molecular Structure and Spectra: A Step toward Predictive Quantum Chemistry. *J. Phys. Chem.* **1989**, *93* (5), 1697–1708. https://doi.org/10.1021/j100342a008.

(20) Bartlett, R. J.; Musiał, M. Coupled-Cluster Theory in Quantum Chemistry. *Rev. Mod. Phys.* **2007**, *79* (1), 291–352. https://doi.org/10.1103/RevModPhys.79.291.

(21) Ĉížek, J. On the Correlation Problem in Atomic and Molecular Systems. Calculation of Wavefunction Components in Ursell-Type Expansion Using Quantum-Field Theoretical Methods. *J. Chem. Phys.* **1966**, *45* (11), 4256–4266. https://doi.org/10.1063/1.1727484.

(22) Kowalski, K.; Piecuch, P. Method of Moments of Coupled-Cluster Equations and the Renormalized CCSD[T], CCSD(T), CCSD(TQ), and CCSDT(Q) Approaches. *J. Chem. Phys.* **2000**, *113* (1), 18–35. https://doi.org/10.1063/1.481769.

(23) Krylov, A. I. Equation-of-Motion Coupled-Cluster Methods for Open-Shell and Electronically Excited Species: The Hitchhiker's Guide to Fock Space. *Annu.*

Rev. Phys. Chem. **2008**, *59*, 433–462. https://doi.org/10.1146/annurev.physchem.59.032607.093602.

(24) Saue, T. Principles and Applications of Relativistic Molecular Calculations. Ph.D. Dissertation, University of Oslo, Oslo, Norway, 1996. http://www.diracprogram.org/doku.php?id=dissertations (accessed 2021-11-10).

(25) Fleig, Timo. Wave Function Based Multi-Reference Electron Correlation Methods. Development and Application to Atomic and Molecular Properties. Ph.D. Dissertation, Heinrich Heine University Düsseldorf, Düsseldorf, Germany, 2006. http://www.diracprogram.org/doku.php?id=dissertations (accessed 2021-11-10).

(26) Saue, T.; Faegri, K.; Helgaker, T.; Gropen, O. Principles of direct 4-component relativistic SCF: application to caesium auride. *Mol. Phys*. **1997**, *91* (5), 937-950. http://dx.doi.org/10.1080/002689797171058.

(27) Saue, T.; Jensen, H. J. Quaternion symmetry in relativistic molecular calculations: The Dirac-Hartree-Fock Method. *J. Chem. Phys.* **1999**, *111* (14), 6211-6222. http://dx.doi.org/10.1063/1.479958.

CHAPTER 3. NAST: NONADIABATIC STATISTICAL THEORY PACKAGE FOR PREDICTING KINETICS OF SPIN-DEPENDENT PROCESSES

A paper submitted to Topics in Current Chemistry

Vsevolod D. Dergachev, Mitra Rooein, Ilya D. Dergachev, Aleksandr O. Lykhin, Robert C. Mauban, and Sergey A. Varganov

Abstract

We present a nonadiabatic statistical theory (NAST) package for predicting kinetics of spin-dependent processes, such as intersystem crossings, spin-forbidden unimolecular reactions, and spin crossovers. The NAST package can calculate the probabilities and rates of transitions between the electronic states of different spin multiplicities. Both the microcanonical (energy dependent) and canonical (temperature dependent) rate constants can be obtained. Quantum effects, including tunneling, zero-point vibrational energy, and reaction path interference can be accounted for. In the limit of an adiabatic unimolecular reaction proceeding on a single electronic state, NAST reduces to the traditional transition state theory. Because NAST requires molecular properties only at a few points on potential energy surfaces, it can be applied to large molecular systems, used with accurate high-level electronic structure methods, and employed to study slow nonadiabatic processes. The essential NAST input data includes the nuclear Hessian at the reactant minimum, as well as the nuclear Hessians, energy gradients, and spin-orbit coupling at the minimum energy crossing point

(MECP) between two states. The additional computational tools included in the NAST package can be used to extract the required input data from the output files of electronic structure packages, calculate the effective Hessian at MECP, and fit the reaction coordinate for more advanced NAST calculations. We describe the theory, its implementation, and three examples of application to different molecular systems.

I. Introduction

Spin-dependent processes, including transitions between electronic states characterized by different values of total electron spin and magnetic quantum numbers, play an important role in many areas of atomic and molecular science. These include multi-state reactivity in transition-metal based catalysis[1-6] and on semiconductor surfaces,[7] design of photosensitizers for various applications,[8-10] and development of single-molecule magnets for applications in quantum sensing, quantum computing and spintronics.[11-15] For example, in photodynamic therapy, intersystem crossing (ISC) populates a manifold of low-lying triplet states of a photosensitizer. The following spin-allowed triplet-triplet reaction with molecular oxygen produces highly reactive oxygen species, which destroys cancer cells.[8-10] Delayed fluorescence in organic light-emitting diodes (OLEDs) is due to a thermally activated reverse ISC between close-lying excited triplet and singlet electronic states.[16-20] A nitrogen-vacancy (NV) center in diamond – one of the most promising candidates for a spin-based qubit – is initialized through the ISC between optically-excited triplet and singlet states.[15] Photolysis of axial ligands from active sites of hemeproteins proceeds via several ISCs on a femtosecond time scale.[21-25] Spin-forbidden low-energy reaction pathways have been proposed for the catalytic mechanisms of molecular hydrogen activation on the NiFe-hydrogenase metalloprotein[6] and the C-H bond activation on Fe(II).[4] Many ligand-metal binding and dissociation reactions, such as the CO binding to $Fe(CO)_4$ [26,27] and the diatomic molecules binding to the active site of hemeproteins, [28-30] are formally spin-forbidden. Spin-crossovers and spin-spin magnetic exchange interactions in d^4 – d^7 transition metal complexes play a fundamental role in the design of magnetic bistable materials.[31-39]

Predicting kinetics of spin-dependent processes is important for understanding the mechanisms of thermally-activated spin-forbidden reactions, ISCs in photochemistry, and spin-crossovers in transition metal-based systems. There are two main approaches to calculate the rate constants and lifetimes of electronic states in spin-dependent processes. In ab initio nonadiabatic molecular dynamics, the classical or quantum nuclei are time propagated on the coupled potential energy surfaces (PESs) of multiple spin states,[40-49] and the time evolution of nuclear trajectories is used to statistically describe the population transfer between the interacting electronic states. Such molecular dynamics simulations can be very accurate; however, they often require thousands of electronic structure calculations and can be computationally expensive if not prohibitive. An alternative nonadiabatic statistical theory (NAST) approach, also called nonadiabatic transition state theory, [4,25,29,43,49-58] largely eliminates the computational burden by exploring only the critical points on PESs. This allows to use NAST with the high-level electronic structure methods and model even slow nonadiabatic kinetics, which is intractable for molecular dynamics. NAST can be viewed as an extension of traditional transition state (TST) theory[60-65] to the nonadiabatic processes. Similarly to TST, NAST assumes that (i) intramolecular energy is statistically distributed among the molecular degrees of freedom (DOF) and (ii) a one-dimensional reaction coordinate can be separated from the remaining spectator DOF. Both microcanonical (energy-dependent) and canonical (temperature-dependent) ensembles can be used to describe internal states leading to two formulations of NAST. Transitions between PESs of two electronic states with different spin multiplicities are driven by various spin-dependent interactions, among which the spin-orbit coupling (SOC) is often the strongest.[66-69] The crossing seam between such two PESs is $3N$-7

dimensional, where *N* is the number of atoms in a molecule, and the seven omitted dimensions include three translational, three rotational and a reaction coordinate DOF. It is also assumed that nonadiabatic transitions between two crossing PESs can be described by effective transitions at a minimum energy crossing point (MECP) on the seam,[4] which plays a similar role to a saddle point in TST (Figure 3.1). At MECP, the reaction coordinate is orthogonal to the rest of (spectator) DOF. To evaluate the rate constant using NAST, the nuclear Hessian at the reactant minimum, as well as the energy gradients, nuclear Hessians and the SOC at MECP are needed. A more advanced treatment requires the knowledge of one-dimensional minimum energy paths from MECP to the reactant and product minima.[59,70] The statistical nature of NAST makes it relatively simple to account for the quantum effects, such as tunneling and zero-point vibrational energy (ZPE).[59]

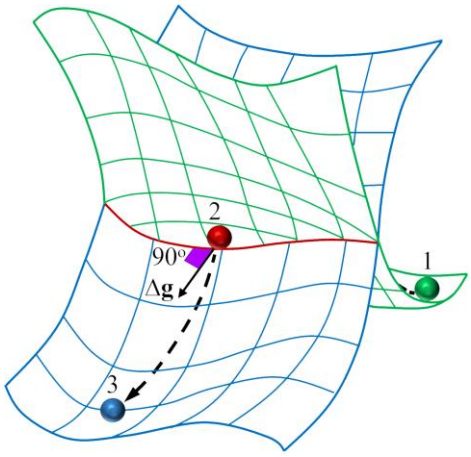

Figure 3.1. Intersection of potential energy surfaces of two electronic states with different spin multiplicities. Point 1 is the reactant minimum, point 2 is the minimum energy crossing point (MECP), point 3 is the product minimum, and $\Delta\mathbf{g} = |\mathbf{g}_1 - \mathbf{g}_2|$ is the gradient vector orthogonal to the crossing seam and aligned with the reaction coordinate at the MECP. The dashed curve shows the minimum energy path connecting MECP with the reactant and product minima.

In this article, we present the NAST package for investigating the mechanisms and predicting the rates of spin-dependent processes. The package includes an implementation of NAST and additional computational tools for processing the output of electronic structure calculations. In Section 2, we describe the fundamentals of NAST. In Section 3, we discuss the NAST package capabilities and implementation. In Section 4, we present several examples of NAST application. In conclusion, we summarize the main strengths and discuss future extensions of NAST.

II. Nonadiabatic Statistical Theory

A. Microcanonical Rate Constants

The microcanonical rate constant $k(E)$ of a unimolecular reaction is calculated as a function of the internal (rovibrational) energy E,

$$k(E) = \sigma \frac{N_{\mathrm{X}}(E)}{h\rho_{\mathrm{R}}(E)}, \tag{3.1}$$

$$N_{\mathrm{X}}(E) = \int_0^E \rho_{\mathrm{X}}(E - \varepsilon_\perp) P(\varepsilon_\perp) d\varepsilon_\perp, \tag{3.2}$$

$$\sigma = \frac{\sigma_{\mathrm{R}}}{\sigma_{\mathrm{X}}} \gamma_{\mathrm{X}}, \tag{3.3}$$

where $N_{\mathrm{X}}(E)$ is the effective number of states at the MECP, ρ_{R} and ρ_{X} are the densities of rovibrational states at reactant and MECP, respectively, and h is Planck's constant. Calculations of the densities of rovibrational states are described in SI. The interstate transition probability $P(\varepsilon_\perp)$ is a function of the energy $\varepsilon_\perp$ partitioned in the reaction coordinate orthogonal to the crossing seam. The reaction path degeneracy σ is defined

in terms of the symmetry numbers of reactant (σ_R) and MECP (σ_{X}),[71] and the number of chiral MECP isomers (γ_{X}).[72]

B. Microcanonical Transition Probabilities

The most popular ways to calculate the interstate transition probability $P(\varepsilon_\perp)$ in Eq. (3.2) are the double passage Landau-Zener (LZ) and weak coupling (WC) formulas.[4,55,73,74] These formulas yield a cumulative probability of transition at MECP for the forward (primary passage) and backward (secondary passages) motions along the reaction coordinate,

$$P_{\mathrm{LZ}}(\varepsilon_\perp) = p_{\mathrm{LZ}} + (1 - p_{\mathrm{LZ}})p_{\mathrm{LZ}} = 2p_{\mathrm{LZ}} - {p_{\mathrm{LZ}}}^2, \tag{3.4}$$

$$p_{\mathrm{LZ}}(\varepsilon_\perp) = 1 - \exp\left(-\frac{2\pi H_{\mathrm{SO}}^2}{\hbar|\Delta\mathbf{g}|}\sqrt{\frac{\mu_\perp}{2(\varepsilon_\perp - E_X)}}\right), \tag{3.5}$$

$$P_{\mathrm{WC}}(\varepsilon_\perp) = 4\pi^2 H_{\mathrm{SO}}^2 \left(\frac{2\mu_\perp}{\hbar^2\bar{\mathbf{g}}|\Delta\mathbf{g}|}\right)^{\frac{2}{3}} \mathrm{Ai}^2\left(-(\varepsilon_\perp - E_X)\left(\frac{2\mu_\perp|\Delta\mathbf{g}|^2}{\hbar^2\bar{\mathbf{g}}^4}\right)^{\frac{1}{3}}\right), \tag{3.6}$$

where p_{LZ} is the single-passage LZ probability, H_{SO} is the spin-orbit coupling constant, $\hbar$ is reduced Planck's constant. The norm of the gradient parallel to the reaction coordinate $|\Delta\mathbf{g}| = |\mathbf{g}_1 - \mathbf{g}_2|$ and the mean gradient $\bar{\mathbf{g}} = (|\mathbf{g}_1||\mathbf{g}_2|)^{1/2}$ are defined in terms of the gradients of two crossing PESs at MECP, $\mathbf{g}_1$ and $\mathbf{g}_2$. In Eqs. (3.5 and 3.6), $\mu_\perp$ is the reduced mass for the motion along the reaction coordinate, and E_{X} is the MECP energy barrier with respect to the reactant minimum. In Eq. (3.6), Ai is the Airy function.

To account for ZPE, the MECP energy can be redefined as $E_{\mathrm{X}} \rightarrow E_{\mathrm{X}} + ZPE_{\mathrm{X}} - ZPE_{\mathrm{R}}$. For a non-linear molecule, the zero-point energies at the reactant minimum and MECP are defined as:

$$ZPE_{\mathrm{R}} = \frac{1}{2}\sum_{i=1}^{3N-6} \hbar\omega_i^{\mathrm{R}}, \tag{3.7}$$

$$ZPE_{\mathrm{X}} = \frac{1}{2}\sum_{i=1}^{3N-7} \hbar\omega_i^{\mathrm{X}}, \tag{3.8}$$

where ω_i^{R} and ω_i^{X} are the fundamental transition frequencies of reactant and MECP, respectively. In Eq. (3.7), index *i* runs over $3N-6$ vibrational DOF, while only $3N-7$ DOF orthogonal to the reaction coordinate contribute to ZPE at MECP. Note that using ZPE_{X} at the classical turning point along the minimum energy reaction path is equivalent to the zero-curvature tunneling approximation in TST, where the density of the rovibrational states is approximated by the density at TS and the effective TS barrier is reduced by the difference between ZPE_{R} and ZPE_{TS}.

The LZ probability is defined only at the reaction energy $\varepsilon_{\perp}$ above MECP, and therefore does not account for quantum tunneling through the MECP barrier. In addition, the LZ probability formula does not describe the quantum interference between primary and secondary passages at MECP.[4] These two quantum effects are included in the WC probability formula. However, both the LZ and WC formulas are only valid within the limited region of the parameters $\varepsilon_{\perp}$, $\mu_{\perp}$, H_{SO} and the energy gradients. For example, the WC formula can predict a greater than unit probability of transition, if the interacting states are strongly coupled as often the case in the complexes containing second- and third-row transition metals.[4] In addition, the LZ and

WC formulas assume a linear behavior of the two crossing potentials, which is often a reasonable approximation in the vicinity of MECP but not in the regions closer to the reactant and product minima. A more sophisticated approach to predict transition probabilities, which does not suffer from these limitations, has been introduced by Zhu and Nakamura (ZN).[75-80] The ZN probability expressions require knowledge of the entire one-dimensional minimum energy path connecting MECP to the reactant and product minima. This path can be obtained in either spin-diabatic or spin-adiabatic representations.[49] The ZN theory distinguishes two intersection types between PESs: a sloped intersection ($\mathbf{g}_1 \cdot \mathbf{g}_2 > 0$) and a peaked intersection ($\mathbf{g}_1 \cdot \mathbf{g}_2 < 0$) (Figure S1). Currently, in the NAST package, the ZN probability is implemented only for a sloped intersection in the spin-adiabatic representation. Because most of the electronic structure calculations produce spin-diabatic PESs, the adiabatic potentials are obtained by diagonalizing the following matrix:

$$\begin{pmatrix} E_1^d(r) & H_{\mathrm{SO}} \\ H_{\mathrm{SO}} & E_2^d(r) \end{pmatrix}, \tag{3.9}$$

where E_1^d and E_2^d are the spin-diabatic energies of two electronic states with arbitrary spin multiplicities, r is the arc length along the minimum energy reaction path in mass-scaled coordinates[81] with the reduced mass set to 1 amu, and H_{SO} is the spin-orbit coupling constant at MECP. The diagonalization of the matrix defined by Eq. (3.9) produces two eigenvalues corresponding to the adiabatic (spin-mixed) state energies, E_1 and E_2 (Figure 2). The ZN double passage transition probability is given by

$$P_{\mathrm{ZN}}(\varepsilon_\perp) = 4p_{\mathrm{ZN}}(1 - p_{\mathrm{ZN}})\sin^2(\psi), \tag{3.10}$$

where ψ is the overall transition phase. The single passage probability p_{ZN} defined in SI depends on several parameters that are functions of the energies at the smallest energy gap point r_0, the turning points at the MECP energy t_1^0 and t_2^0, and the turning points t_1 and t_2 corresponding to the specific value of the energy $\varepsilon_\perp$ (Figure 3.2).

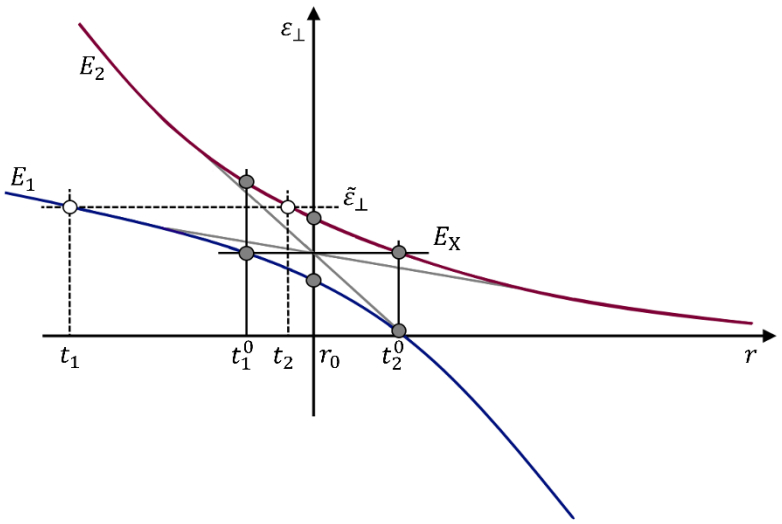

Figure 3.2. Sloped intersection of two spin-adiabatic potentials with the energies E_1 (blue) and E_2 (red) along the reaction coordinate r. Points r_0, t_1^0, t_2^0, t_1 and t_2 are defined in the text.

C. Canonical Rate Constants

A canonical, temperature-dependent, rate constant can be obtained by averaging the microcanonical rate constant (Eq. 3.1) over the internal energy Boltzmann distribution, leading to the following expression:

$$k(T) = \frac{\sigma}{hQ_{\mathrm{R}}(T)} \int_0^\infty N_{\mathrm{X}}(E) e^{-E/k_{\mathrm{B}}T} dE, \tag{3.11}$$

$$Q_{\mathrm{R}}(T) = \int_0^\infty \rho_{\mathrm{R}}(E)\, e^{-E/k_{\mathrm{B}}T}\, dE, \tag{3.12}$$

where Q_{R} is the partition function of the reactant, T is the temperature, and k_{B} is the Boltzmann constant.

D. Velocity-Averaged Probabilities

Velocity-averaged probabilities provide a simple estimate for the likelihood of spin-forbidden reaction mechanism as a function of temperature. The velocity-averaged single passage LZ probabilities (Eqs. 3.13 and 3.14) are derived by averaging the microcanonical LZ probability (Eq. 3.5) using the Maxwell-Boltzmann (MB) and normalized Kuki (K) distributions of the mass-weighted velocity $v^2 = 2(\varepsilon_{\perp} - E_{\mathrm{X}})$.[6-82] The corresponding double passage LZ probabilities can be obtained using Eq. (3.4). The velocity-averaged WC probabilities (Eqs. 3.15 and 3.16) can also be derived using the Maxwell-Boltzmann and normalized Kuki distributions. It is important to note that, in contrast to the microcanonical WC probability, the velocity-averaged WC probabilities do not account for quantum tunneling.

$$\langle p_{\mathrm{LZ}}(T)\rangle_{\mathrm{MB}} = 1 - \left(\frac{2}{\pi k_{\mathrm{B}}T}\right)^{\frac{1}{2}} \int_0^{\infty} \exp\left(-\frac{2\pi H_{\mathrm{SO}}^2 \mu_{\perp}^{\frac{1}{2}}}{\hbar|\Delta \mathbf{g}|v}\right) \exp\left(-\frac{v^2}{2k_{\mathrm{B}}T}\right) dv, \qquad (3.13)$$

$$\langle p_{\mathrm{LZ}}(T)\rangle_{\mathrm{K}} = 1 - \frac{1}{k_{\mathrm{B}}T} \int_0^{\infty} v \exp\left(-\frac{2\pi H_{\mathrm{SO}}^2 \mu_{\perp}^{\frac{1}{2}}}{\hbar|\Delta \mathbf{g}|v}\right) \exp\left(-\frac{v^2}{2k_{\mathrm{B}}T}\right) dv, \qquad (3.14)$$

$$\langle P_{\mathrm{WC}}(T)\rangle_{\mathrm{MB}} = \alpha \left(\frac{2}{\pi k_{\mathrm{B}}T}\right)^{\frac{1}{2}} \int_0^{\infty} \mathrm{Ai}^2\left(-\frac{1}{2}v^2\mu_{\perp}\gamma\right) \exp\left(-\frac{v^2}{2k_{\mathrm{B}}T}\right) dv, \qquad (3.15)$$

$$\langle P_{\mathrm{WC}}(T)\rangle_{\mathrm{K}} = \frac{\alpha}{k_{\mathrm{B}}T} \int_0^{\infty} v\, \mathrm{Ai}^2\left(-\frac{1}{2}v^2\mu_{\perp}\gamma\right) \exp\left(-\frac{v^2}{2k_{\mathrm{B}}T}\right) dv, \qquad (3.16)$$

$$a = 4\pi^2 H_{\mathrm{SO}}^2 \left(\frac{2\mu_\perp}{\hbar^2 \bar{\mathbf{g}}|\Delta\mathbf{g}|}\right)^{\frac{2}{3}}, \tag{3.17}$$

$$\gamma = \left(\frac{2\mu_\perp |\Delta\mathbf{g}|^2}{\hbar^2 \bar{\mathbf{g}}^4}\right)^{\frac{1}{3}}. \tag{3.18}$$

F. Rate Constants and Transition Probabilities Between Individual M_S Components of Spin States

A simple approach to model transitions between electronic states with the different spin quantum numbers S and S' is to calculate the *effective* probabilities and rates accounting for all M_S components of the spin multiplets. In this approach, the effective SOC, also called the SOC constant, is obtained as the RMS of the couplings between individual M_S components,

$$H_{\mathrm{SO}} = \left(\sum_{M_S=-S}^{S} \sum_{M_{S'}=-S'}^{S'} \left|\langle S, M_S | \hat{H}_{\mathrm{SO}} | S', M_{S'} \rangle\right|^2\right)^{1/2}. \tag{3.19}$$

In Eq. (19), $\hat{H}_{\mathrm{SO}}$ is the spin-orbit operator; for example, from the Breit-Pauli Hamiltonian.[67] This approach is easy to justify for a singlet-triplet crossing with the MECP energy gap between the two spin-adiabatic states equal to $2H_{\mathrm{SO}}$.[4] However, for the states with higher spin multiplicities, for example a triplet-quintet crossing, there are multiple energy gaps between the adiabatic states. Therefore, employing a single effective SOC to calculate the transition probability and rate constant is not well-justified.

This issue can be resolved by calculating the rate constants and transition probabilities between individual M_S components of the spin multiplets. As an example, for a singlet-triplet crossing, the non-zero spin-orbit coupling matrix elements are

$$z = \langle 0,0|\hat{H}_{\mathrm{SO}}|1,-1\rangle, \qquad ib = \langle 0,0|\hat{H}_{\mathrm{SO}}|1,0\rangle,$$
$$z^* = \langle 0,0|\hat{H}_{\mathrm{SO}}|1,+1\rangle, \tag{3.20}$$

where z and z^* are complex conjugate to each other, and b is real. The single-passage LZ probabilities $p_{\mathrm{LZ}}^{M_S,M_{S'}}(\varepsilon_\perp)$ between the components M_S and $M_{S'}$ of the spin states $S = 0$ and S'=1 read

$$p_{\mathrm{LZ}}^{0,-1}(\varepsilon_\perp) = p_{\mathrm{LZ}}^{0,+1}(\varepsilon_\perp) = 1 - \exp\left(-\frac{2\pi z z^*}{\hbar|\Delta\mathbf{g}|}\sqrt{\frac{\mu_\perp}{2(\varepsilon_\perp - E_{\mathrm{X}})}}\right), \tag{3.21}$$

$$p_{\mathrm{LZ}}^{0,0}(\varepsilon_\perp) = 1 - \exp\left(-\frac{2\pi b^2}{\hbar|\Delta\mathbf{g}|}\sqrt{\frac{\mu_\perp}{2(\varepsilon_\perp - E_{\mathrm{X}})}}\right). \tag{3.22}$$

The double-passage probabilities $P_{\mathrm{LZ}}^{0,\pm1}$ and $P_{\mathrm{LZ}}^{0,0}$ can be obtained from the single passage probabilities (Eq. 3.4) and employed to calculate the microcanonical rate constants between individual M_S components,

$$k_{0,\pm1}(E) = \frac{\sigma}{h\,\rho_{\mathrm{R}}(E)}\int_0^E \rho_{\mathrm{X}}(E-\varepsilon_\perp)P_{\mathrm{LZ}}^{0,\pm1}(\varepsilon_\perp)d\varepsilon_\perp, \tag{3.23}$$

$$k_{0,0}(E) = \frac{\sigma}{h\,\rho_{\mathrm{R}}(E)}\int_0^E \rho_{\mathrm{X}}(E-\varepsilon_\perp)P_{\mathrm{LZ}}^{0,0}(\varepsilon_\perp)d\varepsilon_\perp. \tag{3.24}$$

The probabilities and rate constants between individual M_S components can be calculated for any pair of spin states with $|S - S'|$ =1, as shown in SI for a triplet-quintet crossing.

G. Transition State Theory Rate Constants

For adiabatic reactions, both microcanonical and canonical NAST rate constants can be reduced to the traditional TST rate constants by replacing MECP with transition state (TS) and the transition probability in Eq. (3.2) with the Heaviside step function.[83] The canonical TST rate constant, obtained by averaging the microcanonical constant over the Boltzmann internal energy distribution, is equivalent to the traditional analytical TST expression:[4]

$$k(T) = \sigma \frac{k_B T}{h} \frac{Q_{\mathrm{TS}}}{Q_{\mathrm{R}}} e^{-E_{\mathrm{TS}}/k_{\mathrm{B}}T}, \tag{3.25}$$

where Q_{TS} and Q_{R} are partition functions of TS and reactant.

H. Effective Hessian

Calculation of the effective number of states $N_{\mathrm{X}}(E)$ defined in Eq. (3.2) requires the density of vibrational states at MECP, which can be obtained using the harmonic vibrational analysis.[84-85] Since MECP is not a stationary point on either of two crossing PESs, a conventional vibrational analysis is not valid. The vibrational frequencies at MECP can be obtained from the *effective Hessian* matrix calculated from the state-specific Hessians $\mathbf{H}_1$ and $\mathbf{H}_2$, and gradients at MECP:[86]

$$\mathbf{H}_{\text{eff}} = \frac{|\mathbf{g}_1|\mathbf{H}_2 \pm |\mathbf{g}_2|\mathbf{H}_1}{|\mathbf{g_1}| \pm |\mathbf{g_2}|}. \quad (3.26)$$

The details of calculating effective Hessian are given in SI.

III. NAST Package Capabilities and Implementation

A. Forward and Reverse Rate Constants

By default, the NAST package calculates only forward rate constants with both the LZ and WC transition probabilities. A forward direction is defined as the transition from the higher energy spin state (reactant) to the lower energy spin state (product). Such calculations require molecular properties only at the reactant minimum and MECP. However, calculation of the reverse rate constants can be requested in the same run, if molecular properties at the product minimum are provided. For such reverse rate calculations, the above definition of reactant and product prevents the reverse unphysical tunneling to the region below the reactant minimum where the density of states is zero (Figure 3.3). If only a forward rate constant with tunneling contribution is calculated, it is important to ensure that the reactant has a higher energy than the product to prevent contribution from unphysical tunneling to the rate constants. This is not required if the rate constants are calculated with the LZ probability or traditional TST, which do not account for tunneling. In the present implementation, the ZN transition probability can be only used to calculate a forward rate constant. For canonical rate constant calculations, the temperature range (default 290-300 K) and step (default 1 K) can be specified in the input file.

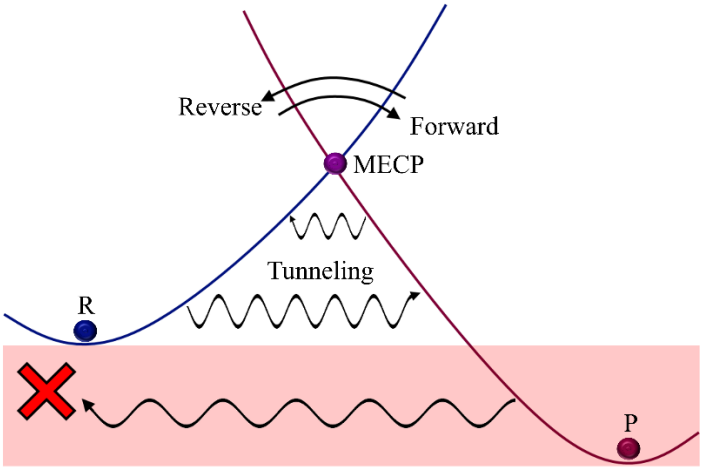

Figure 3.3. Definition of forward and reverse directions. The region of reverse unphysical tunneling is shown by the red box.

B. Transition Probabilities

The LZ, WC, and ZN probabilities (Eqs. 3.4-3.6 and 3.10) are used to calculate the microcanonical and canonical rate constants. The velocity-averaged LZ and WC probabilities (Eq. 3.13-3.16), which are calculated by default, can be used to obtain a qualitative understanding of the spin-dependent reaction kinetics. While calculations of the LZ and WC probabilities require molecular properties at reactants and MECP only, the ZN probability calculations require additional input data discussed together with the intrinsic reaction coordinate (IRC) fit code (Section III.G).

C. Rate Constants and Transition Probabilities Between Individual M_S Components of Spin States

In addition to effective transition probabilities and rate constants between the spin manifolds with the different values of quantum number *S*, the NAST package can

calculate the transition probabilities and rate constants between individual M_S components of different spin manifolds. In the current implementation, the M_S-specific kinetics can be modeled only using the LZ formula. Such calculations can provide insight into the role of individual M_S components in the overall spin-dependent kinetics. Moreover, working in the basis of individual M_S components is necessary to study the effect of an external magnetic field on spin-dependent processes.

D. Rate Constants in Solution

Transition state theories for reactions in solution has been extensively discussed before.[60,87-92] In the current NAST implementation, the solution phase effects can be modeled by simply assuming that all molecular rotations are frozen. In such calculations, only vibrational states contribute to the total density of states, and contributions from rotational states are ignored.

E. Transition State Theory Rate Constants

The NAST package can calculate the traditional TST rate constants for single-state adiabatic reactions by replacing the MECP molecular properties with the TS properties (energy, vibrational frequencies, moments of inertia). Such TST calculations do not require spin-orbit couplings, energy gradients and reduced mass, and can be invoked with a separate keyword.

F. Effective Hessian Tool *effhess*

The effective Hessian tool *effhess*, distributed as a part of the NAST package, calculates and diagonalizes the effective Hessian (Eq. 3.26) to generate the vibrational

frequencies at MECP, the reduced mass $\mu_{\perp}$, $|\Delta\mathbf{g}|$ and $\bar{\mathbf{g}}$. These quantities are needed for the following rate constant calculations. Currently, the tool can read the MECP energy gradient vectors and Hessian matrices from the output files generated by the GAMESS[93] and Molpro[94] electronic structure packages. The *effhess* tool generates a template of an input file for the main NAST code.

G. IRC Fitting Tool *ircfit*

The fitting tool *ircfit* produces the IRC potentials of two crossing spin states. These potentials are required for calculating the ZN probabilities. Currently, *ircfit* can read only the GAMESS IRC output files. Here we summarize the *ircfit* algorithm, the details are included in SI.

1) Perform two IRC calculations from MECP to the minima of reactant and product, generating the two sets of geometries $\{\boldsymbol{Q}_i, E_i\}_{X\to R}$ and $\{\boldsymbol{Q}_i, E_i\}_{X\to P}$, where $\boldsymbol{Q}_i$ and E_i are the coordinates and energy of molecular geometry *i*. Index *i* runs from 1 (MECP) to *n* for the reactant side of IRC and *m* for the product side.

2) Define $n+m$ points along the reaction coordinate as

$$r_j = \left(\sum_{p=1}^{3N} (dQ_{j,p})^2\right)^{1/2}, \tag{3.27}$$

where $dQ_{j,p}$ is the difference between the coordinates of the reactant and the geometry $j \in [1, n+m]$.

3) Build the crossing potentials by fitting the two sets of points $\{r_i, E_i\}_{X\to R}$ and $\{r_i, E_i\}_{X\to P}$ with fourth-order polynomials.

$$f(\mathbf{c}, r) = \sum_{q=0}^{4} c_q \, r^q \, . \tag{3.28}$$

The vector of coefficients **c** is obtained by minimizing the linear least-squares function

$$F = \sum_{i=1}^{k} \left(E_i - f(\mathbf{c}, r_i)\right)^2, \tag{3.29}$$

where $k=n$ for the reactant side of the fit, and $k=m$ for the product side. The coefficients of the polynomials, which represent spin-diabatic states, are used by the main NAST code to generate spin-adiabatic states (Eq. 3.9) required for the ZN probability calculations.

H. Modular Structure of NAST Package

The NAST package consists of a collection of modules written in modern Fortran and runs under Linux (Figure 3.4). The package manual contains a full list of the input file keywords that control the type of rate calculation. Most of the keywords have default values appropriate for the common calculation types. The effective Hessian tool *effhess* can be used to generate an input file template containing MECP properties, further reducing the efforts required to set up a NAST calculation. The rest of the input data, including vibrational frequencies, moments of inertia, electronic energies and SOC must be extracted from the output of electronic structure calculations. The calculated canonical rate constants and velocity-averaged transition probabilities are saved to the main output file *nast.out*. Additional information, including microcanonical rate constants, transition probabilities and density of states are written to separate output files. The amount of output information can be controlled by user.

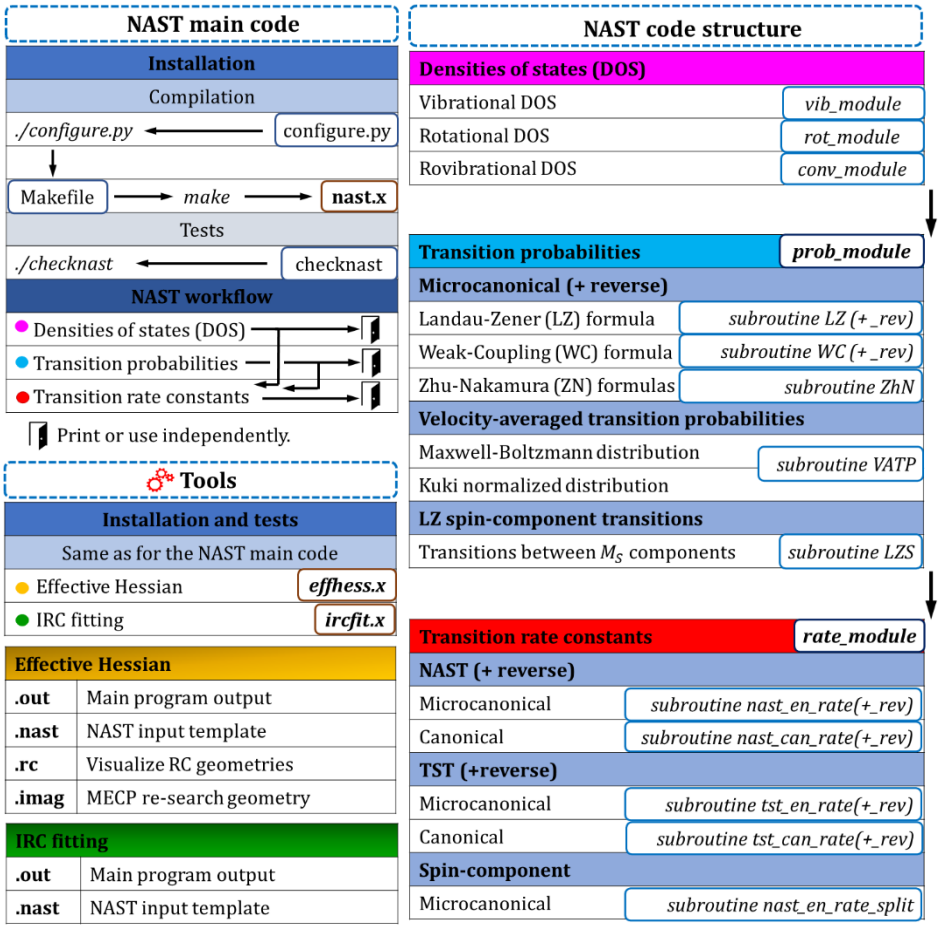

Figure 3.4. Modular structure of the NAST package. The top left panel illustrates the main NAST code installation, testing, and workflow. The bottom left panel lists the output files of the effective Hessian (*effhess*) and IRC fitting (*ircfit*) tools. The right panel shows the main modules and subroutines of the NAST package.

The NAST package requires an external math library. It has been tested with the Intel Math Kernel Library (MKL) but can be linked with other math libraries. The package has been successfully compiled and tested with the *gfortran* and *ifort* compilers. To streamline the package installation, the provided Python configuration script *configure.py* can be used to generate a *Makefile*. The Linux utility *make* is used to compile and link the executable *nast.x*. A new build can be tested by running the script *checknast* that executes several test examples. The installation and testing

procedures are the same for the effective Hessian and IRC tools. The configuration and installation details are provided in the package manual.

IV. Examples of Applications

A. Isomerization of Propylene Oxide to Acetone and Propanal

This example demonstrates how the NAST package can be used to calculate the reaction rates for single-state adiabatic reactions using the traditional TST. We consider the isomerization of propylene oxide to acetone and propanal, following the original theoretical work of Dubnikova and Lifshitz.[95] For each isomerization reaction, four canonical TST rate constants are compared: i) predicted by the NAST package, ii) calculated analytically using Eq. (3.25), iii) calculated analytically using Eq. 3.30 below[95] and iv) obtained from an experiment.[96] In Ref.[95], the following equation has been used:

$$k(T) = \sigma \frac{k_{\mathrm{B}} T}{h} e^{-\Delta S^{\#}/R} e^{-\Delta H^{\#}/RT}, \tag{3.30}$$

where R is the universal gas constant; $\Delta S^{\#}$and $\Delta H^{\#}$ are the entropy and enthalpy of activation, respectively. Because for a unimolecular reaction, $\Delta H^{\#} = E_{\mathrm{TS}} + \Delta\mathrm{ZPE}$, the activation enthalpy is equal to the ZPE-corrected electronic barrier between transition state and reactant. The input data for NAST were obtained from the B3LYP geometry optimization and Hessian calculations in GAMESS, and the single-point CCSD(T) energy calculations in Molpro. The cc-pVDZ basis set was used in all calculations. The partition functions Q_{TS} and Q_{R} used in Eq. (3.25) were taken from the GAMESS Hessian calculations. In Eq. 3.30, the original data from Table 1 of

Dubnikova and Lifshitz[95] was used. The energy profiles for two isomerization reactions are shown in Figure 3.5.

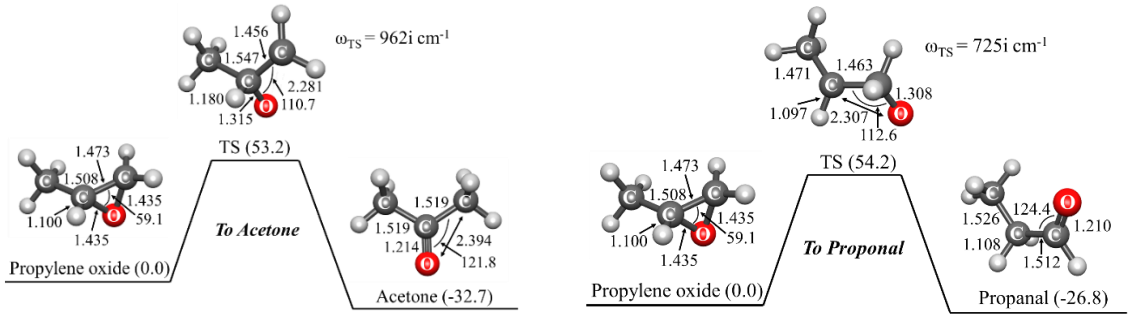

Figure 3.5. Energies and structural parameters for the isomerization reactions of propylene oxide to acetone (left) and propanal (right). The relative CCSD(T) energies (kcal·mol^{-1}) listed in parenthesis are corrected with $\Delta ZPE = ZPE_{\mathrm{X}} - ZPE_{\mathrm{R}}$ calculated with B3LYP. Bond lengths and angles are in Å and degrees, respectively.

The NAST input file and parts of the output file are shown below.

```
&keys zpe = 1 tst = .true. &end          ! TST calculation with ZPE correction
&inputdata
freX = 263, 294, 374, 580, 729, 871, 886, 958, 999, 1081, 1118, 1241, 1283, 1357, 1434, 1452, 1471,
2296, 3026, 3092, 3118, ,3142, 3238      ! Vibrational frequencies (cm-1) of TS/MECP
freR = 240, 370, 416, 773, 848, 903, 974, 102, 1117, 1136, 1153, 1173, 1277, 1381, 1423, 1451, 1471,
1515, 3025, 3059, 3076, 3098, 3117, 3153 ! Vibrational frequencies (cm-1) of reactant
inertX = 170.850, 217.264, 351.144        ! Moments of inertia for TS/MECP
inertR = 100.305, 272.514, 305.514        ! Moments of inertia for reactant
enX = 0.09129754                          ! Energy of TS in hartree (program will add ΔZPE)
enR = 0.0                                 ! Energy of reactant in hartree
maxn = 30000                              ! Maximum energy bin - integration limit in cm-1
T1 = 1000                                 ! Initial temperature in K for canonical rate constant
&end
```

```
   ******************************************************
   ~~~~~~~ NAST: Nonadiabatic Statistical Theory ~~~~~~~~
                ~~~~~ v. 2021.1 ~~~~~
   ******************************************************
----------------------------------------------------------
NAST control parameters and related data

zpe = 1     sp = F     zn = F     solution = F
tst = T     printmore = F     rev = F     extern = F
----------------------------------------------------------
zpe = 1: ZPE correction scheme I (eliminates turning points below ZPE).
Electronic barrier from reactant to MECP is   20037 cm-1
ZPE of reactants =   18586 cm-1
ZPE of MECP =   17150 cm-1
ZPE-corrected MECP energy bin =  18602 cm

  ----------------------------------------------------------
            Start NAST calculation
  ----------------------------------------------------------

   1. Calculating densities of states

......vibrational.
........rotational.
.........rovibrational.

   2. Calculating microcanonical TST rate constant.
..................................... Done.

(The forward rate constant k(E) is multiplied by reaction path degeneracy equal to 1 )

           Canonical rate constant, k(T)

    T(K)     TST rate constant

  1000.0          6.78E+01

 Total CPU time =    10.35
```

Table 3.1 shows the calculated and experimental rate constants for the isomerization of propylene oxide to acetone and propanal. The factor of two difference

between the acetone rate constants calculated with two analytical expressions can be explained by the 1.0 kcal·mol^{-1} discrepancy in the TS barrier (using the same barrier height of 53.2 kcal·mol^{-1} in both analytical expressions reduces this difference to 18%). The difference between the NAST rate constant (67.8 s^{-1}) and the analytical constant obtained with Eq. (3.30) (101.0 s^{-1}) could be due to a finite accuracy of the numerical integration in NAST. For the isomerization to propanal, similar differences in the reaction rates calculated with different methods are observed. All calculated rate constants are in reasonable agreement with the experimental values for both isomerization reactions.

Table 3.1. Canonical TST rate constants for isomerization of propylene oxide to acetone and propanal at T=1000 K.

Product	**Source**	E_{TS}, **kcal·mol^{-1}**	k_{1000}, **s^{-1}**
Acetone	NAST	53.2	67.8
	Analytical, Eq. (3.30)[a]	54.2	50.2
	Analytical, Eq. (3.25)	53.2	101.0
	Experiment[b]	-	30.0
Propanal	NAST	54.2	43.0
	Analytical, Eq. (3.30)[a]	54.4	69.6
	Analytical, Eq. (3.25)	54.2	88.6
	Experiment[b]	-	90.0

[a] Ref.[95]

[b] Experimental values are estimated from the log(k) vs. T plots of Ref.[96]

B. Spin-Forbidden Isomerization of Ni(dpp)Cl2

This example demonstrates the forward and reverse rate constants calculation in a single NAST run. In addition to the overall rate constants, it predicts the rate constants between individual M_S components of two spin states. Spin-forbidden kinetics of interconversion between the singlet (planar) and triplet (tetrahedral) isomers of Ni(dpp)Cl_2 complex (dpp=1,3-bis(diphenylphosphino)propane) has been studied in acetonitrile.[97] To reduce the computational cost, the phenyl groups were replaced by methyls (Figure 3.6). The optimized geometries and Hessians for singlet, triplet, and MECP structures were obtained with the M11-L density functional, implicit solvation model, and def2-TZVP basis set, as implemented in GAMESS. The SOC value of 135 cm^{-1} was calculated with the second-order multiconfigurational quasi-degenerate perturbation theory (MCQDPT2) using the CASSCF(2e, 4o) wave function averaged over the lowest energy singlet and triplet electronic states. The forward ($S_1 \rightarrow T_0$) rate constant calculated using the WC transition probability at 296 K ($4.96 \times 10^6\ s^{-1}$) agrees almost within one order of magnitude with the experimental value of $4.5 \times 10^5\ s^{-1}$. However, the reverse ($T_0 \rightarrow S_1$) rate constant predicted to be $3.50 \times 10^2\ s^{-1}$ is significantly smaller than the experimental value of $6.0 \times 10^5\ s^{-1}$, which could indicate that the barrier for the reverse reaction is overestimated due to the low-level of electronic structure calculations and the reduced model size.

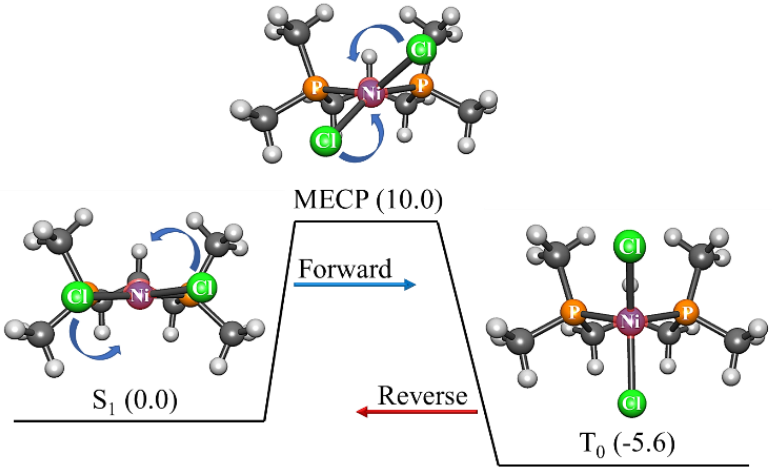

Figure 3.6. Reaction path for the singlet-triplet isomerization of the Ni(dpp)Cl_2 model from the square-planar to tetrahedral geometry. The twist angle between the Cl-Ni-Cl and P-Ni-P planes is 6°, 42° and 90° for the singlet, MECP and triplet geometries, respectively. The phenyl groups of Ni(dpp)Cl_2 are replaced with the methyl groups.

Calculations of the transition probabilities and rate constants between individual M_S components of the singlet and triplet states were carried out using the spin-orbit matrix elements (z = -69.0-63.8i cm^{-1} and b = 21.3 cm^{-1}, as defined in Eq. 3.20) obtained from the same MCQDPT2 calculations. The M_S-specific rate constants $k_{M_S\,,\,M_{S'}}$ for the transitions between the $M_S = 0$ component of singlet state and three $M_{S'} = \pm 1$ and $M_{S'} = 0$ components of the triplet state, calculated using the LZ transition probability are plotted in Figure 3.7. The stronger couplings between the $M_S = 0$ component of the singlet state and the $M_{S'} = \pm 1$ components of the triplet result in the faster population transfer, as evident from the $k_{0,\pm 1}$ rate constant being larger than $k_{0,0}$.

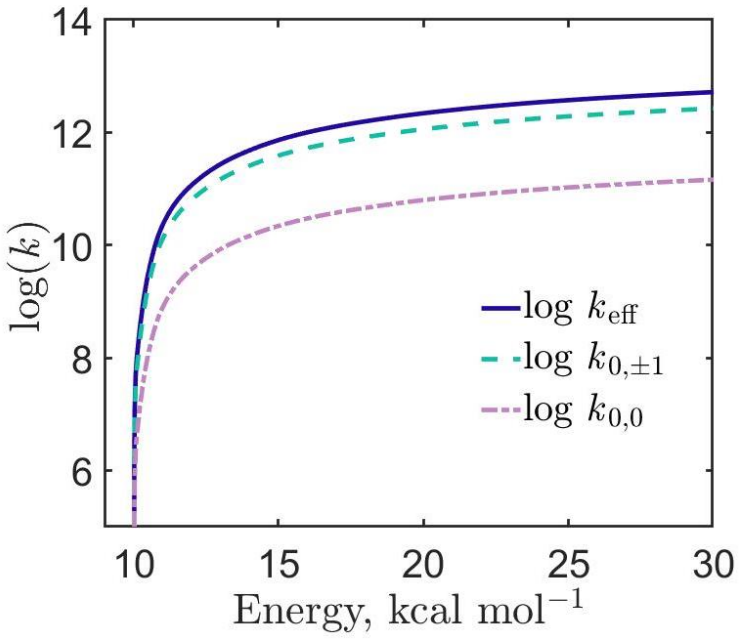

Figure 3.7. The microcanonical rate constants $k_{0,0}$ and $k_{0,+1} = k_{0,-1}$ for transitions between the M_S components of the singlet and triplet states calculated using the LZ probabilities. The effective rate constant k_{eff} corresponds to the overall transition between the singlet state and all three components of the triplet state.

C. $T_1 \rightarrow S_0$ Relaxation in Cyclopropene

This example demonstrates calculation of the rate constant using the ZN transition probability. Miller and Klippenstein published a detailed kinetics study of different reactions of C_3H_4, including those proceeding on multiple PESs with different spin multiplicities.[98] Here we consider the $T_1 \rightarrow S_0$ relaxation in cyclopropane (Figure 3.8). The equilibrium geometries and Hessians of the S_0, T_1 states and MECP were obtained at the B3LYP/cc-pVTZ level of theory. The SOC constant of 4.0 cm^{-1} was calculated with the MCQDPT2 method based on the CASSCF(2,2) wave function averaged over the S_0 and T_1 states, using the same basis set. All calculations were performed in GAMESS. To calculate the $T_1 \rightarrow S_0$ rate constant with the ZN transition

probability, the $T_1 \rightarrow$ MECP $\rightarrow S_0$ minimum energy reaction path was fitted with the *ircifit* tool using the geometries and energies generated by two IRC calculations starting from MECP and following to the T_1 and S_0 minima. The MECP$\rightarrow T_1$ path was fitted with the quartic polynomial, while the MECP$\rightarrow S_0$ path was approximated by a linear fit (Figure 3.9).

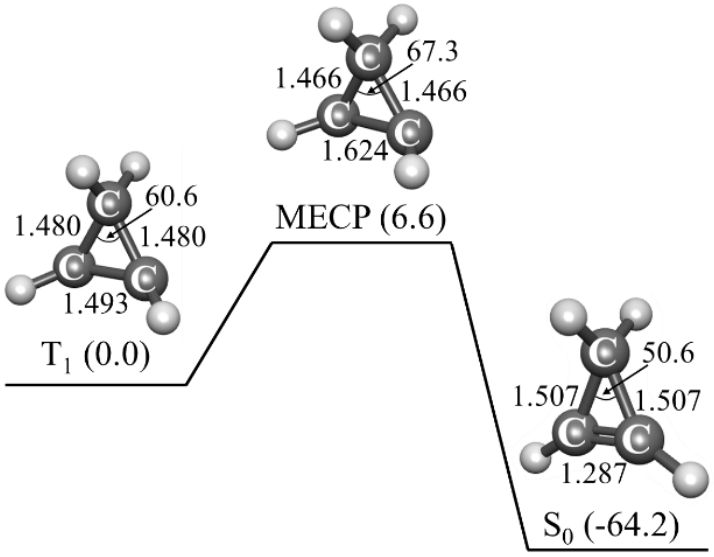

Figure 3.8. The $T_1 \rightarrow S_0$ relaxation path in cyclopropene. The relative energies of the T_1 minimum, the S_0 minimum and MECP (kcal mol^{-1}) are in parentheses. The bond lengths and angles calculated at the B3LYP/cc-pVTZ level of theory are in Å and degrees.

The $T_1 \rightarrow S_0$ canonical rate constant calculated at 1000 K with the ZN transition probability (3.07×10^7 s^{-1}) is almost an order of magnitude smaller than the value obtained with the WC probability (1.24×10^8 s^{-1}). This difference can be explained by the fact that the linear-crossing WC model significantly underestimates the width of the tunneling barrier (Figure 3.9). In contrast, the ZN model uses a more realistic potential energy curves and predicts a wider barrier, leading to a significant reduction in the tunneling contribution to the rate constant. Table 3.2 compares the same rate constant

calculated using the simple LZ transition probability with the values obtained by the MESMER 6.0 package.[99] There is a reasonable agreement between the values predicted by two packages. The larger discrepancies at high temperatures are attributed to the numerical integration errors in Eq. (3.2). It is important to note, that these discrepancies in the rate constants are significantly smaller than the errors expected due to the limited accuracy of the MECP barrier calculated by commonly used electronic structure methods.

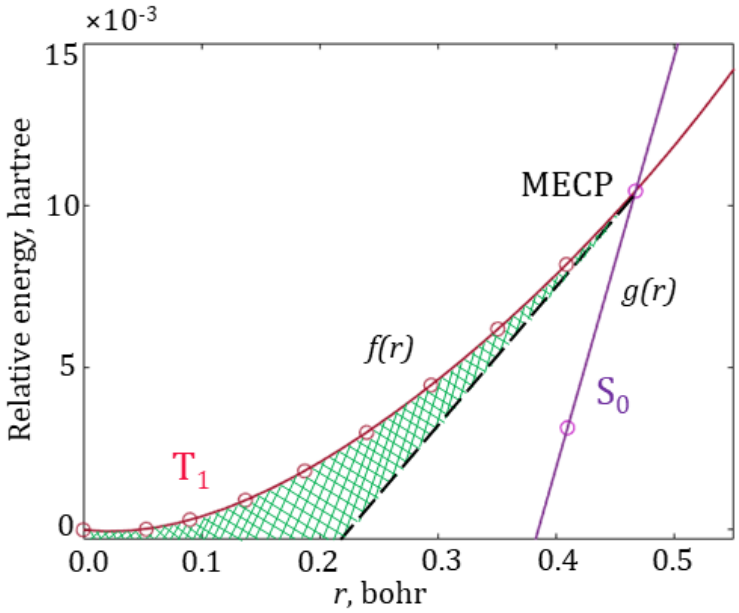

Figure 3.9. Fitted $T_1 \rightarrow$ MECP $\rightarrow S_0$ reaction path. The circles mark the energies of the IRC geometries. Green area shows an increase in the tunneling barrier width compared to the linear model (dashed black line). For the rate constant calculations, the coefficients of the fitting polynomials ($f(r) = 0.092\ r^4 - 0.121\ r^3 + 0.093\ r^2 - 0.004\ r - 1.86 \times 10^{-6}$ and $g(r) = 0.127\ r - 0.048$) are included in the NAST input file.

Table 3.2. The $T_1 \rightarrow S_0$ canonical rate constant (s^{-1}) at different temperatures. The relative difference between the NAST and MESMER values is defined as $(k_{NAST}-k_{MESMER})/k_{MESMER}$.

***T*, K**	**NAST**	**MESMER**	**Relative difference**
100	1.52×10^{-16}	2.37×10^{-16}	-0.36
200	6.71×10^{-4}	7.88×10^{-4}	-0.15
300	1.19×10^{1}	1.29×10^{1}	-0.08
400	1.62×10^{3}	1.68×10^{3}	-0.03
500	3.16×10^{4}	3.09×10^{4}	0.02
600	2.33×10^{5}	2.13×10^{5}	0.09
700	9.81×10^{5}	8.43×10^{5}	0.16
800	2.91×10^{6}	2.35×10^{6}	0.24
900	6.85×10^{6}	5.18×10^{6}	0.32
1000	1.36×10^{7}	9.71×10^{6}	0.40
1100	2.41×10^{7}	1.62×10^{7}	0.49
1200	3.89×10^{7}	2.47×10^{7}	0.58
1300	5.85×10^{7}	3.52×10^{7}	0.66
1400	8.32×10^{7}	4.76×10^{7}	0.75
1500	1.13×10^{8}	6.17×10^{7}	0.83
1600	1.48×10^{8}	7.73×10^{7}	0.91
1700	1.88×10^{8}	9.42×10^{7}	1.00
1800	2.33×10^{8}	1.12×10^{8}	1.08
1900	2.82×10^{8}	1.31×10^{8}	1.15
2000	3.36×10^{8}	1.50×10^{8}	1.24

V. Conclusions

We introduced the NAST software package for predicting kinetics of spin-dependent processes, including intersystem crossings, spin-forbidden reactions, and spin crossovers. The package calculates both the microcanonical and canonical rate constants and can account for quantum tunneling, zero-point vibrational energy, and reaction path interference. Traditional single-state adiabatic TST calculations are also possible. The NAST main strengths steam from its ability to 1) model nonadiabatic kinetics in large systems, 2) use high-level electronic structure methods for predicting

molecular properties, which is critical for accurate kinetics calculations and 3) study slow spin-dependent processes that present a great challenge for nonadiabatic molecular dynamics. Additional computational tools included in the NAST package simplify setting up kinetics calculations using molecular properties obtained with different electronic structure programs. The three presented examples demonstrate various capabilities of the NAST package. Future development will focus on multidimensional tunneling effects, accounting for MECP barrier recrossing, modeling spin-dependent processes in solution, and using an external magnetic field to control the kinetics of spin-dependent processes.

Acknowledgements

This work was supported by the National Science Foundation through a CAREER Award (CHE-1654547). We acknowledge Dr. Ryan Zaari for his contributions to the earlier version of the NAST package and thank Drs. Danil Kaliakin and Saikat Mukherjee for fruitful discussions.

References

(1) Lykhin, A. O.; Kaliakin, D. S.; DePolo, G. E.; Kuzubov, A. A.; Varganov, S. A. Nonadiabatic Transition State Theory: Application to Intersystem Crossings in the Active Sites of Metal-Sulfur Proteins. *Int. J. Quantum Chem.* **2016**, *116* (10), 750–761. https://doi.org/10.1002/qua.25124.

(2) Schröder, D.; Shaik, S.; Schwarz, H. Two-State Reactivity as a New Concept in Organometallic Chemistry. *Acc. Chem. Res.* **2000**, *33* (3), 139–145. https://doi.org/10.1021/ar990028j.

(3) Liao, P.; Carter, E. A. New Concepts and Modeling Strategies to Design and Evaluate Photo-Electro-Catalysts Based on Transition Metal Oxides. *Chem. Soc. Rev.* **2013**, *42* (6), 2401–2422. https://doi.org/10.1039/c2cs35267b.

(4) Sun, Y.; Tang, H.; Chen, K.; Hu, L.; Yao, J.; Shaik, S.; Chen, H. Two-State Reactivity in Low-Valent Iron-Mediated C-H Activation and the Implications for Other First-Row Transition Metals. *J. Am. Chem. Soc.* **2016**, *138* (11), 3715–3730. https://doi.org/10.1021/jacs.5b12150.

(5) Goodrow, A.; Bell, A. T.; Head-Gordon, M. Are Spin-Forbidden Crossings a Bottleneck in Methanol Oxidation? *J. Phys. Chem. C* **2009**, *113* (45), 19361–19364. https://doi.org/10.1021/jp906603r.

(6) Kaliakin, D. S.; Zaari, R. R.; Varganov, S. A. Effect of H2 Binding on the Nonadiabatic Transition Probability between Singlet and Triplet States of the [NiFe]-Hydrogenase Active Site. *J. Phys. Chem. A* **2015**, *119* (6), 1066–1073. https://doi.org/10.1021/jp510522z.

(7) Pohlman, A. J.; Kaliakin, D. S.; Varganov, S. A.; Casey, S. M. Spin Controlled Surface Chemistry: Alkyl Desorption from Si(100)-2×1 by Nonadiabatic Hydrogen Elimination. *Phys. Chem. Chem. Phys.* **2020**, *22* (29), 16641–16647. https://doi.org/10.1039/d0cp01913e.

(8) Zhao, J.; Wu, W.; Sun, J.; Guo, S. Triplet Photosensitizers: From Molecular Design to Applications. *Chem. Soc. Rev.* **2013**, *42* (12), 5323–5351. https://doi.org/10.1039/c3cs35531d.

(9) Zhao, J.; Chen, K.; Hou, Y.; Che, Y.; Liu, L.; Jia, D. Recent Progress in Heavy Atom-Free Organic Compounds Showing Unexpected Intersystem Crossing

(ISC) Ability. *Org. Biomol. Chem.* **2018**, *16* (20), 3692–3701. https://doi.org/10.1039/c8ob00421h.

(10) Pordel, S.; Pickens, R. N.; White, J. K. Release of CO and Production of 1O2 from a Mn-BODIPY Photoactivated CO Releasing Molecule with Visible Light. *Organometallics* **2021**, 40 (17), 2983-2994. https://doi.org/10.1021/acs.organomet.1c00331.

(11) Bogani, L.; Wernsdorfer, W. Molecular Spintronics Using Single-Molecule Magnets. *Nat. Mater.* **2008**, *7* (1), 179–186. https://doi.org/10.1201/b11086-37.

(12) Ullah, A.; Cerdá, J.; Baldoví, J. J.; Varganov, S. A.; Aragó, J.; Gaita-Ariño, A. In Silico Molecular Engineering of Dysprosocenium-Based Complexes to Decouple Spin Energy Levels from Molecular Vibrations. *J. Phys. Chem. Lett.* **2019**, *10* (24), 7678–7683. https://doi.org/10.1021/acs.jpclett.9b02982.

(13) Bayliss, S. L.; Laorenza, D. W.; Mintun, P. J.; Kovos, B. D.; Freedman, D. E.; Awschalom, D. D. Optically Addressable Molecular Spins for Quantum Information Processing. *Science* **2020**, *370* (6522), 1309–1312. https://doi.org/10.1126/science.abb9352.

(14) Gaita-Ariño, A.; Luis, F.; Hill, S.; Coronado, E. Molecular Spins for Quantum Computation. *Nat. Chem.* **2019**, *11* (4), 301–309. https://doi.org/10.1038/s41557-019-0232-y.

(15) Goldman, M. L.; Doherty, M. W.; Sipahigil, A.; Yao, N. Y.; Bennett, S. D.; Manson, N. B.; Kubanek, A.; Lukin, M. D. State-Selective Intersystem Crossing in Nitrogen-Vacancy Centers. *Phys. Rev. B - Condens. Matter Mater. Phys.* **2015**, *91* (16), 1–11. https://doi.org/10.1103/PhysRevB.91.165201.

(16) Goushi, K.; Yoshida, K.; Sato, K.; Adachi, C. Organic Light-Emitting Diodes Employing Efficient Reverse Intersystem Crossing for Triplet-to-Singlet State Conversion. *Nat. Photonics* **2012**, *6* (4), 253–258. https://doi.org/10.1038/nphoton.2012.31.

(17) Mitschke, U.; Bäuerle, P. The Electroluminescence of Organic Materials. *J. Mater. Chem.* **2000**, *10* (7), 1471–1507. https://doi.org/10.1039/a908713c.

(18) Endo, A.; Ogasawara, M.; Takahashi, A.; Yokoyama, D.; Kato, Y.; Adachi, C. Thermally Activated Delayed Fluorescence from Sn4+-Porphyrin Complexes and Their Application to Organic Light-Emitting Diodes -A Novel Mechanism for Electroluminescence. *Adv. Mater.* **2009**, *21* (47), 4802–4806. https://doi.org/10.1002/adma.200900983.

(19) Bergmann, L.; Hedley, G. J.; Baumann, T.; Bräse, S.; Samuel, I. D. W. Direct Observation of Intersystem Crossing in a Thermally Activated Delayed Fluorescence Copper Complex in the Solid State. *Sci. Adv.* **2016**, *2* (1), 1–7. https://doi.org/10.1126/sciadv.1500889.

(20) Wada, Y.; Nakagawa, H.; Matsumoto, S.; Wakisaka, Y.; Kaji, H. Organic Light Emitters Exhibiting Very Fast Reverse Intersystem Crossing. *Nat. Photonics* **2020**, *14* (10), 643–649. https://doi.org/10.1038/s41566-020-0667-0.

(21) Franzen, S.; Kiger, L.; Poyart, C.; Martin, J. L. Heme Photolysis Occurs by Ultrafast Excited State Metal-to-Ring Charge Transfer. *Biophys. J.* **2001**, *80* (5), 2372–2385. https://doi.org/10.1016/S0006-3495(01)76207-8.

(22) Wang, W.; Ye, X.; Demidov, A. A.; Rosca, F.; Sjodin, T.; Cao, W.; Sheeran, M.; Champion, P. M. Femtosecond Multicolor Pump-Probe Spectroscopy of

Ferrous Cytochrome C. *J. Phys. Chem. B* **2000**, *104* (46), 10789–10801. https://doi.org/10.1021/jp0008602.

(23) Dunietz, B. D.; Dreuw, A.; Head-Gordon, M. Initial Steps of the Photodissociation of the CO Ligated Heme Group. *J. Phys. Chem. B* **2003**, *107* (23), 5623–5629. https://doi.org/10.1021/jp0226376.

(24) Mara, M. W.; Hadt, R. G.; Reinhard, M. E.; Kroll, T.; Lim, H.; Hartsock, R. W.; Alonso-Mori, R.; Chollet, M.; Glownia, J. M.; Nelson, S.; *et al*. Metalloprotein Entatic Control of Ligand-Metal Bonds Quantified by Ultrafast x-Ray Spectroscopy. *Science* **2017**, *356* (6344), 1276–1280. https://doi.org/10.1126/science.aam6203.

(25) Falahati, K.; Tamura, H.; Burghardt, I.; Huix-Rotllant, M. Ultrafast Carbon Monoxide Photolysis and Heme Spin-Crossover in Myoglobin via Nonadiabatic Quantum Dynamics. *Nat. Commun.* **2018**, *9* (1), 1–8. https://doi.org/10.1038/s41467-018-06615-1.

(26) Harvey, J. N.; Aschi, M. Modelling Spin-Forbidden Reactions: Recombination of Carbon Monoxide with Iron Tetracarbonyl. *Faraday Discuss.* **2003**, *124* (1), 129–143. https://doi.org/10.1039/b211871h.

(27) Yang, B.; Gagliardi, L.; Truhlar, D. G. Transition States of Spin-Forbidden Reactions. *Phys. Chem. Chem. Phys.* **2018**, *20* (6), 4129–4136. https://doi.org/10.1039/c7cp07227a.

(28) Jensen, K. P.; Ryde, U. How O_2 Binds to Heme. Reasons for Rapid Binding and Spin Inversion. *J. Biol. Chem.* **2004**, *279* (15), 14561–14569. https://doi.org/10.1074/jbc.M314007200.

(29) Strickland, N.; Harvey, J. N. Spin-Forbidden Ligand Binding to the Ferrous-Heme Group: Ab Initio and DFT Studies. *J. Phys. Chem. B* **2007**, *111* (4), 841–852. https://doi.org/10.1021/jp064091j.

(30) Harvey, J. N. Spin-Forbidden CO Ligand Recombination in Myoglobin. **2004**, 165–177. https://doi.org/10.1039/b314768a.

(31) Kahn, O.; Martinez, C. J. Spin-Transition Polymers: From Molecular Materials toward Memory Devices. *Science* **1998**, *279* (5347), 44–48. https://doi.org/10.1126/science.279.5347.44.

(32) Halder, G. J.; Kepert, C. J.; Moubaraki, B.; Murray, K. S.; Cashion, J. D. Guest-Dependent Spin Crossover in a Nanoporous Molecular Framework Material. *Science* **2002**, *298* (5599), 1762–1765. https://doi.org/10.1126/science.1075948.

(33) Gütlich P., Goodwin H.A. *Spin Crossover—An Overall Perspective*; Springer-Verlag: Berlin, Heidelberg, New York, 2004.

(34) Halcrow, M. A. *Spin-Crossover Materials. Properties and Applications*; 1st ed.; Wiley, 2013.

(35) Kumar, S. K.; Ruben, M. Emerging Trends in Spin Crossover (SCO) Based Functional Materials and Devices. *Coord. Chem. Rev.* **2017**, *346*, 176–205. https://doi.org/10.1016/j.ccr.2017.03.024.

(36) Real, J. A.; Gaspar, A. B.; Carmen Muñoz, M. Thermal, Pressure and Light Switchable Spin-Crossover Materials. *Dalt. Trans.* **2005**, 2062–2079. https://doi.org/10.1039/b501491c.

(37) Bonhommeau, S.; Molnár, G.; Galet, A.; Zwick, A.; Real, J. A.; McGarvey, J. J.; Bousseksou, A. One Shot Laser Pulse Induced Reversible Spin Transition in

the Spin-Crossover Complex [Fe($C_4H_4N_2$){$Pt(CN)_4$}] at Room Temperature. *Angew. Chemie - Int. Ed.* **2005**, *44* (26), 4069–4073. https://doi.org/10.1002/anie.200500717.

(38) Gaspar, A. B.; Ksenofontov, V.; Seredyuk, M.; Gütlich, P. Multifunctionality in Spin Crossover Materials. *Coord. Chem. Rev.* **2005**, *249* (23), 2661–2676. https://doi.org/10.1016/j.ccr.2005.04.028.

(39) Muller, R. N.; Elst, L. Vander; Laurent, S. Spin Transition Molecular Materials: Intelligent Contrast Agents for Magnetic Resonance Imaging. *J. Am. Chem. Soc.* **2003**, *125* (27), 8405–8407. https://doi.org/10.1021/ja0349599.

(40) Mukherjee, S.; Fedorov, D. A.; Varganov, S. A. Modeling Spin-Crossover Dynamics. *Annu. Rev. Phys. Chem.* **2021**, *72*, 515–540. https://doi.org/10.1146/annurev-physchem-101419-012625.

(41) Beck, M. The Multiconfiguration Time-Dependent Hartree (MCTDH) Method: A Highly Efficient Algorithm for Propagating Wavepackets. *Phys. Rep.* **2000**, *324* (1), 1–105. https://doi.org/10.1016/S0370-1573(99)00047-2.

(42) Barbatti, M. Nonadiabatic Dynamics with Trajectory Surface Hopping Method. *Wiley Interdiscip. Rev. Comput. Mol. Sci.* **2011**, *1* (4), 620–633. https://doi.org/10.1002/wcms.64.

(43) Curchod, B. F. E.; Martinez, T. J. Ab Initio Nonadiabatic Quantum Molecular Dynamics. **2018**. https://doi.org/10.1021/acs.chemrev.7b00423.

(44) Mai, S.; Marquetand, P.; González, L. Nonadiabatic Dynamics: The SHARC Approach. *Wiley Interdiscip. Rev. Comput. Mol. Sci.* **2018**, *8* (6), 1–23. https://doi.org/10.1002/wcms.1370.

(45) Hammes-Schiffer, S.; Tully, J. C. Nonadiabatic Transition State Theory and Multiple Potential Energy Surface Molecular Dynamics of Infrequent Events. *J. Chem. Phys.* **1995**, *103* (19), 8513–8527. https://doi.org/10.1063/1.470162.

(46) Shenvi, N.; Subotnik, J. E.; Yang, W. Simultaneous-Trajectory Surface Hopping: A Parameter-Free Algorithm for Implementing Decoherence in Nonadiabatic Dynamics. *J. Chem. Phys.* **2011**, *134* (14), 0–12. https://doi.org/10.1063/1.3575588.

(47) Curchod, B. F. E.; Rauer, C.; Marquetand, P.; González, L.; Martínez, T. J. Communication: GAIMS - Generalized Ab Initio Multiple Spawning for Both Internal Conversion and Intersystem Crossing Processes. *J. Chem. Phys.* **2016**, *144* (10), 1–6. https://doi.org/10.1063/1.4943571.

(48) Fedorov, D. A.; Pruitt, S. R.; Keipert, K.; Gordon, M. S.; Varganov, S. A. Ab Initio Multiple Spawning Method for Intersystem Crossing Dynamics: Spin-Forbidden Transitions between 3B1 and 1A1 States of GeH2. *J. Phys. Chem. A* **2016**, *120* (18), 2911–2919. https://doi.org/10.1021/acs.jpca.6b01406.

(49) Fedorov, D. A.; Lykhin, A. O.; Varganov, S. A. Predicting Intersystem Crossing Rates with AIMS-DFT Molecular Dynamics. *J. Phys. Chem. A* **2018**, *122* (13), 3480–3488. https://doi.org/10.1021/acs.jpca.8b00883.

(50) Lorquet, J. C.; Leyh-Nihant, B. Nonadiabatic Unimolecular Reactions. 1. A Statistical Formulation for the Rate Constants. *J. Phys. Chem.* **1988**, *92* (16), 4778–4783. https://doi.org/10.1021/j100327a043.

(51) Nikitin, E. E.; Umanskii, S. Y. *Theory of Slow Atomic Collisions*; Goldanskii, V. I., Gomer, R., Schafer, F. P., Toennies, J. P., Eds.; Springer-Verlag, 1984.

(52) Harvey, J. N. Understanding the Kinetics of Spin-Forbidden Chemical Reactions. **2007**, 331–343. https://doi.org/10.1039/b614390c.

(53) Harvey, J. N.; Aschi, M. Spin-Forbidden Dehydrogenation of Methoxy Cation: A Statistical View. *Phys. Chem. Chem. Phys.* **1999**, *1* (24), 5555–5563. https://doi.org/10.1039/a907723e.

(54) Harvey, J. N. Spin-Forbidden Reactions: Computational Insight into Mechanisms and Kinetics. *Wiley Interdiscip. Rev. Comput. Mol. Sci.* **2014**, *4* (1), 1–14. https://doi.org/10.1002/wcms.1154.

(55) Cui, Q.; Morokuma, K.; Bowman, J. M.; Klippenstein, S. J. The Spin-Forbidden Reaction $CH(^2\Pi)+N_2 \rightarrow HCN + N(^4S)$ Revisited. II. Nonadiabatic Transition State Theory and Application. *J. Chem. Phys.* **1999**, 110 (19), 9469-9482. https://doi.org/10.1063/1.478949.

(56) Zhao, Y.; Mil'nikov, G.; Nakamura, H. Evaluation of Canonical and Microcanonical Nonadiabatic Reaction Rate Constants by Using the Zhu-Nakamura Formulas. *J. Chem. Phys.* **2004**, *121* (18), 8854–8860. https://doi.org/10.1063/1.1801971.

(57) Marks, A. J. Nonadiabatic Transition-State Theory : A Monte Carlo Study of Competing Bond Fission Processes in Bromoacetyl Chloride. **2001**, *114* (4), 1700–1708. https://doi.org/10.1063/1.1333702.

(58) McLafferty, F. J.; George, T. F. On Nonadiabatic Transition State Theory. *Chem. Phys. Lett.* **1976**, *37* (1), 67–71. https://doi.org/10.1016/0009-2614(76)80163-7.

(59) Lykhin, A. O.; Varganov, S. A. Intersystem Crossing in Tunneling Regime: T1 → S0 Relaxation in Thiophosgene. *Phys. Chem. Chem. Phys.* **2020**, *22* (10), 5500–5508. https://doi.org/10.1039/c9cp06956a.

(60) Truhlar, D. G.; Garrett, B. C.; Klippenstein, S. J. Current Status of Transition-State Theory. *J. Phys. Chem.* **1996**, *100*, 12771–12800. https://doi.org/doi.org/10.1021/jp953748q.

(61) Truhlar, D. G.; Garrett, B. C. Variational Transition State Theory. *Ann. Rev. Phys. Chem.* **1984**, *35*, 159–189. https://doi.org/10.1146/annurev.pc.35.100184.001111.

(62) Laidler, K. J.; King, M. C. The Development of Transition-State Theory. *J. Phys. Chem.* **1983**, *87* (15), 2657–2664. https://doi.org/10.1021/j100238a002.

(63) Garrett, B. C.; Truhlar, D. G. Generalized Transition State Theory. Classical Mechanical Theory and Applications to Collinear Reactions of Hydrogen Molecules. *J. Phys. Chem.* **1979**, *83*, 1052–1079. https://doi.org/10.1021/j100471a031.

(64) Miller, W. H. "Direct" and "Correct" Calculation of Canonical and Microcanonical Rate Constants for Chemical Reactions. *J. Phys. Chem. A* **1998**, *102* (5), 793–806. https://doi.org/10.1021/jp973208o.

(65) Bao, J. L.; Truhlar, D. G. Variational Transition State Theory: Theoretical Framework and Recent Developments. *Chem. Soc. Rev.* **2017**, *46* (24), 7548–7596. https://doi.org/10.1039/c7cs00602k.

(66) Marian, C. M. Understanding and Controlling Intersystem Crossing in Molecules. *Annu. Rev. Phys. Chem.* **2021**, *72*, 617–640. https://doi.org/10.1146/annurev-physchem-061020-053433.

(67) Fedorov, D. G.; Koseki, S.; Schmidt, M. W.; Gordon, M. S. Spin-Orbit Coupling in Molecules: Chemistry beyond the Adiabatic Approximation. *Int. Rev. Phys. Chem.* **2003**, *22* (3), 551–592. https://doi.org/10.1080/0144235032000101743.

(68) Marian, C. M. Spin-Orbit Coupling and Intersystem Crossing in Molecules. *Wiley Interdiscip. Rev. Comput. Mol. Sci.* **2012**, *2* (2), 187–203. https://doi.org/10.1002/wcms.83.

(69) Marian, C. M. *Spin-Orbit Coupling in Molecules.* In *Reviews in Computational Chemistry*, Wiley, 2001; Vol. 17, pp 99–204. https://doi.org/10.1002/0471224413.ch3.

(70) Zhu, C.; Nakamura, H. Theory of Nonadiabatic Transition for General Two-State Curve Crossing Problems. I. Nonadiabatic Tunneling Case. *J. Chem. Phys.* **1994**, *101* (12), 10630–10647. https://doi.org/10.1063/1.467877.

(71) Fernández-Ramos, A.; Ellingson, B. A.; Meana-Pañeda, R.; Marques, J. M. C.; Truhlar, D. G. Symmetry Numbers and Chemical Reaction Rates. *Theor. Chem. Acc.* **2007**, *118* (4), 813–826. https://doi.org/10.1007/s00214-007-0328-0.

(72) Lykhin, A. O. Predicting Kinetics of Spin-Forbidden Unimolecular Reactions with Nonadiabatic Transition State Theory. Ph.D. Dissertation, University of Nevada, Reno, Reno, NV, US, 2019. https://www.proquest.com/docview/2270020145?pq-origsite=gscholar&fromopenview=true (accessed 2021-11-10).

(73) Delos, J. B. On the Reactions of N_2 with O. *J. Chem. Phys.* **1973**, *59* (5), 2365–2369. https://doi.org/doi.org/10.1063/1.1680345.

(74) Dashevskaya, E. I.; Nikitin, E. E. Uniform Airy Approximation for Nonadiabatic Transitions in a Curve-Crossing Weak-Coupling. *Z. Phys. Chem.* **2017**, *232* (3), 311–323. https://doi.org/doi.org/10.1515/zpch-2017-1025.

(75) Nakamura, H. *Nonadiabatic Transition : Concepts, Basic Theories and Applications*, 2nd ed.; World Scientific, 2012.

(76) Zhu, C.; Nakamura, H. Theory of Nonadiabatic Transition for General Two-state Curve Crossing Problems. I. Nonadiabatic Tunneling Case. *J. Chem. Phys.* **1994**, *101* (12), 10630–10647. https://doi.org/10.1063/1.469057.

(77) Zhu, C.; Teranishi, Y.; Nakamura, H. Nonadiabatic Transitions Due to Curve Crossings: Complete Solutions of the Landau-zener-stueckelberg Problems and Their Applications. In *Advances in Chemical Physics*, Vol. 117; Wiley Online Librabry, 2001; pp 127–233.

(78) Zhu, C.; Nakamura, H.; Re, N.; Aquilanti, V. The Two-State Linear Curve Crossing Problems Revisited. I. Analysis of Stokes Phenomenon and Expressions for Scattering Matrices. *J. Chem. Phys.* **1992**, *97* (3), 1892–1904. https://doi.org/10.1063/1.463178.

(79) Zhu, C.; Nakamura, H. The Two-state Linear Curve Crossing Problems Revisited. II. Analytical Approximations for the Stokes Constant and Scattering Matrix: The Landau–Zener Case. *J. Chem. Phys.* **1992**, *97* (11), 8497–8514. https://doi.org/10.1063/1.464814.

(80) Zhu, C.; Nakamura, H. Two-state Linear Curve Crossing Problems Revisited. IV. The Best Analytical Formulas for Scattering Matrices. *J. Chem. Phys.* **1994**, *101* (6), 4855–4866. https://doi.org/doi.org/10.1063/1.468505.

(81) Melissas, V. S.; Truhlar, D. G.; Garrett, B. C. Optimized Calculations of Reaction Paths and Reaction-Path Functions for Chemical Reactions. *J. Chem. Phys.* **1992**, *96* (8), 5758–5772. https://doi.org/10.1063/1.462674.

(82) Kuki, A. Adiabaticity Factor for Electron Transfer in the Multimode Case: An Energy Velocity Perspective. *J. Phys. Chem.* **1993**, *97* (50), 13107–13116. https://doi.org/10.1021/j100152a013.

(83) Bracewell, R. N. *The Fourier Transform and Its Applications*, 3d ed.; McGraw-Hill, 2000.

(84) Baer, T.; Hase, W. L. *Unimolecular Reaction Dynamics: Theory and Experiments*, Oxford University Press, 1996. https://doi.org/10.1093/oso/9780195074949.001.0001.

(85) Green, N. J. B. *Unimolecular Kinetics, Part 1. The Reaction Step*; Elsevier, 2003.

(86) Lykhin, A. O.; Truhlar, D. G.; Gagliardi, L. Role of Triplet States in the Photodynamics of Aniline. *J. Am. Chem. Soc.* **2021**, *143* (15), 5878–5889. https://doi.org/10.1021/jacs.1c00989.

(87) Galano, A.; Alvarez-Idaboy, J. R. A Computational Methodology for Accurate Predictions of Rate Constants in Solution: Application to the Assessment of Primary Antioxidant Activity. *J. Comput. Chem.* **2013**, *34* (28), 2430–2445. https://doi.org/10.1002/jcc.23409.

(88) Dzib, E.; Cabellos, J. L.; Ortíz-Chi, F.; Pan, S.; Galano, A.; Merino, G. Eyringpy: A Program for Computing Rate Constants in the Gas Phase and in Solution. *Int. J. Quantum Chem.* **2019**, *119* (2), 11–13. https://doi.org/10.1002/qua.25686.

(89) Garrett, B. C.; Schenter, G. K. Variational Transition State Theory for Activated Chemical Reactions in Solution. *Int. Rev. Phys. Chem.* **1994**, *13* (2), 263–289. https://doi.org/10.1080/01442359409353296.

(90) Truhlar, D.; Pliego, J. R. Transition State Theory and Chemical Reaction Dynamics in Solution. In *Continuum Solvation Models in Chemical Physics: Theory and Application*; Wiley, 2008; pp. 338-366.

(91) Hall, D. G. The Status of Transition-State Theory in Non-Ideal Solutions and Application of Kirkwood-Buff Theory to the Transition State. *J. Chem. Soc. Faraday Trans. 2 Mol. Chem. Phys.* **1986**, *82* (9), 1297–1303. https://doi.org/10.1039/F29868201297.

(92) Henriksen, N. E.; Hansen, F. Y. Static Solvent Effects, Transition-State Theory. In *Theories of Molecular Reaction Dynamics: The Microscopic Foundation of Chemical Kinetics*; Oxford University Press, 2018.

(93) Barca, G. M. J.; Bertoni, C.; Carrington, L.; Datta, D.; De Silva, N.; Deustua, J. E.; Fedorov, D. G.; Gour, J. R.; Gunina, A. O.; Guidez, E.; *et al*. Recent Developments in the General Atomic and Molecular Electronic Structure System. *J. Chem. Phys.* **2020**, *152* (15). https://doi.org/10.1063/5.0005188.

(94) Werner, H. J.; Knowles, P. J.; Manby, F. R.; Black, J. A.; Doll, K.; Heßelmann, A.; Kats, D.; Köhn, A.; Korona, T.; Kreplin, D. A.; *et al*. The Molpro Quantum Chemistry Package. *J. Chem. Phys.* **2020**, *152* (14). https://doi.org/10.1063/5.0005081.

(95) Dubnikova, F.; Lifshitz, A. Isomerization of Propylene Oxide. Quantum Chemical Calculations and Kinetic Modeling. *J. Phys. Chem. A* **2000**, *104* (19), 4489–4496. https://doi.org/10.1021/jp004038+.

(96) Lifshitz, A.; Tamburu, C. Isomerization and Decomposition of Propylene Oxide. Studies with a Single-Pulse Shock Tube. *J. Phys. Chem.* **1994**, *98*, 1161–1170. https://doi.org/10.1021/j100055a020.

(97) McGarvey, J. J.; Wilson, J. Photochemical Perturbation and Chemical Relaxation of the Planar - Tetrahedral Equilibrium in a Di(Tertiary Phosphine) Complex of Nickel(II). *J. Am. Chem. Soc.* **1975**, *97* (9), 2531–2532. https://doi.org/10.1021/ja00842a034.

(98) Miller, J. A.; Klippenstein, S. J. From the Multiple-Well Master Equation to Phenomenological Rate Coefficients: Reactions on a C3H4 Potential Energy Surface. *J. Phys. Chem. A* **2003**, *107* (15), 2680–2692. https://doi.org/10.1021/jp0221082.

(99) Glowacki, D. R.; Liang, C. H.; Morley, C.; Pilling, M. J.; Robertson, S. H. MESMER: An Open-Source Master Equation Solver for Multi-Energy Well Reactions. *J. Phys. Chem. A* **2012**, *116* (38), 9545–9560. https://doi.org/10.1021/jp3051033.

CHAPTER 4. ENHANCED SPIN COHERENCE OF RUBIDIUM ATOMS IN SOLID PARAHYDROGEN

Adopted with permission from

Physical Review B 100, 024106 (2019)

https://doi.org/10.1103/PhysRevB.100.024106

Sunil Upadhyay, Ugne Dargyte, Robert P. Prater, **Vsevolod D. Dergachev**, Sergey A. Varganov, Timur V. Tscherbul, David Patterson, and Jonathan D. Weinstein

Abstract

We measure the transverse relaxation of the spin state of an ensemble of ground-state rubidium atoms trapped in solid parahydrogen at cryogenic temperatures. We find the spin dephasing time of the ensemble (T_2^*) is limited by inhomogeneous broadening. We determine that this broadening is dominated by electrostaticlike interactions with the host matrix, and can be reduced by preparing nonclassical spin superposition states. Driving these superposition states gives significantly narrower electron paramagnetic resonance lines and the longest reported electron spin T_2^* in any solid-phase system other than solid helium.

Measuring the energy splitting between Zeeman levels is at the heart of atomic magnetometry,[1] electron paramagnetic resonance (EPR) spectroscopy,[2] and fundamental physics measurements.[3-5] For an ensemble of N atoms, the shot- noise limited precision of a single measurement is $\sigma_E \sim \frac{\hbar}{T_2^*\sqrt{N}}$,[1] where T_2^* is the ensemble's spin dephasing time. In this paper, we show that rubidium atoms in parahydrogen have favorable T_2^* times for a solid state electron spin ensemble. Moreover, their T_2^* can be further extended by using non-classical superposition states instead of traditional Larmor precession states.

Our apparatus is similar to that described in Refs.[6,7] We grow our crystal by codepositing hydrogen and rubidium gases onto a cryogenically cooled sapphire window at 3 K. We enrich the parahydrogen fraction of hydrogen by flowingthe gas over a cryogenically cooled catalyst. In the data presented in this paper, the orthohydrogen fraction is $< 10^{-4}$. Typical thicknesses of the doped crystals are ~0.3 mm. We use natural-isotopic-abundance rubidium; typical rubidium densities are on the order of 10^{17} cm^{-3}, or a few ppm.

We apply a static "bias" magnetic field (B_z) normal to the surface of the crystal. We polarize the spin state of the implanted Rb atoms by optically pumping the atoms with a circularly polarized laser. To minimize magnetic field inhomogeneities across the sample we optically select a region ofthe crystal with transverse dimensions of roughly 0.1 mm. We measure the polarization through circular dichroism, measuring the relative transmission of left-handed and right-handed circularly polarized light (LHC and RHC). As described in Ref.,[6] the circular dichroism signals observed are roughly an order of magnitude smaller than for gas-phase atoms, and we are unable to

determine if the reduced signal is due to imperfect optical pumping, readout, or both. Hence our"effective" atom number in a typical measurement is $\sim$10% of the $\sim 10^{12}$ atoms in a typical sample volume. Larger number samples could be obtained by using larger-diameter beams (or a thicker crystal) to address a larger volume of atoms. We drive transitions between Zeeman states with transverse rf magnetic fields generated by a wire a few mm above the surface of the crystal. We take data with bias fields ranging from 40 to 120 G, giving Zeeman shifts that are small compared to the hyperfine splitting, but sufficiently large that transitions between different Zeeman levels can be spectrally resolved. The level structure of ground-state ^{85}Rb is shown in Figure 4.1. In the gas phase, the hyperfine splitting is 3.0357 GHz.[8] From prior work, the hyperfine constants of alkali-metal atoms in noble gas matrices are within a few percent of the free-space atom value[9]; we expect alkali- metal atoms in parahydrogen to be similar.

We measure rubidium's transverse relaxation time by free-induction-decay (FID) measurements. After polarizing the spin through optical pumping, an RF pulse is applied to induce Larmor precession. The Larmor precession and its decay are measured optically via circular dichroism.[1] The measured values of T_2^* are on the order of 10 μs or shorter, as presented in the Supplemental Material.[10]

This is significantly shorter than spin-echo measurements under similar conditions (which indicate $T_2 \gtrsim 1$ ms). This indicates that the dominant limit on T_2^* comes from static inhomogeneous broadening (static on the spin-echo timescale). Significant inhomogeneous broadening is not surprising, given that our matrix growth conditions are expected to pro- duce polycrystalline parahydrogen.[11,12]

For a magnetically pure host such as parahydrogen, we hypothesize that the observed inhomogeneous broadening is dominated by electrostatic interactions. We note that the Hamiltonian for electrostatic interactions is unchanged under time reversal. Thus, to first order in the perturbation, the electrostatic energy shift of a state $|\psi\rangle$ and its time-reversed state $|\tilde{\psi}\rangle$ must be identical. A superposition state of Zeeman levels which are time reversals of each other will have a reduced inhomogeneous broadening. For free-space Rb atoms, $|F, \pm m_F\rangle$ pairs are time reversals of each other in the low-field limit (the stretched states $|F = I + J, m_F = \pm F\rangle$ are time reversals of each other at all fields). We can use multiphoton transitions, as shown in Figure 4.1, to prepare superpositions of this kind.

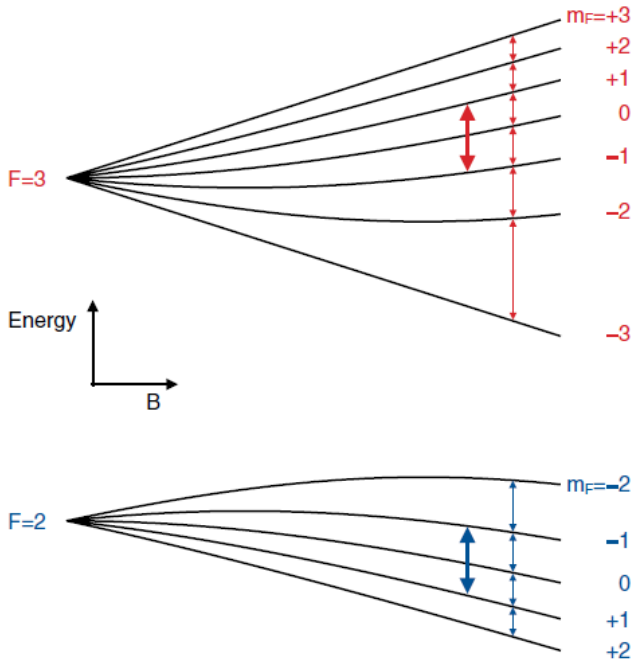

Figure 4.1. Schematic of the Zeeman levels of gas-phase ^{85}Rb, showing some of the relevant transitions of Figure 4.2. The energy eigenstates (black) are labeled by their low-field quantum numbers F and m_F, and we refer to them throughout the paper by that terminology. The slender arrows denote the single-photon transitions. The wide arrows denote the two-photon transitions between states which are approximate time

reversals of each other; each two-photon transition is shown as a single arrow. To better illustrate the nondegenerate frequencies of the transitions, the Zeeman levels are plotted over a larger range of magnetic fields than used in this experiment; likewise, the transition arrows are horizontally offset for ease of viewing.

Superpositions of these states cannot be studied by FID techniques. Only superpositions of Zeeman levels which differ by $\Delta m = 1$ give rise to Larmor precession. For the superpositions of interest, the expectation value of the spin projection along a transverse axis is zero. Thus there is no literal "transverse spin relaxation" time. However, as any other two-level system, a superposition of $|m_F = +1\rangle$ and $|m_F = -1\rangle$ has a well-defined dephasing time.

To measure T_2^* we use "depolarization spectroscopy," wherein we polarize the atoms by optical pumping, then continuously measure the circular dichroism signal as we scan the RF frequency across the resonances. When the frequency is on resonance between two m_F energy eigenstates, population is transferred between them and the polarization signal changes. In the limit of low RF power and a slow frequency sweep, the linewidth of the transition provides a measurement of the inhomogeneous broadening and hence T_2^*.

Figure 4.2 shows depolarization data for ^{85}Rb at two different RF powers. For the low-power sweep, we see a change in the polarization signal at each expected single-photon resonance frequency. The broadening is sufficiently large that the $F = 2$ transitions are not fully resolved from the $F = 3$ transitions.

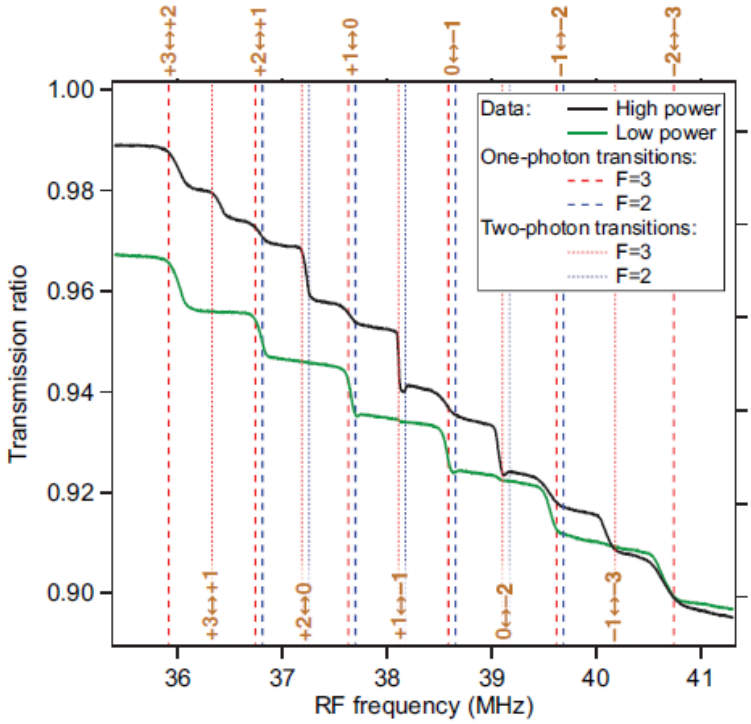

Figure 4.2. Depolarization spectroscopy signals, as discussed in the text, taken with $B_Z = 82$ G. The vertical axis measures the ratio of the transmission of LHC and RHC probe beams; under conditions of no spin polarization the ratio is 1. The signal is plotted as a function of the RF frequency; in these data the RF is swept from high to low frequency. The dashed vertical lines mark the calculated single-photon and two-photon transition frequencies for gas-phase ^{85}Rb [13]; the yellow labels denote $m_F \leftrightarrow m_F'$.

At higher powers, the two-photon transitions become observable. The $+1 \leftrightarrow -1$ transitions at the center of the spectrum are significantly narrower than all other one- and two-photon transitions. This is precisely as expected for inhomogeneous electrostatic broadening, as they are the only two-photon transitions between time-reversed states. This confirms that the dominant inhomogeneous broadening mechanism is time-even in nature (electrostaticlike), as time-odd (magnetostaticlike) perturbations would result in a $+1 \leftrightarrow -1$ linewidth approximately twice that of a $0 \leftrightarrow \pm 1$ transition. For the $+1 \leftrightarrow -1$ transitions, the $F = 2$ and $F = 3$ transitions are

cleanly resolved; the two transitions cause the circular dichroism signal to change in opposite directions.

We extract linewidths from these data by assuming the inhomogeneous broadening is Gaussian and fitting each transition in the depolarization spectrum to a corresponding error function. The extracted linewidths as a function of magnetic field are shown in Figure 4.3 for ^{85}Rb and ^{87}Rb. These linewidths reflect low-field (i.e., non-power-broadened) values. For the single-photon transitions, the linewidths measured through depolarization spectroscopy match those from FID measurements to within our experimental error. A comparison is provided in the Supplemental Material.[10]

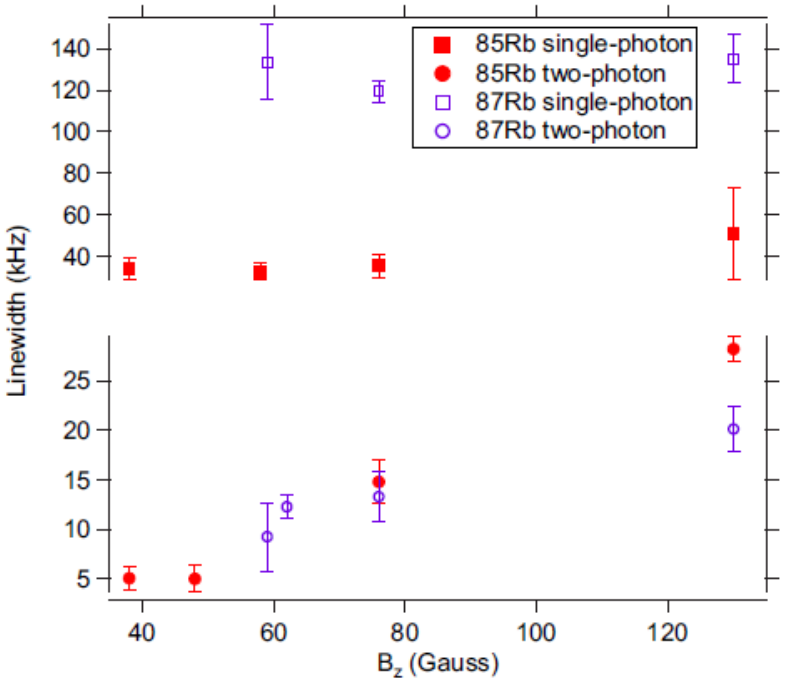

Figure 4.3. Measured linewidths of ^{85}Rb in the $F = 3$ hyperfine state and ^{87}Rb in the $F = 2$ hyperfine state. For the single-photon linewidth, we plot the average of the $|m_F = \pm 1\rangle \leftrightarrow |m_F = 0\rangle$ transitions. For the two-photon linewidth we plot the linewidth of the $+1 \leftrightarrow -1$ transition.

Examining the single-photon linewidths in Figure 4.3, we see that ^{87}Rb exhibits more broadening than ^{85}Rb. This is as one would naively expect for shifts that are electrostatic in nature, as tensor Stark shifts are larger for ground-state ^{87}Rb ($F = 2$) than for ^{85}Rb ($F = 3$).[14] For a static electric field, calculations predict the $\pm 1 \leftrightarrow 0$ transitions in 87Rb ($F = 2$) would show 3.2 times the tensor Stark shift of ^{85}Rb ($F = 3$),[14] consistent with the differences seen in the linewidths of Figure 4.3.

We attribute the dominant contribution to the linewidth of the $+1 \leftrightarrow -1$ transitions to residual electrostatic broadening that arises because these energy eigenstates are not perfect time reversals of each other. While we do not know the exact form of the tensor interaction with the parahydrogen host, we can use perturbation theory to qualitatively predict the linewidth of the $+1 \leftrightarrow -1$ transition. We consider an atom with hyperfine constant of A, a Zeeman splitting of z, and an interaction with the matrix which is symmetric under time reversal and on the order of m. We consider the limit that $A \gg z \gg m$, and only include perturbations from m to lowest-order in perturbation theory. In this limit, we expect the linewidth of the $+1 \leftrightarrow -1$ transition to be smaller than the single-photon transitions by a factor of $\sim z/A$ (ignoring numerical prefactors). The residual broadening is due to the breakdown of the time-reversal symmetry of the$|+1\rangle$ and $|-1\rangle$ energy eigenstates at nonzero magnetic field. This model qualitatively agrees with our linewidth measurements (Figure 4.3), and explains the observed dependence of the $+1 \leftrightarrow -1$ linewidth on the magnetic field. We note that measurements of ^{85}Rb as a function of rubidium density indicate that dipolar broadening does not contribute significantly to the linewidth.

The only energy eigenstates of the free atom which are time reversals of each other at all magnetic fields are the "stretched states": $|F = 3, m_F = \pm 3\rangle$ for ^{85}Rb and $|F = 2, m_F = \pm 2\rangle$ for ^{87}Rb. Inhomogeneous electrostatic broadening should be further suppressed for these states. We have not been successful in observing the six-photon $+3 \leftrightarrow -3$ transition in ^{85}Rb; we suspect this is due to insufficient *rf* power. Observations of the four-photon $+2 \leftrightarrow -2$ transition in ^{87}Rb at 60 G indicated narrower lines, but not at a statistically significant level. We suspect the measured linewidth of the ^{87}Rb stretched state transition is limited by technical limitations of our apparatus (magnetic field gradients, as well as magnetic field instabilities which prevent averaging) and possible coupling to other states in the multiphoton transition.

To estimate the matrix shifts of the alkali-metal atoms trapped in solid p-H2, we use a third-order perturbative expression[15]

$$\Delta E_{\mathrm{hf}} = \sum_{ij}\sum_{kl} \frac{\langle 00|V_{dd}|ij\rangle\langle ij|H_{\mathrm{hf}}|kl\rangle\langle kl|V_{dd}|00\rangle}{(E_{00} - E_{ij})(E_{00} - E_{kl})}$$

$$-\langle 00|H_{\mathrm{hf}}|00\rangle \sum_{kl} \frac{\langle 00|V_{dd}|kl\rangle\langle kl|V_{dd}|00\rangle}{(E_{00} - E_{kl})^2}, \qquad (4.1)$$

where the unperturbed basis functions $|ij\rangle = |i\rangle_A|j\rangle_{\mathrm{H_2}}$ describe the electronic states of noninteracting atom A and $\mathrm{H_2}$, with energies $E_{kl} = E_k^A + E_l^{\mathrm{H_2}}$ and H_{hf} is the atomic hyperfine Hamiltonian,[8] and V_{dd} is the dipole-dipole interaction.[15] The sums in Eq. (4.1) run over all excited electronic, fine, and hyperfine states of A and $\mathrm{H_2}$. The first term in Eq. (4.1) gives rise to an m_F-dependent tensor matrix shift of the atomic hyperfine levels[16] whereas the second term leads to an m_F - independent scalar shift ΔE_{hf}^S. The latter can be estimated by assuming that $E_{00} - E_{ik} \backsimeq E_A + E_{\mathrm{H_2}}$, where E_A is

the average excitation energy of atom A and E_{H_2} is that of H_2.[15] Using the closure relation to eliminate the summations over the excited states in the second term of Eq. (4.1), we obtain[15]

$$\Delta E_{\mathrm{hf}}^{s} \backsimeq -\langle 00|H_{\mathrm{hf}}|00\rangle \left(\frac{1}{E_A + E_{\mathrm{H}_2}}\right) E_{\mathrm{disp}}, \tag{4.2}$$

where $E_{\mathrm{disp}} = \langle 00|V_{dd}^2|00\rangle/(E_A + E_{\mathrm{H}_2})$ is the dispersion interaction energy of A with H_2.

To estimate the tensor matrix shift, we take into account only the diagonal matrix elements of the hyperfine interaction in Eq. (4.1) and assume that $\langle i|H_{\mathrm{hf}}|i\rangle \backsimeq A_P$ is independent of the electronic state i and equal to the hyperfine constant of the lowest excited $^2P_{1/2}$ state of atom A. Since the hyperfine constants of alkali-metal atoms decrease rapidly with increasing i,[8] these assumptions provide a conservative upper bound to the magnitude of the tensor shift

$$\Delta E_{\mathrm{hf}}^{t} < A_P \sum_{i,j} \frac{\langle 00|V_{dd}|ij\rangle\langle ij|V_{dd}|00\rangle}{\left(E_{00} - E_{ij}\right)^2} = 0.1\Delta E_{\mathrm{hf}}^{s}, \tag{4.3}$$

where the ratio of the tensor to scalar matrix shifts $\Delta E_{\mathrm{hf}}^{t}/\Delta E_{\mathrm{hf}}^{s} \leq A_P/A_S = 0.1$ for Rb.[8] This is consistent with the fact that the third-order tensor Stark shifts of alkali-metal atoms are suppressed by a factor of $\backsimeq 100$ compared to the scalar shifts.[17] Note also that the ratio of third-order tensor and scalar polarizabilities of atomic Cs, $\alpha_2^{(3)}/\alpha_0^{(3)} = 0.03$,[17] is four times smaller than the upper bound (Eq. 4.3).

To obtain the dispersion energy needed to estimate the tensor matrix shift via Eq. (4.3), we carried out accurate *ab initio* calculations of the Rb-H_2 interaction

potential using the unrestricted coupled cluster method with single, double, and perturbative triple excitations [UCCSD(T)].[18] A large augmented correlation-consistent polarization valence quadruple-ζ basis set (aug-cc-pVQZ)[19] and the ECP28MDF relativistic effective core potential with the [13*s*10*p*5*d*3*f*] basis set[20] were used for the H and Rb atoms, respectively. The basis set superposition error for Rb-H2 interaction energy was corrected using the standard approach.[21] All calculations were carried out with the MOLPRO suite of programs.[22] The potential energy surface (PES) is expressed in the Jacobi coordinates R and θ, where R is the distance between the Rb atom and the H_2 center of mass, and θ is the angle between the atom-molecule vector R and the H_2 axis. To obtain the effective Rb-H_2 potential $V_0(R)$ used in matrix shift calculations, we averaged 19 PES cuts corresponding to evenly spaced values of $\theta \in [0^\circ, 90^\circ]$ using the hindered rotor model.[23] A contour plot of our *ab initio* PES shown in Figure 4.4(a) demonstrates that the Rb-H_2 interaction is weakly anisotropic.

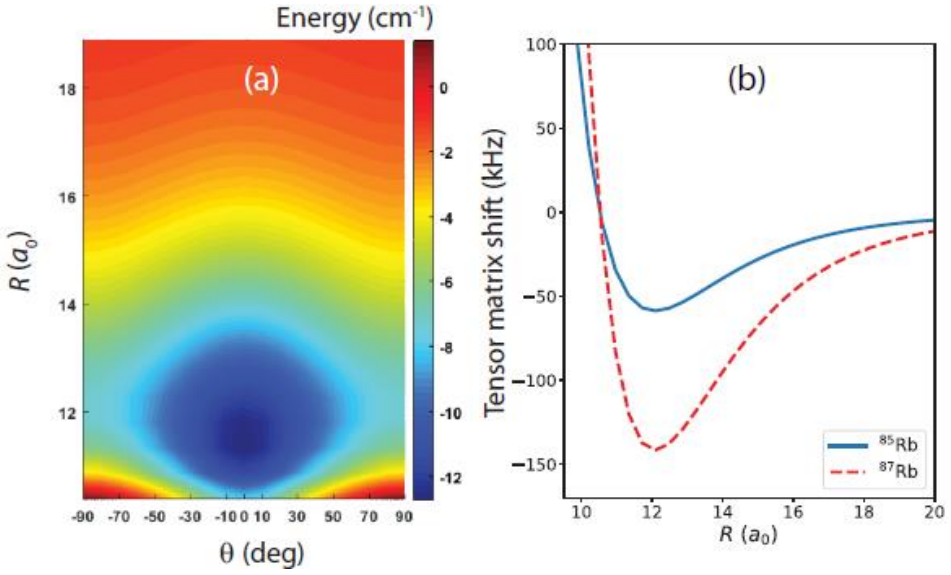

Figure 4.4. (a) *Ab initio* PES for Rb-H_2 plotted as a function of the Jacobi coordinates R and θ. (b) Tensor matrix shifts of ^{85}Rb (solid line) and ^{87}Rb (dashed line) interacting with six *p*-H_2 molecules as a function of the Rb-H_2 distance R.

Figure 4.4(b) shows our calculated upper bounds to the tensor matrix shifts of Rb as a function of the Rb-H_2 distance R, calculated for six *p*-H_2 molecules. The theoretical bounds are consistent with the measured values shown in Figure 3.3, reaching their maxima of 59 kHz for ^{85}Rb and 142 kHz for ^{87}Rb near the minimum of the potential well. The large magnitude of the shift in ^{87}Rb is due to its larger hyperfine constant, which exceeds that of ^{85}Rb by a factor of 3.4. The R dependence of the shifts follows that of the Rb-H_2 interaction energy, reaching a minimum at $R_e \backsimeq 12.1a_0$ and tending to zero at large R. At short values of R to the left of the potential minimum, the dominant mechanism responsible for the matrix shifts is no longer the dispersion interaction, but rather the Pauli exclusion force arising from the overlap of the electronic wave functions of Rb and H_2.[15] Thus, our matrix shift estimates at $R \ll 12a_0$ should not be considered even qualitatively accurate. We also note that the calculated tensor matrix shifts scale with m_F (for a given isotope and F) as m_F^2 due to the second-rank tensor nature of the magnetic dipole hyperfine interaction in the excited atomic states.[17]

In conclusion, we have established that the spin dephasing of Rb atoms in parahydrogen at densities $\lesssim 10^{18}$ cm^{-3} is dominated by interactions that are electrostatic (or "T -even") in nature. As such, the T_2^* can be significantly increased by replacing traditional Larmor precession states (or traditional single-photon EPR spectroscopy) with superposition states of (or multiphoton transitions between) Zeeman levels that are time reversals of each other.

This will enable greater resolution in EPR spectroscopy, and is of use for improving ensemble magnetometry[24,25] and for fundamental physics experiments with atoms and molecules in matrices.[26,27] We note that for these applications, the superposition states we have explored have two advantages: Their inhomogeneous broadening is reduced and they evolve phases faster than Larmor precession states, limited to a factor of $2F$ for the stretched states. The latter advantage has been explored in recent work with dysprosium atoms[28] and with mechanical oscillators,[29] where larger factors can be achieved.

Our results are similar to the "double quantum coherence magnetometry" techniques developed for nitrogen vacancy (NV) centers in diamond,[24,25,30,31] but in a different limit. NV centers are typically used in the regime where the electrostatic coupling of the spin to the lattice is $\gg$ its coupling to B_z; here, we work in a limit where the coupling to B_z is $\gg$ the electrostatic coupling to the matrix. The NV-center limit requires the use of a single-crystal sample with magnetic field parallel to the crystal axis[24]; in the current work we employ what we expect is a polycrystalline sample,[11,12] and see no dependence of the FID linewidths on the magnetic field direction. We speculate the electrostatic broadening comes from a combination of inhomogeneous trapping sites and inhomogeneous crystal axis orientations.

Our narrowest observed linewidth of 5 kHz corresponds to a T_2^* of 60 μs. We note this ensemble T_2^* is longer than reported values for ensembles of NV centers in diamond.[24] It is also, surprisingly, an order of magnitude longer than reported for alkali-metal atoms in superfluid helium.[32] The only condensed-phase electron spin system with longer reported ensemble T_2^* times is atomic cesium in solid He, which was

measured at a significantly lower spin density.[33] We expect even longer T_2^* times can be obtained in parahydrogen by employing stretched-state superpositions and by producing single-crystal samples through different growth parameters or sample annealing.[11,12]

Acknowledgements

This material is based upon work supported by the National Science Foundation under Grants No. PHY-1607072, No. PHY-1607610, and No. CHE-1654547. We gratefully acknowledge assistance in the construction of the experimental apparatus from Wade J. Cline and Carl D. Davidson, Jr. We thank Andrei Derevianko and Amar C. Vutha for valuable conversations and thank Pierre-Nicholas Roy for providing the hindered rotor code.

References

(1) Budker, D.; Romalis, M. Optical Magnetometry. *Nat. Phys.* **2007**, *(3)* 227-234. https://doi.org/10.1038/nphys566.

(2) Al'Tshuler, S. A.; Kozyrev, B. M. *Electron Paramagnetic Resonance*; Academic, New York, 1964.

(3) Andreev, A.; Ang, D. G.; DeMille, D.; Doyle, J. M.; Gabrielse, G.; Haefner, J.; Hutzler, N. R.; Lasner, Z.; Meisenhelder, C.; O'Leary, B. R.; Panda, C. D.; West, A. D.; West, E. P.; Wu, X. Improved Limit on the Electric Dipole Moment of the Electron. *Nature* **2018**, *562* (7727), 355-360.

(4) Pustelny, S.; Jackson Kimball, F.; Pankow, C.; Ledbetter, M. P.; Wlodarczyk, P.; Wcislo, P.; Pospelov, M.; Smith, J. R.; Read, J.; Gawlik, W.; Budker, D. The Global Network of Optical Magnetometers for Exotic physics (GNOME): A novel scheme to search for physics beyond the Standard Model. *Ann. Phys.* **2013**, *525* (8), 659-670. https://doi.org/10.1002/andp.201300061.

(5) Brown, J. M.; Smullin, S. J.; Kornack, T. W.; Romalis, M. V. New Limit on Lorentz- and CPT-Violating Neutron Spin Interactions. *Phys. Rev. Lett.* **2010**, *105*, 1-4. https://doi.org/10.1103/PhysRevLett.105.151604.

(6) Upadhyay, S.; Kanagin, A. N.; Hartzell, C.; Christy, T.; Arnott, W. P.; Momose, T.; Patterson, D.; Weinstein, J. D. Longitudinal spin relaxation of optically pumped rubidium atoms in solid parahydrogen. *Phys. Rev. Lett.* **2016**, *117*, 1-5. https://doi.org/10.1103/PhysRevLett.117.175301.

(7) Kanagin, A. N.; Regmi, S. K.; Pathak, P.; Weinstein, J. D. Optical pumping of rubidium atoms frozen in solid argon. *Phys. Rev. A* **2013**, *88*, 1-4. https://doi.org/10.1103/PhysRevA.88.063404.

(8) Arimondo, E.; Inguscio, M.; Violino, P. Experimental determinations of the hyperfine structure in the alkali atoms. *Rev. Mod. Phys.* **1977**, *49* (1), 31-75. https://doi.org/10.1103/RevModPhys.49.31.

(9) Weltner, W. *Magnetic Atoms and Molecules*; Dover, 1989.

(10) Supplemental Material. https://doi.org/10.1103/PhysRevB.100.024106 (accessed 2021-11-10).

(11) Tam, S.; Fajardo, M. E.; Katsuki, H.; Hoshina, H.; Wakabayashi, T.; Momose, T. High resolution infrared absorption spectra of methane molecules isolated in

solid parahydrogen matrices. *J. Chem. Phys.* **1999**, *111* (9), 4191-4198. https://doi.org/10.1063/1.479717.

(12) Raston, P. L.; Kettwich, S. C.; Anderson, D. T. High-resolution infrared spectroscopy of atomic bromine in solid parahydrogen and orthodeuterium. *J. Chem. Phys.* **2013**, *139* (13), 1-11. https://doi.org/10.1063/1.4820528.

(13) *Alkali D Line Data*. https://steck.us/alkalidata/ (accessed 2021-11-10).

(14) Dzuba, V. A.; Flambaum, V. V.; Beloy, K.; Derevianko, A. Hyperfine-mediated static polarizabilities of monovalent atoms and ions. *Phys. Rev. A*, **2010**, *82*, 1-6. https://doi.org/10.1103/PhysRevA.82.062513.

(15) Adrian, F. J. Matrix Effects on the Electron Spin Resonance Spectra of Trapped Hydrogen Atoms. *J. Chem. Phys.* **1960**, *32* (4), 972-981. https://doi.org/10.1063/1.1730906.

(16) Moroshkin, P.; Hofer, A.; Weis, A. Atomic and molecular defects in solid ^{4}He. *Phys. Rep.* **2008**, *469* (1), 1-57. https://doi.org/10.1016/j.physrep.2008.06.004.

(17) Ulzega, S.; Hofer, A.; Moroshkin, P.; Weis, A. Reconciliation of experimental and theoretical electric tensor polarizabilities of the cesium ground state. *Europhys. Lett.* **2006**, *76* (6), 1074-1080. https://doi.org/10.1209/epl/i2006-10383-2.

(18) Deegan, M. J. O.; Knowles, P. J. Perturbative corrections to account for triple excitations in closed and open shell coupled cluster theories. *Chem. Phys. Lett.* **1994**, *227* (3), 321-326. https://doi.org/10.1016/0009-2614(94)00815-9.

(19) Dunning, T. H. Gaussian basis sets for use in correlated molecular calculations. I. The atoms boron through neon and hydrogen. *J. Chem. Phys.* **1989**, *90* (2), 1007-1023. https://doi.org/10.1063/1.456153.

(20) Lim, I. S.; Schwerdtfeger, P.; Metz, B.; Stoll, H. All-electron and relativistic pseudopotential studies for the group 1 element polarizabilities from K to element 119. *J. Chem. Phys.* **2005**, *122* (10), 1-13. https://doi.org/10.1063/1.1856451.

(21) Boys, S. F.; Bernardi, F. The calculation of small molecular interactions by the differences of separate total energies. Some procedures with reduced errors. *Mol. Phys.* **1970**, *19* (4), 553-566. https://doi.org/10.1080/00268977000101561.

(22) Werner, H.-J.; Knowles, P. J.; Knizia, G.; Manby, F. R.; Schütz, M. Molpro: a general-purpose quantum chemistry program package. *WIREs Comput. Mol. Sci.* **2012**, *2*, 242-253. https://doi.org/10.1002/wcms.82.

(23) Li, H.; Roy, P.-N.; Le Roy, R. J. An "adiabatic-hindered-rotor" treatment allows para- to be treated as if it were spherical. *J. Chem. Phys.* **2010**, *133* (10), 1-10. https://doi.org/10.1063/1.3476465.

(24) Bauch, E.; Hart, C. A.; Schloss, J. M.; Turner, M. J.; Barry, J. F.; Kehayias, P.; Singh, S.; Walsworth, R. L. Ultralong dephasing times in solid-state spin ensembles via quantum control. *Phys. Rev. X* **2018**, *8* (3), 1-11. https://doi.org/10.1103/PhysRevX.8.031025.

(25) Mamin, H. J.; Sherwood, M. H.; Kim, M.; Rettner, C. T.; Ohno, K.; Awschalom, D. D.; Ruglar, D. Multipulse double-quantum magnetometry with near-surface nitrogen-vacancy centers. *Phys. Rev. Lett.* **2014**, *113*, 1-5. https://doi.org/10.1103/PhysRevLett.113.030803.

(26) Weis, A.; Kanorsky, S.; Lang, S; Hänsch, T. Can atoms trapped in solid helium be used to search for physics beyond the standard model? *In Atomic Physics*

Methods in Modern Research; Springer, 2007; pp. 57-75. https://doi.org/10.1007/BFb0104315.

(27) Vutha, A.; Horbatsch, M.; Hessels, E. Oriented polar molecules in a solid inert-gas matrix: a proposed method for measuring the electric dipole moment of the electron. *Atoms*, **2018**, *6* (1), 3-10. https://doi.org/10.3390/atoms6010003.

(28) Chalopin, T.; Bouazza, C.; Evrard, A.; Makhalov, V.; Dreon, D.; Dalibard, J.; Sidorenkov, L. A.; Nascimbene, S. Quantum-enhanced sensing using non-classical spin states of a highly magnetic atom. *Nat. Commun.* **2018**, *9*, 1-8. https://doi.org/10.1038/s41467-018-07433-1.

(29) McCormick, K. C.; Keller, J.; Burd, S. C.; Wineland, D. J.; Wilson, A. C.; Leibfried, D. arXiv:1807.11934. https://doi.org/10.1038/s41586-019-1421-y.

(30) Huang, P.; Kong, X.; Zhao, N.; Shi, F.; Wang, P.; Rong, X.; Liu, R.-B.; Du, J. Observation of an anomalous decoherence effect in a quantum bath at room temperature. *Nat. Commun.* **2011**, *2*, 1-7. https://doi.org/10.1038/ncomms1579.

(31) Fang, K.; Acosta, V. M.; Santori, C.; Huang, Z.; Itoh, K. M.; Watanabe, H,l Shikata, S.; Beausoleil, G. High-sensitivity magnetometry based on quantum beats in diamond nitrogen-vacancy centers. *Phys. Rev. Lett.* **2013**, *110* (13), 1-5. https://doi.org/10.1103/PhysRevLett.110.130802.

(32) Koch, M.; Auböck, G.; Callegari, C.; Ernst, W. E. Coherent spin manipulation and ESR on superfluid helium nanodroplets. *Phys. Rev. Lett.* **2009**, *103* (3), 1-4. https://doi.org/10.1103/PhysRevLett.103.035302.

(33) Kanorsky, S. I.; Lang, S.; Lücke, S.; Ross, S. B.; Hänsch, T. W.; Weis, A. Millihertz magnetic resonance spectroscopy of Cs atoms in body-centered-

cubic ^{4}He. *Phys. Rev. A* **1996**, *54* (2), R1010 – R1013. https://doi.org/10.1103/PhysRevA.54.R1010.

CHAPTER 5. SPIN COHERENCE AND OPTICAL PROPERTIES OF ALKALI-METAL ATOMS IN SOLID PARAHYDROGEN

Adopted with permission from

Physical Review A 100, 063419 (2019)

https://doi.org/10.1103/PhysRevA.100.063419

Sunil Upadhyay, Ugne Dargyte, **Vsevolod D. Dergachev**, Robert P. Prater, Sergey A. Varganov, Timur V. Tscherbul, David Patterson, and Jonathan D. Weinstein

Abstract

We present a joint experimental and theoretical study of spin coherence properties of ^{39}K, ^{85}Rb, ^{87}Rb, and ^{133}Cs atoms trapped in a solid parahydrogen matrix. We use optical pumping to prepare the spin states of the implanted atoms and circular dichroism to measure their spin states. Optical-pumping signals show order-of-magnitude differences depending on both matrix growth conditions and atomic species. We measure the ensemble transverse relaxation times (T_2^*) of the spin states of the alkali-metal atoms. Different alkali species exhibit dramatically different T_2^* times, ranging from submicrosecond coherence times for high-m_F states of ^{87}Rb to $\sim 10^2$ microseconds for ^{39}K. These are the longest ensemble T_2^* times reported for an electron

spin system at high densities ($n \gtrsim 10^{16}$ cm^{-3}). To interpret these observations, we develop a theory of inhomogeneous broadening of hyperfine transitions of ^2S atoms in weakly interacting solid matrices. Our calculated ensemble transverse relaxation times agree well with experiment, and suggest ways to longer coherence times in future work.

I. Introduction

Addressable solid-state electron spin systems are of interest for many physics applications, including quantum computing and quantum information,[1-6] magnetometry,[7-9] nanoscale magnetic resonance imaging,[10-13] and tests of fundamental physics.[14-17]

Atoms trapped in inert matrices—such as hydrogen or noble-gas solids—are promising for these applications. The transparent matrix allows for optical pumping and probing of the electron spin state of the implanted atom, and the weak interaction of the trapped atom with the host matrix should only minimally perturb the atomic properties. The hope is to combine the high densities of solid-state electron spin systems with the (marginally perturbed) excellent properties of gas-phase atoms.

Cesium atoms in the bcc phase of solid helium (at pressures of ∼26 bars and temperatures of ∼1.5 K) exhibit good optical pumping and readout of spin states and excellent ensemble spin coherence times, but to date have been limited to low cesium densities (10^9 cm^{-3}) .[18-20] On the other hand, atoms can be trapped in argon and neon matrices at high densities (10^{17} cm^{-3}),[21-23] but to date optical pumping and readout of the electron spin state has been significantly less efficient than the best solid-state spin systems.[24,25]

Parahydrogen is a promising cryogenic host matrix[26] which combines the respective advantages of solid argon and solid helium. Previously it was demonstrated that the spin state of rubidium in solid parahydrogen could be optically pumped and probed more efficiently than in solid argon.[27] Moreover, demonstrated ensemble

electron spin coherence times for Rb atoms in solid parahydrogen are longer than any other solid-state system capable of comparable electron spin density.[28]

In this work, we compare the optical-pumping properties and ensemble transverse spin relaxation time (T_2^*) for potassium, rubidium, and cesium in solid H_2. The dramatic differences between these alkali-atom species reveal the underlying physical mechanisms affecting optical-pumping and spin coherence times.

We further develop a first-principles theoretical model to describe the coherence properties of matrix-isolated alkali-metal atoms, which shows that the measured T_2^* times are due to the anisotropic hyperfine interaction of the atoms with the host matrix. Our theoretical results are in good agreement with experiment, opening up the possibility of systematic *ab initio* modeling of coherence properties of atomic and molecular guest species in inert matrices.

II. Experiment

The apparatus is as described in references[27,29,30]; the key components are shown in Figure 5.1. Parahydrogen and alkali atoms (from high-purity, natural isotopic abundance samples) are co-deposited onto a cryogenically cooled sapphire substrate in vacuum. Before deposition, normal hydrogen is converted to parahydrogen using a cryogenic catalyst.[27,31] In our current apparatus the remaining orthohydrogen fraction can be varied from 3×10^{-5} to 1×10^{-2}. After deposition, the atoms are optically pumped and probed with both broadband and laser light at near-normal angles of incidence to the surface. A homogeneous magnetic bias field is applied to the crystal, and RF magnetic fields can be applied perpendicular to the bias field.

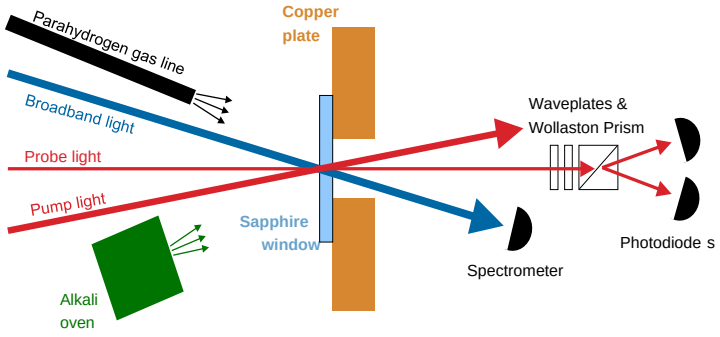

Figure 5.1. Schematic of apparatus. The copper plate and parahydrogen gas line are cooled by a closed-cycle pulse tube refrigerator. In our experiments, the pump and probe light are of the same frequency, and generated from the same laser. The vacuum chamber, its windows, and other optics are omitted for simplicity.

III. Optical-Absorption Spectra

Sample spectra of K, Rb, and Cs are shown in Figure 5.2. The transmission T of the crystal is determined by comparing a spectrum of the light transmitted through the apparatus – as measured by a fiber-coupled grating spectrometer – before and after crystal deposition. The optical depth (OD) is determined from $T \equiv e^{-\mathrm{OD}}$. For ease of comparing spectra the baseline of the spectra has been shifted so that the off-resonance OD = 0; the amplitudes have been normalized so that the peak OD = 1.

All spectra shown were taken at the 3 K base temperature of the cryostat. We note that thermal annealing of the crystal at temperatures of up to 4.2 K and times of up to 24 hours causes negligible changes in the absorption spectrum.

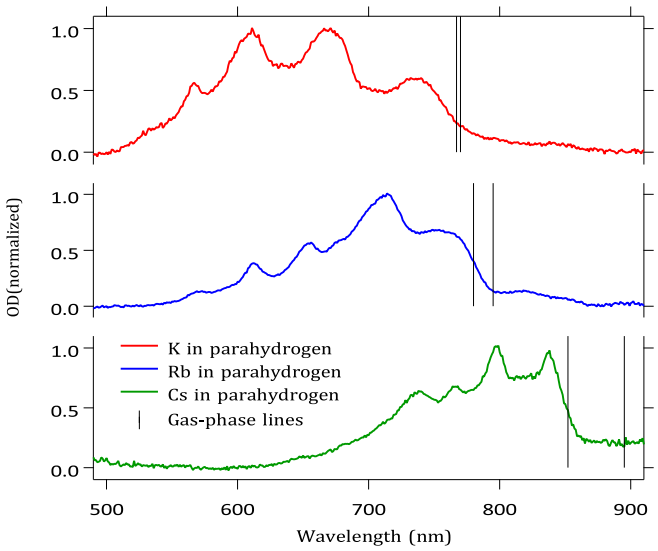

Figure 5.2. Optical spectra of alkali-doped parahydrogen crystals. The spectra are normalized as discussed in the text. In each spectrum, the frequencies of the gas-phase atom transitions[32] are shown for comparison.

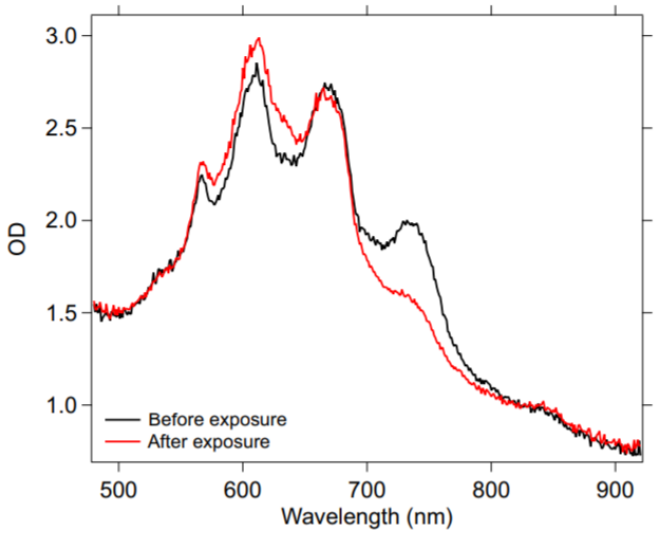

Figure 5.3. Spectra of potassium-doped parahydrogen showing bleaching. Spectra are taken before and after illuminating the matrix with laser light at 757 nm. The light causes a significant reduction in the absorption of the peak it is on resonance with.

In all spectra, we see large spectral shifts, large broadenings, and the splitting of the $s \rightarrow p$ transition into multiple lines. Similar behavior was observed for alkali atoms in noble-gas matrices and superfluid helium.[18,20,21,33,34]

A. Optical Annealing

The spectra of the implanted alkali atoms—if grown in the absence of light—are significantly affected by the application of broadband light to the crystal. This phenomenon, which we call "optical annealing," has been previously reported for Rb atoms.[27] Similar effects were observed for Cs and K. Typically during optical annealing the number of spectral peaks is reduced, and the optical depth of the remaining peaks increases correspondingly. As far as we know, these changes are irreversible; in our observations we have not observed the spectrum returning to its original form, even over timescales of weeks. We attribute the spectral changes to the reconfiguration of trapping sites due to optical excitation.

The data shown in Figure 5.2 are after optical annealing. We have not studied optical pumping of atoms prior to optical annealing (nor have we studied the spectral peaks that disappear in the process), as we expect those sites not to be stable under optical excitation. For the remainder of this paper, we only discuss the properties of samples in this state reached after optical annealing.

B. Bleaching and Broadening Mechanisms

Much as the optical spectrum is changed by the application of broadband light; we observe that it is also altered by the application of narrowband light.

For potassium atoms trapped in parahydrogen, we see "bleaching" effects due to the application of narrowband light, as seen in Figure 5.3. We attribute the changes

in the spectrum to changes in the trapping sites induced by the light, similar to what occurs during optical annealing with broadband light.

The changes to the spectrum indicate that broadening is homogeneous within each peak: application of light with a linewidth ≪ the absorption linewidth effectively bleaches the entire line. The changes also indicate that the different lines originate from different trapping sites, as absorption at other frequencies is not diminished. In fact, absorption at 610 nm increases, indicating that during bleaching the trapping sites that give rise to absorption at 735 nm are changed into trapping sites that absorb at a different frequency.

Similar bleaching effects were observed for Rb atoms trapped in solid argon. We note that in argon, $\sim 10^1$ photon scattering events would cause reconfiguration of the trapping sites.[25] Alkali atoms in parahydrogen are significantly more resistant to bleaching. From the atomic density, the intensity of light, and the timescale of bleaching, we estimate that potassium absorbs on the order of 10^4 photons before bleaching.

Such bleaching effects can be problematic for use of these matrix-trapped atoms for applications. For Rb atoms in argon we found that application of light at other wavelengths would reverse the bleaching effects and return the trapping sites to their "unbleached" states.[25] We have not yet demonstrated similar unbleaching with alkali atoms in parahydrogen; it is not yet known whether this is possible.

C. Effects of Crystal Growth Conditions

The spectra of alkali atoms in parahydrogen can vary significantly with crystal growth conditions.

We did not observe a significant dependence of the spectra on alkali density or orthohydrogen density over the ranges we explored. We saw no noticeable change with ortho fraction over the range from 4×10^{-5} to 3×10^{-3}. Similarly, the spectra show only minor changes with Rb atom density from $1 \times 10^{17}\,\mathrm{cm}^{-3}$ to $1 \times 10^{18}\,\mathrm{cm}^{-3}$. However, the spectra do depend sensitively on the substrate temperature at the time of matrix growth.

Figure 5.4 shows the optical spectra of Rb-doped parahydrogen crystals grown at different substrate temperatures. The temperatures specified in the figure – and throughout this paper—are of the copper plate upon which the sapphire window is mounted.

We measure the temperature of the front surface of the window (onto which the parahydrogen matrix is grown) with a silicon diode temperature sensor attached to the window with varnish. We monitor its temperature during crystal growth as the sensor is embedded in solid hydrogen. From these measurements we conclude that the temperature of the front surface of the window is within 0.4 K of the copper plate temperature during growth. While the crystals in Figure 5.4 were grown at different substrate temperatures, the spectra shown were measured under identical conditions at our base temperature of 3 K. The crystals of Figure 5.4 have Rb densities of 1×10^{17} cm^{-3}, with variations within ±15%, and ortho fractions of 3×10^{-5}, with variations of ±25%. We believe that the spectral differences are primarily due to the substrate temperature.

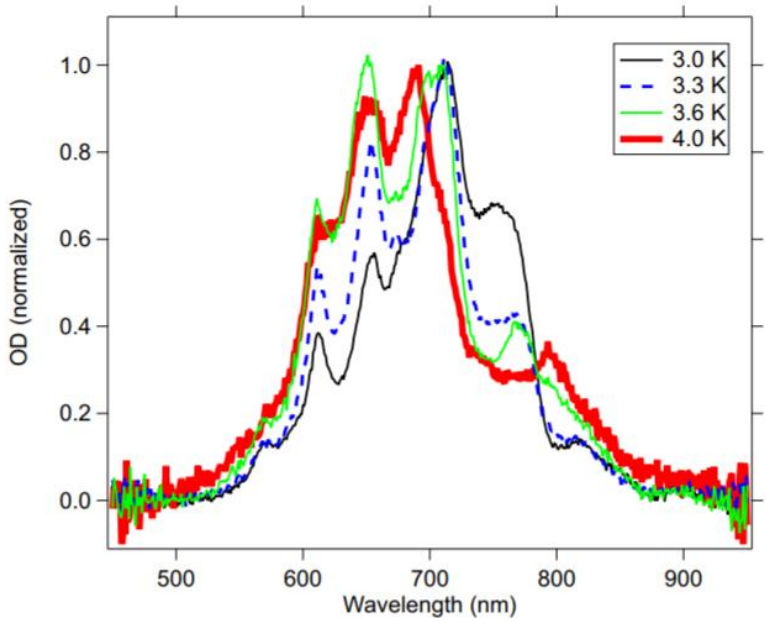

Figure 5.4. Optical spectra of Rb-doped parahydrogen crystals, grown at different substrate temperatures, as labeled. The spectra are normalized in the same manner as in Figure 5.2.

As the substrate temperature increases, the blueshifted peaks become larger in amplitude and the redmost peak becomes smaller and shifts. Qualitatively similar behavior was observed for Cs atoms. (Potassium-doped matrices were only grown at the base temperature.)

Subsequent annealing at temperatures up to 4 K for durations up to ~10 hours can change the background scattering from the crystal (depending on crystal conditions, annealing has been observed to either increase or decrease background scattering). However, annealing has little observable effect on the alkali atom absorption peaks.

The optical spectrum is also affected by the matrix growth rate. Rubidium-doped crystals grown at our base temperature (3 K) with low hydrogen deposition rates (~1 μm per minute) have optical spectra similar to samples grown at normal deposition rates (~3 μm per minute) and higher substrate temperatures (similar to the 3.3 K

spectrum shown in Figure 5.4). However, we have not explored flow rates as comprehensively as substrate temperatures.

As discussed in Section D, these changes in the optical spectrum have significant consequences for our ability to optically pump and measure the spin states of the alkali atoms.

IV. Spin Polarization Signal

We optically pump the implanted atoms using right-hand circular (RHC) laser light, as shown in Figure 5.1. We monitor the spin polarization produced using a linearly polarized probe beam at the same frequency. After passing through the sample, the probe beam is sent through wave plates and a Wollaston prism to separate it into its RHC and left-hand circular (LHC) components, which are measured on two photodetectors. Differential absorption between the RHC and LHC components (circular dichroism) indicates spin polarization. Due to the large broadening of the optical spectrum, the different isotopes and their hyperfine levels cannot be optically distinguished, and the spin polarization signal measured for each species is an average of the naturally occurring isotopes.

To quantify the spin polarization obtained, we measure the ratio of RHC and LHC signals on the two photodiodes and normalize the ratio to a level of 1 before optical pumping. The ratio changes after optical pumping. To ensure that the change is not due to systematic effects, it is measured both with an applied longitudinal magnetic field and with a transverse field (the ambient earth magnetic field); the latter prevents the accumulation of spin polarization during optical pumping. With a transverse field,

the change in the ratio due to optical pumping is typically very small compared to the longitudinal field, as expected.[27] To calculate the polarization signal amplitude, one ratio is subtracted from the other. This is the polarization signal *P* shown below in Figures 5.5, 5.6, and 5.7.

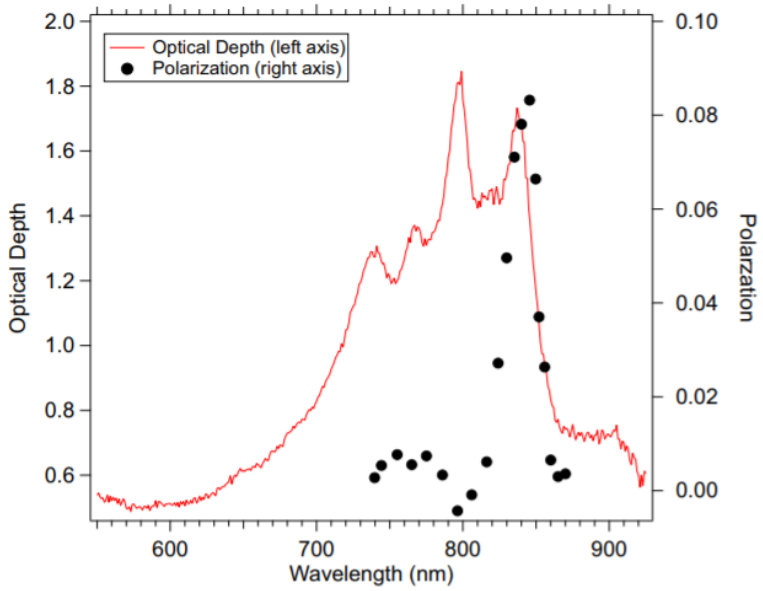

Figure 5.5 Polarization signal amplitude, plotted alongside the optical spectra of a Cs-doped parahydrogen crystal. Crystal grown with a substrate temperature of 3 K, orthohydrogen fraction 3×10^{-5}, and Cs density 6×10^{16} cm^{-3}. Polarization was measured with an 80 G on-axis bias field.

We relate this signal to atomic properties by the following model. Optical pumping changes the hyperfine and spin state of the implanted atoms. This changes the atoms' cross section for scattering RHC and LHC light. We quantify the change with a single parameter Δ, and model the cross-section changes as $\sigma_{\mathrm{RHC}} = \sigma_0(1 - \Delta)$ and $\sigma_{\mathrm{LHC}} = \sigma_0(1 + \Delta)$, consistent with our observations.[27] Before pumping (or after pumping with a transverse magnetic field) we assume $\Delta = 0$, giving identical optical depths for both polarizations of light; we refer to this optical depth as OD_0. Thus, when

we measure the ratio R of transmissions of LHC and RHC light, we obtain $R = e^{-2\Delta \times \mathrm{OD}_0}$. The polarization signal P we measure is then $P = 1 - R$. In the limit $P \ll 1$, $P = 2\Delta \times \mathrm{OD}_0$. For vapor-phase atoms, it is possible to obtain $\Delta \to 1$, as the atoms can be pumped into a spin state that is dark to one of the circular polarizations of light. As presented below, the largest values of Δ observed for alkali atoms in parahydrogen are ~0.065, significantly lower than vapor-phase atoms. Whether this is due to limitations in optical pumping or optical detection is not known; we expect that it is a combination of both.

A. Wavelength Dependence

We examine the polarization signal as a function of the wavelength of the pump and probe (the two wavelengths are identical in all data presented here). For the cesium data presented in Figure 5.5, typical pump and probe beams have waists of 200 μm and 125 μm, respectively, and intensities 5×10^3 mW/cm^2 and 50 mW/cm^2, respectively. We note that while these intensities are above the saturation intensity of a gas-phase alkali atom, they are far below the saturation intensity of alkali atoms in parahydrogen (due to the large spectral broadening of the optical transition). Typical pump durations are ~100 ms; the pumping rate is limited by laser intensity.

While the optical spectrum shows multiple peaks, we only see a significant polarization signal when pumping and probing near the redmost peak.

For Rb polarization, we were not able to scan the entire Rb spectra, and were only able to cover the ranges 655 nm, 680–700 nm, and 730–810 nm (limited by the light sources available to us). Over this range, we saw negligible polarization signal

except in the region from 730–760 nm, with maximum signal near 750 nm. Similarly to Cs, the largest polarization signal was seen near the redmost peak (for crystals grown at low temperature).

For potassium, we likewise were unable to cover the entire spectral range, but were able to compare pumping and probing on the redmost line (at 735 nm) to the line at 660 nm. We were unable to observe spin polarization at 660 nm, but observed a signal when slightly red-detuned from the redmost line.

This behavior is similar to what was previously observed for thermally spin-polarized rubidium atoms in argon, which gave the strongest circular dichroism signal on the redmost line.[24] We do not know whether this is due to similar physics or is simply a coincidence.

Surprisingly, for Rb spectra grown at elevated temperatures (as shown in Figure 5.4), the peak polarization response remains near 750 nm despite the nearly complete "disappearance" of that peak in the absorption spectrum. However, the size of the polarization signal decreases, as discussed below in Section IV B.

Much as the optical spectrum has little dependence on the ortho fraction or alkali density over the ranges we explored, we observed little change in the polarization signal. For rubidium densities from 6×10^{16} to 3×10^{17} cm^{-3} in matrices grown under similar conditions, we see no change in Δ to within ±15%. We note that at higher rubidium densities ($\gtrsim 10^{18}$ cm^{-3}) the polarization signal appeared to decrease, but we did not extensively explore this density region. Increasing the ortho fraction from 5×10^{-3} to 3×10^{-2} resulted in a decrease in the Rb polarization signal of a factor of 2. However, the higher ortho fraction crystal was grown at a substrate temperature 0.16 K

higher than the low ortho fraction crystal (due to the extra heat load on the cryostat from heating the ortho-para catalyst), and we suspect the majority of the difference in polarization signal is due to the substrate temperature change (as discussed below in Section IV B). We did not investigate this behavior for Cs and K in a controlled manner.

B. Effects of Crystal Growth Conditions

Because the crystal growth temperature strongly affects the optical spectrum (as discussed in Section III C), one might expect the polarization signal to be affected as well. This is indeed true: the size of the polarization signal varies strongly with the temperature of the substrate during crystal growth. Figure 5.6 shows this effect for the case of cesium atoms.

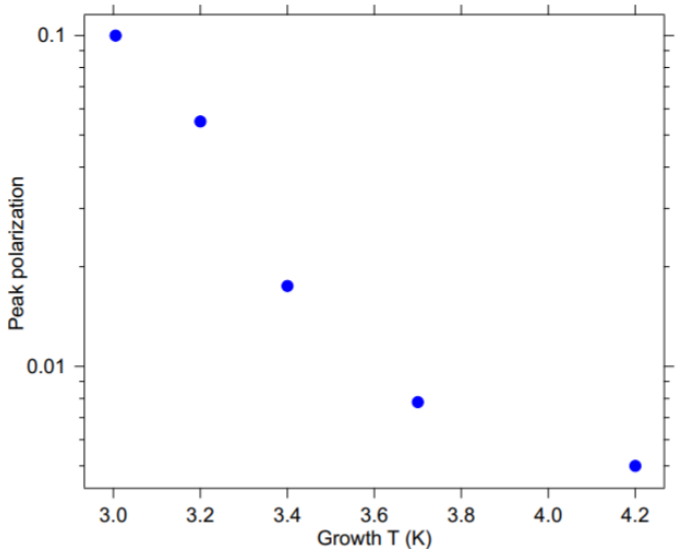

Figure 5.6. Polarization signal amplitude for Cs-doped parahydrogen crystals of optical depth $OD_0 \sim 1$ grown at different substrate temperatures. The optical depths of the different crystals differed by ±25%, and their densities varied by ±30%. As these variations are small compared to the polarization effects observed, we did not correct for them. The change in ortho fraction was small, and separate measurements indicate that ortho fraction has little effect on the size of the polarization signal.

We note that the optical-pumping data in Figure 5.6 were all obtained at our base temperature, having cooled down the crystal after growth. Much as the optical spectrum maintains a "memory" of the temperature at which it was grown, so does the optical pumping and readout. Similar behavior was observed for Rb, with smaller polarization signals for crystals grown at elevated substrate temperatures.

For cesium, some data suggest that matrices grown at higher hydrogen deposition rates give larger polarization signals than samples grown at lower flow. This is consistent with the results of Section III C, indicating that higher hydrogen flow has a similar effect on the optical behavior as lower temperatures. The maximum flow rate is limited by our current ortho-para converter.

Based on these results and those of Sections III C and IV A, we speculate that some trapping sites in the lattice are more favorable for optical pumping and readout. The different growth conditions change the fraction of atoms trapped in such favorable sites, which is reflected in both the optical spectrum and the polarization signal.

We note that these data suggest that it is very likely that significant improvements in the ability to optically pump and read out the spin states of alkali atoms in parahydrogen are possible with an apparatus capable of colder temperatures and faster parahydrogen deposition rates during crystal growth.

C. Magnetic-Field Dependence

As seen in Figure 5.7, the amplitude of the spin polarization signal has a strong dependence on the applied magnetic field. At fields $\ll$ 10 G, the optical-polarization

signal is quite small. The signal size increases with increasing magnetic field, and appears to saturate at fields 10 G.

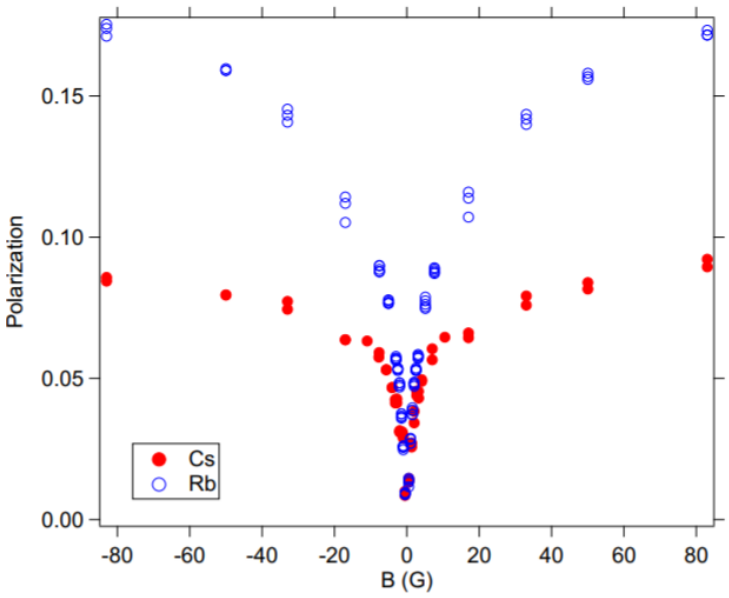

Figure 5.7. Polarization signal *P* for Cs and Rb as a function of the bias magnetic field. The bias field is roughly normal to the matrix surface and roughly parallel to the pump and probe beams. The difference in the high-field value of *P* is partially due to different growth conditions: the cesium-doped sample was grown at a higher substrate temperature; the ODs of Rb and Cs were 1.4 and 1.1, respectively. Both crystals exhibit the same qualitative behavior.

As discussed below in Section VIII (and touched upon previously in Refs.[18,27]) we attribute these effects to coupling to the crystal field in our polycrystalline sample. At magnetic fields 10 G, the Zeeman splitting is much larger than the coupling of the spin to the crystal field, and the m levels are only slightly perturbed by the matrix. At low magnetic fields, the perturbation from the matrix mixes the m eigenstates and interferes with the ability to optically control and probe the spin state with polarized light.

D. Species Dependence

Potassium produces significantly smaller polarization signals than Rb- and Cs-doped crystals produced and measured under similar conditions.

Table 5.1. The optical spin polarization signal Δ, as defined in Section IV, for the atomic species measured. All crystals had an optical depth of 1.1 at the pump-probe wavelength. The excited-state finestructure splittings are from Ref.[32]

Species	*B*(G)	Δ	FS splitting (cm^{-1})
K	80	4×10^{-3}	57
Rb	33	5×10^{-2}	237
Cs	33	4×10^{-2}	554

Table 5.1 compares the spin polarization signals obtained for potassium, rubidium, and cesium. All crystals were grown on the identical cryogenic substrate setup and under similar growth conditions. The potassium datum is the largest polarization signal observed for potassium in our laboratory, and was measured before significant bleaching of the spot occurred (see Section III B). Larger signals were seen for rubidium and cesium crystals grown under different conditions (an improved window mount that was able to reach slightly colder temperatures, and higher parahydrogen flow rates). While the data were taken at different bias fields, rubidium and cesium polarizations do not have a significant dependence on the magnetic field over the range from 30 to 80 G (as seen in Figure 5.7).

E. Interpretation

As discussed below in Section VII B, all three species have similar ground-state interaction potentials with hydrogen. Our interpretation is that the order-of-magnitude

differences in polarization are due to the different fine-structure splittings of their excited states.

First, optical pumping and detection of spin polarization on the $s \rightarrow p$ transition in an alkali atom relies on the fine-structure coupling between orbital angular momentum (L) and spin (S). Inside the matrix, the excited p orbital is coupled to the crystal field of the local-trapping site, which (neglecting spin and fine structure) can split its threefold orbital degeneracy.[24] If the coupling of L to the crystal is large compared to the fine-structure splitting, it can potentially "decouple" L and S and impede the ability to both optically pump and detect the electron spin state.[24] Hence, if the crystal-field interaction is much larger than the fine-structure splitting, we expect poor optical pumping and detection.

Second, if the fine-structure splitting of the excited state is not optically resolved, it will suppress the ability to optically detect spin polarization. However, we note that in the case of repopulation pumping, optical pumping would still be possible in this limit, as discussed in Section IV F.

As expected from both these effects, for Rb and Cs – with large fine-structure splittings – we see large polarization signals; for potassium – with a significantly smaller fine-structure splitting – we see a smaller polarization signal.

F. Nature of Optical Pumping

Optical pumping of spin is characterized as "depopulation" or "repopulation" pumping.[35] In the depopulation limit, the excited-state polarization state is completely randomized prior to decay to the ground state. In the repopulation limit the atomic polarization is conserved in the excited state. These two limits will lead to different

spin-state distributions, as shown in Figure 5.8. For a free ^{85}Rb atom driven on the $^2S_{1/2} \rightarrow {}^2P_{1/2}$ transition, depopulation pumping will result in (semi)dark states for both the $F = 2$ and $F = 3$ manifold. Repopulation pumping will produce a dark state in the $F = 3$ but a bright state in the $F = 2$ manifold.

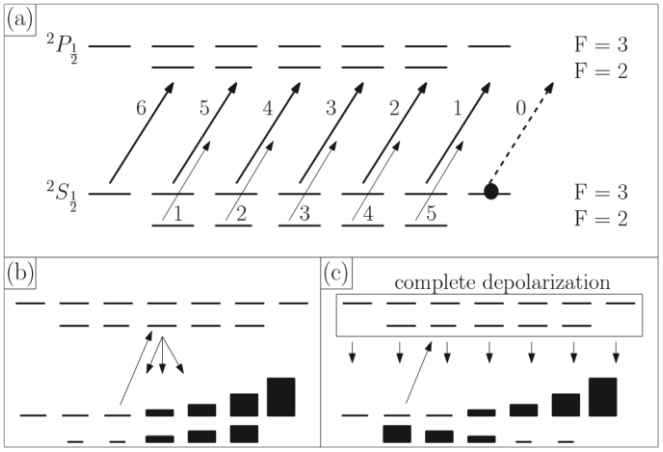

Figure 5.8. Schematic of ^{85}Rb optical pumping. Panel (a) shows the relative line strengths of σ^+ transitions of the $^2S_{1/2} \rightarrow {}^2P_{1/2}$ transition in the limit that the upper level hyperfine structure is unresolved.[36] Panels (b) and (c) show the expected populations in the cases of repopulation and depopulation pumping, respectively, as discussed in the text.

After optical pumping we can sweep an RF field to depolarize the ground-state population. By monitoring the resulting changes in the optical signal we can distinguish between the two cases shown in Figure 5.8. As previously reported in Ref.[28], the polarization signal P of ^{85}Rb shifts in opposite directions for RF depolarization of the $F = 2$ and $F = 3$ levels. This indicates that the pumping is predominantly repopulation pumping. Similar behavior was seen for ^{87}Rb, indicating that it also undergoes repopulation pumping. Cs and K were not measured in this manner.

For comparison, it was previously reported that optical pumping of the spin of cesium atoms in solid helium was predominantly repopulation pumping[18]; however, rubidium atoms in solid helium underwent depopulation pumping.[37]

G. Comparison with Argon

In prior work, the spectra of alkali atoms trapped in argon matrices exhibited multiple absorption peaks, in groups of "triplets".[21,24,25] In those experiments each triplet was attributed to the crystal-field interaction splitting the threefold degeneracy of the excited-state *p* orbital.

The bleaching results presented in Section III B suggest that the crystal-field splitting of the excited *p* orbital in parahydrogen is too small to resolve. Our interpretation is that excited-state alkali atoms in parahydrogen experience a smaller crystal-field interaction than in argon. This may be the reason why the spin polarization signals seen for rubidium in parahydrogen are an order of magnitude larger than the largest signals reported for rubidium in argon.[25]

V. Longitudinal Spin Relaxation

We can measure the longitudinal relaxation time, T_1, by observing the decay of the polarization P over time. The T_1 of rubidium atoms in parahydrogen was previously reported in Ref.[27] It depends strongly on the orthohydrogen fraction in the crystal, with longer T_1 times at lower orthohydrogen fractions. T_1 is on the order of 1 s at ortho fractions $\lesssim 10^{-2}$ and magnetic fields $\gtrsim$ 10 G. At lower magnetic fields, T_1 is considerably shorter. We did not systematically measure the T_1 of Cs and K at high

ortho fractions, but observed T_1 times on the order of 1 s at low ortho fractions. Cs showed a similar strong dependence on the magnetic field, with T_1 shorter at magnetic fields $\lesssim$ 10 G, and saturating at higher fields.

What processes limit T_1 and whether longer times might be achieved is not understood at this time. Our primary interest at present is in the ensemble transverse relaxation time T_2^*. As the measured $T_1 \gg T_2^*$, longitudinal relaxation does not play a significant role in limiting T_2^*.

VI. Ensemble Transverse Relaxation Time

We measure the ensemble transverse spin relaxation time (T_2^*) with free-induction-decay (FID) measurements, as well as other methods detailed in Ref.[28] After optically pumping the spin state of the atoms, we apply a short RF pulse to induce Larmor precession and observe the resulting oscillations in the polarization signal. Because different isotopes typically have different g factors, we can frequency-select a single isotope with the RF pulse, allowing us to measure the FID signals of the different isotopes separately.

For the case of Cs, we use a mostly RHC pump-probe beam at 846 nm whose intensity and waist are about 10^3 mW/cm^2 and 200 μm, respectively. This beam passes through the center of the crystal just above the RF coil and is subsequently focused onto a fast photodiode. The RF coil is about 0.5 cm away from the front surface of the crystal. DC bias magnetic fields ranging from a few gauss to ~80 G are applied at ~45 degrees relative to the pump beam direction. We pump the atoms for ~150 ms which creates magnetization along the direction of the DC bias field. Then we apply a short (and hence

spectrally broadband) RF pulse, which induces Larmor precession. We high-pass-filter the pump beam signal from the photodiode to obtain the time-varying free-induction-decay signal as shown in Figure 5.9. Rubidium and potassium are measured in a similar manner.

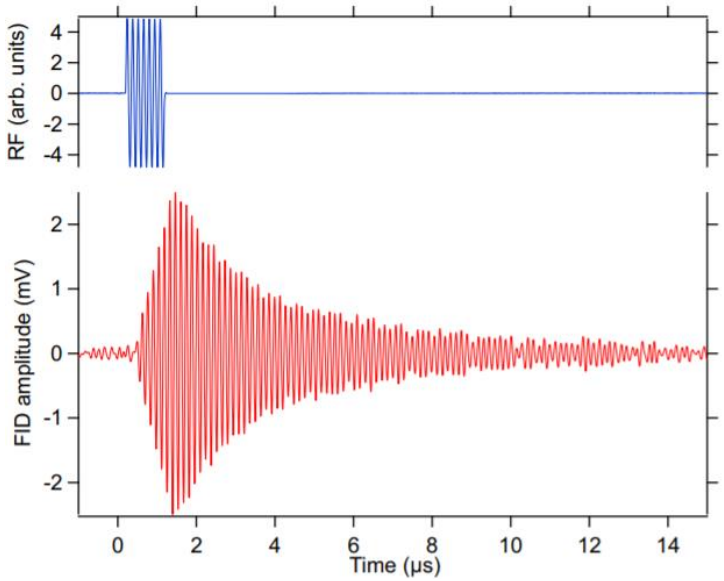

Figure 5.9. ^{133}Cs FID signal, taken at a bias field of 21 G, as described in the text. The FID is excited by a 1 μs pulse, as shown in the figure. A fit to an exponentially decaying sinusoid gives a 3 μs T_2^*.

In the case of Cs, we have made FID measurements over a range of Larmor frequencies from 0.7 to 8 MHz. All return similar values of $T_2^* \approx 3\ \mu$s. At these fields, the nonlinear Zeeman effect is sufficiently small that the different Larmor precession superposition states are unresolved.[38]

This is not the case for ^{39}K, whose much smaller hyperfine splitting[38] results in a much larger splitting between the different Zeeman states. The Zeeman structure of ^{39}K is shown in Figure 5.10. A typical FID signal for potassium is shown in Figure 11. The beating of the different Larmor superposition states makes fitting the decay to a

damped sinusoid impractical. Instead, we Fourier-transform the FID signal and fit the resulting spectral peaks. From their full width at half maximum (FWHM), we determine T_2^* from the relationship $T_2^* = (\pi \times \text{FWHM})^{-1}$, where FWHM is expressed in cycles per unit time (e.g., Hz). From the spectrum, we determine that the four peaks observed are from the $F = 2$ hyperfine manifold of ^{39}K; the shifts of ^{40}K, ^{41}K, and the $F = 1$ manifold of ^{39}K are sufficiently large that their Larmor precession transitions would be spectrally resolved.[38]

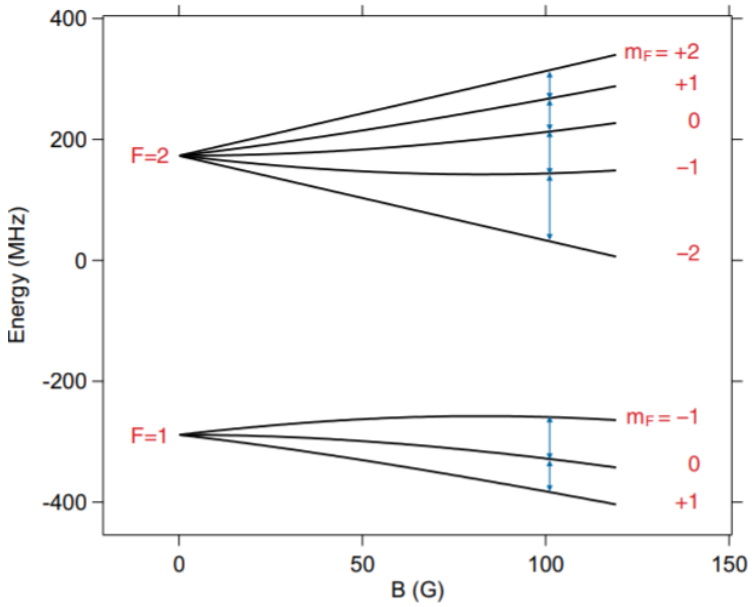

Figure 5.10. ^{39}K Zeeman structure, calculated from Ref.[39] The energy levels are labeled by their low-field quantum numbers. Superposition states of levels differing by $\Delta m_F = 1$ (indicated by arrows) give rise to Larmor precession.

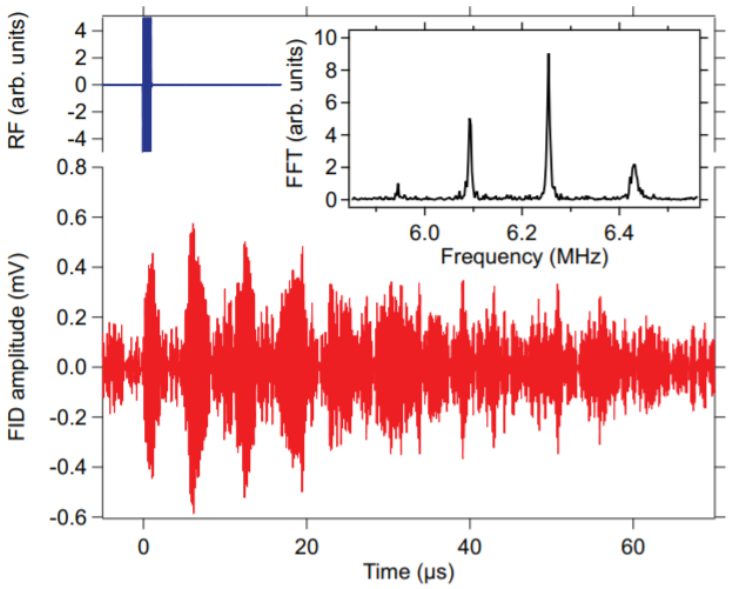

Figure 5.11. ^{39}K FID signal, taken at a bias field of 9 G, as described in the text. On this scale, the individual oscillations of the RF pulse and FID signal are not visible, but their overall envelopes can be observed. The FID signal shows clear beating. The inset shows the Fourier transform (magnitude squared) of the FID signal. Fitting the largest peak to a Lorentzian line shape gives a 6 kHz full width at half maximum, which corresponds to a 53 μs T_2^*. From left to right, the four peaks correspond to superpositions of $|m_F = +2\rangle$ and $|m_F = +1\rangle$; +1 and 0; 0 and −1; and −1 and −2.

We note that the measured T_2^* for ^{39}K is over an order of magnitude longer than for ^{133}Cs. These differences are discussed in Section VI A.

At sufficiently low magnetic fields ($\lesssim$ 2 G) Rb FID exhibits a single line, similar to Cs. At "intermediate" fields, the different Larmor superposition states cannot be fully resolved, but their splitting leads to a decrease in the FID time. At still higher fields ($\gtrsim$ 40 G) beating is clearly observed (as in the case of potassium data shown in Figure 5.11). We present the higher-field data below in Section VI B; for now we concern ourselves with the low-field limit.

We measured the Rb FID time for Rb densities from 10^{17} to 10^{18} cm^{-3}, and saw no variation to within ±15%. Similarly, the Rb FID time showed no dependence on the ortho fraction in the crystal over a range from 5×10^{-5} to 1×10^{-3}, to within ±10%.

Much like Rb, we did not see any dependence of Cs FID decay on Cs density or ortho fraction. We observe no dependence on the Cs density (to within ±15%) over the range from 1×10^{16} to 1×10^{17} cm^{-3}. We observe no dependence on the ortho fraction (to within ±10%) over a range from 3×10^{-5} to 1×10^{-3}. For Cs, T_2^* showed little dependence on the substrate temperature at the time of crystal growth.

We note that for all species, the FID frequency is consistent with the applied magnetic field and the free-atom g factor.[38] However, because we do not know the applied magnetic field accurately, all we can say is that the g factor in the crystal matches the free-atom case to within ±20%. We have verified that magnetic-field gradients do not play a significant role in the T_2^* measurements presented here: we tested for gradients by varying the size of the sample (by growing thicker and thinner crystals, and by changing the probe beam diameter).

A. T_2^* for Different Species

Figure 5.12 shows the measured T_2^* values, expressed as a FWHM linewidth for our measured species.

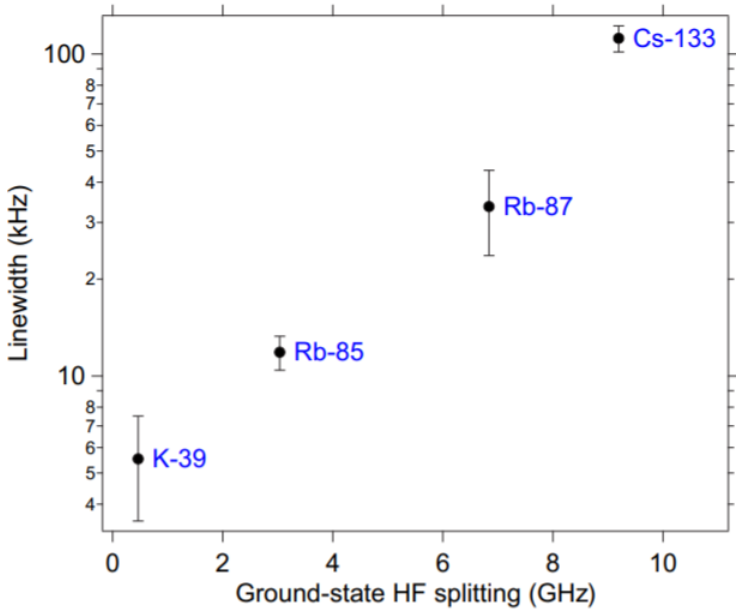

Figure 5.12. T_2^*, expressed as a linewidth $= 1/(\pi T_2^*)$, for the species measured. The linewidths are plotted as a function of the ground-state hyperfine splitting of each species; we believe this is the key parameter in explaining the differences in the observed linewidths, as discussed in the text. Rb and Cs data were taken at sufficiently low fields that the different Larmor precession frequencies were unresolved; the ^{39}K data were taken at similar fields but with resolved structure; the number plotted is the linewidth of the $F = 2$, $|m_F = 0\rangle$ and $|m_F = -1\rangle$ Larmor superposition. All data points were taken in the short-pulse limit. The unresolved splittings of the different Larmor precession states may be artificially broadening the ^{85}Rb linewidth at the level of 10%; less for ^{87}Rb and ^{133}Cs.

The T_2^* times are limited by inhomogeneous broadening, as we have measured spin-echo T_2 times to be 1 ms for rubidium and cesium (we have not measured spin-echo signals in potassium due to its small polarization signal).

We expect that the inhomogeneous broadening which limits T_2^* is primarily due to electrostatic-like interactions with the host matrix.[28] As such, we would expect the energy level shifts to resemble those of the Stark effect. Considering the Stark effect for a ground-state alkali atom, there is a scalar component which shifts all $|F, m_F\rangle$ levels the same, and a tensor component which shifts different F and m_F levels differently. It

is this tensor component which will cause inhomogeneous broadening for Larmor precession. The tensor component is zero in second-order perturbation theory, and only appears in third-order perturbation theory including two electric dipole couplings and one hyperfine interaction.[40-42] Consequently, we would expect atoms with larger hyperfine splittings to have larger shifts due to their interaction with the matrix. In the case of a polycrystalline matrix with inhomogeneous trapping sites, this would result in larger inhomogeneous broadening. This is qualitatively consistent with the observations presented in Figure 5.12.

A more sophisticated and quantitative model based on the rigorous electron spin resonance (ESR) Hamiltonian is presented in Section VII A.

B. T_2^* for Different Larmor Superposition States

At sufficiently high magnetic fields, we can spectrally resolve the different Larmor precession states of rubidium, similarly to the case of potassium shown in Figure 5.11. Figure 5.13 shows data for both the $F = 3$ manifold of ^{85}Rb and the $F = 2$ manifold of ^{87}Rb. Larmor precession arises from all superpositions of states that differ by $\Delta m = 1$.

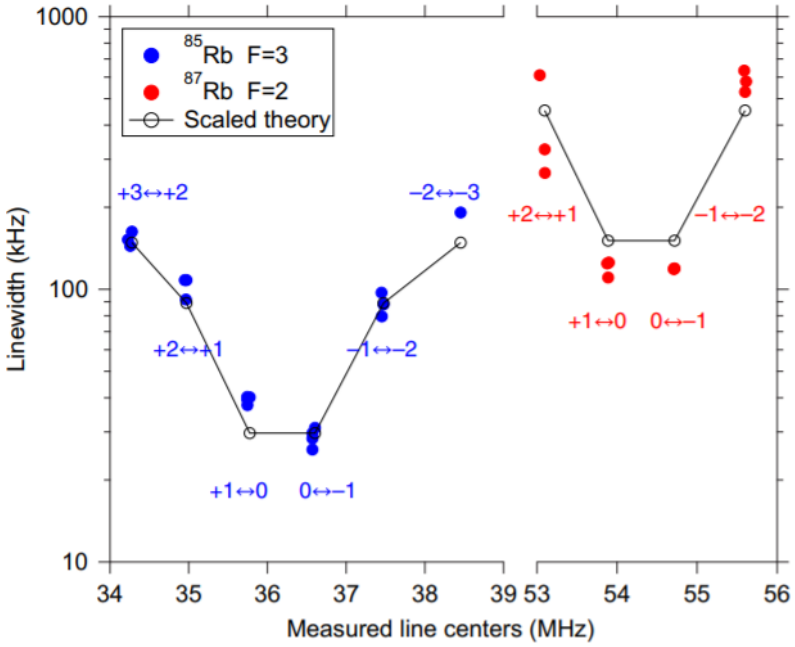

Figure 5.13. The FWHM linewidths of the Rb Larmor precession superposition states at a magnetic field of 80 G, as discussed in the text. The data are labeled by the m_F states of their corresponding Larmor superposition. Plotted alongside the data is the theory of Section VII A, scaled by a factor of 1.35.

As observed in Section VI A at low fields, the ^{87}Rb linewidths are larger than those of the corresponding superpositions in ^{85}Rb. For both isotopes, the linewidths are larger for superposition states of higher m_F. Qualitatively, this is as one would expect for inhomogeneous broadening from electrostatic interactions: tensor Stark shifts scale as m_F^2.[41,43]

The data in Figure 5.13 are presented alongside the quantitative theory of Section VII A. The theory reproduces the dependence of the linewidth on both isotope and m_F. The significant isotope effect is mainly due to the hyperfine anisotropy of ^{87}Rb, which is 3.4 times larger than that of ^{85}Rb (see Table 5.4) owing to the difference in the nuclear magnetic moments. The m_F scaling arises from the tensor nature of the anisotropic hyperfine interaction, as presented in Section VII A.

More subtle features of the spectrum, such as why the Larmor precession linewidth of the (−1,0) superposition of $F = 3$ ^{85}Rb is consistently narrower than the (+1,0) superposition, are not understood. The low signal-to-noise ratio of the potassium polarization signal does not permit similar comparisons of different Larmor precession states, and we did not take Cs data at sufficiently high field to resolve the different superpositions.

C. Temperature Dependence

We measured rubidium T_2^* in the low-field limit at different crystal temperatures. The Rb linewidth showed no dependence on the crystal temperature over a range from 3 to 4.2 K, to within ±30%.

We do, however, see a dependence of the FID decay time on temperature for Cs. We warmed a Cs-doped crystal (grown at 3.2 K substrate temperature, with our "base" ortho fraction) crystal to 4 K and held it there overnight to allow the crystal to anneal. This produced, surprisingly, longer free-induction decay times by roughly 40%. Cooling back to our base temperature of 3 K returned our original FID times. Subsequent cycling between 3 and 4 K consistently showed longer FID decay times at the elevated temperature. These data are presented in Figure 5.14.

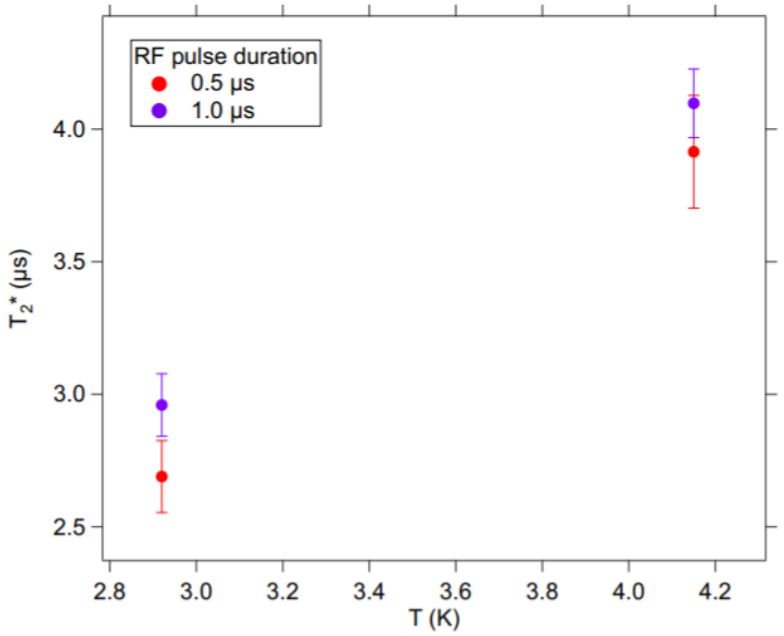

Figure 5.14. Cs FID T_2^* measured at different temperatures. Each point is an average of multiple measurements over multiple temperature cycles of the same sample; the warmer temperatures consistently gave longer FID decay times.

The link between elevated matrix temperature and longer T_2^* times is not understood, but we speculate that it may be due to larger amplitude atomic motion (on a timescale much shorter than T_2^*) reducing the anisotropy of individual trapping sites and/or reducing the inhomogeneities between different trapping sites, similarly to "motional narrowing" effects observed in NMR.[44]

VII. Theory

A. Inhomogeneous Broadening due to Hyperfine Interactions

In this section, we present a theoretical analysis of inhomogeneous broadening of hyperfine transitions of ^2S atoms embedded in an inert matrix. The theory is based on the hyperfine Hamiltonian commonly used to calculate powder ESR spectra,[45-47]

which we extend to the low-field limit of interest to the matrix isolation experiments described here. The primary focus will be on alkali-metal atoms trapped in solid *p*-H_2, although our theory is sufficiently general to be applicable to any *S*-state atom in an inert matrix.

To model the broadening of the hyperfine transitions $F, m_F \leftrightarrow F', m_F'$, we assume that it is due to the tensor matrix shifts of the hyperfine levels caused by the interaction with the host matrix. As shown below, the tensor matrix shifts depend on the orientation of the principal axes of the hyperfine tensor **A** with respect to the magnetic-field axis. We derive analytical expressions for these shifts as a function of the orientation angle and then calculate them for all possible orientations to obtain the linewidth of the hyperfine transitions of an atom in a polycrystalline (powder) matrix. Our results establish a direct connection between the experimentally observable transition linewidths and the elements of the hyperfine tensor, calculated *ab initio* for a range of alkali-H_2 complexes as described in Section VII B. At the end of this section, we compare our calculated transition linewidths with experiment, finding good semiquantitative agreement, and discuss the limitations of our model.

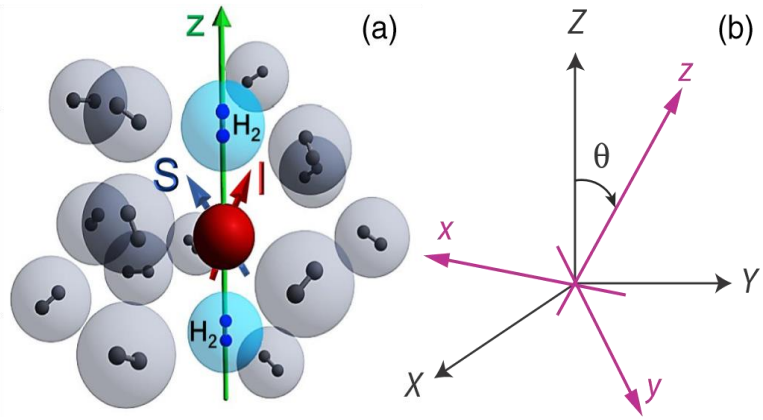

Figure 5.15 (a) A schematic representation of our model for the alkali-metal trapping site in a *p*-H_2 matrix. The red circle represents the central alkali-metal atom; the blue circles represent the axial *p*-H_2 molecules taken into account in the present calculations; the gray circles are all other *p*-H_2 molecules. The electron and nuclear spins of the alkali-metal atom are indicated by arrows. (b) Space-fixed (black) and principal-axes (magenta) coordinate systems. The *Z* axis of the space-fixed system is defined by the direction of the external magnetic field. The positions of the principal axes *x*, *y*, *z* in the space-fixed coordinate system are defined by the Euler angles $\Omega = \varphi, \theta, \chi$.

We begin with the ESR Hamiltonian for a central $S = 1/2$ atom embedded in a solid *p*-H_2 host matrix,[45,46,48] as illustrated in Figure 5.15 (a),

$$H_{\mathrm{hf}} = A_a \boldsymbol{S}\cdot\boldsymbol{I} + 2\mu_0 \boldsymbol{S}\cdot\mathbf{g}\cdot\boldsymbol{B} + \boldsymbol{S}\cdot\mathbf{A}\cdot\boldsymbol{I} + \sum_{\alpha}\boldsymbol{S}\cdot\mathbf{A}^{\alpha}\cdot\boldsymbol{I}^{\alpha}, \tag{5.1}$$

where $\boldsymbol{S}$ and $\boldsymbol{I}$ are the electron and nuclear spins of the central atom **A**, is the hyperfine tensor on the central nucleus of interest, and $\mathbf{A}^{\alpha}$ are the hyperfine tensors on the surrounding nuclei bearing nuclear spin angular momenta $\boldsymbol{I}^{\alpha}$ (we neglect this final term in the following calculations). In Eq. (5.1), **g** is the *g* tensor of the central atom, [45,46,48] assumed here to be proportional to the unit matrix, $\mathbf{g} = g_e\mathbf{1}$, where $g_e \backsimeq 2$ is the electron *g* factor. In defining the hyperfine tensor, we separate out the contribution due to the hyperfine structure of the free atom $A_a\boldsymbol{S}\cdot\boldsymbol{I}$, which allows us to define unperturbed atomic states $|F, m_F\rangle$ in the weak-field limit. Here, $\boldsymbol{F} = \boldsymbol{I} + \boldsymbol{S}$ is the total angular momentum of the atom, and m_F is the projection of $\boldsymbol{F}$ on the space-fixed quantization axis defined by the external magnetic field.

The hyperfine tensor accounts for the modification of the atomic hyperfine structure due to the interaction with the matrix, and can be decomposed as

$$\boldsymbol{A} = A_{\mathrm{iso}}(R)\mathbf{1} + \mathbf{T}, \tag{5.2}$$

where the scalar constant A_{iso} describes the isotropic (Fermi contact) interaction and the traceless tensor **T** describes the anisotropic hyperfine interaction. Note that the isotropic hyperfine interaction does not affect the splitting between the m_F sublevels of the same F state, so we do not consider this term in the following. However, it must be taken into account when considering the transitions involving hyperfine states of different F. We further assume that matrix perturbations are weak, i.e., $A_a \gg T_{ij}$.

The third term in Eq. (5.1) can be written as a sum over Cartesian components of vector operators ***S*** and ***I***:

$$H_{\mathrm{ahf}} = \sum_{i,j=x,y,z} S_i T_{ij} I_j \,. \tag{5.3}$$

In general, the form of this operator depends on the choice of the coordinate system. Here, we choose the principal axes (PAs) of the tensor **T** as coordinate axes. The orientation of the PAs with respect to space-fixed axes defined by the external magnetic field is specified by the Euler angles $\Omega = (\varphi, \theta, \chi)$ as shown in Figure 5.15 (b). In this coordinate system, **A** and **T** take the diagonal form and Eq. (5.3) reduces to

$$H_{\mathrm{ahf}}^{\mathrm{PA}} = T_{xx} S_x I_x + T_{yy} S_y I_y + T_{zz} S_z I_z, \tag{5.4}$$

where T_{xx}, T_{yy}, and T_{zz} are the PA components of **T** calculated *ab initio* as described in the next section.

In first-order perturbation theory, the energy shift of the atomic level $|F, m_F\rangle$ due to the interaction with the host matrix is given by the diagonal matrix element of the perturbation

$$\Delta E_{F m_F} = \langle F m_F | H_{\mathrm{ahf}}^{\mathrm{PA}} | F m_F \rangle. \tag{5.5}$$

To evaluate the matrix elements in Eq. (5.5) in terms of the PA components of the hyperfine tensor, we express the Hamiltonian via the spherical tensor operators expressed in the space-fixed frame [see Figure 15 (b)]. Following Appendix A of Ref.[49] and keeping in mind that $\bar{T} = \frac{1}{3}\left(T_{xx} + T_{yy} + T_{zz}\right) = 0$, we have

$$H_{\mathrm{ahf}}^{\mathrm{PA}} = \sum_{p=-2}^{2} \left[\frac{1}{2}\left(T_{xx} - T_{yy}\right)\left[D_{\mathrm{p},2}^{2}(\Omega) + D_{\mathrm{p},-2}^{2}(\Omega)\right]\right.$$

$$\left. + \frac{1}{\sqrt{6}}\left(2T_{zz} - T_{xx} - T_{yy}\right)D_{\mathrm{p},0}^{2}(\Omega)\right][\boldsymbol{I} \otimes \boldsymbol{S}]_{p}^{(2)}, \qquad (5.6)$$

where $[\boldsymbol{I} \otimes \boldsymbol{S}]_{p}^{(2)}$ is a rank-2 tensor product of two rank-1 spherical tensor operators and $D_{\mathrm{p},2}^{2}(\Omega)$ are the Wigner D functions of the Euler angles that define the orientation of the PA coordinate system relative to the space-fixed axes [see Figure 15 (b)].

In the case of axial symmetry assumed below,[46,48] $T_{xx} = T_{yy}$ and the expression (Eq. 5.6) simplifies to

$$H_{\mathrm{ahf}}^{\mathrm{PA}} = \frac{2}{\sqrt{6}}\Delta T \sum_{p=-2}^{2} D_{\mathrm{p},0}^{2}(\Omega)\,[\boldsymbol{I} \otimes \boldsymbol{S}]_{p}^{(2)}, \qquad (5.7)$$

where we define $\Delta T = T_{zz} - T_{xx}$ as the hyperfine anisotropy. The matrix shifts in Eq. (5.5) thus become, for a given orientation Ω of the PA coordinate system relative to the space-fixed axes,

$$\Delta E_{Fm_F}(\Omega) = \frac{2}{\sqrt{6}}\Delta T \sum_{p=-2}^{2} D_{\mathrm{p},0}^{2}(\Omega)\left\langle Fm_F\middle|[\boldsymbol{I} \otimes \boldsymbol{S}]_{p}^{(2)}\middle|Fm_F\right\rangle. \qquad (5.8)$$

Applying the Wigner-Eckart theorem[50] to evaluate the matrix elements on the right-hand side, we find

$$\left\langle (IS)Fm_F \middle| [\boldsymbol{I}\otimes\boldsymbol{S}]^{(2)}_p \middle| (IS)F'm'_F \right\rangle = (-1)^{F-m_F}\begin{pmatrix} F & 2 & F' \\ -m_F & p & m'_F \end{pmatrix}$$
$$[(2F+1)5(2F'+1)]^{1/2} p_3(I)p_3(S)\begin{Bmatrix} I & I & 1 \\ S & S & 1 \\ F & F' & 2 \end{Bmatrix}, \qquad (5.9)$$

where the symbols in parentheses and curly brackets are 3-j and 9-j symbols, and $p_3(X) = [(2X+1)X(X+1)]^{1/2}$. For $m_F = m'_F$, the 3-j symbol in Eq. (5.9) is nonzero only when $q = 0$. Setting $D^2_{\mathrm{p},0}(\Omega) = d^2_{00}(\theta) = \frac{1}{2}(3\cos^2(\theta)-1)$ in Eq. (5.9), we obtain the angular dependence of the tensor matrix shift

$$\Delta E_{Fm_F}(\theta) = \frac{3\cos^2(\theta)-1}{\sqrt{6}}\Delta T(-1)^{F-m_F}\begin{pmatrix} F & 2 & F \\ -m_F & 0 & m_F \end{pmatrix}$$
$$[(2F+1)5(2F+1)]^{1/2} p_3(I)p_3(S)\begin{Bmatrix} I & I & 1 \\ S & S & 1 \\ F & F & 2 \end{Bmatrix}. \qquad (5.10)$$

For a polycrystalline *p*-H2 matrix, the orientation of the PA coordinate system with respect to the external magnetic field is random[45]; i.e., all possible θ angles will contribute to the linewidth. In the presence of axial symmetry, Eq. (5.10) shows that there is a distribution of matrix shifts proportional to $(3\cos^2(\theta)-1)$. The transition linewidth can then be evaluated as a difference between the maximum (2) and minimum (-1) values of the angular function $(3\cos^2(\theta)-1)$ for $\theta \in [0, \pi]$. Replacing $3\cos^2(\theta)-1 \rightarrow 3$ in Eq. (5.10), we obtain the linewidth of the atomic state $|F, m_F\rangle$ in a polycrystalline matrix

$$\Delta E_{Fm_F} = 3\sqrt{\frac{5}{6}}\Delta T(-1)^{F-m_F}(2F$$

$$+ 1)p_3(I)p_3(S)\begin{pmatrix} F & 2 & F \\ -m_F & 0 & m_F \end{pmatrix}\begin{Bmatrix} I & I & 1 \\ S & S & 1 \\ F & F & 2 \end{Bmatrix}. \quad (5.11)$$

The 3-j symbol on the right is equal to $(-1)^{F-m_F}[(2F+3)(2F+2)(2F+1)2F(2F-1)]^{-1/2}[3m_F^2 - F(F+1)]$.[50] Eq. (2.11) thus establishes that for a given alkali-metal atom (fixed I, S, and ΔT), the linewidth of the F, m_F level scales with F and m_F as

$$\Delta E_{Fm_F} \propto [(2F+3)(2F+2)(2F+1)2F(2F-1)]^{-1/2}$$

$$(2F+1)\begin{Bmatrix} I & I & 1 \\ S & S & 1 \\ F & F & 2 \end{Bmatrix}[3m_F^2 - F(F+1)]. \quad (5.12)$$

Given the broadening of the individual hyperfine levels (Eq. 5.11), we can calculate the inhomogeneous transition linewidth assuming that the hyperfine levels F, m_F and F', m_F' involved in the magnetic dipole transition are broadened by the interaction with the matrix. Both of the hyperfine levels experience tensor matrix shifts according to Eq. (5.11). Taking the difference of the F, m_F and F', m_F' level shifts given by Eq. (5.11) and averaging the result over θ as described above, we obtain the inhomogeneous linewidth of the $F, m_F \leftrightarrow F', m_F'$ transition

$$\Delta E_{F,m_F\leftrightarrow F',m_F'} = 3\sqrt{5/6}p_3(I)p_3(S)\Delta T\left[(-1)^{F-m_F}(2F\right.$$

$$+ 1)\begin{pmatrix} F & 2 & F \\ -m_F & 0 & m_F \end{pmatrix}\begin{Bmatrix} I & I & 1 \\ S & S & 1 \\ F & F & 2 \end{Bmatrix}$$

$$-(-1)^{F'-m_F'}(2F'+1)\begin{pmatrix} F' & 2 & F' \\ -m_F' & 0 & m_F' \end{pmatrix}\begin{Bmatrix} I & I & 1 \\ S & S & 1 \\ F' & F' & 2 \end{Bmatrix}\Bigg]. \tag{5.13}$$

For the transitions involving different m_F sublevels of the same F state of interest here, $F = F'$ and Eq. (5.13) simplifies to [omitting the irrelevant overall phase $(-1)^{F-m_F}$]

$$\Delta E_{F,m_F\leftrightarrow F',m_F'} = 3\sqrt{5/6}p_3(I)p_3(S)(2F+1)\Delta T$$

$$\left[\begin{pmatrix} F & 2 & F \\ -m_F & 0 & m_F \end{pmatrix} - (-1)^{m_F-m_F'}\begin{pmatrix} F & 2 & F \\ -m_F' & 0 & m_F' \end{pmatrix}\right]\begin{Bmatrix} I & I & 1 \\ S & S & 1 \\ F & F & 2 \end{Bmatrix}. \tag{5.14}$$

Table 5.2 presents the theoretical linewidths of m_F-changing transitions in different alkali-metal atoms. The linewidths are calculated using Eq. (5.14) based on the *ab initio* values of the hyperfine anisotropy ΔT from Section VII B. We observe good semiquantitative agreement between theory and experiment across all species and isotopes, confirming that anisotropic hyperfine interactions are the dominant source of broadening.

Table 5.2. Calculated linewidths (in kHz) for the $F, m_F \leftrightarrow F', m_F'$ transitions in different alkali-metal isotopes. The theoretical values are computed using Eq. (5.14) based on the *ab initio* hyperfine anisotropies ΔT calculated as described in Section VII B. The theoretical $m_F \leftrightarrow m_F'$ transition linewidths are invariant with respect to the simultaneous sign reversal $m_F \rightarrow -m_F$ and $m_F' \rightarrow -m_F'$; thus only positive values are presented.

Transition ($m_F \leftrightarrow m_F'$)	Theory
^{39}K; $F = 2$:	
$2 \leftrightarrow 1$	6.19
$1 \leftrightarrow 0$	2.06
^{85}Rb; $F = 3$:	
$3 \leftrightarrow 2$	109.6
$2 \leftrightarrow 1$	65.78
$1 \leftrightarrow 0$	21.93
^{87}Rb; $F = 2$:	
$2 \leftrightarrow 1$	334.4
$1 \leftrightarrow 0$	111.5

^{133}Cs; $F = 4$:	
$4 \leftrightarrow 3$	546.27
$3 \leftrightarrow 2$	390.18
$2 \leftrightarrow 1$	234.11
$1 \leftrightarrow 0$	78.04

For the same alkali-metal isotope, Eq. (5.14) predicts F-independent broadening of the $F, m_F \leftrightarrow F', m_F'$ transitions. Within the same F manifold, the linewidths are expected to increase linearly with m_F and to be independent of its sign, again consistent with the trend observed experimentally (Figure 5.13). Significantly, Eq. (5.12) predicts that $+m_F \rightarrow -m_F$ transitions will have dramatically reduced inhomogeneous broadening, as these pairs of levels are (to first order) shifted identically by the anisotropic hyperfine interaction. Experimentally, such transitions are found to have much smaller linewidths than the Larmor-precession transitions, as discussed in Section VIII.[28]

While our theoretical results are in nearly quantitative agreement with experiment, small disagreements remain. We suspect these disagreements are due to differences between our model trapping site and the true trapping site. To compensate for this, we scale our theoretical Rb anisotropies by a single constant factor (common to both isotopes). This scaled calculation is presented alongside experimental data in Figure 5.13. With this scaling, we see nearly quantitative agreement with experiment.

Additional work is warranted to provide more detailed models of trapping sites, which are different not only in their orientations, but also in their geometries and coordination numbers,[51] bringing about additional broadening mechanisms. A theoretical study of these mechanisms would require a detailed investigation of trapping site structure (using, e.g., quantum Monte Carlo simulations) combined with extensive

ab initio calculations of the hyperfine and *g*-tensor elements corresponding to different site structures.

B. *Ab initio* Calculations of Alkali-H_2 Potentials and Hyperfine Interactions

As discussed in Section VII A, the linewidths of alkali-metal atoms trapped in solid *p*-H_2 are determined by the hyperfine anisotropy ΔT. To estimate this quantity, we adopt a minimal model for the alkali-metal trapping site illustrated in Figure 5.15. In this axially symmetric model, commonly used in theoretical simulations of molecular ESR spectra,[46,48] the central alkali-metal atom A is surrounded by two H_2 molecules in the linear configuration H_2-A-H_2. We then use the eigenvalues of the hyperfine tensor calculated *ab initio* at the equilibrium A-H_2 geometry R_e to approximate the hyperfine anisotropy ΔT defined in Section VII A above.

To estimate the equilibrium configuration of the axial trapping site, we carried out *ab initio* calculations of the alkali-H_2 interaction potentials using the unrestricted coupled cluster method with singles, doubles, and perturbative triples [UCCSD(T)],[52] as implemented in MOLPRO.[53] The aug-cc-pVQZ[54] and Jorge-AQZP[55] one-electron basis sets were employed for H and K atoms, respectively. For Rb and Cs atoms, n core electrons were replaced with the ECPnMDF relativistic effective potential ($n = 28$ for Rb and $n = 46$ for Cs). The remaining valence electrons of Rb and Cs were described with the uncontracted [13*s*10*p*5*d*3*f*] and [12*s*11*p*5*d*3*f*] basis sets,[56] respectively. The alkali-H_2 interaction potentials were corrected for the basis set superposition error[57] and expressed in Jacobi coordinates R and θ, where R is the interatomic distance between an A atom and the H_2 center of mass, and θ is the angle between the A-H_2 vector R and

the H_2 interatomic axis. The two-dimensional interaction energies were averaged over 19 equally spaced values of $\theta \in [0,\ 90^o]$ using the hindered rotor model[58] and fitted with cubic splines to produce the isotropic potentials shown in Figure 5.16.

As shown in Section VII A, the hyperfine tensor on the nucleus of interest has the isotropic ($A_{\rm iso}\mathbf{1}$) and anisotropic ($\mathbf{T}$) components, which can be expressed as the Fermi contact and spin-dipolar terms in SI units:

$$A_{\rm iso} = \frac{g_N e^2 \hbar}{6\pi\epsilon_0 c^2 m_e m_p} |\Psi(\mathbf{r})|^2, \tag{5.15}$$

$$\mathbf{T} = \frac{g_N e^2 \hbar}{16\pi^2\epsilon_0 c^2 m_e m_p} \left\langle \frac{\mathbf{r}^t \cdot \mathbf{r} \cdot \mathbf{1} - 3\mathbf{r} \cdot \mathbf{r}^t}{r^3} \right\rangle, \tag{5.16}$$

where g_N is the nuclear g factor, e is the electron charge, $\hbar$ is reduced Planck constant, ϵ_0 is vacuum permittivity, c is the speed of light, m_e and m_p are electron and proton masses, $|\Psi(\mathbf{r})|^2$ is the electron spin density at the nucleus, and the expectation value $\langle ... \rangle$ is that of the spin-dipolar interaction. We carried out *ab initio* calculations of the spin density $|\Psi(\mathbf{r})|^2$ and the spin-dipolar interaction on the alkali-metal nucleus using the UCCSD(T) method and all-electron fully uncontracted basis sets augmented by the large-exponent *s* functions in CFOUR.[59] The aug-cc-pwCV5Z[60] and relativistic ANO-RCC[61] basis sets augmented with four *s* functions obtained by multiplying the largest exponent by a factor of 4 were used for H and alkali-metal atoms, respectively, as described in our previous work on alkali-He hyperfine interactions.[62,63] We carried out test calculations of the hyperfine tensor for ^{1}H, ^{39}K, ^{85}Rb, ^{87}Rb, and ^{133}Cs with the corresponding nuclear spins I = 1/2, 3/2, 5/2, 3/2, and 7/2.

To validate the level of theory used to predict the anisotropic component of the hyperfine tensor, we also calculated its isotropic component A_{iso} in Eq. (2.15). Table 5.3 compares the calculated and experimental values of the hyperfine constants for ^{1}H and the alkali-metal atoms. For the light ^{1}H, ^{7}Li, and ^{39}K isotopes, the calculated and experimental values are in good agreement. For Rb isotopes, we observe significant deviations from experiment because of the relativistic properties of the core electrons, which are not accounted for in our *ab initio* calculations. It is important to note that the isotropic part of hyperfine interaction depends on the electron density at a nucleus, while the anisotropic part is defined by the spin-dipolar interaction, which is much less affected by the electron density of the core electrons. Therefore, we expect a much higher accuracy in our anisotropic hyperfine constant calculations on heavy alkali-metal isotopes.

Table 5.3. Calculated isotropic hyperfine interaction constants (in MHz) compared with experiment for atomic hydrogen (Ref.[64]) and alkali-metal atoms (Ref.[38]).

Atom	This work	Experiment
^{1}H	1418	1420.405 726(3)
^{7}Li	399	401.752 043 3(5)
^{39}K	221	230.859 860 1(3)
^{85}Rb	848	1011.910 813(2)
^{87}Rb	2875	3417.341 306 42(15)

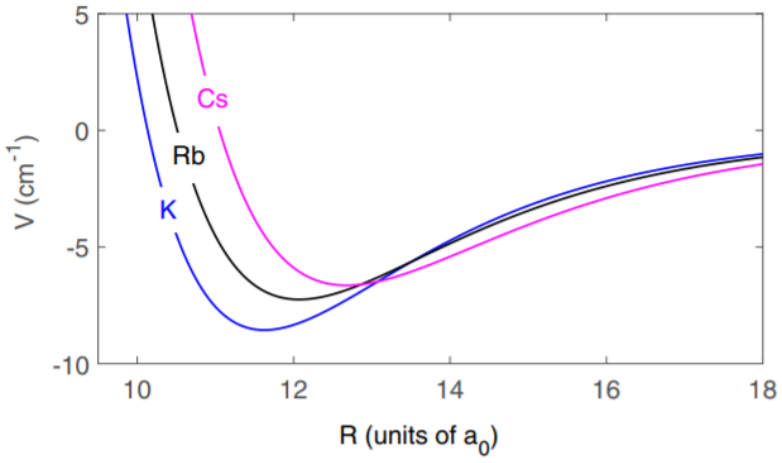

Figure 5.16. *Ab initio* isotropic interaction potentials for K, Rb, and Cs atoms with H_2.

Figure 5.16 shows the radial dependence of the isotropic part of our *ab initio* alkali-H_2 interaction potentials. We note that the potential minima of all alkali-H_2 complexes occur at much larger distances than the H_2-H_2 potential minimum, and also they are much larger than the 7 a_0 nearest-neighbor spacing in zero-pressure solid hydrogen.[65] This "mismatch" in sizes may explain the existence of multiple trapping sites in the solid,[51] as there may be multiple different configurations of similar (or lower) energy than a simple interstitial or single-substitution site. The well depths of the potentials are $D_e = -8.5$ cm^{-1} at 11.7 a_0 for K-H_2, $D_e = -7.2$ cm^{-1} at 12.1 a_0 for Rb-H_2, and $D_e = -6.6$ cm^{-1} at 12.5 a_0 for Cs-H_2.

Table 5.4. Principal-axis components (T_{xx} , T_{yy}, T_{zz}) of the hyperfine tensor (in kHz) for the H_2-A-H_2 complexes. The hyperfine anisotropy $\Delta T = T_{zz} - T_{xx}$. The value of R is fixed at the equilibrium distance R_e of the corresponding A-H_2 interaction potential (see Figure 5.16).

Transition ($m_F \leftrightarrow m_F'$)	(T_{xx} , T_{yy}, T_{zz})
H_2-^{39}K-H_2	(-1.8, -1.8, 3.7)
H_2-^{85}Rb-H_2	(-29.2, -29.2, 58.5)
H_2-^{87}Rb-H_2	(-99.1, -99.1, 198.2)
H_2-^{133}Cs-H_2	(-138.7, -138.7, 277.5)

In Table 5.4, we report the values of anisotropic components of the hyperfine tensor for the linear H_2-A-H_2 complex at the equilibrium A-H_2 separation determined from the *ab initio* potentials plotted in Figure 5.16. In these calculations, the H_2 bond is taken to be collinear to the symmetry axis of the axially symmetric H_2-A-H_2 complex. We estimate the upper limits to the hyperfine anisotropy $\Delta T = T_{zz} - T_{xx}$ to be 5.5, 87.7, 297.3, and 416.2 kHz for ^{39}K, ^{85}Rb, ^{87}Rb, and ^{133}Cs, respectively.

VIII. Properties of Inhomogeneous Broadening from Generic Time-Symmetric Perturbations

Our measured T_2^* times for Larmor precession states agree well with the theoretical model for inhomogeneous broadening due to hyperfine interactions with an inhomogeneous host matrix, as presented in Section VII A. First-order perturbation theory – in the limit that F and m_F are good quantum numbers – finds that states of the same F and $|m_F|$ undergo identical shifts. This will be the case not only for the specific interaction Hamiltonian used in Section VII A, but for any electrostatic-like perturbation (i.e., a perturbation which is unchanged under time reversal).

Because electrostatic interactions are unchanged under time reversal, the electrostatic shift of the $|F, m_F\rangle$ and the $|F, -m_F\rangle$ level should be the same to first order. Hence, superpositions of such levels should show dramatically reduced broadening when compared to Larmor precession levels. This effect has been demonstrated in previous measurements of ^{85}Rb in parahydrogen.[28] We wish to consider the specific behavior of this phenomena in greater detail here, and compare the broadening of different superposition states.

We first construct a Hamiltonian for the known gas-phase hyperfine and Zeeman structure of the ground state of ^{85}Rb (I =5/2), working in the 12-dimensional subspace of the $^2S_{1/2}$ electronic ground state [66]. We model the crystal-field interaction as a random Hermitian matrix in this subspace, with each element a Gaussian distribution of amplitudes chosen to roughly match our observed T_2^*. We then "time-symmetrize" the matrix by adding it to a time-reversed copy of itself. We solve for the eigenvalues of the total Hamiltonian, calculate the energy differences between each pair of levels (labeled by their low-field, perturbation-free eigenvalues), and then repeat the process multiple times and calculate the standard deviation of the distribution of energy differences.

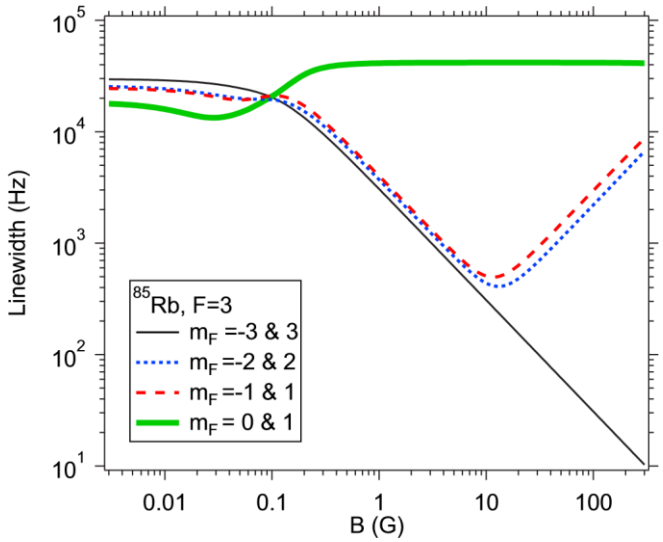

Figure 5.17. Simulation of inhomogeneous broadening for different superpositions of Zeeman levels of the F = 3 manifold of ^{85}Rb, plotted as a function of magnetic field. The simulations were for "random matrix" perturbations that were symmetric under time reversal (i.e., electrostatic-like), as explained in the text. The states are labeled by F and m_F quantum numbers; we note that these are good quantum numbers only in the limit of small magnetic fields (Zeeman shifts small compared to the hyperfine splitting) and small random matrix perturbations (small compared to the Zeeman splitting).

This simple model will capture some of the generic effects of a time-symmetric perturbation, but will miss many of the important details of the inhomogeneous broadening. The model omits the specific structure and symmetry of the trapping sites. It also emits the specific nature of the electrostatic interactions (which will cause different shifts for different m_F levels and different species, as discussed in Sections VI A, VI B, and VII A). Additionally, it has no predictive capability for the magnitude of the broadening, as the magnitude of the random matrix elements are chosen to match experiment. However, it does reveal interesting behavior which we expect will be general, as shown in Figure 5.17, which plots the simulated linewidths as a function of the applied magnetic field, for Zeeman shifts small compared to the hyperfine splitting.

As shown in Figure 5.13, ^{85}Rb ($F = 3$) has six superpositions which give rise to Larmor precession. All show roughly similar behavior in this simple calculation; in Figure 5.17 we have plotted the linewidth of a single superposition to simplify the graph. All show a linewidth which is roughly independent of the applied field. More interesting is the behavior of the other states shown. The $m_F = +3$ and -3 levels are, in the absence of the crystal field, time reversals of each other. At high magnetic fields, where the Zeeman splitting is much greater than the crystal-field interaction, this leads to a large suppression of the inhomogeneous broadening, as the perturbation by the crystal field is zero to first order. At lower fields, this "protection" is reduced as higher-order perturbations begin to play a larger role. In the low-field limit, where the crystal field is greater than the Zeeman splitting, the levels are fully mixed by the crystal-field perturbation and the protection is lost, as seen in Figure 5.17. Slightly more complex are the m_F, $-m_F$ superpositions which are not stretched states (+2 and −2, and +1 and

−1 for ^{85}Rb). In the absence of the crystal field, these states are time reversals of each other only in the low-magnetic-field limit. Hence, they show behavior similar to the stretched-state superposition at low magnetic fields, but at higher magnetic fields lose their "protection" due to the nonlinear Zeeman effect.

These simulations qualitatively agree with our experimental measurements. First, we typically find that our optical pumping signal is reduced in amplitude if we work at longitudinal magnetic fields $\lesssim$ 1 G, as discussed in Section IV C. This is qualitatively consistent with the idea that the m_F levels are fully mixed by the crystal-field perturbation at low magnetic fields. Second, in Ref.,[28] we measured the linewidth of a superposition of $|F = 3, m_F = +1\rangle$ and $|F = 3, m_F = -1\rangle$ at magnetic fields ranging from 60 to 150 G. The linewidth observed was significantly narrower than any of the Larmor precession superpositions. The linewidth increased linearly with the magnetic field over the measured range, in qualitative agreement with the model shown in Figure 5.17. From the simulation, we expect significant improvements could be obtained by working with a superposition of stretched states, and at higher fields.

IX. Discussion

The optical spin polarization signals obtained for Rb and Cs in solid parahydrogen are significantly larger than had previously been reported for alkali atoms in solid argon or neon,[25,67] but not as large as what has been observed in solid helium.[18] However, the behavior observed in Section IV B suggests that significant improvement could be obtained in an apparatus capable of colder substrate temperatures and higher parahydrogen deposition rates.

The measured T_2^* times are significantly shorter than those of cesium atoms in solid helium,[19] but are predominantly due to matrix inhomogeneities. Significant improvement would be observed with a sample of uniform trapping sites in a single-crystal hydrogen matrix. Even in the absence of uniform trapping sites, significant gains in the spin T_2^* would be expected by employing stretch-state superpositions rather than Larmor precession states,[28] as discussed in Section VIII.

Considering the other alkali-metal atoms, we would expect lithium and sodium to have long T_2^* times due to their small hyperfine splitting,[38] as explained in Sections VI A and VII A. Unfortunately, we would expect poor polarization signals from lithium and sodium due to their small excited-state fine-structure splitting, as discussed in Section IV D.

Considering other elements of the periodic table, we expect that – unless one is able to grow single-crystal samples with uniform trapping sites – atoms with ground states with $J > 1/2$ will have short T_2^* times, as tensor Stark shifts would be expected to be significantly larger. Among the $J = 1/2$ elements, silver appears promising: it has a large excited-state fine-structure splitting (which should be favorable for optical pumping and readout of spin) and a small ground-state hyperfine splitting (which should be favorable for a long T_2^*). Moreover, silver's nuclear spin of $I = 1/2$ makes it straightforward to obtain stretched-state superpositions with a simple two-photon transition.[28] In addition, silver's smaller "size" may allow it to fit into the lattice in a more stable or favorable configuration.

Acknowledgements

This material is based upon work supported by the National Science Foundation under Grants No. PHY-1607072, No. PHY-1912425, No. PHY-1607610, No. PHY-1912668, and No. CHE-1654547. We gratefully acknowledge helpful conversations with Andrei Derevianko, Amar C. Vutha, Eric A. Hessels, Pierre-Nicholas Roy, and Peng Zhang.

References

(1) Büch, H.; Mahapatra, S.; Rahman, R.; Morello, A.; Simmons, M. Spin readout and addressability of phosphorus-donor clusters in silicon. *Nat. Commun.* **2017**, *4*, 1-6. https://doi.org/10.1038/ncomms3017.

(2) Tyryshkin, A. M.; Tojo, S.; Morton, J. J.; Riemann, H.; Abrosimov, N. V.; Becker, P.; Pohl, H.-J.; Schenkel, T.; Thewalt, M. L.; Itoh, K. M.; Lyon, S. A. Electron spin coherence exceeding seconds in high-purity silicon. *Nat. Mater.* **2012**, *11*, 143-147. https://doi.org/10.1038/nmat3182.

(3) Balasubramanian, G.; Neumann, P.; Twitchen, D.; Markham, M.; Kolesov, R.; Mizuochi, N.; Isoya, J.; Achard, J.; Beck, J.; Tissler, J.; Jacques, V.; Hemmer, P. R.; Jelezko, F.; V. Jacques, P. R. Hemmer, F. Jelezko, and J. Wrachtrup, J. Ultralong spin coherence time in isotopically engineered diamond. *Nat. Mater.* **2009**, *8*, 383-387. https://doi.org/10.1038/nmat2420.

(4) Robledo, L.; Childress, L.; Bernien, H.; Hensen, B.; Alkemade, P. F.; Hanson, R. High-fidelity projective read-out of a solid-state spin quantum register. *Nature* **2011**, *477*, 574-578. https://doi.org/10.1038/nature10401.

(5) Childress, L.; Hanson, R. Diamond NV centers for quantum computing and quantum networks. *MRC Bull.* **2013**, *38*, 134-138. https://doi.org/10.1557/mrs.2013.20.

(6) Cappellaro, P.; Jiang, L.; Hodges, J. S.; Lukin, M. D. Coherence and Control of Quantum Registers Based on Electronic Spin in a Nuclear Spin Bath. *Phys. Rev. Lett.* **2019**, *102* (21), 1-4. https://doi.org/10.1103/PhysRevLett.102.210502.

(7) Acosta, V. M.; Bauch, E.; Ledbetter, M. P.; Santori, C.; Fu, K.-M. C.; Barclay, P. E.; Beausoleil, R. G.; Linget, H.; Roch, J. F.; Treussart, F.; Chemerisov, S.; Gawlik, W.; Budker, D. Diamonds with a high density of nitrogen-vacancy centers for magnetometry applications. *Phys. Rev. B* **2009**, *80* (11), 1-15. https://doi.org/10.1103/PhysRevB.80.115202.

(8) Taylor, J.; Cappellaro, P.; Childress, L.; Jiang, L.; Budker, D.; Hemmer, P.; Yacoby, A.; Walsworth, R.; Lukin, M. High-sensitivity diamond magnetometer with nanoscale resolution. *Nat. Phys.* **2008**, *4*, 810-816. https://doi.org/10.1038/nphys1075.

(9) Bauch, E.; Hart, C. A.; Schloss, J. M.; Turner, M. J.; Barry, J. F.; Kehayias, P.; Singh, S.; Walsworth, R. L. Ultralong dephasing times in solid-state spin ensembles via quantum control. *Phys. Rev. X* **2018**, *8* (3), 1-11. https://doi.org/10.1103/PhysRevX.8.031025.

(10) Ajoy, A.; Bissbort, U.; Lukin, M. D.; Walsworth, R. L.; Cappellaro, P. Atomic-Scale Nuclear Spin Imaging Using Quantum-Assisted Sensors in Diamond. *Phys. Rev. X* **2015**, *5* (1), 1-11. https://doi.org/10.1103/PhysRevX.5.011001.

(11) Staudacher, T.; Shi, F.; Pezzagna, S.; Meijer, J.; Du, J.; Meriles, C.; Reinhard, F.; Wrachtrup, J. Nuclear Magnetic Resonance Spectroscopy on a (5-

Nanometer)^3 Sample Volume. *Science* **2013**, *339* (6119), 561-563. https://doi.org/ 10.1126/science.1231675.

(12) Mamin, H.; Kim, M.; Sherwood, M.; Rettner, C.; Ohno, K.; Awschalom, D.; Rugar, D. Nanoscale Nuclear Magnetic Resonance with a Nitrogen-Vacancy Spin Sensor. *Science* **2014**, *339* (6119), 557-560. https://doi.org/ 10.1126/science.1231540.

(13) Sushkov, A. O.; Lovchinsky, I.; Chisholm, N.; Walsworth, R. L.; Park, H.; Lukin, M. D. Magnetic Resonance Detection of Individual Proton Spins Using Quantum Reporters. *Phys. Rev. Lett.* **2014**, *113* (19), 1-5. https://doi.org/10.1103/PhysRevLett.113.197601.

(14) Arndt, M.; Kanorsky, S.; Weis, A.; Hänsch, T. Can paramagnetic atoms in superfluid helium be used to search for permanent electric dipole moments? *Phys. Lett. A* **1993**, *174* (4), 298-303. https://doi.org/10.1016/0375-9601(93)90142-M.

(15) Kinoshita, T.; Takahashi, Y.; Yabuzaki, T. Optical pumping and optical detection of the magnetic resonance of alkali-metal atoms in superfluid helium. *Phys. Rev. B* **1994**, *49* (5), 3648-3651. https://doi.org/10.1103/PhysRevB.49.3648.

(16) Vutha, A.; Horbatsch, M.; Hessels, E. A. Oriented polar molecules in a solid inert-gas matrix: a proposed method for measuring the electric dipole moment of the electron. *Atoms,* **2018**, *6* (1), 3-10. https://doi.org/10.3390/atoms6010003.

(17) Vutha, A.; Horbatsch, M.; Hessels, E. A. Orientation-dependent hyperfine structure of polar molecules in a rare-gas matrix: A scheme for measuring the

electron electric dipole moment. *Phys. Rev. A* **2018**, *98* (3), 1-8. https://doi.org/10.1103/PhysRevA.98.032513.

(18) Lang, S.; Kanorsky, S.; Eichler, T.; Müller-Siebert, R.; Hänsch, T. W.; Weis, A. Optical Pumping of Cs Atoms in Solid ^{4}He. *Phys. Rev. A* **1999**, *60* (5), 3867-3877. https://doi.org/10.1103/PhysRevA.60.3867.

(19) Kanorsky, S. I.; Lang, S.; Lücke, S.; Ross, S. B.; Hänsch, T. W.; Weis, A. Millihertz magnetic resonance spectroscopy of Cs atoms in body-centered-cubic ^{4}He. *Phys. Rev. A* **1996**, *54* (2), R1010 – R1013. https://doi.org/10.1103/PhysRevA.54.R1010.

(20) Moroshkin, P.; Hofer, A.; Ulzega, S.; Weis, A. Spectroscopy of atomic and molecular defects in solid He4He4 using optical, microwave, radio frequency, and static magnetic and electric fields (Review). *Low Temp. Phys.* **2006**, *32* (11), 981-998. https://doi.org/10.1063/1.2389001.

(21) Weyhmann, W.; Pipkin, F. M. Optical Absorption Spectra of Alkali Atoms in Rare-Gas Matrices. *Phys. Rev.* **1965**, *137* (2A), A490 – A496. https://doi.org/10.1103/PhysRev.137.A490.

(22) Xu, C.-Y.; Hu, S.-M.; Singh, J.; Bailey, K.; Lu, Z.-T.; Mueller, P.; O'Connor, T. P.; Welp, U. Optical Excitation and Decay Dynamics of Ytterbium Atoms Embedded in a Solid Neon Matrix. *Phys. Rev. Lett.* **2011**, *107* (9), 1-4. https://doi.org/10.1103/PhysRevLett.107.093001.

(23) Gaire, V.; Raman, C. S.; Parker, C. V. Subnanometer optical linewidth of thulium atoms in rare-gas crystals. *Phys. Rev. A* **2019**, *99* (2), 1-6. https://doi.org/10.1103/PhysRevA.99.022505.

(24) Kupferman, S. L.; Pipkin, F. M. Properties of Rubidium Atoms Trapped in a Solid Argon Matrix. *Phys. Rev.* **1968**, *166* (2), 207-218. https://doi.org/10.1103/PhysRev.166.207.

(25) Kanagin, A. N.; Regmi, S. K.; Pathak, P.; Weinstein, J. D. Optical pumping of rubidium atoms frozen in solid argon. *Phys. Rev. A* **2013**, *88*, 1-4. https://doi.org/10.1103/PhysRevA.88.063404.

(26) Momose, T.; Shida, T. Matrix-Isolation Spectroscopy Using Solid Parahydrogen as the Matrix: Application to High-Resolution Spectroscopy, Photochemistry, and Cryochemistry. *Bull. Chem. Soc. Jpn.* **1998**, *71* (1), 1-15. https://doi.org/10.1246/bcsj.71.1.

(27) Upadhyay, S.; Kanagin, A. N.; Hartzell, C.; Christy, T.; Arnott, W. P.; Momose, T.; Patterson, D.; Weinstein, J. D. Longitudinal spin relaxation of optically pumped rubidium atoms in solid parahydrogen. *Phys. Rev. Lett.* **2016**, *117*, 1-5. https://doi.org/10.1103/PhysRevLett.117.175301.

(28) Upadhyay, S.; Dargyte, U.; Prater, R. P.; Dergachev, V. D.; Varganov, S. A.; Tscherbul, T. V.; Patterson, D.; Weinstein, J. D. Enhanced spin coherence of rubidium atoms in solid parahydrogen. *Phys. Rev. B* **2019**, *100* (2), 1-5. https://doi.org/10.1103/PhysRevB.100.024106.

(29) Hartzell, C. Matrix isolation of rubidium in a solid parahydrogen substrate. B.Sc. Thesis, University of Nevada, Reno, Reno, NV, U.S., 2014. https://weinsteinlab.org/wp-content/uploads/2019/12/ChaseHartzell2014.pdf (accessed 2021-09-17).

(30) Kanagin, A. N. Creation and analysis of para-hydrogen crystals. B.Sc. Thesis, University of Nevada, Reno, Reno, NV, US. 2015.

(31) Fajardo, M. E.; Tam, S. Rapid vapor deposition of millimeters thick optically transparent parahydrogen solids for matrix isolation spectroscopy. *J. Chem. Phys.* **1998**, *108* (10), 4237-4241. https://doi.org/10.1063/1.475822.

(32) National Institute of Standards and Technology. Physical Measurement Laboratory. *Handbook of Basic Atomic Spectroscopic Data, Ver. 1.1.3*. National Institute of Standards and Technology, 2013. https://www.nist.gov/pml/handbook-basic-atomic-spectroscopic-data (accessed 2021-09-17).

(33) Gerhardt, I.; Sin, K.; Momose, T. Excitation and emission spectra of rubidium in rare-gas thin-films. *J. Chem. Phys.* **2012**, *137* (1), 1-7. https://doi.org/10.1063/1.4730032.

(34) Takahashi, Y.; Sano, K.; Kinoshita, T.; Yabuzaki, T. Spectroscopy of alkali atoms and molecules in superfluid helium. *Phys. Rev. Lett.* **1993**, *71* (7), 1035-1038. https://doi.org/10.1103/PhysRevLett.71.1035.

(35) Happer, W. Optical Pumping. *Rev. Mod. Phys.* **1972**, *44* (2), 169-249. https://doi.org/10.1103/RevModPhys.44.169.

(36) Metcalf, H.; Van der Straten, P. Laser cooling and trapping of atoms. *J. Opt. Soc. Am. B* **2003**, *20* (5), 887-908. https://doi.org/10.1364/JOSAB.20.000887.

(37) Eichler, T.; Müller-Siebert, R.; Nettels, D.; Kanorsky, S.; Weis, A. Optical Detection of Nonradiating Alkali Atoms in Solid Helium. *Phys. Rev. Lett.* **2002**, *88* (12), 1-4. https://doi.org/10.1103/PhysRevLett.88.123002.

(38) Arimondo, E.; Inguscio, M.; Violino, P. Experimental determinations of the hyperfine structure in the alkali atoms. *Rev. Mod. Phys.* **1977**, *49* (1), 31-75. https://doi.org/10.1103/RevModPhys.49.31.

(39) Tiecke, T. Feshbach resonances in ultracold mixtures of the fermionic quantum gases ^{6}Li and ^{40}K, Ph.D. Dissertation, University of Amsterdam, Amsterdam, Netherlands, 2009. https://dare.uva.nl/search?identifier=19aa5a15-6b3d-4f1f-b9b9-6736f1eab5c1 (accessed 2021-09-17).

(40) Angel, J. R. P.; Sandras, P. The hyperfine structure Stark effect I. Theory. *Proc. R. Soc. London, Ser. A* **1968**, *305*, 125-138. https://doi.org/10.1098/rspa.1968.0109.

(41) Dzuba, V. A.; Flambaum, V. V.; Beloy, K.; Derevianko, A. Hyperfine-mediated static polarizabilities of monovalent atoms and ions. *Phys. Rev. A*, **2010**, *82*, 1-6. https://doi.org/10.1103/PhysRevA.82.062513.

(42) Robyr, J.-L.; Knowles, P.; Weis, A. Measurement of the scalar third-order electric polarizability of the Cs ground state using coherent-population-trapping spectroscopy in Ramsey geometry. *Phys. Rev. A* **2014**, *90* (1), 1-13. https://doi.org/10.1103/PhysRevA.90.012505.

(43) Ulzega, S.; Hofer, A.; Moroshkin, P.; Weis, A. Reconciliation of experimental and theoretical electric tensor polarizabilities of the cesium ground state. *Europhys. Lett.* **2006**, *76* (6), 1074-1080. https://doi.org/10.1209/epl/i2006-10383-2.

(44) Bloembergen, N.; Purcell, E. M.; Pound, R. V. Relaxation Effects in Nuclear Magnetic Resonance Absorption. *Phys. Rev.* **1948**, *73* (7), 679-715. https://doi.org/10.1103/PhysRev.73.679.

(45) Murphy, D. M. Electron Paramagnetic Resonance Spectroscopy of Polycrystalline Oxide Systems. In Metal Oxide Catalysis, Weinheim: Wiley-VCH, 2009; pp. 1-50. DOI: 10.1002/9783527626113.ch1.

(46) Carrington, A.; McLachlan, A. D. *Introduction to Magnetic Resonance: With Applications to Chemistry and Chemical Physics*; Chapman and Hall Ltd., 1979.

(47) Slichter, C. P. *Principles of Magnetic Resonance*, 3rd ed.; Springer, Berlin, 1990.

(48) Lund, A.; Shiotani, M. Shimada, S. *Principles and Applications of ESR Spectroscopy*; Springer Science & Business Media, 2011.

(49) Tscherbul, T. V.; Grinev, T. A.; Yu, H.-G.; Dalgarno, A.; Kłos, J. Ma, L. Alexander, M. H. Cold collisions of polyatomic molecular radicals with S-state atoms in a magnetic field: An ab initio study of He + $CH_2(\tilde{X})$ collisions. *J. Chem. Phys.* **2012**, *137* (10), 1-15. https://doi.org/10.1063/1.4748258.

(50) Zare, R. N. *Angular Momentum*; Wiley, 1988.

(51) Scharf, D.; Martyna, G. J.; Li, D.; Voth, G. A.; Klein, M. L. Nature of lithium trapping sites in the quantum solids *para*-hydrogen and *ortho*-deuterium. *J. Chem. Phys.* **1993**, *99* (11), 9013-9020. https://doi.org/10.1063/1.465569.

(52) Deegan, M. J. O.; Knowles, P. J. Perturbative corrections to account for triple excitations in closed and open shell coupled cluster theories. *Chem. Phys. Lett.* **1994**, *227* (3), 321-326. https://doi.org/10.1016/0009-2614(94)00815-9.

(53) Werner, H.-J.; Knowles, P. J.; Knizia, G.; Manby, F. R.; Schütz, M. Molpro: a general-purpose quantum chemistry program package. *WIREs Comput. Mol. Sci.* **2012**, *2*, 242-253. https://doi.org/10.1002/wcms.82.

(54) Kendall, R. A.; Dunning, T. H., Harrison, R. J. Electron affinities of the first-row atoms revisited. Systematic basis sets and wave functions. *J. Chem. Phys.* **1992**, *96* (9), 6796-6806. https://doi.org/10.1063/1.462569.

(55) Arruda, P. M.; Neto, A. C.; Jorge, F. E. Some considerations about Gaussian basis sets for electric property calculations. *Int. J. Quantum Chem.* **2009**, *109*, 1189-1199. https://doi.org/10.1002/qua.21934.

(56) Lim, I. S.; Schwerdtfeger, P.; Metz, B.; Stoll, H. All-electron and relativistic pseudopotential studies for the group 1 element polarizabilities from K to element 119. *J. Chem. Phys.* **2005**, *122* (10), 1-13. https://doi.org/10.1063/1.1856451.

(57) Boys, S. F.; Bernardi, F. The calculation of small molecular interactions by the differences of separate total energies. Some procedures with reduced errors. *Mol. Phys.* **1970**, *19* (4), 553-566. https://doi.org/10.1080/00268977000101561.

(58) Li, H.; Roy, P.-N.; Le Roy, R. J. An "adiabatic-hindered-rotor" treatment allows para- to be treated as if it were spherical. *J. Chem. Phys.* **2010**, *133* (10), 1-10. https://doi.org/10.1063/1.3476465.

(59) *CFOUR*. http://www.cfour.de (accessed 2021-09-17).

(60) Weigend, F.; Kohn, A.; Hattig, C. Efficient use of the correlation consistent basis sets in resolution of the identity MP2 calculations. *J. Chem. Phys.* **2002**, *116* (8), 3175-3183. https://doi.org/10.1063/1.1445115.

(61) Roos, B. O.; Veryazov, V.; Widmark, P.-O. Relativistic atomic natural orbital type basis sets for the alkaline and alkaline-earth atoms applied to the ground-state potentials for the corresponding dimers. *Theor. Chem. Acc.* **2004**, *111*, 345-351. https://doi.org/10.1007/s00214-003-0537-0.

(62) Tscherbul, T. V.; Zhang, P.; Sadeghpour, H. R.; Dalgarno, A. Collision-induced spin exchange of alkali-metal atoms with ^{3}He: An *ab initio* study. *Phys. Rev. A* **2009**, *79* (6), 1-11. https://doi.org/10.1103/PhysRevA.79.062707.

(63) Tscherbul, T. V.; Zhang, P.; Sadeghpour, H. R.; Dalgarno, A. Anisotropic Hyperfine Interactions Limit the Efficiency of Spin-Exchange Optical Pumping of ^{3}He Nuclei. *Phys. Rev. Lett*. **2011**, *107* (2), 1-4. https://doi.org/10.1103/PhysRevLett.107.023204.

(64) Anderson, L. W.; Pipkin, F. M.; Baird, Jr., J. C. Hyperfine Structure of Hydrogen, Deuterium, and Tritium. *Phys. Rev.* **1960**, *120* (4), 1279-1289. https://doi.org/10.1103/PhysRev.120.1279.

(65) Silvera, I. F. The solid molecular hydrogens in the condensed phase: Fundamentals and static properties. *Rev. Mod. Phys.* **1980**, *52* (2), 393-452. https://doi.org/10.1103/RevModPhys.52.393.

(66) *Alkali D Line Data*. https://steck.us/alkalidata/ (accessed 2021-11-10).

(67) Pathak, P. Absorption spectrum of rubidium in a solid neon matrix, M.Sc. Thesis, University of Nevada, Reno, Reno, NV, US, 2014. https://www.proquest.com/docview/1618217513?pq-origsite=gscholar&fromopenview=true (accessed 2021-11-10).

CHAPTER 6. MR. TOMPKINS WORLD: EFFECTS OF EXTREME VARIATIONS IN FUNDAMENTAL CONSTANTS ON THE STRUCTURE OF ATOMS, MOLECULES, AND PERIODIC TABLE

Vsevolod D. Dergachev, H. B. Tran Tan,

Sergey A. Varganov, and Andrei Derevianko

Abstract

In 1939, George Gamow published a popular-science book "Mr. Tompkins in Wonderland", which tells a story about Mr. Tompkins dreaming of alternative reality where fundamental constants have radically different values from those they have in the real world. Gamow's classic predates modern theories which generically promote fundamental constants to dynamical entities. Constants are no longer constant. Enter Mr. Tompkins world where speed of light c is reduced to that of a speeding bicycle. Here we show that gradually reducing c from its nominal value truncates periodic system of elements. It also leads to qualitative changes in Aufbau principle, atomic ground states, nature of chemical bond, and molecular geometry. Noble gasses are no longer inert. In addition to pushing relativistic quantum chemistry to its limits, we find that Mr. Tompkins world would be uninhabitable.

I. Introduction

Quantum chemistry primarily depends on a set of three fundamental constants (FCs): the electron mass m_e, its charge e, and the Plank constant $\hbar$. Relativity brings in the speed of light c or, equivalently, the fine-structure constant $\alpha = e^2/\hbar c$. These constants, together with nuclear parameters are fixed in conventional computations to their empirical (nominal) values. Modern theories, however, generically promote FCs to dynamical entities[1,2]. Constants are no longer constant. The effects in variation of FCs in non-relativistic Born-Oppenheimer (NR-BO, infinitely heavy point-like nuclei) approximation reduce to isotropic scaling of all nuclear and electronic coordinates by the Bohr radius $a = \hbar^2/m_e e^2$, see Supplementary Information. Similarly, all the FC-dependence of energies factorizes out (common factor is Hartree energy $m_e e^4/\hbar^2$). Then chemical bond angles and transition frequency ratios do not depend on FCs. Effects beyond the NR-BO approximation violate these scaling laws and lead to changes in chemical bond angles and frequency ratios with varying FCs. For concreteness, here we focus on the effects of relativity and examine the effect of variation in α. In atomic units ($m_e = |e| = \hbar \equiv 1$), conventionally used in quantum chemistry, $\alpha = 1/c$. Then variations in α are equivalent to those in speed of light: $c/c_0 = \alpha_0/\alpha$. Here and below all quantities sub-scripted with 0 refer to their nominal values. Our choice of atomic system of units does not affect our conclusions[3].

Previous literature on variations of FCs predominately focused on small deviations of FCs from their nominal values[4]. Here we explore a novel regime of extreme variations and find an abundance of remarkable effects. The periodic system of elements is truncated with reduction in c.

The Aufbau principle, atomic ground states, nature of chemical bond, and molecular geometry all exhibit substantial qualitative changes. Noble gasses are no longer inert.

Beyond connection to novel theories, there is a practical utility in enhancing relativity[5]. As an electron near the nucleus of charge Z moves with speed $v/c \sim \alpha Z$, relativistic effects are most pronounced in heavy systems. However, in heavy molecules, the effects of relativity are masked by large electron correlations. Reducing c magnifies the role of relativity in light molecules, where correlations can be treated with much higher accuracy. We carry out most of our *ab initio* relativistic quantum chemistry calculations with the state-of-the-art Dirac package[6-8], testing its capabilities in the ultra-relativistic regime.

II. Dirac Theory of the Relativistic Electron in the Potential

We start with a hydrogen atom. Its ground state energy is given by

$$\varepsilon_{1s_{1/2}} = c^2\left(\sqrt{1-\left(\frac{Z}{c}\right)^2}-1\right). \tag{6.1}$$

We remind the reader that Dirac equation has two continua: above the ionization threshold, $\varepsilon > 0$, and below the rest-mass gap, $\varepsilon < -2c^2$, see Figure 6.1. In the Dirac sea paradigm, the lower continuum is fully occupied by electrons. Then the atomic electron cannot spontaneously decay into the lower continuum due to the Pauli exclusion principle. As we increase c, the $1s_{1/2}$ energy is lowered deeper into the rest-mass gap until we reach a value of $c = Z$ with $\varepsilon_{1s_{1/2}} = -c^2$. Above this value, the

argument of the square root, $1-(Z/c)^2$, becomes negative and the energy acquires an imaginary part: the ground state becomes unstable. Point-like nucleus approximation of Eq. (6.1), however, is inadequate in determining the critical value of c. Bound states become unstable when their energies "dive" into Dirac sea[9,10], i.e. $\varepsilon_{1s_{1/2}} = -2c^2$, and not c^2 per Eq. 6.1).

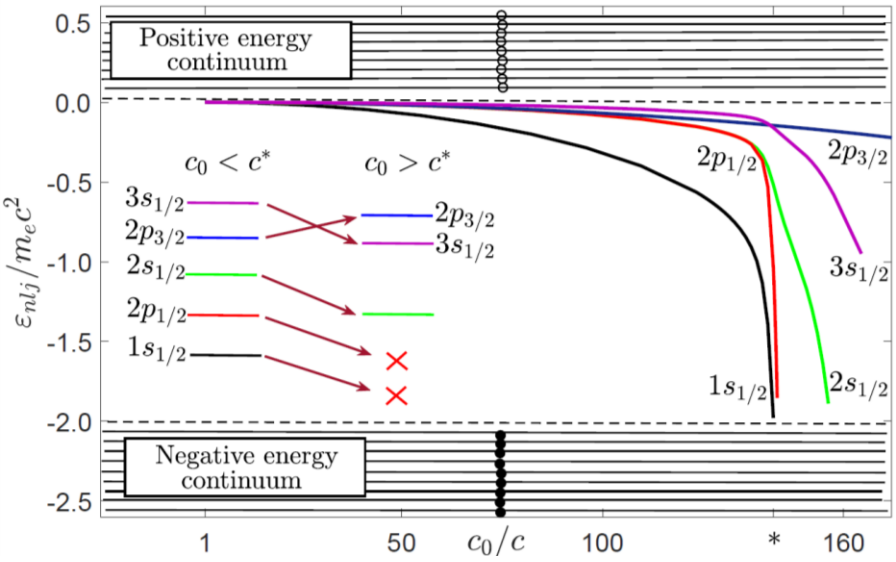

Figure 6.1. Energy states of atomic hydrogen a function of speed of light. The $1s_{1/2}$ "dives'" into Dirac sea at the critical value $c^* \approx c_0/143$.

To rectify the failure of the point-like nucleus approximation, Eq. (6.1), we solved Dirac equation with finite-size nuclei numerically. Resulting energies of several lowest-energy orbitals for hydrogen are shown in Figure 6.1. As expected, the solutions remain stable until the energy dives into Dirac sea. The $1s_{1/2}$ energy breaches the rest-energy gap at the critical value of $\alpha^* \approx 1.04$ corresponding to an ≈ 143-fold reduction in the speed of light.

What happens when c is driven below its critical value c^*? This question has been explored in a related problem of determining the critical nuclear charge with α fixed to its nominal value[9,10]. The bound state becomes embedded into the Dirac sea continuum, and, as such, becomes unstable, similar to Fano resonances in chemical physics. An electron-positron pair is emitted spontaneously and the vacuum becomes electrically charged.

We show in Supplementary Information that the critical value c^* increases with nuclear charge,

$$\frac{c^*}{c_0} = \frac{\alpha_0}{\alpha^*} \approx \frac{Z}{168}. \tag{6.2}$$

This remains a good approximation for multi-electron systems as the $1s_{1/2}$ electrons tend to see the unscreened nuclear charge with minor correlation corrections. In a chemical compound, $c^*$is determined by the charge of the heaviest nucleus. Inverting Eq. (6.2), we observe that at a given value of c/c_0, only elements with $Z \lesssim 168c/c_0$ are stable. As c is gradually decreased from its nominal value, the heavier elements are destabilized first and the periodic system is truncated. If c is reduced ten-fold, only elements with $Z \lesssim 16$ remain stable. The entire periodic system shrinks to elements from hydrogen to sulfur. In Mr. Tompkins alternative reality[11], with c reduced to that of a speeding bicycle, $c/c_0 \approx 4 \times 10^{-8}$ and even the hydrogen atom fails to exist.

III. Effects of Extreme Variation of the Speed of Light on Structure of Many-Electron Atoms

For multi-electron systems, the role of Dirac sea becomes explicit even at the stage of formulating the many-body atomic Hamiltonian,

$$H_{\mathrm{no-pair}} = \sum_i h_{\mathrm{D}}(i) + \frac{1}{2}\sum_{i\neq j} \Lambda_{++}\frac{1}{r_{ij}}\Lambda_{++}. \tag{6.3}$$

Here the first term is a sum of Dirac Hamiltonian $h_{\mathrm{D}}(i)$ of an electron i moving in the potential of a finite-size nucleus and the second term describes the Coulomb repulsion between the electrons. Breit interaction is usually included as well. Notice that the $e-e$ interaction is sandwiched between projection operators Λ_{++}. These exclude states from the Dirac sea continuum of h_{D}, to avoid collapse of many-electron wavefunctions into Dirac sea[12]. This is the no-pair Hamiltonian of relativistic atomic and molecular structure calculations[13,14] and we use it as a starting point in our computation.

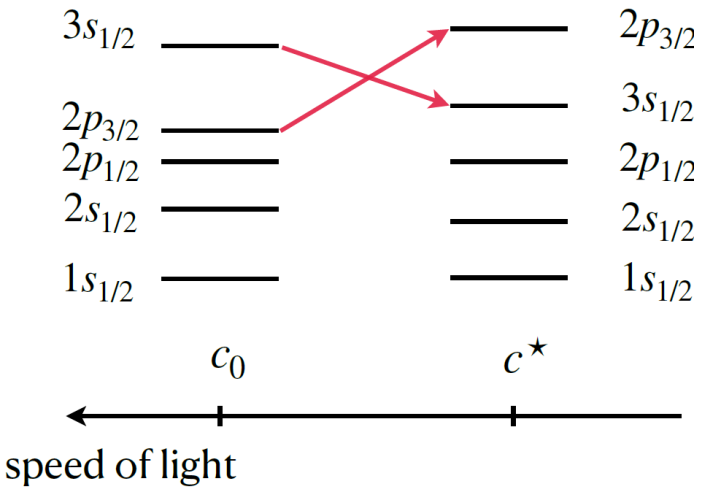

Figure 6.2. Evolution of the Aufbau principle's sequence of orbital occupation in many-electron atoms with varying speed of light c (or fine-structure constant). c_0 and c^* are the nominal and the critical values, respectively.

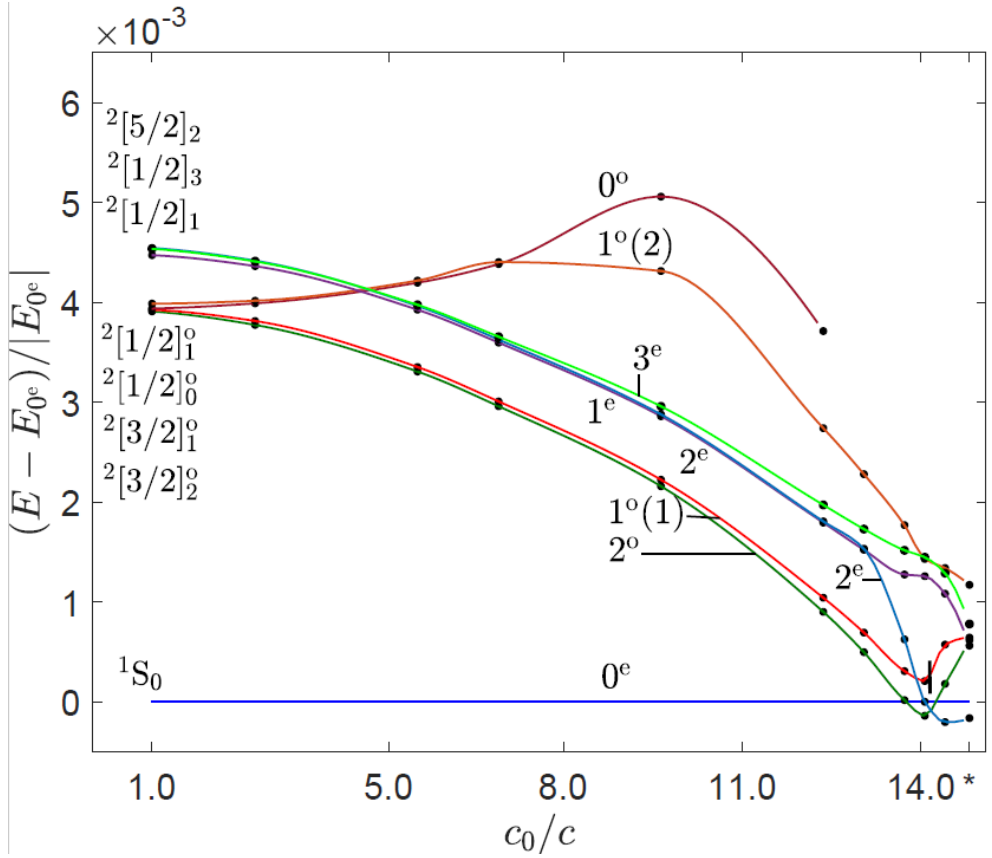

Figure 6.3. Energy spectrum of neon atom as a function of speed of light (or α) with the energy E_{0^e} of the closed-shell state $0^e(^1S_0)$ serving as a reference. At the nominal c, the states are labeled using the conventional Russell-Saunders LS coupling scheme[15], and the closed-shell ground state is labeled as $^1S_0$. At the smaller values of c, the states are labeled as J^π, where J is the total angular momentum and π is the parity of the state. Multiple state crossings lead to the open-shell state 2^e becoming the ground state near the critical c ($c_0/c^* = 14.8$).

The Aufbau (building-up) principle states that electrons fill atomic orbitals with the lowest energies. For $c \approx c_0$, the textbook sequence of orbitals is $1s_{1/2}2s_{1/2}2p_{1/2}2p_{3/2}3s_{1/2}$. This sequence is explained by the screening of the nuclear charge by the electrons in inner shells, which is more effective for the orbitals with

larger l due to centrifugal potential. When c approaches its critical value, our calculations for the hydrogen atom result in the $1s_{1/2}2p_{1/2}2s_{1/2}3s_{1/2}2p_{3/2}$ sequence of energies, while for the multi-electron atoms, it becomes $1s_{1/2}2s_{1/2}2p_{1/2}3s_{1/2}2p_{3/2}$ (Figure 6.1), which is attributed to relativistic stabilization of $2s_{1/2}$, $2p_{1/2}$, and $3s_{1/2}$. For example, at $c \lesssim c^*$, neon (Z = 10) has the ground-state configuration $1s_{1/2}^2 2s_{1/2}^2 2p_{1/2}^2 3s_{1/2}^2 2p_{3/2}^2$ with the total angular momentum J = 2, as shown in Figure 6.3. Neon becomes an open-shell atom with a half-occupied $2p_{3/2}$ atomic orbital, and, as such, is no longer inert. The "effective" configuration of the ultra-relativistic neon, $3s_{1/2}^2 2p_{3/2}^2$ (occupied $2s_{1/2}$ and $2p_{1/2}$ atomic orbitals are omitted since their energies are significantly lowered), closely resembles configuration of carbon at nominal speed of light, $2s_{1/2}^2 2p_{1/2}^2$. Therefore, such neon is expected to have as reach chemistry as carbon, including the ultra-relativistic version of organic chemistry. It is intriguing to imagine polymers, nanostructures, and entire new biology where neon plays the traditional role of carbon.

IV. Effects of Extreme Variation of the Speed of Light on Structure of Molecules

How will the extreme variation of the speed of light affect the structure and properties of molecules? Here we address this question by investigating the properties of water and ammonia, which are common and very important molecules in the Universe. Water is abundant in the Solar System, including liquid water that is believed to exist under the surface of the Jupiter's moon Europa and in early atmospheres of Venus and Mars [16-17]. All known forms of life use water as a universal solvent for various chemicals and as an essential component of many metabolic processes.

Ammonia is an important source of nitrogen required for synthesis of amino acids and building proteins in living systems[18]. Ammonia is present in the atmospheres of the gas giants, in comets and interstellar ices, and on the moons of Pluto and Saturn[19-20].

In the worlds where $c \ll c_0$, the geometry of water molecule will undergo dramatic changes. We find that at c 13.7 times smaller than its nominal value, the calculated bond angle in water reduces from 106º to 90º. If c decreases to 17.8 times of the nominal value, the water molecule becomes linear and therefore nonpolar. These dramatic changes in molecular geometry are induced by the relativistic stabilization of the $2s_{1/2}$ and $3s_{1/2}$ spin-orbitals of oxygen atom, and by the increased spin-orbit splitting between the $2p_{1/2}$ and $2p_{3/2}$ spin-orbitals (Figure 6.4). The effect on molecular geometry can be understood considering two common theories of molecular bonding: the valence shell electron pair repulsion (VSEPR) model and molecular orbital (MO) model.

According to the VSEPR model, at nominal c, the valence s and three p atomic orbitals of oxygen mix to produce four equivalent hybrid orbitals (sp^3 hybridization, or $2s_{1/2}2p_{1/2}2p_{3/2}$ in spin-orbital notation). Two of the hybrid orbitals overlap with the orbitals of the hydrogen atoms, and another two hold the two lone electron pairs. The repulsion between the four electron pairs on the hybrid orbitals leads to the slightly distorted tetrahedral arrangement, corresponding to the calculated bond angle of 106º. At intermediate $c_0/c = 13.7$, the stabilization of the $2s_{1/2}$ and $2p_{1/2}$ spin-orbitals breaks down the hybridization and results in only the doubly degenerate $2p_{3/2}$ spin-orbital participating in the formation of the oxygen-hydrogen bonds. This stabilizes the molecular structure with the 90º bond angle[5]. The loss of hybridization is supported by

the contraction of the electron radial density distributions (RDDs) of HOMO-3 and HOMO-2 (HOMO is the highest occupied molecular orbital), as the speed of light decreases (Figure S8). This indicates a reduction of these two molecular orbitals to $2s_{1/2}$ and $2p_{1/2}$ atomic spin-orbitals of oxygen. As the speed of light decreases further, relativistic stabilization of the $3s_{1/2}$ spin-orbital of oxygen and destabilization of the $2p_{3/2}$ spin-orbital due to large spin-orbit splitting lead to these spin-orbitals becoming quasi-degenerate. Such quasi-degeneracy induces the ps hybridization between these two spin-orbitals, stabilizing the linear molecular geometry. The participation of the $3s_{1/2}$ spin-orbital in chemical bonding is supported by the shape of the HOMO-1 RDD that becomes similar to the RDD of the $3s$ atomic orbital (Figure S8).

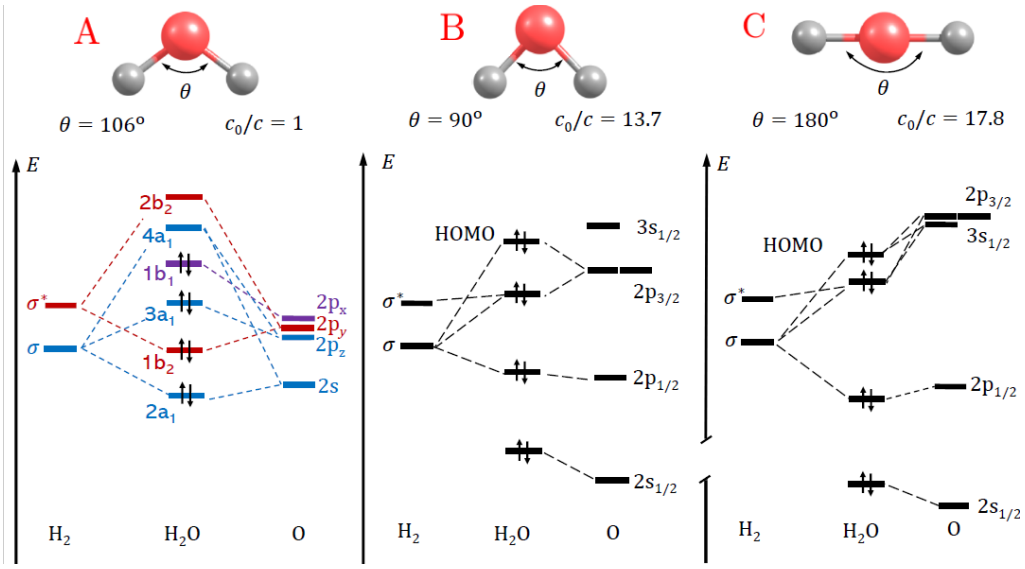

Figure 6.4. Molecular geometry and orbital diagram of water at different speeds of light, c_0/c = 1 (A), 13.7 (B) and 17.8 (C). The energy scale is the same in all panels. At the nominal speed of light (panel A), the orbitals are labeled and colored according to their irreducible representations in the C_{2v} point group. At decreased speed of light (panels B and C), the spin-orbital notation is used for atomic oxygen, and only the occupied MOs are shown.

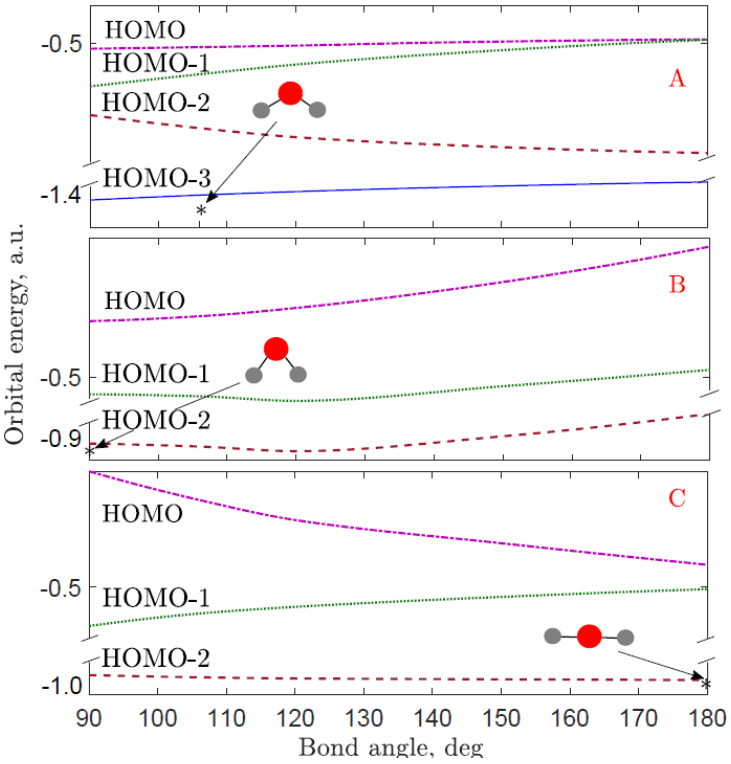

Figure 6.5. Walsh correlation diagrams of water showing the energies of four valence molecular orbitals as functions of bond angle at different speeds of light c_0/c = 1 (A), 13.7 (B), and 17.8 (C). In panels B and C, HOMO-3 is not shown because it reduces to the $2s_{1/2}$ atomic spin-orbital of oxygen and does not participate in the formation of oxygen-hydrogen bonds.

The Walsh correlation diagrams of the MO theory provide more insight into the relation between the electronic structure and geometry of the water molecule (Figure 6.5). These diagrams show the energies of valence MOs as functions of the bond angle. Because the total electron energy of a molecule can be approximated as the sum of MO energies, the Walsh diagrams can be used to predict the values of the bond angle that minimize the total electron energy. At $c_0/c = 1$, the interplay between mostly the HOMO-1 and HOMO-2 energies minimizes the total electron energy at the calculated bond angle of 106°. As the speed of light decreases, the energy of the $2s_{1/2}$ spin-orbital is reduced and its contribution to HOMO is diminished, leading to the minima of the

HOMO and total electron energies at the 90° bond angle. At even slower speed of light, the realistically stabilized $3s_{1/2}$ spin-orbital contributes to HOMO, minimizing the HOMO and total electron energies at the linear geometry.

Changes in molecular geometry of ammonia at slower speed of light resemble those of water and can be explained by the similarity in changes in electronic structure of the nitrogen and oxygen atoms (Figures S4 and S5). At the nominal speed of light, the VSEPR model predicts formation of four equivalent sp^3 hybrid orbitals in tetrahedral arrangement. In ammonia, three of these hybrid orbitals form chemical bonds with hydrogen atoms, while the fourth orbital holds the lone electron pair, leading to the trigonal pyramidal geometry, with calculated bond angle of 108° (Figure 6.6). As speed of light decreases, the angle reduces to its minimum values of 87°, which can be explained by the loss of hybridization due to relativistic stabilization of the $2s_{1/2}$ spin-orbital of nitrogen. This is supported by the RDD plot of HOMO-3, showing the transformation of this molecular orbital to the atomic $2s_{1/2}$ spin-orbital at reduced c (Figure S10). Further decrease in the speed of light leads to the planar molecule geometry with the 120° bond angle, which can be explained by the formation of new p^2s hybrid orbitals from the $2p_{3/2}$ and relativistically stabilized $3s_{1/2}$ spin-orbitals. The participation of $3s_{1/2}$ spin-orbital in the chemical bonding is reflected in the RDD shape of HOMO-1 (Figure S10, panels C and D).

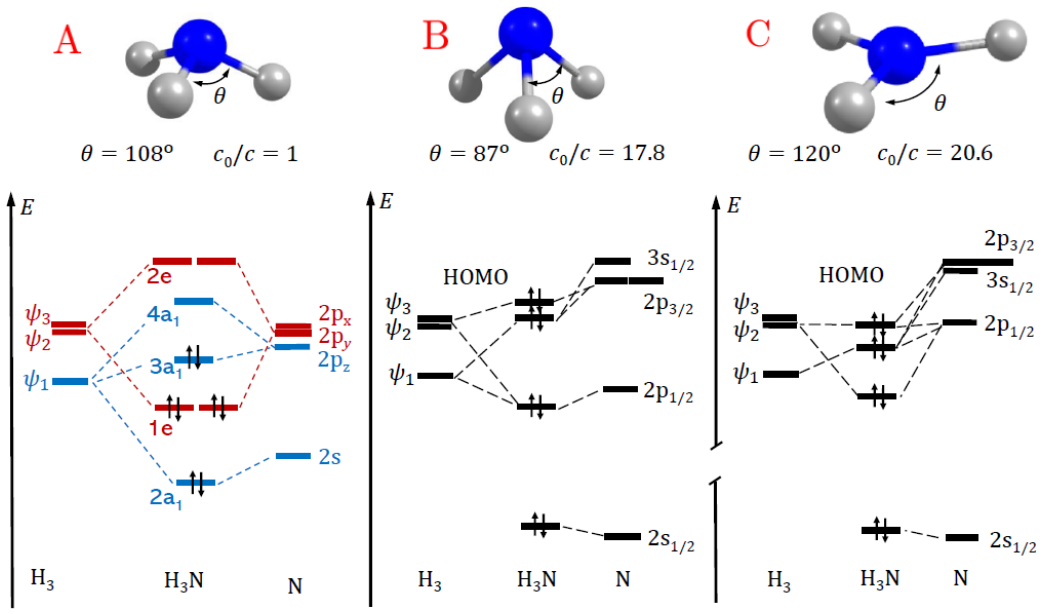

Figure 6.6. Molecular geometry and orbital diagram of ammonia at different speeds of light, c_0/c = 1 (A), 17.8 (B) and 20.6 (C). The energy scale is the same in all panels. At the nominal speed of light (panel A), the orbitals are labeled and colored according to their irreducible representations in the C_{3v} point group. At decreased speed of light (panels B and C), the spin-orbital notation is used for atomic nitrogen, and only the occupied MOs are shown.

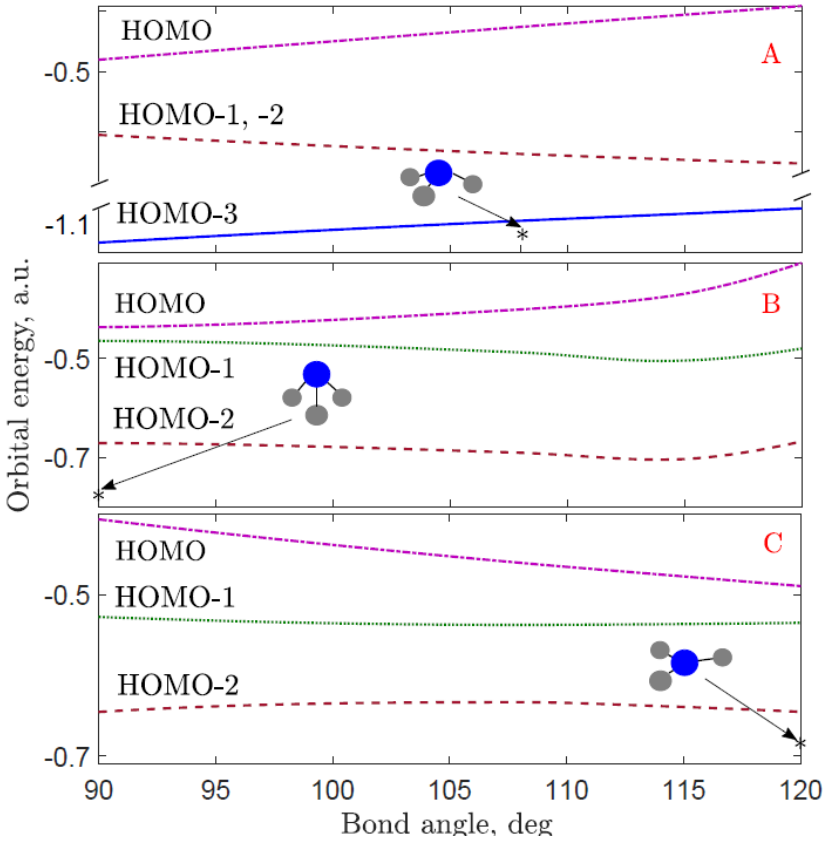

Figure 6.7. Walsh correlation diagrams of ammonia showing the energies of four valence molecular orbitals as functions of bond angle at different speeds of light c_0/c = 1 (A), 17.8 (B), and 20.6 (C). In panels B and C, the HOMO-3 molecular orbital is not shown because it reduces to $2s_{1/2}$ core spin-orbital of nitrogen and does not participate in the formation of nitrogen-hydrogen bonds.

The Walsh correlation diagrams for ammonia show the molecular orbital energies as functions of the bond angle (see Figure 6.7). At the nominal and intermediate c, the minima of the sum of orbital energies correspond to the trigonal pyramidal molecular geometries. For a very slow c, the HOMO stabilization at large angles dominates the energy changes of other molecular orbitals, leading to the planar molecular geometry.

V. Conclusion

Dramatic changes in the geometries of the oxygen and nitrogen-containing molecules will lead to alternative chemistry and biology. For example, the linear water molecule will have no dipole moment, and therefore will not be able to act as the universal solvent. Such molecules will be able to form only two-dimensional networks of hydrogen bonds, which should dramatically decrease the freezing and boiling points of water. The predicted changes in the geometry of ammonia, which is one of the most abundant polyatomic molecules in the interstellar space, can be used to search for the variations of fundamental constants in the Universe. If the underlying field driving the variations of fundamental constants permeates the visible Universe, there are strong anthropic-principle and observational constraints on how large the variations can be. However, if the field is self-interacting, it can clump into a few small patches on cosmic scales[21]. Then the constraints are evaded: fundamental constants can be radically different inside these patches.

Acknowledgements

We thank Mikhail Kozlov and Xiaoyong Chu for discussions. This work was supported in part by the U.S. National Science Foundation under Grants No. PHY-1912465 and CHE-1654547, and by the Sara Louise Hartman endowed professorship in Physics.

References

(1) Uzan, J.-P. Varying Constants, Gravitation and Cosmology. *Living Rev. Relativity*, **2011** *14* (2), 7-155. https://doi.org/10.12942/lrr-2011-2.

(2) Safronova, M. S; Budker, D.; DeMille, D.; Kimball, D. F. J.; Derevianko, A. Clark, C. W. Search for new physics with atoms and molecules. *Rev. Mod. Phys.* **2018** *90*, 25008. https://doi.org/10.1103/RevModPhys.90.025008.

(3) Savalle, E.; Roberts, B. M.; Frank, F.; Pottie, P.-E.; McAllister, B. T.; Dailey, C. B.; Derevianko, A.; Wolf, P. Novel approaches to dark-matter detection using space-time separated clocks. arXiv:1902.07192.

(4) Flambaum, V. V.; Dzuba, V. A. Search for variation of the fundamental constants in atomic, molecular, and nuclear spectra. *Can. J. Phys.* **2009** *87* (1), 8-72. https://doi.org/10.1139/p08-072.

(5) Dubillard, S.; Rota, J. B.; Saue, T.; Faegri, K. Bonding analysis using localized relativistic orbitals: Water, the ultrarelativistic case and the heavy homologues H_2X (X = Te, Po, eka-Po). *J. Chem. Phys.* **2006** *124* (15), 154307. https://doi.org/10.1063/1.2187001.

(6) Bast, R.; Gomes, A. S. P.; Saue, T.; Visscher, L.; Jensen, H. J. Aa.; Aucar, I. A.; Bakken, V.; Dyall, K. G.; Dubillard, S.; Ekström, U.; Eliav, E.; Enevoldsen, T.; Faßhauer, E.; Fleig, T.; Fossgaard, O.; Halbert, L.; Hedegård, E.D.; Helgaker, T.; Helmich–Paris, B.; Henriksson, J.; Iliaš, M.; Jacob, Ch. R.; Knecht, S.; Komorovsky', S.; Kullie, O.; Lærdahl, J. K.; Larsen, C. V.; Lee, Y. S.; List, N. H.; Nataraj, H. S.; Nayak, M. K.; Norman, P.; Olejniczak, G.; Olsen,

J.; Olsen, J. M. H.; Papadopoulos, A.; Park, Y. C.; Pedersen, J. K.; Pernpointner, M.; Pototschnig, J. V.; di Remi-gio, R.; Repisky, M.; Ruud, K.; Sałek, P.; Schimmelpfennig, P.; Senjean, B.; Shee, A.; Sikkema, J.; Sunaga, A.; Thorvaldsen, A. J.; Thyssen, J.; van Stralen, J.; Vidal, M. L.; Villaume, S.; Visser, O.; Winther, T.; Yamamoto, S. DIRAC, a relativistic ab initio electronic structure program, Release DIRAC21 (2021). http://www.diracprogram.org (accessed 2021-11-01).

(7) Saue, T.; Jensen, H. J. Aa. Quaternion symmetry in relativistic molecular calculations: The Dirac-Hartree-Fock method. *J. Chem. Phys.* **1999** *111* (14), 6211 – 6222. https://doi.org/10.1063/1.479958.

(8) Saue, T.; Bast, R.; Gomes, A. S. P.; Jensen, H. J. A.; Visscher, L.; I. A. Aucar, I. A.; Di Remigio, R.; Dyall, K. G.; Eliav, E.; Fasshauer, E.; Fleig, T.; Halbert, L.; Hedegård, E. D.; Helmich-Paris, B.; Iliaš, M.; Jacob, C. R.; Knecht, S.; Laerdahl, J. K.; Vidal, M. L.; Nayak, M. K.; Olejniczak, M.; Olsen, J. M. H.; Pernpointner, M.; Senjean, B.; Shee, A.; Sunaga, A.; van Stralen, J. N. The DIRAC code for relativistic molecular calculations. *J. Chem. Phys.* **2020** *152* (20), 204104. https://doi.org/10.1063/5.0004844.

(9) Zeldovich, Y. B.; Popov, V. S. Electronic structure of superheavy atoms. *Soviet Physics Uspekhi* **1972** *14*, 673. http://dx.doi.org/10.1070/PU1972v014n06ABEH004735.

(10) Greiner, W.; Reinhardt, J. *Quantum Electrodynamics*, 3rd ed.; Springer-Verlag, 2002.

(11) Gamow, *G. Mr. Tompkins in Wonderland; or Stories of c, G, and h*; The Macmillan Company, 1940.

(12) Brown, G. E.; Ravenhall, D. G. On the interaction of two electrons. *Proc. R. Soc. A* **1951** *208* (1095), 552 – 559. https://doi.org/10.1098/rspa.1951.0181.

(13) Sapirstein, J. Theoretical methods for the relativistic atomic many-body problem. *Rev. Mod. Phys.* **1998** *70* (1), 55 – 76. https://doi.org/10.1103/RevModPhys.70.55.

(14) Barysz, M.; Ishikawa, Y. Relativistic Methods for Chemists. *in Challenges and Advances in Computational Chemistry and Physics*, vol. 10; Springer, 2010.

(15) NIST Atomic Spectra Database. https://www.nist.gov/pml/atomic-spectra-database (accessed 2021-11-01).

(16) Cleeves, L. I.; Bergin, E. A.; Alexander, C. M. O'D.; Du, F.; Graninger, D.; Öberg, K. I.; Harries, T. J. The ancient heritage of water ice in the solar system. *Science* **2014** *345* (6204), 1590-1593. https://www.science.org/doi/abs/10.1126/science.1258055#pill-con3

(17) Encrenaz, T. Water in the Solar System. *Annu. Rev. Astron. Astrophys.* **2008** *46*, 57-87. https://doi.org/10.1146/annurev.astro.46.060407.145229

(18) Christensen, H. N. Role of Amino Acid Transport and Countertransport in Nutrition and Metabolism. *Physiol. Rev.* **1990** *70* (1), 43-77.

(19) Brown, M. E.; Calvin, W. E. Evidence for Crystalline Water and Ammonia Ices on Pluto's Satellite Charon. *Science* **2000** *287* (5450), 107-109. https://www.science.org/doi/abs/10.1126/science.287.5450.107

(20) Mandt, K.E.; Mousis, O.; Lunine, J.; Gautier, D. Protosolar Ammonia as the Unique Source of Titan's Nitrogen. *Ap. J. L.* **2014** *788* (2), 1-5. https://iopscience.iop.org/article/10.1088/2041-8205/788/2/L24/meta

(21) Derevianko, A.; Pospelov, M. Hunting for topological dark matter with atomic clocks. *Nat. Phys.* **2014** *10*, 933 – 936.

SUMMARY AND CONCLUSION

In the first part of this work, we presented the nonadiabatic statistical theory (NAST) to predict kinetics of spin-dependent processes. We discussed the NAST program package that calculates the probabilities and rate constants of intersystem crossings and spin-forbidden chemical reactions mediated by the spin-orbit coupling between electronic states with different spin multiplicities. NAST is a computationally inexpensive tool that requires the knowledge of molecular properties only at a few points on the potential energy surfaces of two spin states. Therefore, in contrast to nonadiabatic molecular dynamics, NAST can be applied to large molecular systems and is ideally suited to study slow nonadiabatic processes. NAST accounts for quantum effects, such as zero-point vibrational energy, quantum tunneling and reaction path interference. The key capabilities of the NAST package include calculations of i) reverse rate constants, ii) velocity-averaged transition probabilities, iii) rate constants in solutions, iii) adiabatic transition state theory (TST) rate constants, iv) effective Hessian matrix to obtain vibrational frequencies at the minimum energy crossing point, and v) spin-adiabatic potentials for obtaining the Zhu-Nakamura transition probabilities. We discussed three examples of NAST application. In the first example, the TST rate constants for isomerization of propylene oxide to acetone and propanal are calculated. The second example illustrated calculations of the forward and reverse rate constants for spin-forbidden isomerization of $Ni(dpp)Cl_2$. The third example demonstrated the rate constant calculations for $T_1 \rightarrow S_0$ relaxation in cyclopropene.

In the second part, we presented experimental and theoretical study of decoherence between spin states in ^{39}K, ^{85}Rb, ^{87}Rb, and ^{133}Cs atoms trapped in solid parahydrogen matrix. To explain experimental decoherence times T_2^*, we proposed a model of inhomogeneous broadening of hyperfine transitions between spin states of the central alkali atom due to its interaction with the host matrix. The largest contribution to the inhomogeneous broadening was identified to come from the anisotropic dipole-dipole interaction between the magnetic moments of the unpaired electron and nucleus of the metal atom. This anisotropic dipole-dipole interaction is induced by a change in the electronic structure of the alkali atom in presence of the host matrix. The T_2^* values predicted by our model, which was parametrized using the hyperfine anisotropy constant obtained from high-level electronic structure calculations, were in semi-quantitative agreement with the experimental results.

In the last part, we investigated how extreme variations of the speed of light impact electronic structure of atoms and molecules. This work was motivated by modern theories of physics which admit variation of fundamental constants. The changes in electronic structures were induced by increased relativistic effects when the speed of light c is reduced from its nominal value. To model these changes, we solved the fully relativistic Dirac equation at different values of c. We showed that atoms remain stable under variation of c up to a critical atom-specific value c^*. All first-row atoms with electrons in the $2p_{3/2}$ subshell (N, O, F, and Ne) exhibit a change in the ground states at c close to c^* due to the relativistic stabilization of the $3s_{1/2}$ spin-orbital and the large spin-orbit splitting between the $2p_{1/2}$ and $2p_{3/2}$ spin-orbitals. We also found that an extreme variation of c leads to dramatic changes in the molecular

geometries of ammonia and water. At the speed of light close to c^*, the water molecule becomes linear, while the ammonia molecule becomes planar.

APPENDIX A. CHAPTER 3 SUPPLEMENTAL MATERIALS

Density of rovibrational states

The rovibrational density of states measures the number of states of the system per unit energy at the given energy *E*,

$$\rho(E) = \int_0^E \rho_{\text{vib}}\,(E - E_{\text{rot}})\rho_{\text{rot}}(E_{\text{rot}})dE_{\text{rot}}, \quad (1)$$

where ρ_{vib} and ρ_{rot} are the vibrational and rotational densities of states, respectively. The vibrational density of states are calculated using the direct counting algorithm,[1,2] which is implemented in the NAST package as follows:

```
define Emax, where [0, Emax] is desired energy range
 do loop over all vibrational frequencies:
    do j = 1 till number_of_frequencies
       set counter k = 0
       do while frequency(j)*k < Emax
             k = k +1;  e_bin = ceil(frequency(j)*k)
             vib_density(e_bin) = vib_density(e_bin) + 1
       end do
    end do
```

The rotational density of states is calculated using the classical equation for asymmetric top model[3]:

$$\rho_{\text{rot}}(E_{\text{rot}}) = \frac{4\sqrt{2E_{\text{rot}}}}{h^3}\sqrt{I_{\text{A}}I_{\text{B}}I_{\text{C}}}, \quad (2)$$

where h is Planck's constant, and I_{A}, I_{B} and I_{C} are the principal moments of inertia of a molecule.

Sloped and peaked intersections

The difference between sloped and peaked intersections is shown in Fig. 1 below.

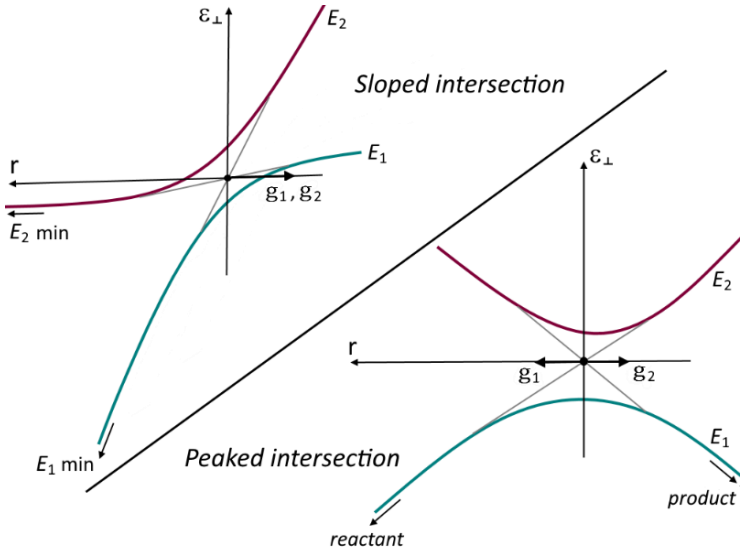

Figure 1. Sloped (upper left) and peaked (lower right) intersections of two states along the one-dimensional reaction coordinate r, $\varepsilon_\perp$ is the internal energy contained in r. The two states E_1 and E_2 are shown in spin-diabatic (grey) and spin-adiabatic (green and red) representations. In sloped intersection, the gradients $\mathbf{g}_1$ and $\mathbf{g}_2$ point in the same direction at MECP.

Zhu-Nakamura formulas for sloped intersection

The Zhu-Nakamura (ZN) probability of transition at the reaction energy $\varepsilon_\perp$ is given by

$$P_{\mathrm{ZN}}(\varepsilon_\perp) = 4p_{\mathrm{ZN}}(1-p_{\mathrm{ZN}})\sin^2(\psi), \tag{3}$$

where P_{ZN} is the ZN double passage probability, and ψ is the overall transition phase.[3,4] The single passage probability p_{ZN} is parametrized as a function of a, b, d, σ, δ and ψ. For a sloped intersection, the parameters a, b and d are defined as:

$$a^2 = (d^2-1)^{1/2}\frac{\hbar^2}{\mu(t_2^0-t_1^0)^2(E_2(r_0)-E_1(r_0))}, \tag{4}$$

$$b^2(\varepsilon_\perp) = (d^2-1)^{1/2}\frac{\varepsilon_\perp-(E_2(r_0)+E_1(r_0))/2}{(E_2(r_0)-E_1(r_0))/2}, \tag{5}$$

$$d^2 = \frac{(E_2(t_1^0)-E_1(t_1^0))((E_2(t_2^0)-E_1(t_2^0))}{(E_2(r_0)-E_1(r_0))^2}, \tag{6}$$

where r_0 is a point of the smallest energy gap between two spin-adiabatic states, and t_1^0 and t_2^0 are the turning points (see Fig. 2 in the main text). The single passage probability p_{ZN} reads

$$p_{\mathrm{ZN}}(\varepsilon_\perp) = \begin{cases} \exp\left(-\frac{\pi}{4ab}\sqrt{\frac{2}{1+\sqrt{1+b^{-4}(0.4a^2+0.7)}}}\right), b(\varepsilon_\perp)\geq 0 \\ \left(1+\mathrm{B}\left(\frac{\sigma}{\pi}\right)e^{2\delta}-g_2\sin^2(\sigma)\right)^{-1}, \quad b(\varepsilon_\perp)<0 \end{cases} \tag{7}$$

$$\mathrm{B}(x) = \frac{2\pi x^{2x}e^{-2x}}{x\Gamma^2(x)}, \tag{8}$$

where parameter g_2 and phases σ, δ and ψ are defined for different energy ranges as:

i) $\varepsilon_\perp \leq E_1(r_0)$

$$\sigma = \sigma_0, \tag{9}$$

$$\delta = -\int_{r_0}^{t_1}|K_1(r)|dr + \int_{r_0}^{t_2}|K_2(r)|dr + \delta_0, \tag{10}$$

ii) $E_1(r_0) < \varepsilon_\perp \leq E_2(r_0)$

$$\sigma = \int_{t_1}^{r_0} K_1(r)dr + \sigma_0, \tag{11}$$

$$\delta = \int_{r_0}^{t_2} |K_2(r)|dr + \delta_0, \tag{12}$$

iii) $\varepsilon_\perp > E_2(r_0)$

$$\sigma = \int_{t_1}^{r_0} K_1(r)dr - \int_{t_2}^{r_0} K_2(r)dr + \sigma_0, \tag{13}$$

$$\delta = \delta_0. \tag{14}$$

K_i, σ_0 and δ_0 are

$$K_i(r) = \sqrt{\frac{2\mu_\perp}{\hbar^2}\left(\varepsilon_\perp - E_i(r)\right)}, \tag{15}$$

$$\sigma_0 + i\delta_0 = \frac{\pi}{a\sqrt{8}} \frac{C_- + iC_+}{F_-^2 + F_+^2}, \tag{16}$$

$$F_\pm = \sqrt{\sqrt{(b^2+\gamma_1)^2+\gamma_2} \pm (b^2+\gamma_1)} + \sqrt{\sqrt{(b^2-\gamma_1)^2+\gamma_2} \pm (b^2-\gamma_1)}, \tag{17}$$

$$C_+ = F_+\left(b^2 \to \left[b^2 - \frac{0.16 b_\mathrm{x}}{\sqrt{b^4+1}}\right]\right), \tag{18}$$

$$C_- = F_-\left(\gamma_2 \to \left[\frac{0.45d}{1 + 1.5\exp\left(2.2 b_\mathrm{x} |b_\mathrm{x}|^{0.57}\right)}\right]\right), \tag{19}$$

$$b_\mathrm{x} = b^2 - 0.9553, \qquad \gamma_1 = 0.9\sqrt{d^2-1}, \qquad \gamma_2 = \frac{7}{16}d. \tag{20}$$

For the internal energies below MECP, $b < 0$, and ψ is an argument of the Stock's constant U_1:

i) $b(\varepsilon_\perp) < 0$

$$\psi = \arg(U_1), \tag{21}$$

$$\mathrm{Re}(U_1) = \cos(\sigma)\left[e^{\delta}\sqrt{\mathrm{B}(\sigma/\pi)} - g_1 \sin^2(\sigma)\frac{e^{-\delta}}{\sqrt{\mathrm{B}(\sigma/\pi)}}\right], \tag{22}$$

$$\mathrm{Im}(U_1) = \sin(\sigma)\left[e^{2\delta}\mathrm{B}(\sigma/\pi) - g_1^2 \sin^2(\sigma)\cos^2(\sigma)\frac{e^{-2\delta}}{\mathrm{B}(\sigma/\pi)} + 2g_1\cos^2(\sigma) - g_2\right], \tag{23}$$

$$g_1 = 1.8(a^2)^{0.23}e^{-\delta}, \qquad g_2 = \frac{3\sigma}{\pi\delta}\ln(1.2 + a^2) - \frac{1}{a^2}, \tag{24}$$

where function B is defined by Eq. 8. For the internal energies above MECP, ψ is defined as:

ii) $b(\varepsilon_\perp) \geq 0$

$$\psi = \sigma + \varphi_s, \tag{25}$$

$$\varphi_s = -\frac{\delta_\psi}{\pi} + \frac{\delta_\psi}{\pi}\ln\left(\frac{\delta_\psi}{\pi}\right) - \arg\Gamma\left(i\frac{\delta_\psi}{\pi}\right) - \frac{\pi}{4}, \tag{26}$$

$$\delta_\psi = \delta\left(1 + \frac{5\sqrt{a}}{\sqrt{a} + 0.8}10^{-\sigma}\right). \tag{27}$$

Rate constants and transition probabilities between individual M_S components for triplet-quintet crossing

The spin-orbit Hamiltonian in the basis of spin-diabatic states $\{|S, M_s\rangle\}$ is:

$$\boldsymbol{H}_{\mathrm{SO}} = \begin{array}{c} \\ |1,-1\rangle \\ |1,0\rangle \\ |1,+1\rangle \\ |2,-2\rangle \\ |2,-1\rangle \\ |2,0\rangle \\ |2,+1\rangle \\ |2,+2\rangle \end{array} \begin{array}{c} \begin{array}{cccccccc} |1,-1\rangle & |1,0\rangle & |1,+1\rangle & |2,-2\rangle & |2,-1\rangle & |2,0\rangle & |2,+1\rangle & |2,+2\rangle \end{array} \\ \begin{pmatrix} 0 & 0 & 0 & z_1 & ib_1 & z_2 & 0 & 0 \\ 0 & 0 & 0 & 0 & z_3 & ib_2 & z_3^* & 0 \\ 0 & 0 & 0 & 0 & 0 & z_2^* & ib_1 & z_1^* \\ z_1^* & 0 & 0 & 0 & 0 & 0 & 0 & 0 \\ -ib_1 & z_3^* & 0 & 0 & 0 & 0 & 0 & 0 \\ z_2^* & -ib_2 & z_2 & 0 & 0 & 0 & 0 & 0 \\ 0 & z_3 & -ib_1 & 0 & 0 & 0 & 0 & 0 \\ 0 & 0 & z_1 & 0 & 0 & 0 & 0 & 0 \end{pmatrix} \end{array}, \tag{28}$$

where the non-zero spin-orbit coupling matrix elements include three complex numbers (z_1 , z_2, z_3) and two real numbers (b_1, b_2):

$$z_1 = \langle 1,-1|\hat{H}_{\mathrm{SO}}|2,-2\rangle, \qquad ib_1 = \langle 1,-1|\hat{H}_{\mathrm{SO}}|2,-1\rangle,$$

$$z_2 = \langle 1,-1|\hat{H}_{\mathrm{SO}}|2,0\rangle,$$

$$z_3 = \langle 1,0|\hat{H}_{\mathrm{SO}}|2,-1\rangle, \qquad ib_2 = \langle 1,0|\hat{H}_{\mathrm{SO}}|2,0\rangle. \tag{29}$$

The single-passage LZ probabilities $p_{LZ}^{M_S, M_{S'}}(\varepsilon_\perp)$ between the components M_S and $M_{S'}$ of the spin states $S = 1$ and $S' = 2$ read

$$p_{LZ}^{-1,-2}(\varepsilon_\perp) = p_{LZ}^{1,+2}(\varepsilon_\perp) = 1 - \exp\left(-\frac{2\pi z_1 z_1^*}{\hbar|\Delta \boldsymbol{g}|}\sqrt{\frac{\mu_\perp}{2(\varepsilon_\perp - E_{\mathrm{X}})}}\right), \tag{30}$$

$$p_{LZ}^{-1,-1}(\varepsilon_\perp) = p_{LZ}^{+1,+1}(\varepsilon_\perp) = 1 - \exp\left(-\frac{2\pi b_1^2}{\hbar|\Delta \boldsymbol{g}|}\sqrt{\frac{\mu_\perp}{2(\varepsilon_\perp - E_{\mathrm{X}})}}\right), \tag{31}$$

$$p_{LZ}^{-1,0}(\varepsilon_\perp) = p_{LZ}^{1,0}(\varepsilon_\perp) = 1 - \exp\left(-\frac{2\pi z_2 z_2^*}{\hbar|\Delta \boldsymbol{g}|}\sqrt{\frac{\mu_\perp}{2(\varepsilon_\perp - E_{\mathrm{X}})}}\right), \tag{32}$$

$$p_{LZ}^{0,-1}(\varepsilon_\perp) = p_{LZ}^{0,+1}(\varepsilon_\perp) = 1 - \exp\left(-\frac{2\pi z_3 z_3^*}{\hbar|\Delta \boldsymbol{g}|}\sqrt{\frac{\mu_\perp}{2(\varepsilon_\perp - E_{\mathrm{X}})}}\right), \tag{33}$$

$$p_{LZ}^{0,0}(\varepsilon_\perp) = 1 - \exp\left(-\frac{2\pi b_2^2}{\hbar|\Delta \boldsymbol{g}|}\sqrt{\frac{\mu_\perp}{2(\varepsilon_\perp - E_{\mathrm{X}})}}\right), \tag{34}$$

where $p_{LZ}^{M_S, M_{S'}} = p_{LZ}^{-M_S, -M_{S'}}$. The double-passage probabilities $P_{LZ}^{M_S, M_{S'}}$ are calculated from the single passage probabilities using Eq. (3.4) from the main text and used to obtain the microcanonical rate constants between individual M_S components,

$$k_{\pm1,\pm2}(E) = \frac{\sigma}{h\,\rho_{\mathrm{R}}(E)}\int_0^E \rho_{\mathrm{X}}(E-\varepsilon_\perp)P_{LZ}^{\pm1,\pm2}(\varepsilon_\perp)d\varepsilon_\perp, \tag{35}$$

$$k_{\pm1,\pm1}(E) = \frac{\sigma}{h\,\rho_{\mathrm{R}}(E)}\int_0^E \rho_{\mathrm{X}}(E-\varepsilon_\perp)P_{LZ}^{\pm1,\pm1}(\varepsilon_\perp)d\varepsilon_\perp, \tag{36}$$

$$k_{\pm1,0}(E) = \frac{\sigma}{h\,\rho_{\mathrm{R}}(E)}\int_0^E \rho_{\mathrm{X}}(E-\varepsilon_\perp)P_{LZ}^{\pm1,0}(\varepsilon_\perp)d\varepsilon_\perp, \tag{37}$$

$$k_{0,\pm1}(E) = \frac{\sigma}{h\,\rho_{\mathrm{R}}(E)}\int_0^E \rho_{\mathrm{X}}(E-\varepsilon_\perp)P_{LZ}^{0,\pm1}(\varepsilon_\perp)d\varepsilon_\perp, \tag{38}$$

$$k_{0,0}(E) = \frac{\sigma}{h\,\rho_{\mathrm{R}}(E)}\int_0^E \rho_{\mathrm{X}}(E-\varepsilon_\perp)P_{LZ}^{0,0}(\varepsilon_\perp)d\varepsilon_\perp. \tag{39}$$

Similarly, the rate constants between individual M_S components can be obtained for any pair of spin states with $|S - S'|$ =1.

Effective Hessian

The complete derivation of the effective Hessian using the method of Lagrange multipliers is described in detail elsewhere.[5] Here, we skip the initial steps up to the more general form of Eq. (3.26) from the main text:

$$\mathbf{H}_{\text{eff}} = \frac{|\mathbf{g}_1|\cos(\theta)\mathbf{H}_2 + [|\Delta\mathbf{g}| - |\mathbf{g}_1|\cos(\theta)]\mathbf{H}_1}{|\Delta\mathbf{g}|}, \tag{40}$$

At MECP, the angle θ between the collinear gradient vectors $\mathbf{g}_1$ and $\mathbf{g}_2$ is equal to 0° or 180°, and Eq. *S*40 can be reduced to

$$\mathbf{H}_{\text{eff}} = \frac{|\mathbf{g}_1|\mathbf{H}_2 + |\mathbf{g}_2|\mathbf{H}_1}{|\mathbf{g}_1| + |\mathbf{g}_2|}, \qquad \text{if } \mathbf{g}_1^{\mathrm{T}}\mathbf{g}_2 < 0, \quad \begin{cases} |\mathbf{g}_1| < |\mathbf{g}_2|, |\Delta\mathbf{g}| = |\mathbf{g}_1| + |\mathbf{g}_2|, \cos(\theta) = 1 \\ |\mathbf{g}_1| > |\mathbf{g}_2|, |\Delta\mathbf{g}| = |\mathbf{g}_1| + |\mathbf{g}_2|, \cos(\theta) = 1' \end{cases} \tag{41}$$

or to

$$\mathbf{H}_{\text{eff}} = \frac{|\mathbf{g}_1|\mathbf{H}_2 - |\mathbf{g}_2|\mathbf{H}_1}{|\mathbf{g}_1| - |\mathbf{g}_2|}, \qquad \text{if } \mathbf{g}_1^{\mathrm{T}}\mathbf{g}_2 > 0, \quad \begin{cases} |\mathbf{g}_1| < |\mathbf{g}_2|, |\Delta\mathbf{g}| = |\mathbf{g}_2| - |\mathbf{g}_1|, \cos(\theta) = -1 \\ |\mathbf{g}_1| > |\mathbf{g}_2|, |\Delta\mathbf{g}| = |\mathbf{g}_1| - |\mathbf{g}_2|, \cos(\theta) = 1 \end{cases}, \tag{42}$$

where $\mathbf{g}_1^{\mathrm{T}}\mathbf{g}_2 < 0$ and $\mathbf{g}_1^{\mathrm{T}}\mathbf{g}_2 > 0$ correspond to peaked and sloped intersections, respectively. Eq. (26) in the main text is a unified form of Eqs. (41) and (42).

Effective Hessian tool *effhess*

Because an MECP is not a stationary point on either of two PESs of the crossing spin states, the traditional vibrational analysis cannot be used. Instead, an *effective* Hessian defined on the crossing seam of two PESs using the state-specific gradients

and Hessian matrices must be constructed. This can be accomplished with the computational tool *effhess*, which is included in the NAST package. Currently, *effhess* can automatically extract the state-specific gradients and Hessians from the GAMESS and Molpro output files. However, it can use the state-specific gradients and Hessians from any electronic structure program. The code is automated to deal with imaginary frequencies, if any are found after diagonalization of the effective Hessian matrix. Such imaginary frequencies indicate that the found critical point is not a true MECP and a subsequent re-search is required. In this case, the *effhess* tool generates a series of molecular geometries with displacements along the imaginary frequency normal modes. The generated geometries can be used to restart the MECP search. The *effhess* tool also generates a template of a NAST input file containing the calculated MECP properties.

The effective Hessian matrix is calculated as:

$$\mathbf{H}_{\text{eff}} = \frac{|\mathbf{g}_1|\mathbf{H}_2 \pm |\mathbf{g}_2|\mathbf{H}_1}{|\mathbf{g_1}| \pm |\mathbf{g_2}|}, \tag{43}$$

where **g** and **H** are the state-specific gradients and Hessian matrices at MECP obtained from standard electronic structure calculations. The mass-weighted effective Hessian (MWEH) reads

$$\mathbf{H}_{\text{eff}}^{\text{mw}}(i,j) = \frac{\mathbf{H}_{\text{eff}}(i,j)}{\sqrt{m_i m_j}}, \tag{44}$$

where m_i and m_j are masses of atoms i and j, respectively. To remove the seven frequencies associated with the translational, rotational and the reaction coordinate (RC) degrees of freedom, the following projection is performed:

$$\mathbf{H}_{\mathrm{proj}} = (\mathbf{I} - \mathbf{P})\mathbf{H}_{\mathrm{eff}}^{\mathrm{mw}}(\mathbf{I} - \mathbf{P}), \tag{45}$$

where **I** is the identity matrix, and the projection matrix $\mathbf{P} = \mathbf{P}_{\mathrm{tr}} + \mathbf{P}_{\mathrm{rot}} + \mathbf{P}_{\mathrm{RC}}$ is the sum of the translational, rotational and RC projection matrices. Elements of **P** are defined in the earlier work.[3] To calculate the reduce mass along the reaction coordinate, we also project MWEH on RC.

$$\mathbf{H}_{\mathrm{proj}}^{\mathrm{RC}} = \mathbf{P}_{\mathrm{RC}}\mathbf{H}_{\mathrm{eff}}^{\mathrm{mw}}\mathbf{P}_{\mathrm{RC}}. \tag{46}$$

The $\mathbf{H}_{\mathrm{proj}}^{\mathrm{RC}}$ matrix is diagonalized to obtain the eigenvector **k** corresponding to the non-zero eigenvalue. This vector is mass-weighted by dividing each component by the square root of mass of the corresponding atom. The resulting mass-weighted eigenvector $\mathbf{k}^{\mathrm{mw}}$ is used to calculate the reduced mass along RC,

$$\mu_{\perp} = (\mathbf{k}^{\mathrm{T,mw}}\,\mathbf{k}^{\mathrm{mw}})^{-1}. \tag{47}$$

Intrinsic reaction coordinate fit tool *ircfit*

To ensure the quality of the fit in the vicinity of MECP, the MECP→product path is fitted using only the IRC points lying above the reactant minimum. The *ircfit* tool works with polynomials up to the fourth order. The choice of the polynomial order (from 1 to 4) is based on the number of the IRC points above the reactant minimum. If the number of points is equal or greater than five, the quartic polynomial is used. Otherwise, the order of the fitting polynomial is smaller than the number of points by one. Different polynomial fittings are shown in Fig. 2.

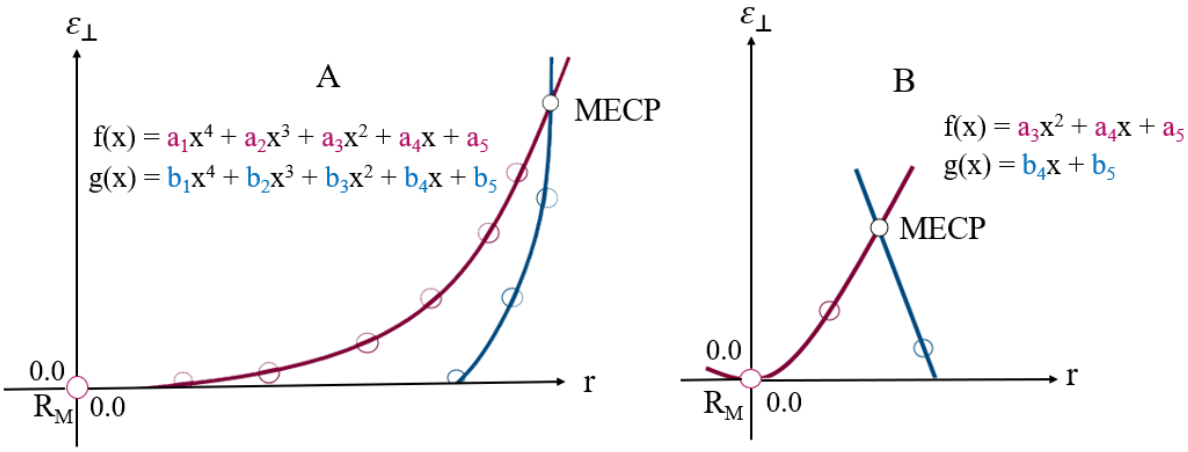

Figure 2. Two examples of the fitted IRC paths along the reaction coordinate r. R_M is the reactant minimum, $\varepsilon_\perp$ is the energy partitioned in the reaction coordinate. A) Sloped intersection with the reactant and product IRC points fitted by quartic polynomials. B) Peaked intersection with the reactant and product IRC points fitted by quadratic and linear functions, correspondingly.

The vector of the fitting polynomial coefficients **c** is obtained by solving the following system of linear equations:

$$\frac{\partial F}{\partial \mathbf{c}} = 0, \tag{48}$$

$$F = \sum_{i=1}^{k} \left(E_i - f(\mathbf{c}, r_i)\right)^2, \tag{49}$$

$$f(\mathbf{c}, r) = \begin{cases} c_1 r^4 + c_2 r^3 + c_3 r^2 + c_4 r + c_5 \text{ or} \\ c_2 r^3 + c_3 r^2 + c_4 r + c_5 \text{ or} \\ c_3 r^2 + c_4 r + c_5 \text{ or} \\ c_4 r + c_5 \end{cases}, \tag{50}$$

where k is the number of IRC points used in the fit, and F is the linear least squares function.

Input files for the electronic structure, NAST and MESMER calculations

The input files for the electronic structure, NAST and MESMER calculations discussed in the main text are included in the file **NAST_Topics_SI_files.tar.gz**.

References

(1) Baer, T.; Hase, W. L. *Unimolecular Reaction Dynamics: Theory and Experiments*, Oxford University Press, 1996.

(2) Green, N. J. B. *Unimolecular Kinetics, Part 1. The Reaction Step*; Elsevier, 2003.

(3) Lykhin A. O.; Varganov, S. A. Intersystem crossing in tunneling regime: $T_1 \rightarrow S_0$ relaxation in thiophosgene. *Phys. Chem. Chem. Phys.* **2020**, *22*, 5500-5508. https://doi.org/10.1039/c9cp06956a.

(4) Nakamura, H. *Nonadiabatic transition: concepts, basic theories and applications*, 2nd ed.; World Scientific, 2012.

(5) Lykhin, A. O., Truhlar D. G., Gagliardi L. Role of Triplet States in the Photodynamics of Aniline. *J. Am. Chem. Soc.* **2021**, *143*, 5878-5889. https://doi.org/10.1021/jacs.1c00989.

APPENDIX B. CHAPTER 4 SUPPLEMENTAL MATERIALS

Here we present the raw data for free-induction decay (FID) measurements of T_2^* and a comparison to the depolarization spectroscopy presented in the main paper. All data presented in this supplementary material is for ^{85}Rb, and was taken in the low-field limit with respect to the hyperfine splitting.

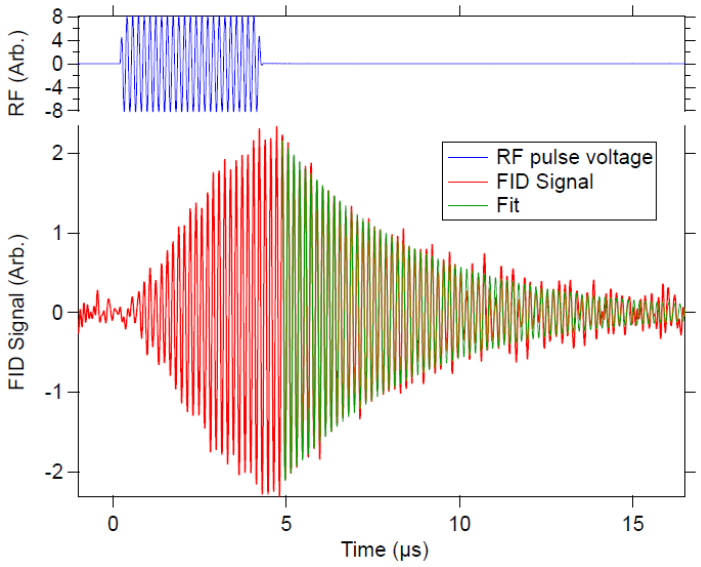

Figure 1. FID data taken at a "low" bias field, such that all Larmor precession frequencies are nearly degenerate.

We first present the raw FID data. Figure 1 presents FID data taken at a sufficiently low magnetic field such that the different single-photon lines cannot be spectrally resolved. After optical pumping, Larmor precession is excited by an RF pulse. The circular dichroism signal is monitored continuously by a single weak probe beam at an angle to the magnetic field, and this signal is put through a high-pass filter to remove changes in the DC level. The data presented in Figure 1 was taken at a bias

field of $\sim$ 13 Gauss. At this field all Larmor precession frequencies (for the free atom) differ by $\lesssim$ 0.1 MHz due to the nonlinear Zeeman shift. The observed Larmor precession is fit to an exponentially decaying sine wave $A\sin(\omega t+\phi)e^{-t/T_2^*}$, giving a measured T_2^* of 4 μs. It is possible that this is partially limited by the unresolved substructure (see Figure 4.1 of the main paper).

At higher magnetic fields the nonlinear Zeeman effect is sufficiently large that the different single-photon lines can be spectrally resolved; sample FID data under these conditions is shown in Figure 2. The beating of multiple frequencies makes it impractical to fit this FID data as in the low-field case. Instead, we Fourier transform the signal to obtain a spectrum. In this spectrum we observe six Larmor precession lines from the $F = 3$ hyperfine manifold, as discussed in the main text.

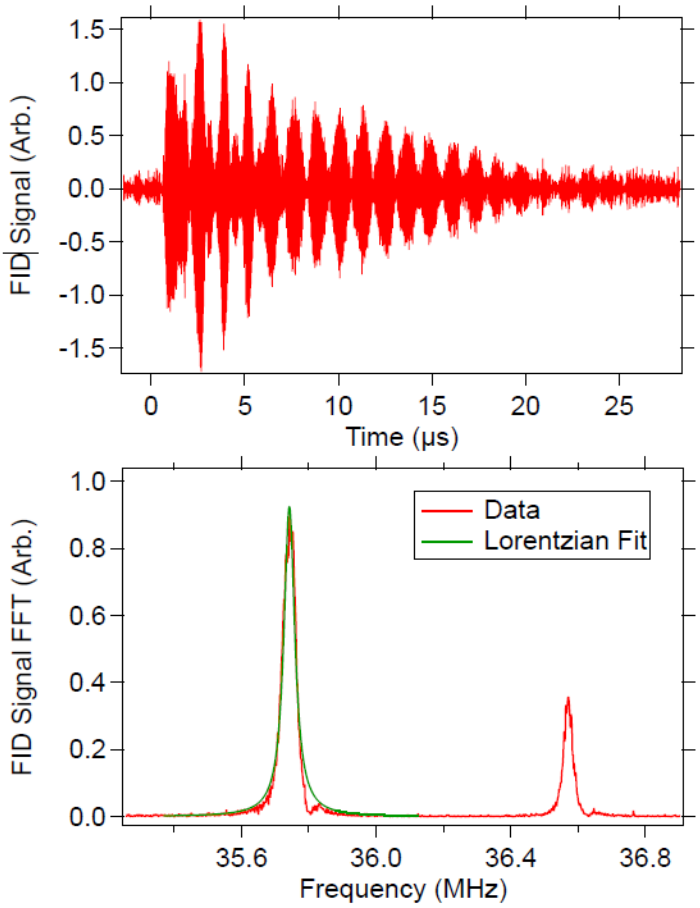

Figure 2. FID data taken at a "high" magnetic bias field of ~ 78 G. The raw data is shown at the top; the RF pulse was applied from 0.4 to 1.4 μs. The FID oscillations are too fast to be seen on this timescale, but the beating from multiple frequencies (due to the nonlinear Zeeman shift) can be clearly observed. A Fourier transform of the signal (at times after the RF pulse is off) is shown below, and fit as described in the text.

The lower graph of Figure 2 shows two of those peaks, the $+1 \leftrightarrow 0$ and $-1 \leftrightarrow 0$ transitions. Each has a small side peak from the $F = 2$ manifold, as discussed in the main text. We fit each $F = 3$ peak to a Lorentzian and determine its full width at half maximum (FWHM). T_2^* is determined for each transition from the measured FWHM via $T_2^* = \frac{1}{\pi \mathrm{FWHM}}$, where FWHM is expressed in cycles per unit time. Repeating the measurements of Figure 2 multiple times, we obtain linewidths of 40 kHz and 28 kHz.

From multiple measurements we obtain an average FWHM for the $|F = 3, m_F = 0\rangle \leftrightarrow |F = 3, m_F = \pm 1\rangle$ transitions of 34 ± 3 kHZ, corresponding to a T_2^* of 10 ± 1 μs.

All the data presented in the body of the paper is from "depolarization" data. A fit to raw depolarization data is shown in Figure 3. This data is taken at a similar magnetic field as Figure 2, with a slight difference in the magnetic field leading to a small difference ($\lesssim 0.2\%$) in the center frequencies.

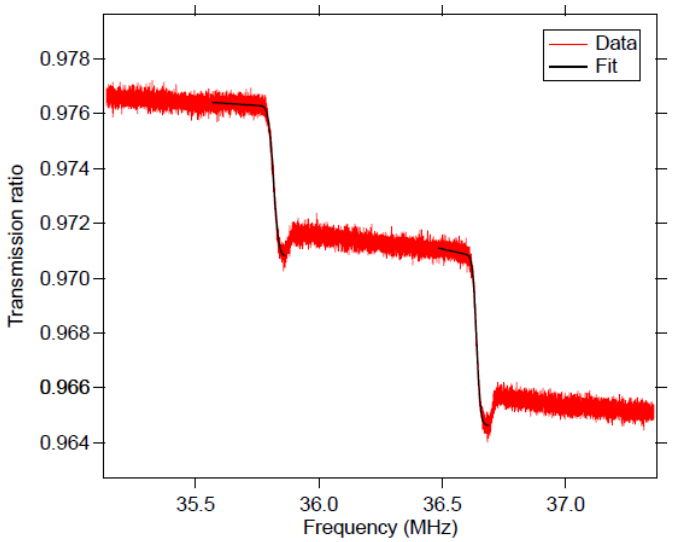

Figure 3. Sample raw depolarization data, taken at a magnetic field of $B_z \sim 78$ G, plotted over a range showing the $|m_F = 0\rangle \leftrightarrow |m_F = \pm 1\rangle$ transitions. Each transition in the $F = 3$ manifold is fit to an error function plus an offset and a constant slope. To the right of each $F = 3$ transition is a transition in the $F = 2$ manifold, as discussed in the main text.

In the data of Figure 2, we operate at a Rabi frequency much greater than the linewidth, so that we can excite multiple Larmor superpositions with a single pulse. In the data of Figure 3 we operate in the opposite limit of small Rabi frequencies to avoid power broadening.

The fits shown in Figure 3 give a FWHM of 38 kHz and 30 kHz. An average of similar fits yields an average FWHM for the $|F = 3, m_F = 0\rangle \leftrightarrow |F = 3, m_F = \pm 1\rangle$ transitions of 37 $\pm$ 3 kHZ, corresponding to a T_2^* of 9 $\pm$ 1 μs.

Thus, the linewidths from the FID and depolarization methods agree to within our experimental error.

Finally, Figure 4 shows the raw depolarization data for the $|F = 3, m_F = +1\rangle \leftrightarrow |F = 3, m_F = -1\rangle$ two-photon transition. This data was taken at a small Rabi frequency to avoid power broadening. To maximize the signal we wish to maximize the population difference between the m_F = +1 and -1 states prior to the depolarization sweep. To do so, we first conducted high-power "pre-sweeps" over the -3 ↔ -2 and -2 ↔ -1 transitions, followed by the +1 ↔ +2 and +2 ↔ +3 transitions. The data was fit in the same manner as Figure 3, giving a FWHM of 5.2 kHz and a T_2^* of 60 μs.

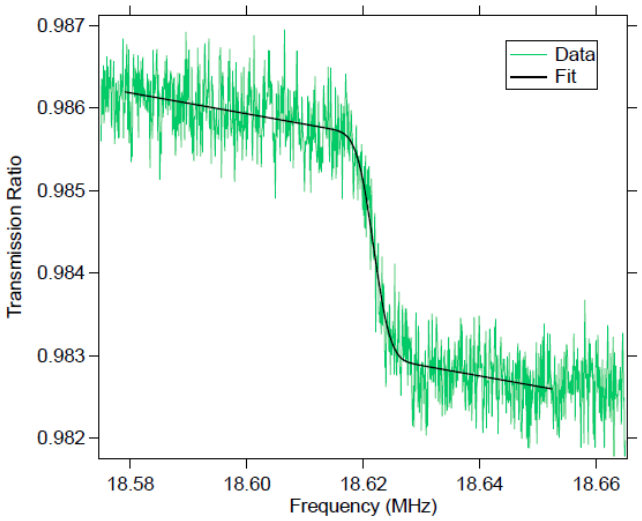

Figure 4. Simple raw depolarization data, taken at a magnetic field of $B_z \sim$ 38 G, showing the $|m_F = +1\rangle \leftrightarrow |m_F = -1\rangle$ two-photon transition.

APPENDIX C. CHAPTER 6 SUPPLEMENTAL MATERIALS

A. Invariance of molecular geometry under variation of fundamental constants in the non-relativistic Born-Oppenheimer approximation

The goal of this section is to prove that the effect of variation of fundamental constants cause all the molecular bonds to stretch/dilate by the very same scaling factor, leaving the angles between chemical bonds unaffected, see Figure 1. This statement holds only in the assumption of (i) non-relativistic approximation, (ii) infinitely-heavy nuclei (Born-Oppenheimer approximation) and (iii) point-like spin-less nuclei. If either of these assumptions is broken, chemical bond angles would vary with changing FCs.

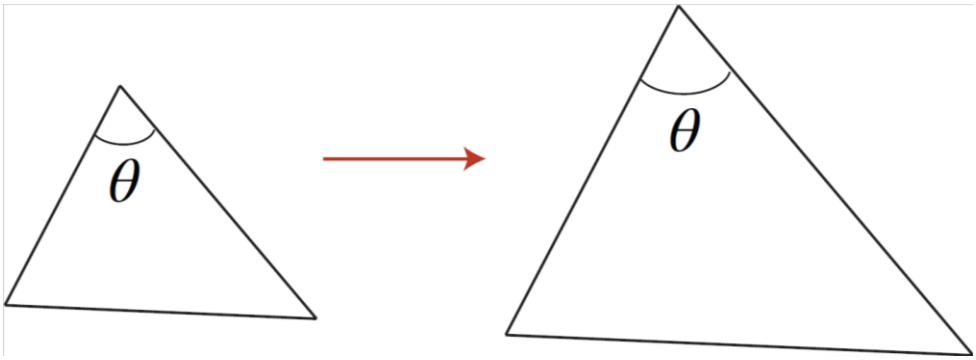

Figure 1. Scaling all the sides of the triangle by the very same numerical factor does not affect the value of angle θ (or of any other angle in the triangle). This example can be generalized to 3D geometry: angles and thus the molecular geometry are not affected by scaling of all the inter-nuclear distances by the same factor (isotropic scaling transformation).

Consider an arbitrary molecule containing N_n point-like nuclei and N_e electrons. Under the enumerated assumptions, the non-relativistic Born-Oppenheimer (NR-BO) Hamiltonian reads

$$H_{\mathrm{NR-BO}} = \sum_i -\frac{\hbar^2}{2m_e}\Delta_{r_i} + \frac{1}{2}\sum_{i\neq j}\frac{e^2}{|\mathbf{r}_i - \mathbf{r}_j|} + \frac{1}{2}\sum_{n\neq n'}\frac{Z_n Z_{n'} e^2}{|\mathbf{R}_n - \mathbf{R}_{n'}|} - \sum_{i,n}\frac{Z_n e^2}{|\mathbf{R}_n - \mathbf{r}_i|}. \quad (1)$$

Here, for clarity, we retained all the fundamental constants (FCs). We labeled positions of electrons as $\mathbf{r}_i$ and those of nuclei as $\mathbf{R}_n$. All the terms in $H_{\mathrm{NR-BO}}$ have their usual meaning: kinetic energy of electrons, electron repulsion, nuclear repulsion, and electron-nucleus attraction. Z_n are nuclear charges. To determine the molecular geometry in the Born-Oppenheimer approximation, one solves the time-independent Schrödinger equation with fixed positions of nuclei,

$$H_{\mathrm{NR-BO}}(\mathbf{r}_e|\mathbf{R}_n)\Psi(\mathbf{r}_e|\mathbf{R}_n) = E(\mathbf{R}_n)\Psi(\mathbf{r}_e|\mathbf{R}_n). \quad (2)$$

Here the Hamiltonian H and thus the eigenfunctions Ψ and energies E depend on fundamental constants: $E(\mathbf{R}_n|m_e, \hbar, e)$. After the potential surfaces $E(\mathbf{R}_n|m_e, \hbar, e)$ are obtained as functions of nuclear coordinates, the equilibrium nuclear positions, $\{\mathbf{R}_n^{\mathrm{eq}}\}$, are determined by minimizing the energy

$$\min_{\{\mathbf{R}_n\}} E(\mathbf{R}_n|m_e, \hbar, e) \Rightarrow \{\mathbf{R}_n^{\mathrm{eq}}\}. \quad (3)$$

We would like to explicitly factor out the dependence on FCs from Eq. (2). To this end we rescale all the coordinates by the same factor ξ: $\mathbf{r}_i \rightarrow \xi\boldsymbol{\rho}_i$, $\mathbf{R}_n \rightarrow \xi\boldsymbol{\rho}_n$. Upon

substitution into $H_{\mathrm{NR-BO}}$, the kinetic energy term transforms into $-\sum_i^{N_e} \frac{\hbar^2}{2m_e\xi^2}\Delta_{\rho_i}$ and all the electrostatic interaction potentials are divided by ξ. We pick the dimension-full pre-factors in the kinetic and potential energy contributions to be equal.

$$\frac{\hbar^2}{m_e\xi^2} = \frac{e^2}{\xi}. \tag{4}$$

This particular choice enables factoring out the dependence on the FCs from the Hamiltonian H. Solving the above equation results in

$$\xi = \frac{\hbar^2}{m_e e^2}, \tag{5}$$

which is the Bohr radius a. Then the Hamiltonian is $H_{\mathrm{NR-BO}} = E_h h(\boldsymbol{\rho}_e|\boldsymbol{\rho}_n)$, where

$$E_h = \hbar^2/m_e\xi^2 \ = e^2/\xi = m_e e^4/\hbar^2 \tag{6}$$

is atomic unit of energy (Hartree). Moreover, the scaled Hamiltonian $h(\boldsymbol{\rho}_e|\boldsymbol{\rho}_n)$ no longer depends on FCs. Thereby, the solution of the eigenvalue equation (Eq. 2)

$$h(\boldsymbol{\rho}_e|\boldsymbol{\rho}_n)\varphi(\boldsymbol{\rho}_e|\boldsymbol{\rho}_n) = \varepsilon(\boldsymbol{\rho}_n)\varphi(\boldsymbol{\rho}_e|\boldsymbol{\rho}_n) \tag{7}$$

does not depend on FCs either. For any value of FCs,

$$E(\mathbf{R}_n|m_e,\hbar,e) = \frac{m_e e^4}{\hbar^2}\varepsilon(\boldsymbol{\rho}_n). \tag{8}$$

Finding equilibrium positions as prescribed by Eq. (9) also does not depend on FCs,

$$\min_{\{\boldsymbol{\rho}_n\}} \varepsilon(\boldsymbol{\rho}_n) \ \Rightarrow \ \{\boldsymbol{\rho}_n^{\mathrm{eq}}\}. \tag{9}$$

Thereby,

$$\mathbf{R}_n^{\mathrm{eq}} = \frac{\hbar^2}{m_e e^2}\boldsymbol{\rho}_n^{\mathrm{eq}}, \tag{10}$$

where $\boldsymbol{\rho}_n^{\mathrm{eq}}$ are FC-independent.

To reiterate, in the non-relativistic Born-Oppenheimer approximation, as the FCs are varied from their nominal values, all the equilibrium positions are scaled by the very same factor,

$$\mathbf{R}_n^{\mathrm{eq}} = \frac{a}{a_0}\mathbf{R}_{n,0}^{\mathrm{eq}}. \tag{11}$$

Here and below all the quantities with the subscript 0 refer to the nominal values. This scaling of all the coordinates by the same factor belongs to the class of isotropic scaling transformations; as such it does not affect molecular bond angles, see Figure 1.

The fact that the isotropic scaling does not affect angles in a molecule of arbitrary geometry can be formally proven as follows. Choose $\{\mathbf{R}_n\}, n = \overline{1,N}$ to be (equilibrium) position vectors of all N nuclei in a molecule. The angle θ_{ab} between a pair of these vectors, $\mathbf{R}_a$ and $\mathbf{R}_b$, is given by

$$\theta_{ab} = \cos^{-1}\left[\frac{(\mathbf{R}_a \cdot \mathbf{R}_b)}{|\mathbf{R}_a||\mathbf{R}_b|}\right], \tag{12}$$

where we used the conventional definition of scalar products and $|\mathbf{R}_a| = \sqrt{(\mathbf{R}_a \cdot \mathbf{R}_a)}$ is the length of the vector. Should all the position vectors be scaled by some factor λ, $\$\mathbf{R}_n \rightarrow \lambda\mathbf{R}_n$, the factors of λ in Eq. (12) cancel out. Thereby, the angles between chemical bonds are not affected by the isotropic scaling. The entire molecule undergoes isotropic stretching or dilation as the FCs are varied.

In addition, as follows from our derivation, all the electron coordinates undergo the same isotropic scaling,

$$\mathbf{r}_e = \frac{a}{a_0}\mathbf{r}_{e,0}. \tag{13}$$

In particular, it means that the sizes of electronic clouds and atoms are scaled by the same a/a_0 ratio. Another point is that all the energies (both atomic and molecular) are scaled by the atomic unit of energy

$$E = \frac{E_h}{E_{h,0}}E_0. \tag{14}$$

These observations offer a visualization: as a clump of FCs sweeps through an atom or a molecule, all the energy states are gently modulated and the atoms and molecules "breathe" in accordance with the local values of FCs. This picture is valid in the regime of sufficiently large and slow FC clumps. The clumps need to be sufficiently large, so there are no gradients of FCs across individual atoms and molecules. The clumps have to be sufficiently slow, so that the induced perturbation does not cause transitions between molecular or atomic states. Then the molecules follow the change in FCs adiabatically.

It is worth emphasizing that our proof heavily relied on the possibility of factoring out all the dependence on FCs in various contributions to the $H_{\mathrm{NR-BO}}$ Hamiltonian. If we were to add kinetic energies of the nuclei to $H_{\mathrm{NR-BO}}$, our coordinate scaling procedure would result in the requirement

$$\frac{\hbar^2}{m_e\xi^2} = \frac{e^2}{\xi} = \frac{\hbar^2}{M_1\xi^2} = \cdots = \frac{\hbar^2}{M_N\xi^2}, \tag{15}$$

where M_n are nuclear masses. Generically, these equalities cannot be satisfied simultaneously by any choice of the scaling parameter ξ.

Our factorization procedure depended on the fact that the Coulomb interactions in the $H_{\mathrm{NR-BO}}$ Hamiltonian exhibited power-law dependence with respect to distances. If the nuclei have finite size, the Hamiltonian no longer admits simple coordinate scaling. Moreover, introducing nuclear properties (such as finite-size charge distribution or hyperfine interactions with nuclear moments) into the problem brings in another FC, $m_q/\Lambda_{\mathrm{QCD}}$, where m_q is the average mass of up and down quarks and Λ_{QCD} is the energy scale of quantum chromo-dynamics.

Similarly, Dirac equation does not admit factoring out all the FCs in the Hamiltonian. Indeed, even in the simplest case of hydrogen atom with an infinitely-heavy point-like nucleus, Dirac Hamiltonian contains three terms,

$$h_{\mathrm{D}} = -i\hbar c\boldsymbol{\alpha}\cdot\boldsymbol{\nabla} + \beta m_e c^2 - \frac{e^2}{r}. \tag{16}$$

Since the 4 × 4 Dirac matrices $\boldsymbol{\alpha}$ and β are collections of FC-independent c-numbers, our coordinate scaling procedure results in the requirement

$$\frac{\hbar c}{\xi} = m_e c^2 = \frac{e^2}{\xi}. \tag{17}$$

For arbitrary values of FCs (m_e, $\hbar$, e, and c), these equalities are mutually exclusive. We conclude that relativity must lead to the breakdown of the isotropic scaling of atomic structure and molecular geometry with varying FCs. Chemical bond angles vary with changing FCs due to relativistic effects.

Since the theory of quantum electrodynamics (QED) is built on quantizing relativistic fields, field-theoretic effects also lead to the breakdown of the isotropic scaling with varying FCs. This can be easily seen by examining effects of vacuum polarization by the nucleus[1]. In QED, a nucleus is immersed into a nuclear-field-polarized cloud of virtual pairs of particles and anti-particles. Vacuum polarization leads to the replacement of the $-Z/r$ Coulomb potential of a point-like nucleus by the Uehling potential. The success of our factorization procedure depends on the fact that the Coulomb interactions in the NR-BO Hamiltonian exhibits a power-law dependence with respect to distances. The Uehling potential lacks this power-law dependence and, thereby, does not admit factoring out FCs in the resulting Hamiltonian.

Scaling of molecular geometry preserves angles between chemical bonds in the NR-BO approximation. Molecular geometry "breathes" with varying FCs. Consider a thought experiment where we compare lengths of two rulers of different chemical composition. Suppose at the nominal values of FCs both rulers have the same lengths. As the FCs change, both rulers are expanding/contracting by the same factor in the NR-BO approximation. The observer would not be able to tell if FCs have changed. The very same argument applies to transition frequency comparisons: in the NR-BO approximation, all the dependence of energies on FCs is governed by the common factor of Hartree energy $m_e e^4/\hbar^2$. Corrections to the most basic NR-BO approximation violate this isotropic scaling law: the lengths of two rulers in our though experiment would differ for varying FCs. Similarly, the ratios of transition frequencies for two different atoms or molecules would change with varying FCs.

B. Critical values of α for finite-size nuclei

The critical value α^* of varying electromagnetic fine structure constant α is determined by the requirement that the energy ε of the bound electron becomes equal to the Dirac sea threshold, $\varepsilon = -2m_e c^2$. Here and below the energy excludes the rest mass energy. This problem can be solved analytically[1,2], where the authors were interested in determining the critical nuclear charge value for the fixed nominal value of α.

The analytical solution can be developed for nuclear spherical shell-like charge density distribution, $\rho_{\text{shell}}(r) \propto \delta(r - R)$, where R is the radius of the nuclear charge shell. Qualitatively, inside the nuclear shell, $r < R$, the potential is constant $V(r) = -Ze^2/R$ and the solution to the Dirac equation is given by the energy-offset free particle solutions. Outside the nuclear shell, the potential is of the Coulomb character, $V(r) = -Ze^2/r$, and the solution to the Dirac equation is given by the linear combinations of the regular and irregular Coulomb wavefunctions. Setting $\varepsilon = -2m_e c^2$ and matching the inner and outer solutions at $r = R$ leads to a transcendental equation for α^*

$$\xi \frac{K'_{i\nu}(\xi)}{K_{i\nu}(\xi)} = 2(\alpha^* Z)\cot(\alpha^* Z), \tag{18}$$

where $\xi = \sqrt{8ZR/\alpha_0}$, $K_{i\nu}(\xi)$ is the modified Bessel function of the second kind (Macdonald function) with index $\nu \equiv 2\sqrt{(\alpha^* Z)^2 - 1}$ with $K'_{i\nu}(\xi)$ being its derivative with respect to ξ. Eq. (18) is specific to the $ns_{1/2}$ orbitals. Subsequently increasing

roots of this equation correspond to larger values of principle quantum number n. Similar equations can be derived for orbitals of larger total angular momenta.

In estimates based on solving Eq. (18), we need to specify the spherical shell radius R. We make the connection to the more realistic nuclear charge distributions by noticing that for the spherical shell distribution, the r.m.s. radius $R_{\rm rms}$ is identical to R. For proton, we take the 2018 CODATA[3] recommended value, $R_{\rm rms}(^1{\rm H}) = 0.8414(19)$ fm. For heavier elements, we use an approximation[1] $R \approx 1.6Z^{1/3}$ fm, adequate for our semi-qualitative discussions.

From Eq. (18) we find the critical value of α for hydrogen $1s_{1/2}$ orbital occurs at $\alpha^* \approx 1.04$ or $c^* \approx c_0/143$. One may argue that the spherical shell approximation for the nuclear charge distributions used in deriving Eq. (18) is not realistic. To address this question, we solved the Dirac equation for hydrogen using numerical finite-differencing techniques[4]; for the uniform nuclear charge distribution we find $\alpha^* \approx 1.042$. This is to be compared to the spherical shell result of 1.040. A similar exercise for Fermium ($Z = 100$, $A = 257$, $R_{\rm rms} = 7.1717$ fm) shows that $1s_{1/2}$ α^* for the spherical shell distribution is 1.20×10^{-2} versus 1.18×10^{-2} for both the uniform and the Fermi nuclear charge distributions. Thereby, more realistic models of charge distributions lead to somewhat smaller values of α^* than those resulting from the spherical shell distribution.

We notice that Dirac code internally uses Gaussian nuclear charge distributions with $R_{\rm rms}$ given by the fitting formula[5]

$$R_{\rm rms} = 0.836A^{1/3} + 0.570(\pm 0.05)\ \text{fm}. \qquad (19)$$

For a given charge Z we use the most abundant isotope mass number A. This formula results in the proton $R_{\mathrm{rms}}(^1\mathrm{H}) = 1.406$ fm which is almost as twice as large than the CODATA recommended value, $R_{\mathrm{rms}}(^1\mathrm{H}) = 0.8414(19)$ fm. The simple reason for this discrepancy is that Eq. (19) is a fit for atomic mass numbers $A > 9$ [5]. If we use the value $R_{\mathrm{rms}}(^1\mathrm{H}) = 1.406$ fm, Eq. (18) results in $\alpha^*(^1\mathrm{H}) = 1.044$, slightly larger than the value of 1.040 obtained with the CODATA $R_{\mathrm{rms}}(^1\mathrm{H})$.

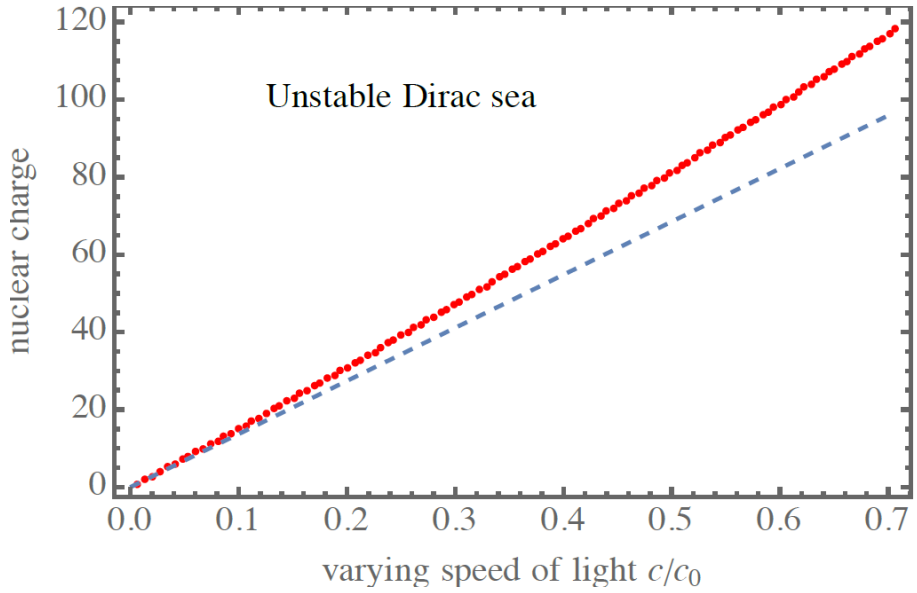

Figure 2. Phase diagram of periodic system of elements as a function of varying speed of light. Red curve are the results for critical values of c^*/c_0 as a function of nuclear charge Z for finite-size nuclei. Blue curve is the same dependence but for point-like nuclei. To borrow an analogy from condensed matter physics, α (or c) is an order parameter that governs phase transitions.

The results of our calculations are shown in Figure 2. In this plot, the red curve are the results for critical values of c^*/c_0 as a function of nuclear charge Z for finite-size nuclei. Blue curve is the same dependence but for point-like nuclei, $\alpha^* = 1/Z$. This parameter space can be interpreted as a phase diagram: any point $(c/c_0, Z)$ above the

red curve corresponds to unstable Dirac sea. Here, for comparison, we also plot the critical values for point-like nucleus, $Z_{\max} = 1/\alpha^*$, i.e. $Z_{\max} = \alpha_0 c^*/c_0$.

Finite-size nuclei critical curve exhibit nearly linear dependence with a fit,

$$Z_{\max} \approx 168\frac{c}{c_0}. \tag{20}$$

The nearly linear dependence can be understood by examining the graphical solution of transcendental Eq. (18), see Figure 3 for hydrogen. Plots for heavier elements are similar. Even without solving the Eq. (18), it is apparent that the critical value of α for the $1s_{1/2}$ orbital occurs in the vicinity of the first zero of Macdonald function $K_{i\nu}(\xi)$, where the l.h.s. approaches vertical asymptote. The first zero of $K_{i\nu}(\xi)$ is given by $\ln\xi \approx -\pi/\nu + \ln 2 - \gamma_{\text{Euler}}$, where $\gamma_{\text{Euler}} = 0.5772156649\ldots$ is the Euler constant[6]. This leads to an analytical estimate

$$\alpha^* \lesssim \frac{1}{Z}\left(1 + \frac{\pi^2}{8}\frac{1}{\left(\gamma_{\text{Euler}} + \frac{1}{2}\ln\left(\frac{\sqrt{2}ZR}{a_0}\right)^2\right)}\right). \tag{21}$$

The leading $1/Z$ term can be recognized as the critical value for point-like nucleus. We use the smaller sign ($\lesssim$) because the true value of α^* lies below this asymptotic estimate, see Figure 3. The fractional contribution of the corrective term has a weak logarithmic dependence on the nuclear charge, $\ln(Z^{4/3})$, explaining the nearly linear dependence of maximum allowed nuclear charge in Figure 2. In approximate Eq. (21) we also restored the Bohr radius a_0, showing that the dominant dependence is the ratio of nuclear radius R to the characteristic size of atomic orbital a_0/Z. Approximation

(Eq. 21) tends to overestimate α^*. Its relative accuracy ranges from 2% for hydrogen to 50% for Fermium ($Z = 100$) as follows from comparison with our numerical results.

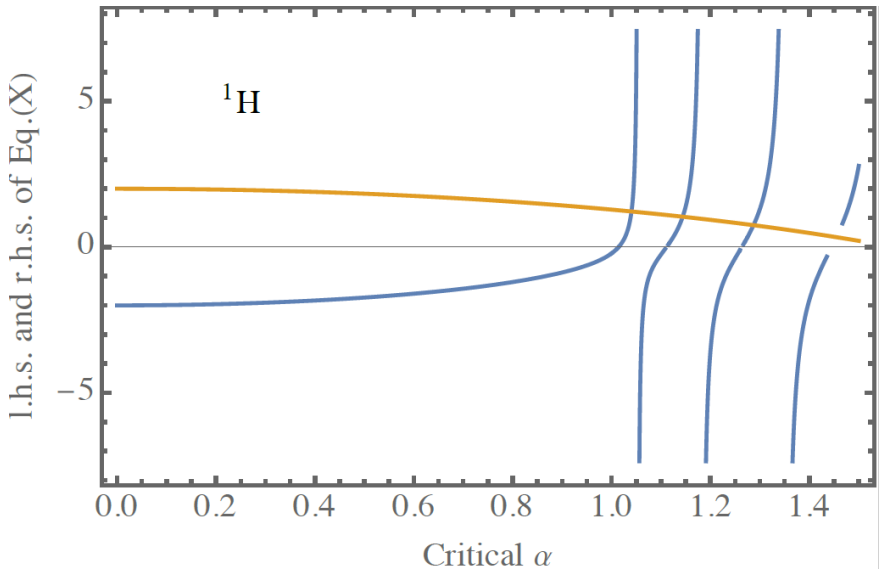

Figure 3. Graphical determination of critical values of fine-structure constant for hydrogen ($Z = 1$, $R = 0.8414$ fm). The r.h.s and the l.h.s of transcendental Eq. (18) are drawn as blue and brown curves, respectively. The values of α at the intersection of two curves are critical values, α^*. The lowest α^* is the critical value for $1s_{1/2}$, next lowest α^* is for $2s_{1/2}$ and so on.

QED corrections to the $1s_{1/2}$ energy (vacuum polarization and self-energy) tend to cancel[1], leaving critical values largely unaffected.

For multi-electron systems, the stability of an atom with respect to varying FCs requires further qualifiers. Indeed, unlike in H-like ions, a Dirac sea electron cannot transition into the fully occupied $1s_{1/2}$ orbital due to the Pauli exclusion principle[2]. Yet, because the rest-mass energy gap is lowered, background photons can promote Dirac sea electrons into unoccupied orbitals, i.e., Dirac sea becomes unstable with respect to the interaction with photon bath. As to the critical values, we computed Dirac-Hartree-Fock energies of $1s_{1/2}$ orbitals in several atoms as a function of c. We find that the

hydrogen-like ion result (Eq. 6.2) for c^* remains a good approximation. Indeed, energies of the deeply-bound $1s_{1/2}$ orbitals in atoms and molecules are strongly dominated by the interaction with the nucleus with small corrections from the interaction with other electrons.

C. Many-electron atoms

The electronic structures of selected atoms and molecules were calculated by solving the many-electron Dirac equation as implemented in the DIRAC package[7,8]. Since the typical distance of an electron from the nucleus decreases with decreasing c, e.g., for a $1s$ electron, $\langle r\rangle/a_0 \sim 3/(2Z) - Z\alpha^2/2$ in the regime of small α, the basis sets used in the calculations needed to be calibrated to accurately describe the electron density near the nucleus at reduced c. For the hydrogen atom and hydrogen-like ions of N, O, F, and Ne, the calibration procedure was designed as follows. For a selected ion, the speed of light was gradually lowered until the $1s_{1/2}$ ground state was lowered into the Dirac sea. The size of the basis set and the largest exponents were chosen by matching the critical values of c obtained using such a basis set with that predicted by solving the transcendental equation (Eq. 1). In addition, the validity of these basis sets was verified by comparing the energy state orderings they engendered with those predicted by the analytical solution of the Dirac equation, e.g., the relative order of $2s_{1/2}$ and $2p_{1/2}$ states in hydrogen as presented in Figure 6.1 in the main text.

For example, for H, the six p basis functions in the original uncontracted aug-cc-pV6Z basis set were augmented to a total of twenty. Next, the exponents of the new

functions were obtained by subsequently multiplying the largest p exponent by 3. For simplicity, the same exponents were used for s functions. This procedure was carried out until a match with the solution of Eq. 1 was obtained, while maintaining the correct ordering of the energy states (Figure 6.1). The resulting basis included twenty s and twenty p basis functions with the largest exponent of 4.1×10^7. The basis functions with higher angular momenta were left unchanged. The same strategy was applied to N, O, F, and Ne. For these elements, the modified basis sets contained nineteen s and nineteen p basis functions. The largest exponents were 6.9×10^8 for N, 8.8×10^8 for O, 1.1×10^9 for F, and 1.4×10^9 for Ne. With such modified basis sets, the DIRAC calculated values of c^* perfectly matched those predicted by Eq. 1. The critical values are $\alpha_{\mathrm{H}}^* = 1.040$, $\alpha_{\mathrm{N}}^* = 0.154$, $\alpha_{\mathrm{O}}^* = 0.135$, $\alpha_{\mathrm{F}}^* = 0.120$, and $\alpha_{\mathrm{Ne}}^* = 0.108$.

The atomic spectra of N, O, F, and Ne atoms were calculated at different values of the speed of light using the Kramer Restricted Configuration Interaction (KR CI) method, as implemented in DIRAC19. The Dirac-Hartree-Fock (DHF) calculations were first carried out to obtain the reference wavefunction for the CI step. In DHF calculations, the $3s_{1/2}$ orbital was included in the average-of-configuration open-shell framework to ensure the balanced description of the selected atomic states at the CI step and to assess the effect of relativistic stabilization of this orbital on chemical bonding in molecules. At the nominal c, the atomic states were labeled in the conventional intermediate coupling scheme. At decreased c, the states were labeled as J^{π}, where J is the value of the total angular momentum and π is the parity of the state. In all atomic calculations, the $2s$ sub-shell remained doubly occupied; therefore, in the

notation for electronic configurations $2s^2$ part is omitted. The equilibrium molecular structures of water and ammonia were obtained using the DHF method.

1. Nitrogen

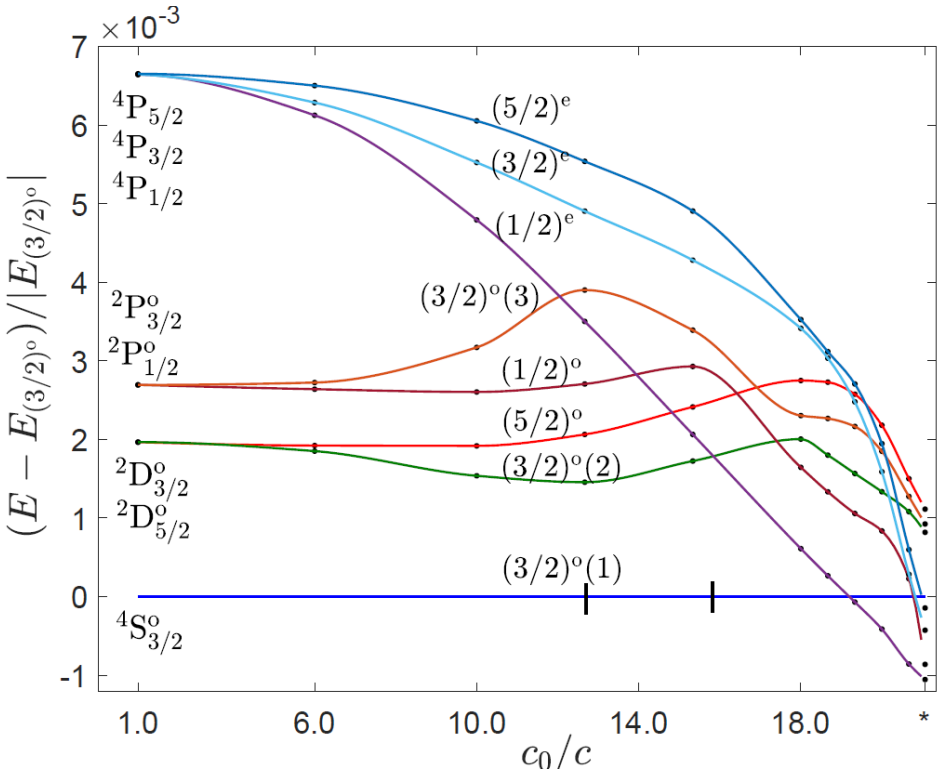

Figure 4. Energy spectrum of a nitrogen atom as a function of the speed of light (or α). The critical value of c_0/c is marked with star $(*)$.

For a nitrogen atom, we describe changes in eight lowest energy states induced by variations of c (Figure 4). The $2p^3$ ground electron configuration of the nitrogen atom produces five states arising from all possible distributions of three valence electrons over the six spin-orbitals ($2p_{1/2,\pm1/2}$, $2p_{3/2,\pm1/2}$ and $2p_{3/2,\pm3/2}$). The ground state, labeled as $^4S^o_{3/2}$ at nominal c, is the spin quartet with the total orbital angular momentum L = 0. The excited states of the $2p^3$ configuration are the spin doublet states

$^2D^o$ and $^2P^o$, where D and P stand for L = 2 and L = 1, the left superscript is the spin multiplicity, and the right superscript o indicates odd parity. Both $^2D^o$ and $^2P^o$ states split into the components with different values of the total angular momentum quantum number J, giving rise to $^2D^o_{5/2}$, $^2D^o_{3/2}$ and $^2P^o_{1/2}$, $^2P^o_{3/2}$ atomic states. The first excited configuration $2p^2 3s$ produces the following quartet states of even parity: $^4P_{1/2}$, $^4P_{3/2}$ and $^4P_{5/2}$.

At smaller c, these eight states are labeled as $(3/2)^o(1)$, $(5/2)^o$, $(3/2)^o(2)$, $(1/2)^o$, $(3/2)^o(3)$, $(1/2)^e$, $(3/2)^e$, and $(5/2)^e$, correspondingly, using the J^π notation (π is the state parity). Throughout this discussion, the "nominal" ground state $(3/2)^o$ (1), which corresponds to $^4S^o_{3/2}$ at nominal c, is used as a reference; and all state energies are reported as the ratio $(E - E_{(3/2)^o})/|E_{(3/2)^o}|$. This choice does not imply, however, that the energy of $(3/2)^o(1)$ remains unaffected as c varies. Indeed, the dominant electronic configuration of $(3/2)^o(1)$ changes twice within the variation range of c. In the range $1.0 \leq c_0/c < 13.0$, the dominant configurations are $2p^2_{1/2}2p_{3/2}$, $2p_{1/2}2p^2_{3/2}$ and $2p^3_{3/2}$. As c decreases, the splitting between the spin-orbital components $2p_{1/2}$ and $2p_{3/2}$ increases as $\sim (c_0/c)^2$ [9]. As a result, at $c_0/c \geq 13.0$, the $2p^3_{3/2}$ configuration becomes energetically unfavorable and does not contribute to the ground state. At $c_0/c \approx 15.0$, the $2p_{1/2}2p^2_{3/2}$ configuration becomes energetically unfavorable, leading to the $2p^2_{1/2}2p_{3/2}$ and $2p^2_{1/2}3p_{3/2}$ configurations dominating in the $(3/2)^o$ (1) state.

As can be seen from Figure 4, in the region $1.0 \leq c_0/c < 7.0$, the energies of the four components of the $^2D^o$ and $^2P^o$ states remain almost constant with respect to

the energy of the ground state. However, the $(5/2)^o$ and $(3/2)^o$ (2) states change order. At nominal c, $(5/2)^o$ is around 8 cm^{-1} lower in energy than $(3/2)^o$ (2). In the region $1.0 \leq c_0/c < 7.0$, both states are dominated by the $2p_{1/2}2p_{3/2}^2$ configuration. However, the $(3/2)^o$ (2) state, due to lower value of J, contains a second dominant configuration, $2p_{1/2}^2 2p_{3/2}$. As c decreases, the weight of this configuration grows because of the stabilization of the doubly occupied $2p_{1/2}$ spin-orbital. Due to this effect, the $(3/2)^o$ (2) states becomes lower in energy than $(5/2)^o$. At $c_0/c > 7.0$, components of the $^2D^o$ and $^2P^o$ states significantly split in energy due to increased relativistic effects. In case of the $(3/2)^o$ (2) and $(5/2)^o$ pair, the splitting increases due to the gradual stabilization of the doubly occupied $2p_{1/2}$ spin-orbital in the dominant configuration of the $(3/2)^o$ (2) state. In case of the $(1/2)^o$ and $(3/2)^o$ (3) pair, the splitting results from the different fraction occupation of the $2p_{3/2}$ spin-orbital in these two states. In the region, $c_0/c > 7.0$, the dominant configurations of $(1/2)^o$ and $(3/2)^o$ (3) states are $2p_{1/2}2p_{3/2}^2$ and $2p_{3/2}^3$. As c decreases, $2p_{3/2}^3$ becomes more unfavorable than $2p_{1/2}2p_{3/2}^2$. This is reflected as the sharp increase in the relative energy of the $(3/2)^o$ (3) state in Figure 4.

At smaller c, the $(3/2)^o$ (2), $(5/2)^o$, $(1/2)^o$ and $(3/2)^o$ (3) states stabilize with respect to the reference nominal ground state. This happens for two reasons. The first is appearance of the $2p_{1/2}^2 3p_{3/2}$ dominant configuration in the nominal ground state $(3/2)^o$ (1). Because the $(3/2)^o$ (1) state now contains an occupied higher energy $3p_{3/2}$ spin-orbital, it destabilizes, which results in relative stabilization of $(3/2)^o$(2), $(5/2)^o$, $(1/2)^o$, and $(3/2)^o$ (3) with respect to this reference state. The second reason is related

to the weights of dominant configurations of these four states. Since these weights vary with c, energies of these states change at different rate as c decreases. Among these four states, the strongest stabilization takes place for $(1/2)^{o}$ (Figure 4). At $c_0/c \approx 15.0$, the dominant configuration of this state switches from $2p_{1/2}2p_{3/2}^2$ to $2p_{1/2}^2 3p_{1/2}$.

The changes in the energy of the $(1/2)^{e}$, $(3/2)^{e}$ and $(5/2)^{e}$ states, which at nominal c correspond to $^4P_{1/2}$, $^4P_{3/2}$ and $^4P_{5/2}$, can be explained by noting that as c decreases, the energies of the $3s_{1/2}$ and $2p_{1/2}$ spin-orbitals decrease, while the energy of $2p_{3/2}$ increases[9]. Near the nominal c, the state $(1/2)^{e}$ is comprised of the $2p_{1/2}^2 3s_{1/2}$, $2p_{3/2}^2 3s_{1/2}$ and $2p_{1/2}2p_{3/2}3s_{1/2}$ configurations. As c decreases, the energy of the $2p_{3/2}$ spin-orbital rises destabilizing the last two configurations and leading to $2p_{1/2}^2 3s_{1/2}$ dominating in the $(1/2)^{e}$ state. In a similar manner, at $c = c_0$, $(3/2)^{e}$ and $(5/2)^{e}$ start out as the mixtures of $2p_{3/2}^2 3s_{1/2}$ and $2p_{1/2}2p_{3/2}3s_{1/2}$ configurations but become dominated by $2p_{1/2}2p_{3/2}3s_{1/2}$ as c decreases. This explains the near degeneracy of the $(3/2)^{e}$ and $(5/2)^{e}$ states at very small values of c (Figure 4). It also explains why the energy lowering of the $(3/2)^{e}$ and $(5/2)^{e}$ states proceeds at a slower rate than that of the $(1/2)^{e}$ state.

The most remarkable feature is the replacement of $(3/2)^{o}$ (1) by $(1/2)^{e}$ as the ground state of atomic nitrogen at $c_0/c \approx 19.0$. As discussed in the previous two paragraphs, for small c, the configurations of the nominal ground state $(3/2)^{o}$ (1) and the state $(1/2)^{e}$ differ only in the highest valence orbitals, ($2p_{3/2}$ or $3p_{1/2}$ in $(3/2)^{o}$ (1), and $3s_{1/2}$ in $(1/2)^{e}$). As c decreases, the relativistic contraction and the spin-orbit splitting result in the stabilization of the $3s_{1/2}$ spin-orbital relative to $3p_{1/2}$ and large

destabilization of the $2p_{3/2}$ spin-orbital. These effects lead to the $(1/2)^{e}$ state becoming more energetically favorable than $(3/2)^{o}$ (1) inducing the change of the nitrogen ground state.

2. Oxygen

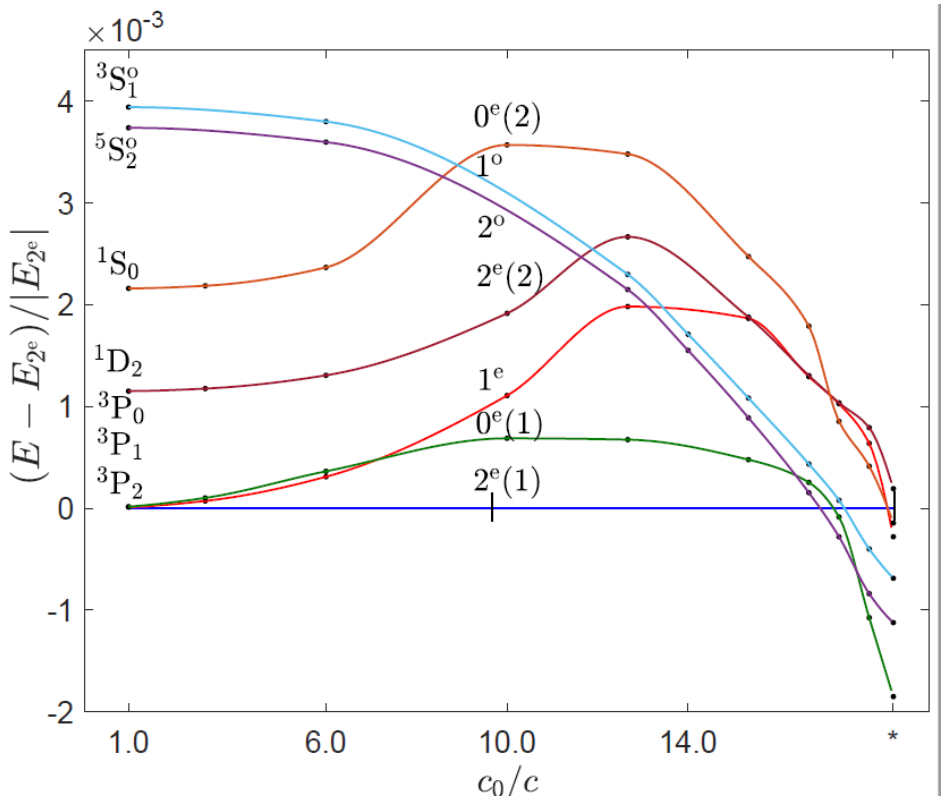

Figure 5. Energy spectrum of an oxygen atom as a function of speed of light (or α). The critical value of c_0/c is marked with star $(*)$.

For oxygen, we consider five states of even parity, $^3P_2$, $^3P_1$, $^3P_0$, $^1D_2$, and $^1S_0$, produced from the $2p^4$ ground electron configuration of oxygen. We also include the lowest $^5S_2^o$ and $^3S_1^o$ excited states of the $2p^3 3s$ configuration (Figure 5). The "nominal" ground state of oxygen is $2^e(1)$ or $^3P_2$ at c_0, and used as a reference. The electron

configuration of $2^e(1)$ state changes twice within the variation of c. In the region $1 \leq c_0/c < 10.0$, the dominant configurations of the $2^e(1)$ state are $2p_{1/2}^2 2p_{3/2}^2$ and $2p_{1/2}2p_{3/2}^3$. At $c_0/c \approx 10.0$, $2p_{1/2}2p_{3/2}^3$ becomes energetically unfavorable and does not contribute to $2^e(1)$. At $c = c^*$, the $3s_{1/2}$ spin-orbital becomes near degenerate with $2p_{3/2}$ and the promotion of a p electron to the $3s_{1/2}$ shell is possible, which leads to the $2p_{1/2}2p_{3/2}3s_{1/2}^2$ new dominant configuration of the $2^e(1)$ state. In this promotion, both the $2p_{1/2}$ and $2p_{3/2}$ electrons were transferred to conserve total angular momentum and parity.

Similar to nitrogen, there occurs "early" crossing between the 1^e (red) and $0^e(1)$ (green) states of the oxygen atom (Figure 5). At c_0, $0^e(1)$ lies 65 cm^{-1} higher in energy than 1^e. The respective dominant configurations of the $0^e(1)$ and 1^e states are i) $2p_{1/2}^2 2p_{3/2}^2$ and $2p_{3/2}^4$, and ii) $2p_{1/2}2p_{3/2}^3$. At $c_0/c \approx 7.0$, the effect of the spin-orbit splitting increases and $2p_{3/2}^4$ configuration does not contribute to the $0^e(1)$ state. Since the $2p_{1/2}^2 2p_{3/2}^2$ remaining configuration of $0^e(1)$ is more energetically favorable than $2p_{1/2}2p_{3/2}^3$ of the 1^e state, $0^e(1)$ crosses below 1^e.

The 1^e (red), $2^e(2)$ (dark red), and $0^e(2)$ (dark orange) states exhibit maxima in destabilization in the variation range of c (Figure 5). This is related to multiple changes in weights of the dominant configurations of these states. In the region $1 \leq c_0/c < 10.0$, destabilization of $0^e(2)$ is the fastest among these three states. This is explained by different fraction occupation of the $2p_{3/2}$ spin-orbital in dominant configurations of these states: $2p_{3/2}^4$ for $0^e(2)$ vs. $2p_{1/2}2p_{3/2}^3$ for 1^e and $2^e(2)$. In the same region, the $2^e(2)$ state destabilizes slightly slower than 1^e, because $2^e(2)$, in addition to

$2p_{1/2}2p_{3/2}^3$, also contains the $2p_{1/2}^2 2p_{3/2}^2$ dominant configuration. At smaller c, all these three states - 1^e, $2^e(2)$, and $0^e(2)$ - rapidly stabilize in energy. In case of the 1^e and $2^e(2)$ states, this is due to change of their dominant configurations to $2p_{1/2}^2 2p_{3/2}3p_{1/2}$ due to avoided crossings with higher lying excited states of the same value of J and parity π. In case of the $0^e(2)$ state, the stabilization at is initiated by change of the dominant configuration from $2p_{3/2}^4$ to $2p_{1/2}^2 2p_{3/2}3p_{3/2}$, which now contains doubly occupied $2p_{1/2}$ spin-orbital. At even smaller c, the dominant configuration of $0^e(2)$ changes to $2p_{1/2}^2 3s_{1/2}^2$ due to energy stabilization of the $3s_{1/2}$ spin-orbital. At near c^*, the dominant configuration of this state changes from $2p_{1/2}^2 3s_{1/2}^2$ to $2p_{1/2}^2 2p_{3/2}^2$ due to avoided crossing with the lower lying $0^e(1)$ (dark green) state.

At near c^*, there are three states - $0^e(1)$ (dark green), 2^o (magenta) and 1^o (light blue) - competing to be the new ground states (Figure 5). Their respective dominant configurations are $2p_{1/2}^2 3s_{1/2}^2$ for $0^e(1)$, and $2p_{1/2}^2 2p_{3/2}3s_{1/2}$ for 2^o and 1^o. Since the $0^e(1)$ state has no electrons on $2p_{3/2}$ and has $2p_{1/2}$ and $3s_{1/2}$ spin-orbitals doubly occupied, it wins the competition and becomes the new ground state of the oxygen atom.

3. Fluorine

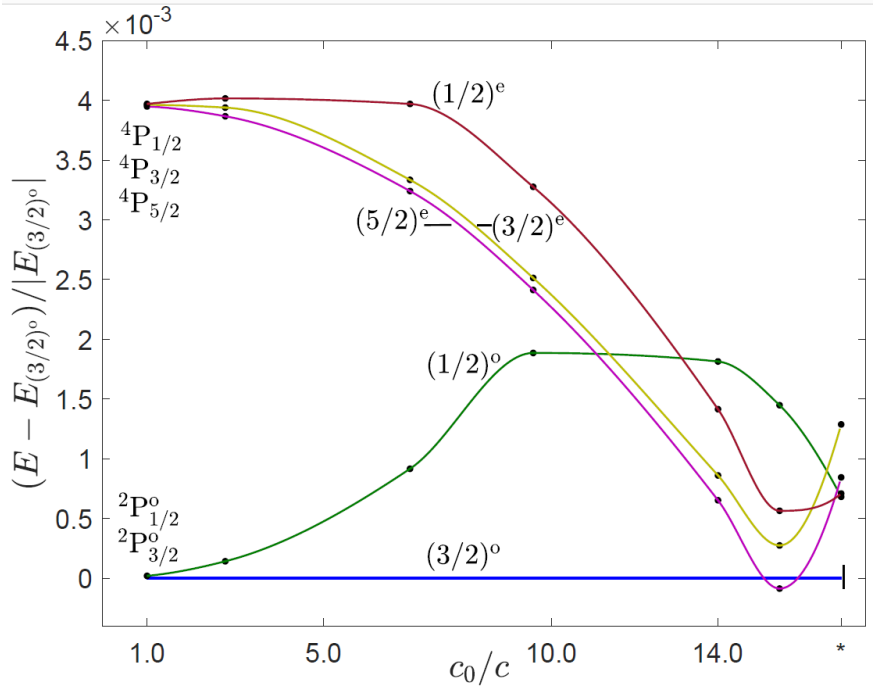

Figure 6. Energy spectrum of a fluorine atom as a function of speed of light (or α). The critical value of c_0/c is marked with star $(*)$.

For fluorine, we consider five lowest atomic states (Figure 6). The $2p^5$ ground electron configuration produces two atomic states of the odd parity, $^2\mathrm{P}^{\mathrm{o}}_{3/2}$ and $^2\mathrm{P}^{\mathrm{o}}_{1/2}$. From the $2p^4 3s$ first excited configuration of fluorine we include three low-lying states, $^4\mathrm{P}_{5/2}$, $^4\mathrm{P}_{3/2}$ and $^4\mathrm{P}_{1/2}$. The nominal ground state, $(3/2)^{\mathrm{o}}$, consists of a single dominant configuration $2p^2_{1/2}2p^3_{3/2}$ for all c larger than c^*. A single hole in this configuration prevents recombination of electrons among $2p$ spin-orbitals. Therefore, the ground state configuration can be changed only if electrons are transferred to virtual spin-orbitals, among which $3s_{1/2}$ is the lowest. To conserve parity of $(3/2)^{\mathrm{o}}$, two electrons need to be transferred from $2p$ to $3s_{1/2}$ which requires substantial energy. As a result, the change in the ground state configuration takes place only close to c^*, when

the $3s_{1/2}$ spin-orbital lowers in energy enough to facilitate the electron transfer, and the new dominant configuration of the $(3/2)^{o}$ ground state changes to $2p_{1/2}^2 2p_{3/2} 3s_{1/2}^2$.

In the region $1 \leq c_0/c < 10.0$, there occurs rapid destabilization of the $(1/2)^{o}$ state (Figure 6). It can be explained by the fourfold occupied $2p_{3/2}$ spin-orbital in its single dominant configuration of $2p_{1/2}2p_{3/2}^4$. In the region $10.0 \leq c_0/c \lesssim 14.0$, however, the $(1/2)^{o}$ state becomes quasi-constant. This is due to change of the dominant configuration to $2p_{1/2}^2 2p_{3/2}^2 3p_{3/2}$, which is in close resemblance with the dominant configuration $2p_{1/2}^2 2p_{3/2}^3$ of the reference ground state. At c^*, the $(1/2)^{o}$ state stabilizes in energy as its dominant configuration changes to $2p_{1/2}^2 3s_{1/2}^2 3p_{1/2}$.

The $(5/2)^{e}$ (magenta), $(3/2)^{e}$ (gold) and $(1/2)^{e}$ (dark red) states begin to rapidly stabilize at near nominal c as they contain singly occupied $3s_{1/2}$ in their dominant configurations: $2p_{1/2}^2 2p_{3/2}^2 3s_{1/2}$ and $2p_{3/2}^4 3s_{1/2}$ for $(1/2)^{e}$, and $2p_{1/2}^2 2p_{3/2}^2 3s_{1/2}$ and $2p_{1/2}2p_{3/2}^3 3s_{1/2}$ for $(3/2)^{e}$ and $(5/2)^{e}$. Close to c^*, $2p_{1/2}^2 2p_{3/2}^2 3s_{1/2}$ remains the only dominant configuration of these states and there occurs a temporary change of the ground state of fluorine from $(3/2)^{o}$ to $(5/2)^{e}$. At $c_0/c \approx 15.0$, the dominant configurations of these two states are $2p_{1/2}^2 2p_{3/2}^3$ for $(3/2)^{o}$ and $2p_{1/2}^2 2p_{3/2}^2 3s_{1/2}$ for $(5/2)^{e}$. Since the $(5/2)^{e}$ state contains singly occupied $3s_{1/2}$ spin-orbital, in contrast to $(3/2)^{o}$, it becomes lower in energy and the new ground state. However, at critical c, as the dominant configuration of the "nominal" ground state $(3/2)^{o}$ changes to $2p_{1/2}^2 2p_{3/2} 3s_{1/2}^2$, $(3/2)^{o}$ again becomes lower in energy than $(5/2)^{e}$ and restores as the ground state of the fluorine atom.

4. Neon

At nominal $c = c_0$, the $2p^6$ ground electronic configuration of neon gives a single atomic state of the even parity, $^1S_0$. The $2p^5 3s$ first excited configuration contains four excited states of the odd parity, $^2[3/2]^o_2$, $^2[3/2]^o_1$, $^2[3/2]^o_0$, and $^2[1/2]^o_1$. The second excited configuration, $2p^5 3p$, produces a manifold of atomic states of the even parity, among which we include three lowest states, $^2[1/2]_1$, $^2[5/2]_3$, and $^2[5/2]_2$. We therefore include a total of eight atomic states of neon in our discussion (see Figure 6.3 in the main text). At smaller c, these states are labeled as 0^e, 2^o, $1^o(1)$, 0^o, $1^o(2)$, 1^e, 3^e, and 2^e.

In the range $1 \leq c_0/c < 14.0$, the 0^e "nominal" ground state retains its closed-shell configuration of $2p^2_{1/2}2p^4_{3/2}$. At $c_0/c \approx 14.0$, $2p^2_{1/2}2p^2_{3/2}3s^2_{1/2}$ becomes the second dominant configuration of 0^e due to the electron transfer from $2p_{3/2}$ to $3s_{1/2}$. At c^*, the closed-shell configuration does not contribute to the ground state and $2p^2_{1/2}2p^2_{3/2}3s^2_{1/2}$ becomes the only dominant configuration of 0^e.

At c close to c^*, the 2^o and 2^e states cross below the nominal ground state. The 2^o state contains a single configuration of $2p^2_{1/2}2p^3_{3/2}3s_{1/2}$, which remains dominant at all values of c. At $c \lesssim c^*$, 2^o crosses the 0^e nominal ground state in the reverse direction, becoming back higher in energy. It can be explained by rapid stabilization of the nominal ground state at c^*, when the $2p^2_{1/2}2p^4_{3/2}$ configuration drops off 0^e. As a consequence, the 0^e state stabilizes faster than 2^o, which is reflected as reverse crossing. At near c^*, the other crossing state, 2^e, contains a single dominant configuration of $2p^2_{1/2}2p^2_{3/2}3s^2_{1/2}$, which is the same as of the 0^e state at the same c. However, total angular momentum J of the 2^e state equals two and is than J equals zero

of the 0^e nominal ground state. Therefore, according to the third Hund's rule, 2^e becomes the new ground state of neon.

D. Molecules

In relativistic picture, the states of atoms and molecules are described by four component Dirac spinors $\psi = (\psi_L^\alpha, \psi_L^\beta, \psi_S^\alpha, \psi_S^\beta)^T$, where L and S correspond to the large and small components of the spinor (not to be confused with the total orbital angular and spin momenta), and α and β describe spin degrees of freedom. The spinor components are in general complex functions, and therefore, the Dirac spinor has eight degrees of freedom. Since the Dirac Hamiltonian commutes only with the total angular momentum J, the spatial and spin degrees of freedom are coupled. Consequently, the symmetry of the Dirac spinors is described by double groups, where the total spinor transforms under the fermion irreducible representations spanned by the half-integer spin functions[7]. However, the real and imaginary parts of each spinor component are spanned by boson irreducible representations, which are the irreducible representations of conventional single point groups. Therefore, each spinor component can be described by scalar functions, 'orbitals'. The symmetries of the ammonia and water molecules are described by the C_{3v} and C_{2v} double groups. For example, by exploiting the symmetry of the Dirac Hamiltonian, it can be shown that in the C_{2v} double group, the real and imaginary parts of the large component transform under (a_1, a_2) and (b_1, b_2) boson irreducible representations for ψ_L^α and ψ_L^β, correspondingly[7]. At nominal c, the molecular orbitals of ammonia and water are spanned only by a real or imaginary part of a single component, neglecting the vanishing contributions from other components.

Therefore, these orbitals are described by a single irreducible representation, in compliance with results from non-relativistic calculations. At decreased c, however, the molecular orbitals become spanned by multiple real and imaginary parts of the spinor components. Therefore, no longer a single irreducible representation can be assigned to molecular orbitals when relativity is strongly increased, that is when values of c largely decreased from nominal. For this reason, the symmetry labels in orbital diagrams of ammonia and water are kept only at nominal speed of light, and are excluded otherwise.

In the water molecular orbital diagram (Figure 6.4 in the main text), the σ and σ^* linear combinations of $1s$ orbitals of two hydrogen atoms have the a_1 and b_2 symmetries. At nominal c, the atomic spin-orbitals of oxygen have symmetries of a_1 for $2s_{1/2}$ and $3s_{1/2}$, and a_1, b_2, and b_1 for spatial components of each $2p$ spin-orbital. In the ammonia molecular orbital diagram, the three linear combinations ψ_1, ψ_2, and ψ_3 of $1s$ orbitals of three hydrogen atoms have a_1 and doubly degenerate e symmetries. At nominal c, the atomic spin-orbitals of nitrogen have symmetries of a_1 for $2s_{1/2}$ and $3s_{1/2}$, and a_1 and e for spatial components of each $2p$ spin-orbital. In atomic calculations of oxygen and nitrogen, the $3s_{1/2}$ spinor was included in the average-of-configuration Dirac-Hartree-Fock method to assess effect of stabilization of higher lying spinors on molecular bonding. For clearer comparison of diagrams, we keep the energy unit constant and equal to those at nominal c.

1. Water

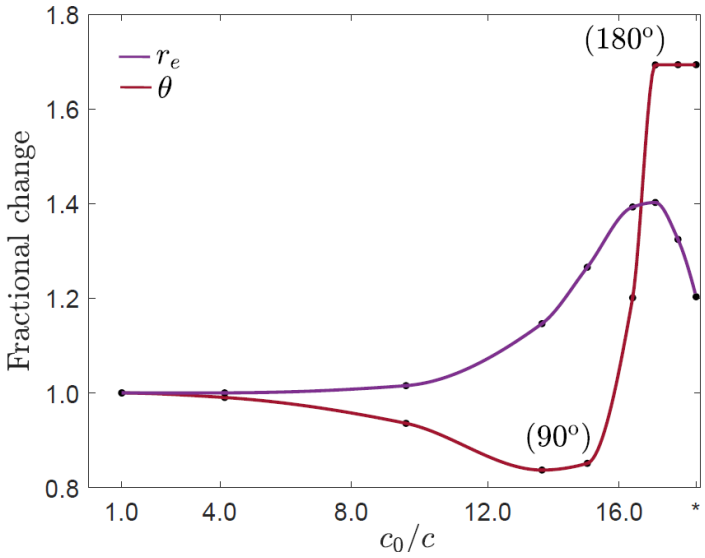

Figure 7. Changes in equilibrium geometry of a water molecule induced by variation of c from nominal to critical value (marked with * on the x-axis): c_O^*= 7.46 (or equivalently c_0/c_O^* = 18.4). The changes in the O-H bond distance and the H-O-H bond angle are shown as fractional changes.

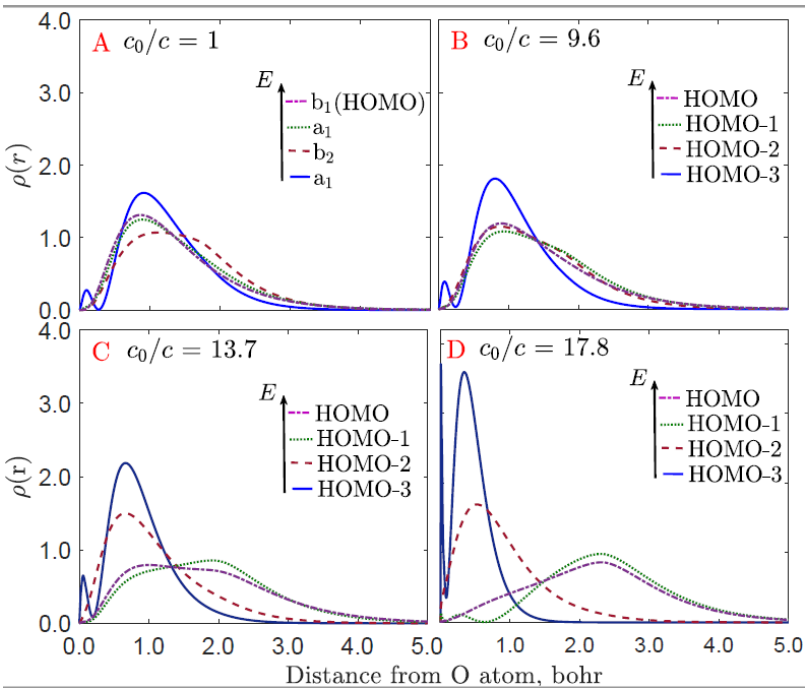

Figure 8. Radial density distributions (RDDs) of four MOs of water at different values of c. The oxygen atom is put to the coordinate origin. The MOs are given in the increasing energy order: dark blue solid line (HOMO-3), dark red dashed line (HOMO-

2), dark green dotted line (HOMO-1), and magenta dot-dashed line (HOMO). For clearer comparison, distance is given in unit of unscaled nominal bohr radius.

2. Ammonia

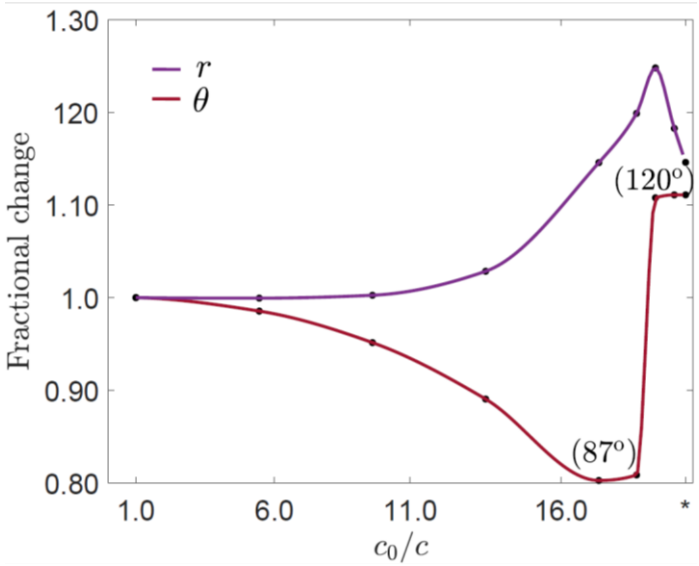

Figure 9. Changes in equilibrium geometry of an ammonia molecule induced by variation of c from nominal to critical value (marked with * on the x-axis): c_{N}^{*}= 6.5 (or equivalently c_0/c_{N}^{*} = 20.9). The changes in the N-H bond distance and the H-N-H bond angle are shown as fractional changes.

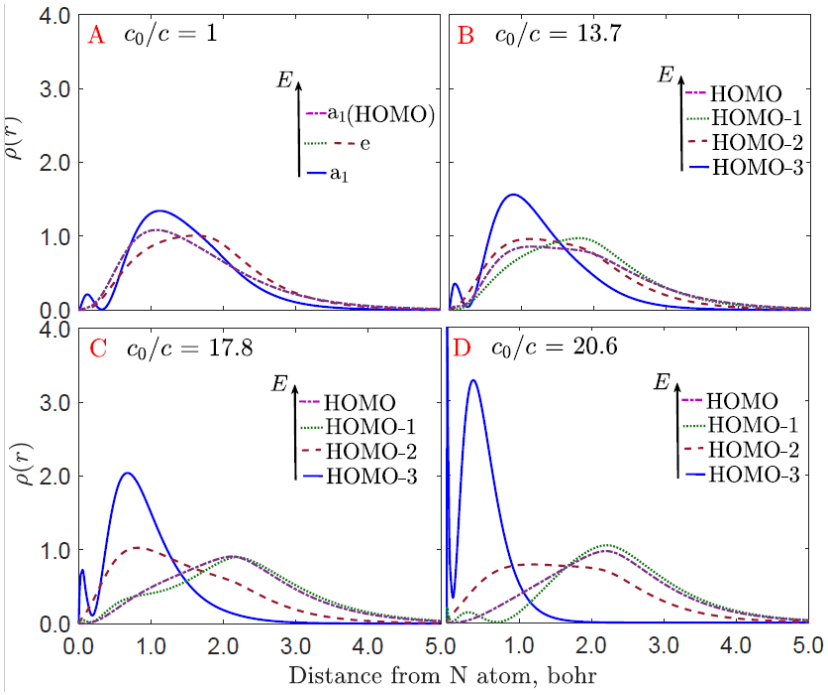

Figure 10. Radial density distributions (RDDs) of four valence MOs of ammonia at different values of the speed of light *c*. The nitrogen atom is put to the coordinate origin. The MOs are given in the increasing energy order: dark blue solid line (HOMO-3), dark red dashed line (HOMO-2), dark green dotted line (HOMO-1), and magenta dot-dashed line (HOMO). For clearer comparison, distance is given in unit of unscaled nominal bohr radius.

References

(1) Greiner, W.; Reinhardt, J. *Quantum Electrodynamics*, 3rd ed.; Springer-Verlag, 2002.

(2) Zeldovich, Y. B.; Popov, V. S. Electronic structure of superheavy atoms. *Soviet Physics Uspekhi* **1972** *14*, 673. http://dx.doi.org/10.1070/PU1972v014n06ABEH004735.

(3) Tiesinga, E.; Mohr, P. J.; Newell, D. B.; Taylor, B. N. Web Version 8.1, Tech. Rep. National Institute of Standards and Technology, Gaithersburg, MD 20899, 2020.

(4) Johnson, W. R. Atomic Structure Theory: Lectures on Atomic Physics. Springer-Verlag, Berlin Heidelberg, 2007.

(5) Johnson, W. R.; Soff, G. Atomic Data and Nuclear Data Tables *33*, 405, 1985.

(6) Ferreira, E. M.; Sesma, J. *J. Comput. Appl. Math.* **2008** *211*, 223, arXiv:0607471 [math].

(7) Saue, T.; Jensen, H. J. Aa. Quaternion symmetry in relativistic molecular calculations: The Dirac-Hartree-Fock method. *J. Chem. Phys.* **1999** *111* (14), 6211 – 6222. https://doi.org/10.1063/1.479958.

(8) Saue, T.; Bast, R.; Gomes, A. S. P.; Jensen, H. J. A.; Visscher, L.; I. A. Aucar, I. A.; Di Remigio, R.; Dyall, K. G.; Eliav, E.; Fasshauer, E.; Fleig, T.; Halbert, L.; Hedegård, E. D.; Helmich-Paris, B.; Iliaš, M.; Jacob, C. R.; Knecht, S.; Laerdahl, J. K.; Vidal, M. L.; Nayak, M. K.; Olejniczak, M.; Olsen, J. M. H.; Pernpointner, M.; Senjean, B.; Shee, A.; Sunaga, A.; van Stralen, J. N. The DIRAC code for relativistic molecular calculations. *J. Chem. Phys.* **2020** *152* (20), 204104. https://doi.org/10.1063/5.0004844.

(9) Dzuba, V. A.; Flambaum, V. V.; Webb, J. K. Calculations of the relativistic effects in many-electron atoms and space-time variation of fundamental constants. *Phys. Rev. A* **1999**, *59* (1), 230-237. https://doi.org/10.1103/PhysRevA.59.230